

ABSTRACT

HUSSAIN, MAQBOOL. Tuning Ground and Excited States Oxidation Potentials of Novel Ru (II) Polypyridyl Complexes for High Efficiency Dye-sensitized Solar Cells. (Under the direction of Dr. Ahmed El-Shafei.)

Dye-sensitized solar cells (DSSCs) are a potential alternative to traditional silicon solar cells because of their cost-effective solar-to-power conversion and wide arrays of practical applications. DSSCs based on polypyridyl Ru (II) complexes have attracted strong attention due to their unique photophysical and electrochemical properties. N719 is the most commonly used polypyridyl Ru (II) complex and is considered the benchmark dye for DSSCs. However, its hydrophilic nature, low molar absorptivity and low long-term device stability, due to the labile isothiocyanate (NCS), are properties that need improvements. Further advancement of Ru (II) complexes, however, requires deeper understanding of electronic, kinetic and thermodynamic properties of sensitizers at the molecular level. With this in mind, this research effort is devoted to the design, synthesis and characterizations of nine novel bipyridyl Ru (II) complexes for DSSCs. These Ru (II) complexes are based on novel ancillary bidentate ligands functionalized from 4,4'-dimethyl-2,2'-bipyridyl using the Knoevenagel reaction. The new heterocyclic ancillary ligands were engineered with strong electron donating groups coupled with an extended π -conjugated system to study the influence of different homo and heterocyclic electron donors on the interrelationship among the photophysical, electrochemical and photovoltaic properties of DSSCs. Incorporation of strong electron donating groups and extending the conjugations on the bipyridyl moiety furnished efficient light harvesting properties and a bathochromic shift in the UV-Vis spectra compared to **N719**. This was attributed to electron donor destabilization of the HOMO of Ru,

leading to a smaller HOMO-LUMO energy gap, smaller zero-zero electronic excitation energy (E_{0-0}), and hence better light harvesting properties. Furthermore, these new ancillary ligands were also engineered so that their LUMOs lie above the conduction band edge of TiO_2 , to maintain thermodynamically favorable electron injection from the excited states, and their HOMOs lie below the redox potential of the electrolyte to maintain thermodynamically favorable dye regeneration.

Complexes MH06 and MH11 were molecularly engineered with strong electron donating group coupled with extended π -conjugated system. In an effort to understand their photovoltaic and photoelectrochemical properties, ground and excited state oxidation potentials and UV-Vis absorption properties were investigated. The UV-Vis results showed intense MLCT absorption peaks of MH06 and MH11 in the visible region with red shift of 12 and 18nm, respectively, with significantly higher molar extension coefficient compared to N719. Tetrabutylammonium (TBA) substituted MH11-TBA demonstrated the most efficient IPCE over 90% in the plateau region covering the entire visible spectrum and extended into the near IR region (ca. 890 nm), which showed a solar-to-power conversion yield (η) of 10.06%, significantly higher than that of benchmark N719-dye (9.32%). The superior performance of the IPCE and J_{sc} of MH11 can be attributed to the bulky and highly hydrophobic nature of the pyrene-based ancillary ligand, which behaves as a shielding barrier for hole-transport recombination between TiO_2 and electrolyte.

Complexes, MH01, MH03, and MH05, with oxygen-containing-electron-donor stilbazole-based ancillary ligands were synthesized to study the influence of cyclic-electron-donor (MH01), presence of freely rotating electron-donor auxochromes (MH03) *ortho* to the

CH=CH bridge of stilbazole, and presence of only acyclic electron-donor methoxy (MH05) on structure-property relationship and photovoltaic performance for DSSCs. The highest photocurrent density (J_{SC}) was observed for the longest interatomic distance between the CH=CH bridge of stilbazole moiety and cyclic-electron-donor auxochrome (MH01). It was also shown that while incorporation of a freely-rotating (acyclic) electron-donor auxochrome *ortho* to the CH=CH (MH03) has little effect on the ground and excited state oxidation potentials, λ_{max} of the low energy MLCT, and molar absorptivity, the lowest photovoltage was observed. When compared under the same experimental device conditions using 0.3M tert-butylpyridine (TBP) only MH01-TBA achieved 18% more in J_{SC} and 8.6% higher in η than the reference dye N719.

© Copyright 2013 Maqbool Hussain

All Rights Reserved

Tuning Ground and Excited States Oxidation Potentials of Novel Ru (II) Polypyridyl
Complexes for High Efficiency Dye-sensitized Solar Cells

by
Maqbool Hussain

A dissertation submitted to the Graduate Faculty of
North Carolina State University
in partial fulfillment of the
requirements for the degree of
Doctor of Philosophy

Fiber and Polymer Science

Raleigh, North Carolina

2013

APPROVED BY:

Dr. Ahmed El-Shafei
Committee Chair

Dr. Harold S. Freeman

Dr. Peter Hauser

Dr. David Hinks

BIOGRAPHY

Maqbool Hussain was born in Astore-Gilgit, Pakistan. He completed his high schooling from Gilgit and then moved to Karachi for further studies. He obtained his Bachelor of Science and Masters degree in Chemistry (2003) from the University of Karachi with 1st class marks. Following completion of his Masters degree, he joined Liberty Textiles Mill, where he worked as senior chemist for five years. In the meantime, he was awarded an “international research support initiative scholarship” from the Higher Education Commission of Pakistan to carry out collaborative research work at North Carolina State University with Dr. Renzo Shamey, Dr. David Hinks and Dr. Ahmed El-Shafei for six months. After completion of this project, Dr. El-Shafei offered him a research assistantship. In January 2009, Maqbool joined the Ph.D. Fiber and Polymer Science Program at North Carolina State University where he was actively involved in extracurricular activities. He served as Vice-President of the Textiles Association for Graduate Students and was a member of a diversity committee at the College of Textiles. He enjoyed living in the city of Raleigh, North Carolina, with its suburban greenery and unpredictable weather, and the hospitality of the North Carolina State University Community.

ACKNOWLEDGMENTS

The author would like to first thank his Ph.D. advisor, Dr. El-Shafei, for his encouraging guidance and exceptional support throughout this research and dissertation process. The author is also grateful to Dr. El-Shafei for his kind assistance, wise suggestions, enlarging his views with various academic and research challenges and preparing the manuscripts. Appreciation is also extended to Dr. Renzo Shamey, Dr. David Hinks and Dr. Rust for their wonderful support and constant guidance throughout his stay at North Carolina State University. Author is sincerely thankful to his committee members including Dr. Freeman, Dr. Hinks, and Dr. Hauser for their advice, time and support. Appreciation also goes to Dr. Ashraf Islam and Prof. Liyuan Han at the National Institute for Materials Science, Tuskuba, Japan, for helping with device optimization and photovoltaics measurements.

He would also like to thank Andrew, Aasim Atiq, Hammad Cheema, Birgit Andersen and Judy Elson for sharing their knowledge and providing hands-on support, helpful discussions and instrumentation. He also appreciates his friends especially Aisha Khan for her helpful discussions, support and encouragement. The author would like to express his deep gratitude to his loving mother and other family members for their precious love, prayers and support throughout the years.

Author is also thankful to the College of Textiles, Graduate School of North Carolina State University for the financial support of his Ph.D degree.

TABLE OF CONTENTS

LIST OF TABLES.....	viii
LIST OF FIGURES.....	ix
LIST OF ABRIVATIONS.....	xii
CHAPTER 1: INTRODUCTION	1
1.1. Introduction to Dye-sensitized Solar Cells.....	2
1.2. Components of Dye-sensitized Solar Cells	3
1.3. Dye-sensitizers	5
1.4. Dye-sensitizers Requirement.....	6
1.5. Molecular Engineering for Optimization of DSSCs	8
1.5.1. Panchromatic Dye-sensitizers	8
1.5.2. Modifying the Oxidation Potential of Sensitizers	12
1.5.3. Strategies to Extend the Excited State Life Time.....	17
1.5.4. Minimizing the Charge Recombination Reactions.....	20
1.6. The Usage of Co-adsorbent.....	33
1.7. The Interaction between Sensitizer and Electrolyte	38
1.8. Electrolyte Additives.....	41
REFERENCES	45
CHAPTER 2: RESEARCH PROPOSAL	53
2.1. Research Objects	54

2.2. Proposed Ru (II) Bipyridyl Sensitizers	56
CHAPTER 3: STRUCTURE-PROPERTY RELATIONSHIP.....	58
Abstract.....	59
3.1. Introduction	59
3.2. Experimental	60
3.2.1. Synthesis of Ru (II) bipyridyl complexes.....	60
3.2.2. UV-Visible and Emission Properties	61
3.2.3. Ground and Excited State Potentials Properties.....	62
3.2.4. Photovoltaic Device Characterizations	63
3.2.5. CEM and IMVS Characterization	63
3.2.6. Electrochemical Impedance Spectroscopy Characterization.....	65
CONCLUSIONS	65
REFERENCES	65
SUPPORTING INFORMATION	67
CHAPTER 4: STERRIC/ISOMERIZATION EFFECTS	82
Abstract.....	83
4.1. Introduction	84
4.2. Result and Discussion	87
4.2.1. Proposed Reaction Mechanism.....	86
4.2.2. UV-Visible Spectra	89

4.2.3. Electrochemical Data	90
4.2.4. DFT/TD-DFT calculations.....	94
4.2.5. Photovoltaic Properties	94
4.2.6. Photovoltaic Properties	94
4.2.7. CEM and IMVS Characterization	98
4.2.8. EIS Characterization	99
4.2.9. Long-term Stability Measurements of Complexes and Devices	102
CONCLUSIONS	106
REFERENCES	108
SUPPORTING INFORMATION	111
CHAPTER 5: STRUCTURE-PROPERTY RELATIONSHIP	136
Abstract	137
5.1. Introduction	137
5.2. Experimental Section	139
5.3. Results and Discussion.....	141
5.3.1. UV-Visible Absorption	141
5.3.2. Electrochemical Data	142
5.3.3. DFT/TD-DFT Calculations	142
5.3.4. Attenuated Total Reflectance-FTIR	144
5.3.5. Photovoltaic Properties	144
CONCLUSIONS	145

REFERENCES	146
SUPPORTING INFORMATION	149
GENERAL CONCLUSIONS	163

LIST OF TABLES

Table 1. 1. Some representative of Ru (II) polypyridyl dye-sensitizers	25
Table 1. 2. The molecular structures of some representative co-adsorbents	35
Table 1. 3. The molecular structures of some representative additives	43
Table 2. 1. Ru(II) polypyridyl complexes and molecular structures of ligands (Ar).....	57
Table 3. 1. Absorption, luminescence properties of MH06	61
Table 3. 2. Shows the excited state oxidation potential of MH06	62
Table 3. 3. Photovoltaic characteristic of MH06	63
Table 4. 1. Absorption, luminescence and electrochemical properties of MH01	89
Table 4. 2. Experimental and calculated ground and excited state oxidation potentials	91
Table 4. 3. Photovoltaic performance of complexes MH01-TBA	97
Table 5. 1. Absorption, luminescence properties for MH08-10	142
Table 5. 2. Calculated and experimental ground and excited states energy levels.....	142
Table 5. 3. Photovoltaic performance of MH08-TBA, MH08-10	144

LIST OF FIGURES

Figure 1. 1. A schematic diagram of photo-induced metal-to-ligand charge transfer	5
Figure 1. 2. The molecular structures of Ru (II) polypyridyl Dye-sensitizers.....	8
Figure 1. 3. Molecular structures of Ru (II) polypyridyl	11
Figure 1. 4. Molecular structures of Ru (II) polypyridyl	12
Figure 1. 5. Illustration of the thermodynamically favorable interfacial	13
Figure 1. 6. Thiocyanates free (-NCS) Ru (II) Polypyridyl heteroleptic	14
Figure 1. 7. Excited-state stabilization through cyclometalization.....	16
Figure 1. 8. Ru (II) tridentate dye-sensitizer strong σ -donors	18
Figure 1. 9. Molecular structure of substituted phenyl groups	19
Figure 1. 10. A schematic diagram of the electron injection	21
Figure 1. 11. The schematic diagram of long-lived charge separation process	22
Figure 1. 12. Ru (II) bipyridyl dye-sensitizer that contains a strong electron donating	23
Figure 1. 13. Molecular structure of donor-acceptor type co-adsorbents	37
Figure 1. 14. Molecular structure of Z-709 and 1-Decylphosphonic acid.....	38
Figure 1. 15. Molecular structure of the different cobalt polypyridyl redox	39
Figure 1. 16. Molecular structure of heteroleptic ruthenium (II) polypyridyl	40
Figure 2. 1. A schematic representation of modifying ground	55
Figure 2. 2. Proposed bidentate Ru (II) polypyridyl dye-sensitizers	56
Figure 3. 1. Illustration of the thermodynamically favorable interfacial	66
Figure 3. 2. Molecular structures of complexes MH06 and MH11	61
Figure 3. 3. UV-Vis absorption (solid-line) and emission spectra MH06	61

Figure 3. 4. UV-Vis absorption spectra of complexes.....	62
Figure 3. 5. Calculated HOMO and LUMO isosurfaces of MH01 and MH11	62
Figure 3. 6. Photocurrent action spectra (IPCE) obtained with dyes MH01 and MH11	63
Figure 3. 7. Photocurrent voltage characteristics of DSSCs sensitized	64
Figure 3. 8. Voc as a function of electron density	64
Figure 3. 9. Electron lifetime (τ) as a function of Voc for DSCs sensitized.....	64
Figure 3. 10. Schematic representation of MH11 anchored on	64
Figure 3. 11. EIS Nyquist plots.....	65
Figure 3. 12. EIS Bode plots.....	65
Figure 4. 1. Molecular structures of Z-907, Z-910, K19, and K73.....	85
Figure 4. 2. Molecular structures of dye-N719, MH01-TBA.....	86
Figure 4. 3. Proposed reaction mechanism	87
Figure 4. 4. UV-Vis absorption and emission spectra of.....	89
Figure 4. 5. Calculated isosurfaces of the HOMO (left) and LUMO	94
Figure 4. 6. Photocurrent action spectra (IPCE).....	95
Figure 4. 7. Photocurrent voltage characteristics.....	98
Figure 4. 8. Voc as a function of electron density	99
Figure 4. 9. Electron lifetime (τ) as a function of Voc	100
Figure 4. 10. EIS Nyquist plots.....	101
Figure 4. 11. EIS Bode plots.....	102
Figure 4. 12. Absorption spectra of MH01 and MH03 adsorbed on	104
Figure 4. 13. Evolutions of photovoltaic performance parameters.....	104

Figure 5. 1. Tuning HOMO/LUMO gap of MH08-10 for high efficiency DSSCs	138
Figure 5. 2. Molecular structures of complexes MH08-TBA, MH08-10	138
Figure 5. 3. UV-Vis absorption (solid-line) and emission spectra	141
Figure 5. 4. Absorption spectra of MH08-10 adsorbed on nonporous TiO ₂	142
Figure 5. 5. Calculated isosurfaces of the HOMO (left) and LUMO	143
Figure 5. 6. Photocurrent action spectra (IPCE)	144
Figure 5. 7. Photocurrent voltage characteristics	145
Figure 5. 8. Interrelationship between experimental ESOP and JSC of MH08-10	145

LIST OF ABBREVIATIONS

ϵ_{max} :	molar extension coefficient
λ_{max} :	absorption maximum wavelength
π :	bonding orbital
π^* :	anti-bonding orbital
τ	emission decay lifetime
η :	solar-to-power conversion efficiency
AM:	air mass
CB:	conduction band
CEM:	charge extraction method
DFT:	density functional theory
DMPII:	dimethylpropyl-imidazolium iodide
DSSCs:	dye sensitized solar cells
EIS:	electrochemical impedance spectroscopy
ESI-MS:	electrospray ionization mass-spectroscopy
ESOP:	excited state oxidation potential
FF:	fill factor
GSOP:	ground state oxidation potential
HOMO:	highest occupied molecular orbital
IMVS:	intensity modulated photovoltage spectroscopy
IP:	ionization potential
IPEC:	incident photon to current conversion efficiency

J_{sc} :	short-circuit photocurrent density
LUMO:	lowest unoccupied molecular orbital
MC:	metal (centralized) charge transfer
MH	Maqbool Hussain
MLCT:	metal-to-ligand charge transfer transition
TBA:	tetrabutylammonium
TBP:	4-ter-butylpyridine
TCSPC:	time-correlated single photon counting
V_{oc} :	open-circuit voltage

CHAPTER 1

1. INTRODUCTION

1.1. Introduction to Dye-sensitized Solar Cells

Today human society is facing enormous pressure because of increasing energy demand and depletion of energy resources. Also, emissions from burning fossil fuels contributing to global warming and air pollution that affecting human life with chronic illnesses. Therefore, alternative sustainable and renewable energy sources are vital to fulfill the increasing global energy demand. Among renewable sources, solar energy is abundant and freely available with sunlight supplied directly to planet Earth. The amount of solar energy reaching the Earth's surface is 3×10^{24} Joules per year, covering only 0.13% of the Earth surface with solar cells that have an efficiency of about 10% could be enough to meet the present global energy needs.¹ In addition, solar energy is environmentally friendly, abundant, and exploitable. It is ideal for remote and mobile applications, which can be produced and handled locally or individually instead of producing them only at a centralized energy system through a corporate or a state entity. Rapid advancement of photovoltaic technologies is hope and potentials breakthroughs in the field of green energy. Among photovoltaic technologies, dye-sensitized solar cells (DSSCs) are emerging as a promising solar technology based on low-cost materials.

In 1976, a new approach to photovoltaic energy conversion by dye-sensitization was reported by Tributsch, who demonstrated a solar-to-power conversion efficiency of 1.5% using Rose Bengal as a dye-sensitizer and zinc oxide (ZnO_2) as a semiconductor.² Nearly two decades later (1991), O'Regan and Graetzel achieved a remarkable efficiency of 7.9% using Ru (II)

bipyridyl complex (N3) as a sensitizer and TiO₂ as a semiconductor.³ To date, the maximum efficiency achieved of DSSCs has been 12.3% by co-sensitization of an organic (Y123) and a phorpherene complex (YD2-o-C8), using Co(II/III)tris(bipyridyl) based redox electrolyte,⁴ which is about half the 15% to 20% module efficiencies of silicon-cells⁵ and comparable to thin-film technologies with module efficiencies of 10–12.5%.⁴ Overall, the DSSCs currently stand out as economical and the most efficient among the third generation solar technologies.⁶ However, in order to compete over the photovoltaic and fossil fuel market, it is important to further improve the solar-to-power efficiency of these devices beyond the current benchmark of 12.1%.⁷

1.2. Components of Dye-sensitized Solar Cells

DSSCs are composed of five main components including a dye-sensitizer, an electrolyte, a semiconductor (e.g., TiO₂, ZnO), a counter electrode, and conducting glass. The device is prepared by sandwich arrangement of two transparent conducting electrodes. The transparent conducting glass (TCG) is normally fluorine doped tin oxide (TTO: F-SnO₂) because of its reasonable conductivity and stability.⁸⁻⁹ The top of the TCG layer, a thin porous layer (~ 20 nm), is coated with a semiconductor oxide (TiO₂/ ZnO₂) paste with a particle size of 10-15 μm (thick) forming a highly porous layer using screen printing/ doctor blading.¹⁰ A sufficient amount of dye-sensitizer loading is achieved with a surface area 1000 times larger than the electrode's actual area. The plate is immersed in a sensitizer solution to allow covalent bonding between the TiO₂ and the dye-sensitizer molecule. The top of the

TCG is coated with finely deposited platinum, forming a counter electrode. Both conducting electrodes are joined together to form a cell. The inter-layer space is then filled with a redox electrolyte solution to form a contact between the dye-sensitizer molecule and platinum (Pt) coated counter electrode. Typically the redox electrolyte is a mixture of iodine and iodide in an organic solvent acting as a mediator. Finally, both electrodes are sealed together with a sealant in order to prevent the evaporation of the solvent.

The DSSCs function by converting solar photons into usable energy through photoelectrochemical process. This occurs as photons interact with dye molecules and produce electrons in the excited energy state. On exposure to sunlight, the solar cell starts to work with the ultrafast injection of electrons from the excited state of the dye-sensitizer to the conduction band of semiconductor oxide. This electron is further transported to the outer circuit where it attracted towards counter electrode that ultimately generates electrical current. Same time, the iodide/triiodide electrolyte acts as a redox species by regenerating the dye via electron transfer and subsequent reduction at the counter electrode. A schematic diagram of a dye-sensitization process, components and current flow in solar cell is shown in Figure 1-1.

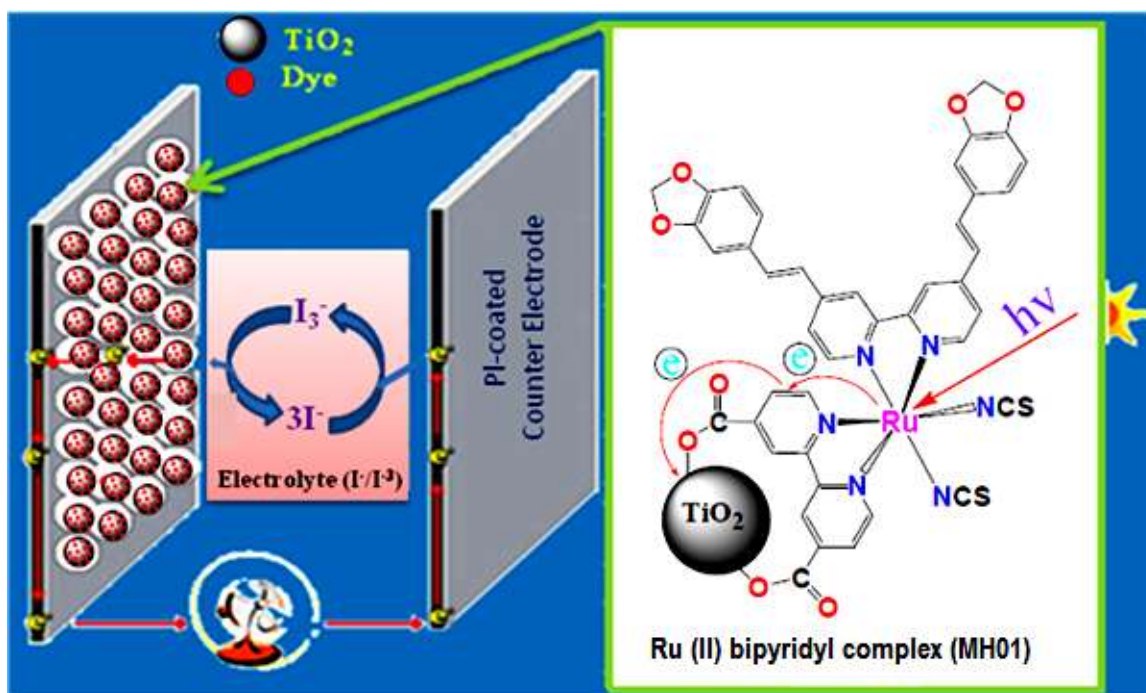


Figure 1-1. A schematic diagram of photo-induced metal-to-ligand charge transfer (MLCT) transition and current flow in DSSCs by using MH01 and (I-/I₃⁻) electrolyte.

1.3. Dye-sensitizers

Dye-sensitizers are one of the most important components in DSSCs. A dye-sensitizer is typically an organometallic or an organic molecule that harvests solar photons and converts them into a current. Its redox chemistry, photochemical, photophysical, and molecular electronic properties play an important role in the electron transfer process and absorption of the solar spectrum at the semiconductor interface. Currently, the most popular dye-sensitizers are polypyridyl complexes of ruthenium (II), which consists of a central ruthenium (II) with ancillary ligands having at least one anchoring group and a light harvesting group. During photo-excitation of the dye-sensitizer, an electron transfer takes place from the metal to the π^* -orbital, which is typically located on the ligand carrying the

anchoring group, then the electron is injected from the excited state of the dye-sensitizer into the conduction band (CB) edge of TiO₂ on the femto-to-picoseconds time scale.¹¹

The best performing DSSCs, both in terms of overall conversion efficiency and stability, were shown by Ru (II) polypyridyl complexes.¹²⁻¹⁴ Most Ruthenium (II) polypyridyl complexes are characterized by strong metal-to-ligand charge transfer (MLCT) properties in the visible region between 400 nm to 600 nm, thermodynamically favorable ground and excited states potentials, and long excited state life times.¹⁵ Ru (II) polypyridyl complexes have been employed for different applications because of their long excited state life time, e.g., chemiluminescence¹⁶, optical sensors¹⁷, light-emitting diodes¹⁸, photoelectrochemical cells¹⁹, and currently extensively used in DSSCs.

1.4. Dye-sensitizers Requirements

An ideal dye-sensitizer for DSSCs should fulfill the following essential requirements:

- 1) The dye-sensitizer should show strong light harvesting efficiency capabilities through the whole visible range, including the red region, and extend up to the NIR region of the solar spectrum.
- 2) It must contain anchoring groups (-COOH, -H₂PO₃, -SO₃H, -OH, etc.) to firmly bond the dye-sensitizer onto the semiconductor oxide surface, and to ensure strong electronic coupling between the dye-sensitizer and CB of TiO₂.
- 3) Upon photo-excitation, it should inject electrons into the semiconductor oxide with a quantum yield of one-photon giving one-electron.

4) The energy level of the excited state of the dye sensitizer should lay above the edge of CB of the semiconductor oxide in order to minimize energy loss during the charge transfer process in the DSSC. Since the charge transfer occurs from the excited state of the dye-sensitizer, the excited state lifetime must be long enough to allow for electron injection into the semiconductor before relaxing back to the ground state.²⁰

5) The redox potential of the dye-sensitizer should be higher than that of the electrolyte/hole conductor in order to regenerate the dye-sensitizer via an electron donation from the electrolyte. In addition, both the oxidation and the reduction processes must be reversible and stable.²¹

6) It should be stable during both its ground and excited states towards light soaking stress. It must be inert to avoid the side reactions with the electrolyte in order to function properly for a period of at least 20 years without significant loss of performance.²²

Researchers have been attempting to identify and synthesize such dye-sensitizers that match these requirements. In this regard, many dye-sensitizers were developed and characterized for DSSCs, including metal complexes, porphyrins, phthalocyanines, perylene derivatives, and metal free organic sensitizers in the past two decades.²³ However, to date, no dye-sensitizer exists that fulfills all the above requirements. There are many problems associated with the current dye-sensitizers including low efficiency, low extension coefficient, low scalability and poor stability.

1.5. Molecular Engineering for Optimization of DSSCs

1.5.1. Panchromatic Dye-sensitizers

The energy distribution within the solar spectrum at air mass 1.5, hemispherical solar spectral irradiance typical of North American insolation is approximately 5% ultraviolet (300-400 nm), 43% visible (400-700 nm) and 52% near-infrared (700-2500 nm).²⁴ Therefore, an ideal sensitizer for a single junction photovoltaic cell should be panchromatic and absorb photons across the full solar spectrum especially from 400 nm to 920 nm to effectively convert sunlight to electricity. To accomplish better light harvesting from the visible to near-IR region by a monolayer of dye-sensitizer molecules, the dye-sensitizer should have a suitable chromophore that has high molar absorptivity in a wide range of solar spectrum.

In 1991, O'Regan and Grätzel introduced a sensitizer which consisted of cis-dithiocyanato-bis-2,2'-bipyridyl-4,4-dicarbonylate ruthenium(II), and was designated the "N3-sensitizer" (Figure 1-2). Using the N3-sensitizer, they were able to achieve a remarkable solar-to-power conversion efficiency of 7.9% for the first time.²⁵ Furthermore, formation of N719 on deprotonation of carboxylic protons of the N3-sensitizer (Figure 1-2) caused a considerable shift in oxidation and reduction potentials towards negative, and a significant increase in total conversion efficiency.²⁶ It was suggested that the fully protonated sensitizer (N3) transfers most of its protons to the TiO₂ surface, thus increasing the positive charge on the TiO₂ surface. The resulting high short-circuit photocurrent density (J_{SC}) (19 mA/cm²) as compared to N719 (17 mA/cm²) increases electron injection. On the contrary, the open-circuit

photovoltage (V_{oc}) decreases due to the positive shift of the TiO_2 -CB level because of surface protonation, hence the V_{oc} of N3 (0.6 V) is significantly reduced over that of the doubly protonated N719 (0.73 V). After extensive study of the number of protons vs photovoltaic performance, they concluded that one protonated dye-sensitizer is ideal to achieve maximum photovoltaic performance of DSSCs as compared to multi protons.²⁶⁻²⁷ The molecular structure of the sensitizers N3, N719, and black dye are shown in Figure 1-2.

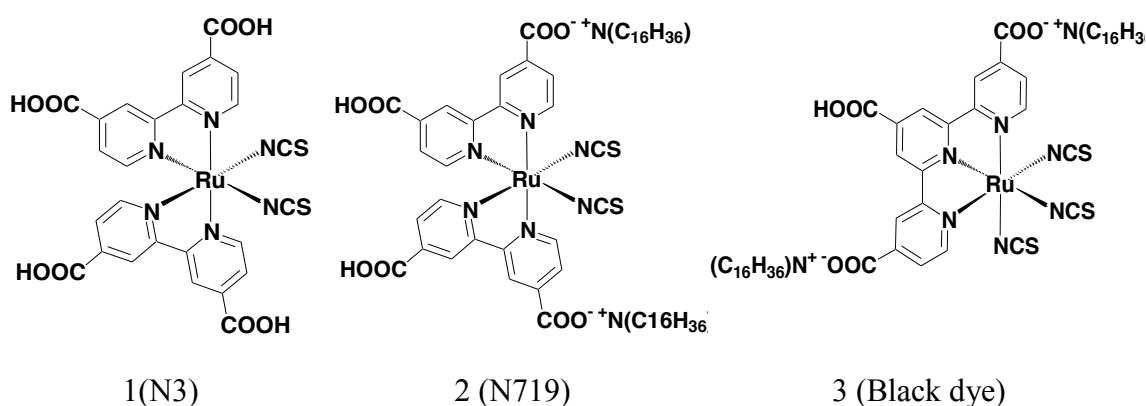


Figure 1-2. The molecular structures of Ru (II) polypyridyl Dye-sensitizers 1-3.

The N3-sensitizer was the benchmark for a decade. However, in 2001, Grätzel and Nazeeruddin reported a novel Ru (II) based on a terpyridyl dye-sensitizers which was called “black dye” (Figure 1-2), which performed a record solar to power efficiency of 10.4% under one sun illumination.²⁹ It was suggested that three thiocyanato (-N=C=S) and terpyridine tricarboxylic acid ligands imparted a significant red shift in the MLCT band due to the decrease in the π^* energy levels of terpyridine ligands, enabling the sensitizer to harvest

photons throughout the visible range up to the near infrared region of the solar spectrum,²⁹ thus the panchromatic sensitizer.

Another approach to enhancing the light harvesting properties of ruthenium (II) polypyridyl dye-sensitizers is to increase the conjugation of the bipyridine ligand, modifying the lowest unoccupied molecular orbital (LUMO) of the sensitizer, and enhancing the absorption properties. In this regard, many sensitizers have been developed by replacing the carboxylic acid anchoring groups on one of the bipyridyl ligands with extended conjugated systems. In 2004, P. Wang reported two conjugated polypyridyl sensitizers, Z-910 and K19 (Figure 1-3), which showed broader maxima at 410 nm and 543 nm with a 20nm red-shift and a significantly higher molar extension coefficient compared to standard N719. The extended conjugations increase the absorption properties and impart a red shift in the absorption spectrum due to the higher electron donating power of the extended ligand translating into improved photovoltaic performance of the solar cell. Both extended conjugated sensitizers Z-910 and K19 exhibited a prominent light-to-power conversion efficiency of 10.2% and 7.0%,³⁰ respectively. In addition, Z-910 showed an impressive thermal stability due to its long alkyl chain,³¹ the molecular structure of sensitizers Z-910 and K-19 shown in Figure 1-3.

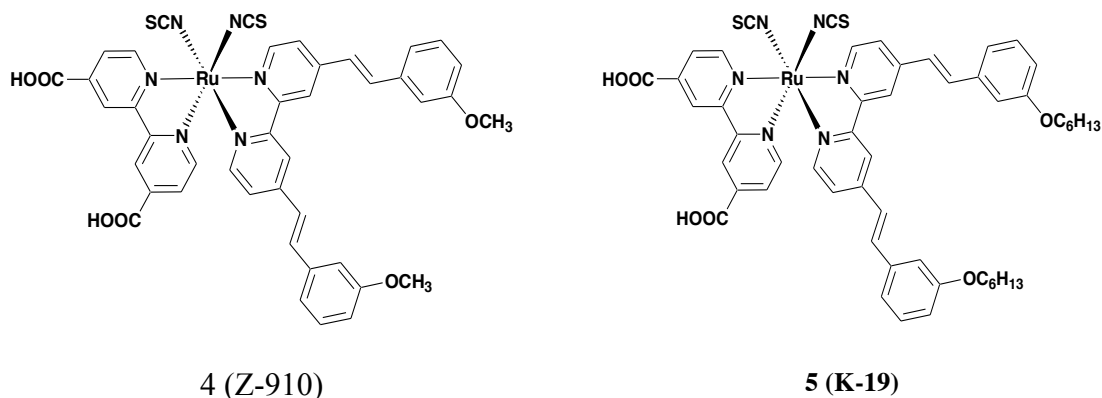


Figure 1-3. Molecular structures of Ru (II) polypyridyl dye-sensitizers 4-5.

Yanagida and co-workers reported an extended conjugated 2-thiophen-2-yl-vinyl ruthenium complex named HRS-1, which showed a 30% higher molar extension coefficient and a 10nm red shift of its UV-Vis absorption spectrum with respect to the N719 sensitizer. Results showed an overall conversion efficiency of 9.5% for the sensitizer HRS-1 compared to the benchmark sensitizer N719 of 8.9%.³² The higher efficiency and stability of HRS-1 is attributed to the cathodically shifted potential of 0.11V (compared to N719) due to the strong electron donating thienyl groups in the 4,4,9-di(hexylthienylvinyl)-2,2,9-bipyridyl ligand.³²

In similar studies, Qingjiang et al., reported another electron rich ruthenium complex-C107 that exhibits a similar absorption profile, and a red shift with higher molar extension coefficient ($27.4 \times 10^3 \text{ M}^{-1} \text{ cm}^{-1}$ at 559 nm) than that of its analogue C103 ($20.5 \times 10^3 \text{ M}^{-1} \text{ cm}^{-1}$ at 550 nm), which resulted in a higher solar-to-power conversion efficiency of 10.7% compared to 10.4% of C 103. It was suggested that the red shift and higher molar extension coefficient is due to the extended and large ligand imparting higher electro donating power.

The strong electron donating ligand destabilized the metal-based HOMO by transferring electron density into the metal center, and as a result the overall gap between HOMO-metal and LUMO-ligand decreased, translating into a red shift in the absorption spectrum.³³ The molecular structure of C103 and C107, are shown in Figure 1-4.

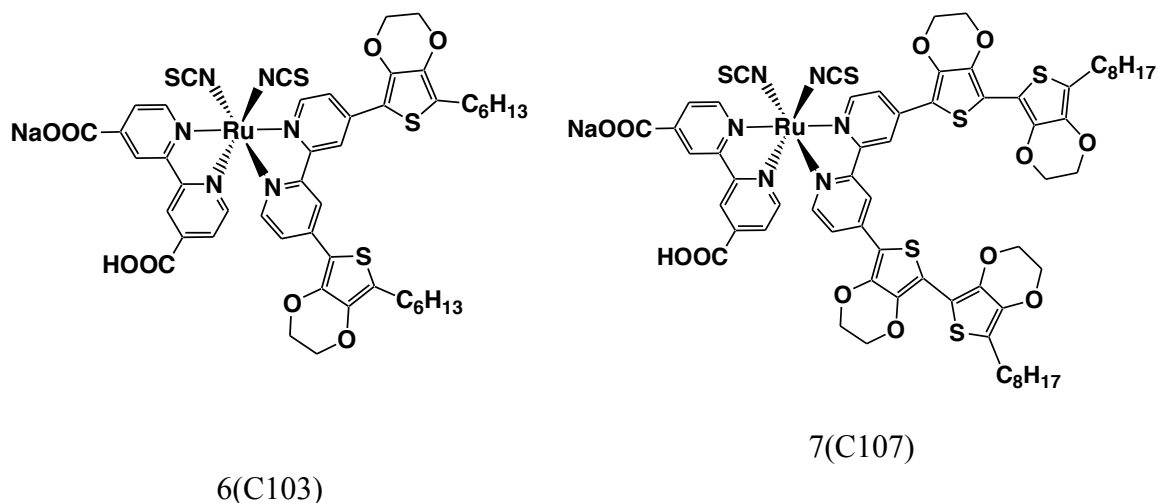


Figure 1-4. Molecular structures of Ru (II) polypyridyl dye-sensitizers 6-7 (C103 and C107).

1.5.2. Modifying the Oxidation Potential of Sensitizers

In general, an ideal dye sensitizer with its best corresponding oxidation potential is vital for thermodynamically favorable electron transfer reaction in DSSCs. The excited state (HOMO) oxidation potential of dye-sensitizers should be below that of the oxidation potential of redox couple while maintaining the LUMO of the dye-sensitizer above the CB of semiconductor oxide for effective electron injection and dye-sensitizer regeneration process. Therefore, the spectral properties need to be modified in a way that the excited state energy

should lay above the CB edge of the TiO_2 for efficient electron injection from the excited state of the dye-sensitizer to TiO_2 -CB, and at the same time the redox potential should be more negative (-) than that of the electrolyte to regenerate the oxidized dye-sensitizer.³⁴⁻³⁸

The schematic diagram in Figure 1-5 shows the thermodynamically favorable interfacial electron transfer oxidation potential in a dye-sensitized solar cell.

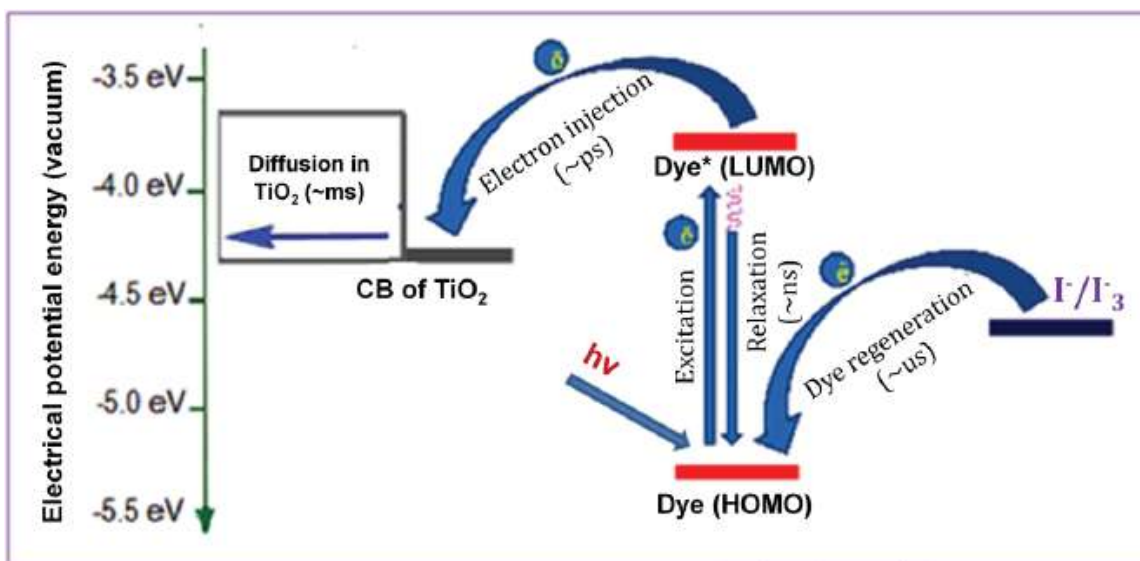


Figure 1-5. Illustration of the thermodynamically favorable interfacial electron transfer process in a dye-sensitized solar cell; absorption of photon by the dye-sensitizer leads to excited state (step 1), followed by electron injection (step 2) into TiO_2 -CB and at the same time the oxidized dye-sensitizer gets reduced by (I^-/I_3^-) redox couple.

Thus, the ideal Ru (II) polypyridyl sensitizer should exhibit excited-state and ground-state oxidation potential of about -0.9 V and 0.5 V (vs. SCE), respectively³⁹ for effective electron injection and rapid regeneration of sensitizer by obtaining electrons from the electrolyte (I^-/I_3^- , redox couple) lower excited-state oxidation potential values reduce electron injection efficiencies and maximum recombination reactions.

Chou and co-workers designed and synthesized a tridentate ancillary ligand to replace the traditional thiocyanates to increase the light harvesting capabilities shown in Figure 1-6.

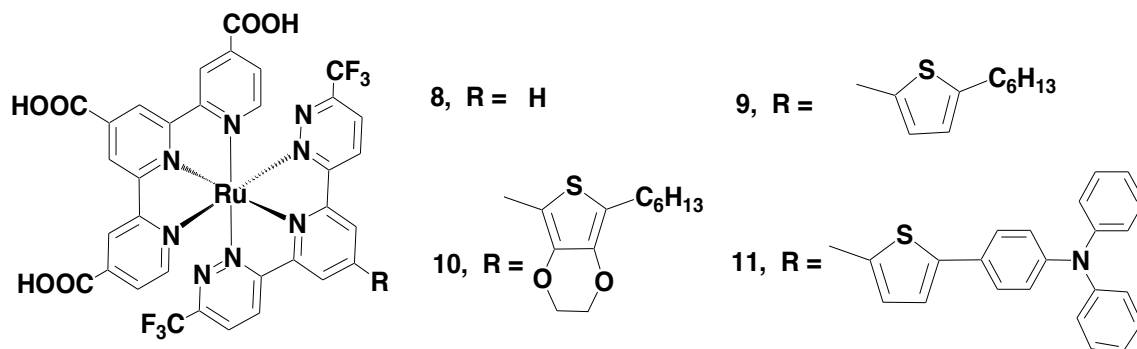


Figure 1-6. Thiocyanates free Ru (II) Polypyridyl heteroleptic tridentate complexes.

These tridentate complexes shows exceptional absorption peak around 510 nm, and two weaker absorption at about 650 nm and 720 nm, it was suggested that the high intensity and additional absorption peaks are attributed to the combined contribution of the metal-to-ligand charge (MLCH) transfer and ligand-to-ligand charge transfer (LLCH) from the pyrazolate groups. The oxidation potential of these complexes is between 0.94-0.97 V (vs. NHE) and LUMO potential level is between -0.73 to -0.76, indicating that redox potentials are optimized, as all HOMOs potentials are higher than that of $\text{TiO}_2\text{-CB}$, and all LUOMOs potentials are less negative than that of I^-/I_3^- redox couple, thus all complexes are able to regenerate effectively. The V_{oc} of complex 9-11 are between 760-790 V, remarkably higher than that of thiocyanate based tridentate complexes (Black-dye, V_{oc} , 720 V). It is hypothesized that the extremely bulky 2,6-bis(5-pyrazolyl)pyridine ligand allows more efficient packing to form a compact layer on the TiO_2 surface that may minimize the

recombination reactions, thus increasing the V_{oc} which translates into higher total solar-to-power conversion efficiencies of 9.50-10.70 $\eta\%$ compared to the benchmark black-dye of 9.22 $\eta\%$. Moreover, the negative pole of the dipole moment in complex 9-11 is expected to be located much closer to the TiO_2 surface as a result of the uplifting of the TiO_2 -CB level and consequently higher V_{oc} .⁴⁰

Barigelletti and co-workers synthesized two types of ruthenium (II) complexes, cyclometallated and noncyclometallated using phenyl-phenanthroline-type ligands,⁴¹ shown in Figure 1-7.

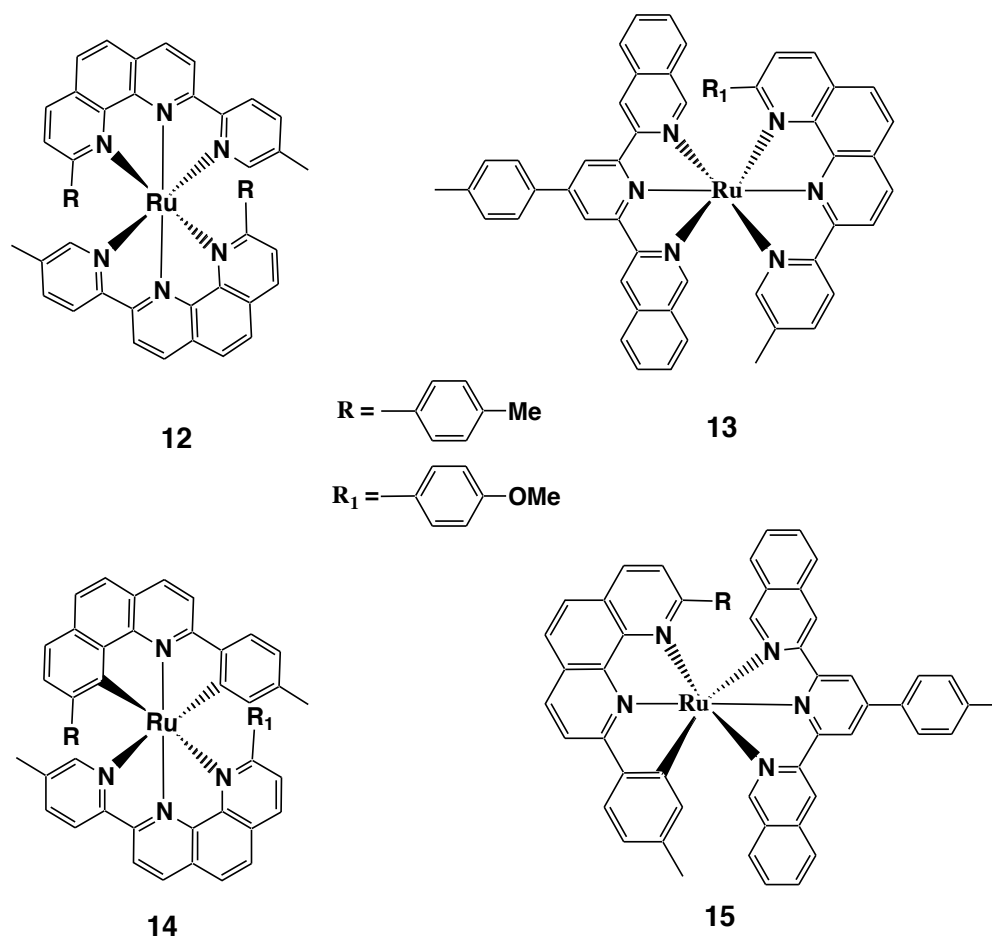


Figure 1-7. Excited-state stabilization through cyclometalization and inter-ligand π - π interactions.

It was suggested that there are two types of factors affecting the excited states of these complexes. The rigidity of the phenanthroline type ligands increases the steric strain at the Ru-metal center due to the bulky moiety, thus lowering the energy of metal centered excited state. However, cyclometallating ligands destabilized the metal-based HOMO more than that of ligand based LUMO by transferring electron density into the metal center. As a result, the overall gap between HOMO-metal and LUMO-ligand decreases

translating into a red shift in the absorption spectrum. For instance non-cyclometallated complexes **12** and **13** (Figure 1-7) showed absorption λ_{max} (nm) at 503, 344, 300 and 495, 474, 347, but analogous cyclometallated complexes **14** and **15** showed a red-shifted, absorption at 523, 440, 314 and 520, 493, 351, respectively.⁴¹

1.5.3. Strategies to Extend the Excited State Life Time

The key requirement to an efficient dye-sensitizer is its excited state properties because during the dye-sensitization process electrons are injected from an excited state of the dye to the semiconductor oxide. The most important are its excited state lifetime, excited state potential, and the emission quantum yield. For effective electron injection the excited state lifetime should be long enough to allow sufficient amount of electron transfer reactions before the complex-sensitizer relaxes back to its ground state. The excited state lifetime of a dye-sensitizer depends on molecular structure and can be structurally modified by introducing appropriate ligands and electron donating groups to the dye-sensitizer moiety.⁴²

Another approach to increasing the lifetime of terpyridine dye-sensitizers is using ligands with extended π - systems; the aromatic moiety can conjugate with low-lying π^* levels of the terpyridine ligands to establish extended π - systems, the excess electron can delocalize easily and hence increases the stability of the excited state and therefore an increased lifetime.⁴³⁻⁴⁴

The excited state properties of tridentate ($\text{Ru}(\text{tpy})2^{2+}$) complexes can be enhanced by manipulating the energies of the MLCT, the metal centralized charge transfer (MC) states or a combination of both states by reducing the energy difference between these two states. Two

different approaches are normally used to modify the terpyridine-type ligands: (a) methods that involve changing the coordination sphere of the terpyridine (tpy) moiety by incorporating alternate heterocycles, or (b) introducing new substituents to terpyridine ligand while maintaining the core moiety.

For instance alternate heterocyclic moieties can be used to replace the central and peripheral pyridyl rings to form tridentate ligands. A series of Ru (II) tridentate complexes based on carbenes were reported ⁴⁵ and shown to have promising photophysical properties (Figure 1-8).

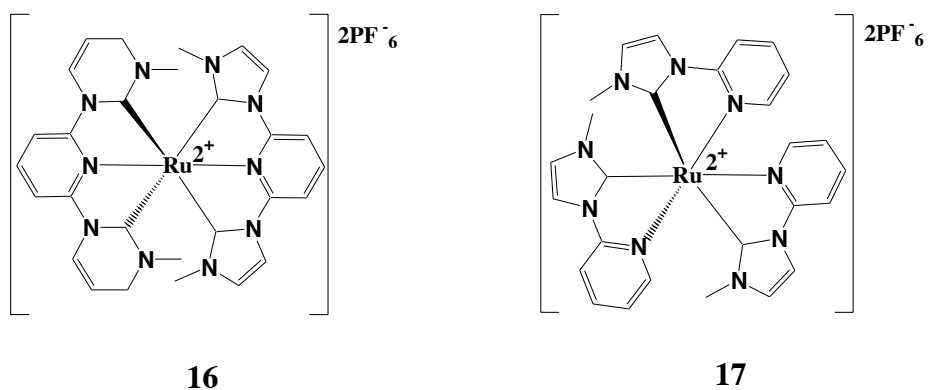


Figure 1-8. Ru (II) tridentates dye-sensitizer strong σ -donors: complex 16-17, carbene and trizole respectively.

It was suggested that carbenes are good electron donors, are strongly bonded to the ruthenium metal center, destabilize the LUMO, and increase the energy of MC states. At wavelengths between 340 nm and 380 nm, the MLCT transitions for carbene complex 16 show a shift toward blue when compared to Ru (II) terpyridine (475 nm). The excited state life times are enhanced significantly, as is PF6 salt in acetonitrile (820 ns), which is

positioned for practical use.⁴⁶ Duati and co-workers reported that the heteroleptic dye-sensitizer which contains strong σ -donor ligands destabilize the ground state, hence lowering the energy gap between metal LUMO and ligand HOMO. Consequently the dye-sensitizer emits at a lower energy, around 700 nm, with a prolonged excited state of 77 ns. It was found that the protonation of these triazole rings quenches the excited state since the protonation of rings decreases the electron donating ability and hence reverses the process.⁴⁷ Cyclometalated ligands, which are strong σ -donors, destabilized the HOMO of metal thus reducing the gap between metal-HOMO and ligand-LUMO, and as result the excited state lifetime decreased significantly.⁴⁸⁻⁴⁹

Barigelletti and co-worker reported that the substituted phenyl groups, *para* to the coordinating N-atom (Figure 1-9) on the phenanthroline-type ligand cause significant increases in excited-state lifetime. This is attributed to the phenyl group stabilizing the phenanthroline ligand via inter-ligand π - π interactions.

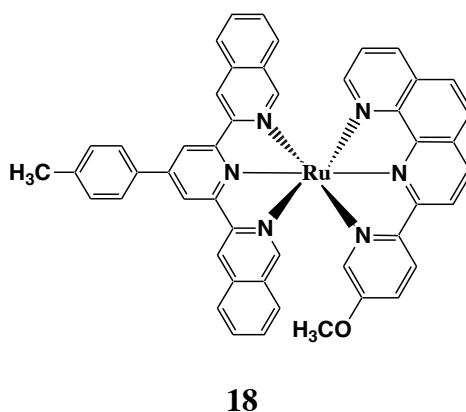
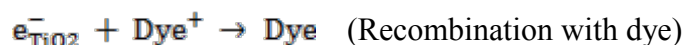
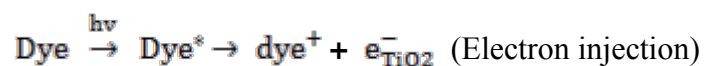


Figure 1-9. Molecular structure of substituted phenyl groups, *para* to the coordinating N-atom, phenanthroline-type ligand.

Interestingly, a mononuclear Ru(II) dye-sensitizer (**18**) which contains a phenyl group *Para* to the coordinating N-atom showed a prolonged excited-state lifetime of 106 ns with a low energy emission (816 nm).⁴¹

1.5.4. Minimizing the Charge Recombination Reactions

Electron recombination at the interface of the semiconductor/dye/electrolyte is detrimental to the photovoltages in DSSCs, which leads to significant loss in the solar-to-power conversion efficiency of the device.⁵⁰



Hence, it is vital to minimize the charge recombination between TiO₂ and oxidized dye molecules and/or redox couples in DSSCs in order to obtain the maximum output from the device. An overview of the kinetics including electron injection, recombination reactions and dye-sensitizer regeneration with the time scale for each process is shown in Figure 1-10.

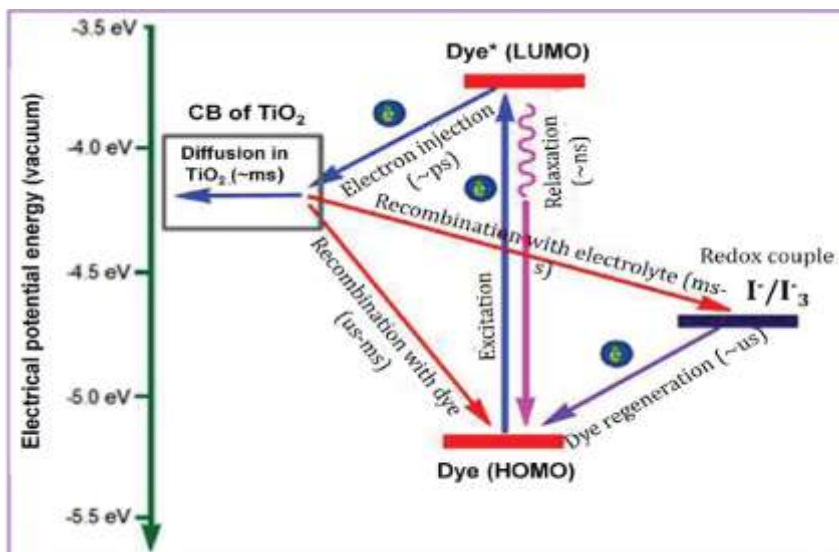


Figure 1-10. A schematic diagram of the electron injection and recombination process in DSSCs with time scale.

In conventional DSSCs, the electron recombination reactions are very slow compared to the electron injection from the excited dye-sensitizer to the conduction band of TiO_2 . However, due to the relatively slow diffusion process through the nanoporous TiO_2 , electrons are not very far from the semiconductor/electrolyte interface, and therefore, it is possible that these electrons may recombine with the oxidized dye molecules and/or the electrolyte.²³ The regeneration of dye depends on the molecular structure of the dye-sensitizer, electrolyte concentration and its viscosity. In order to achieve a decent photocurrent, the regeneration reaction should be fast enough to compete effectively with the competing recombination reaction.⁵¹

The kinetics of the recombination reaction are almost linearly dependent on the electron density in the semiconductor conduction band. Because the electron diffusion through the semiconductor is a very slow process due to the trapping/detrapping processes,

recombination reactions may occur, which take place in the microseconds to seconds time scale depending on the electron density in the film of the semiconductor.⁵¹

The influence of dye-sensitizer molecular structure on recombination reactions has been investigated. It has been reported that incorporating strong electron donating groups to the dye-sensitizer moiety, and increasing the physical separation of dye-sensitizer cation centers from the semiconductor oxide surface (TiO_2) causes a significant reduction of charge recombination.⁵² These supermolecular or multifunctional dye-sensitizers exhibit a multistep charge transfer process, and as a result show remarkably long-lived charge separation at dye-sensitizer/ TiO_2 interface,⁵³ illustrated in Figure 1-11.

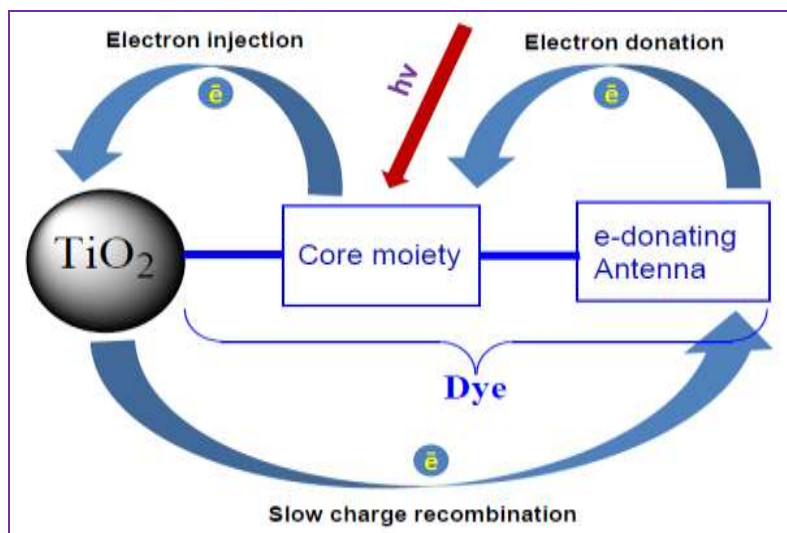


Figure 1-11. The schematic diagram of long-lived charge separation process at the dye-sensitizer/ TiO_2 interface using a supermolecular-dye-sensitizer attached to TiO_2 and a strong electron-donating group.

Haque and coworkers studied the charge-recombination dynamics of three Ru-multifunctional dye-sensitizers, which contains different triphenylamine antennas, shown in Figure 1-12, by using transient absorption spectroscopy⁵³.

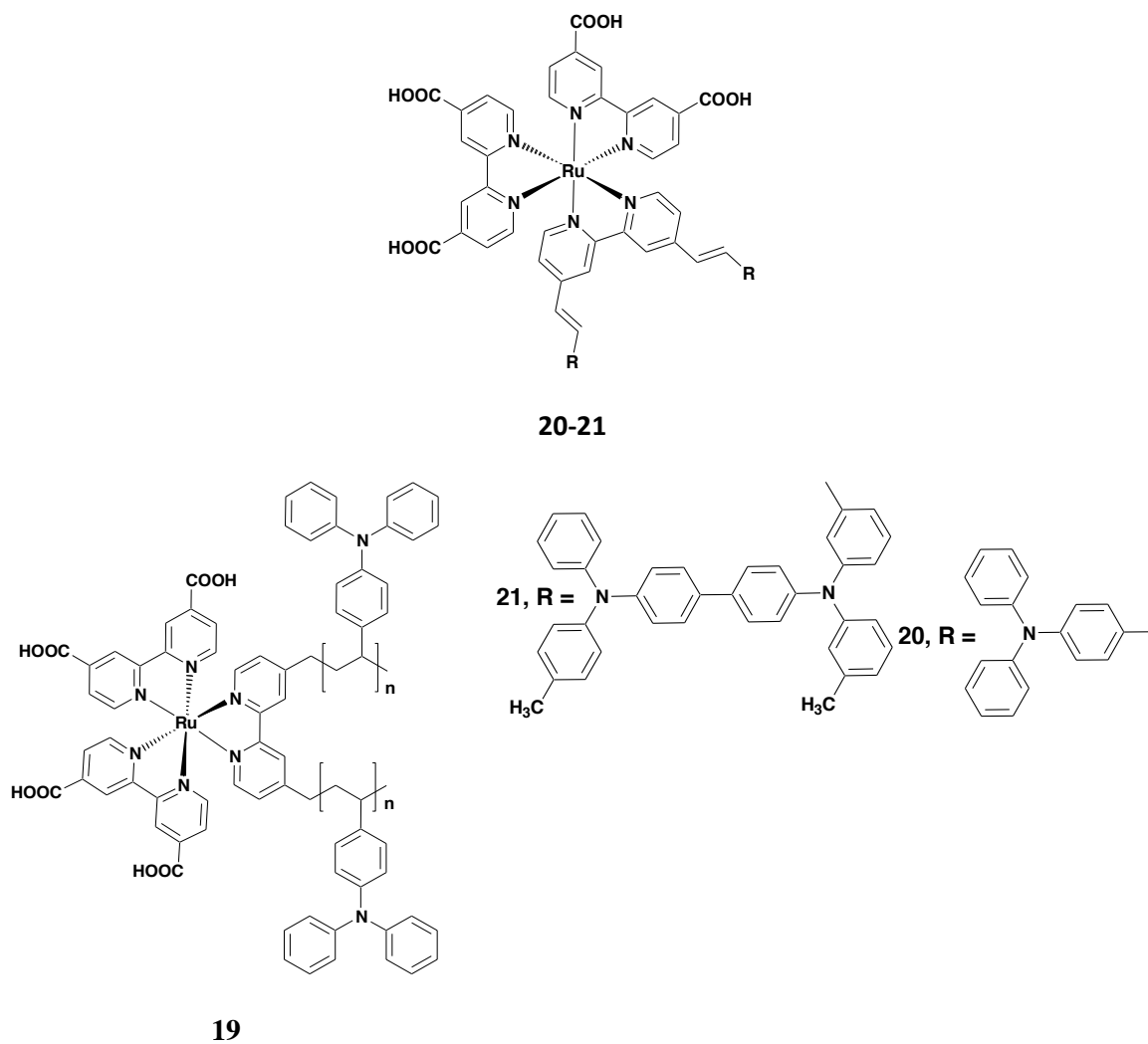


Figure 1-12. Ru (II) bipyridyl dye-sensitizer that contains a strong electron donating triphenylamine antenna.

The recombination dynamics of all three complexes differ significantly depending on the physical separation of the dye-sensitizer cation center from the semiconductor oxide surface. The dye-sensitizer, which contains a large antenna, showed remarkably longer recombination half-time ($t_{50\%}$); complexes **19**, **20**, and **21**-exhibited 350 μ s, 5 ms and 4 s, respectively. The key parameter that controls the charge transfer at the interface of dye-sensitizer/TiO₂ is attributed to the spatial separation of the dye-sensitizer cation from the TiO₂ surface as a result of multistep translation of the dye-sensitizer moiety away from the TiO₂ surface.⁵³ The recombination between the injected electron and redox couple (triiodide) was effectively decreased by the connection of triphenylamine antennas units. The result of the dark current under a reverse bias of 0.55 V showed a significant suppression of 6.8 mA/cm², 4.0 mA/cm² and 3.4 mA/cm² for the dye-sensitizers 6, 7 and 8 respectively. A similar strong correlation between spatial separation and recombination dynamics was reported by J. N. Clifford and coworkers Increasing spatial separation by 3 Å causes a more than 10-fold change in the recombination half-time ($t_{50\%}$).⁵⁴ S. Y. Huang and co-worker reported that soaking [RuL2(NCS)2] (L) 2,2'-bipyridyl-4,4'-dicarboxylic-dye-coated TiO₂ electrodes in CH₃CN for 15min along with pyridine derivatives (50:50 wt %) such as 4-*tert*-butylpyridine (TBP), 2-vinylpyridine (VP) and poly(2-vinylpyridine) (PVP) improved the photovoltaic performance of DSSCs significantly, as the open-circuit photovoltage (V_{oc}) improved from 0.57 to 0.73 V and light-to-power conversion efficiency improved from 5.8% to 7.5% with respect to the untreated electrode. The significant increase in the open-circuit photovoltage (V_{oc}) was attributed to the small size of pyridine compounds that fills the interspace between dye molecules to forms a compact layer on the TiO₂ surface, as a result a suppression in the

electron recombination at the interface of the TiO₂/electrolyte, hence increase in V_{oc} .⁵⁵ The molecular structures and solar-to-power conversion efficiency of some Ru (II) polypyridyl complexes used in DSSCs are listed in Table 1-1.

Table 1-1. Some representative of Ru (II) polypyridyl dye-sensitizers and their total solar-to-power conversion efficiency (η %).

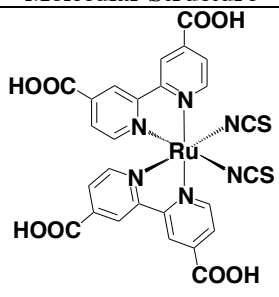
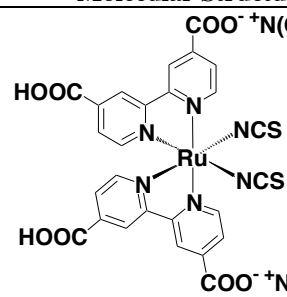
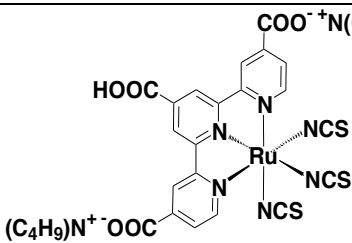
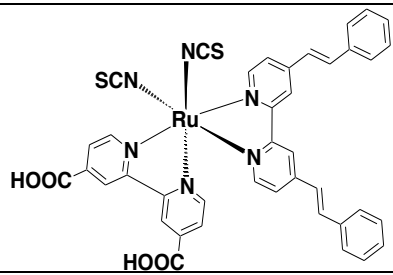
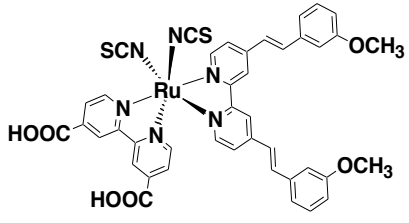
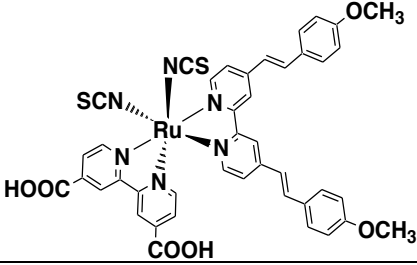
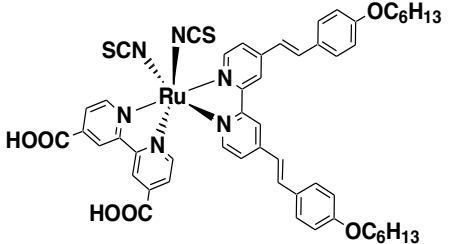
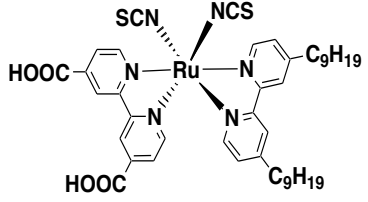
Molecular Structure	(η %)	Molecular Structure	(η %)
	7.90 ⁵⁶		11.20 ³²
	10.30 ³⁵		10.20 ³⁷
	10.20 ²⁷		9.00 ³⁶
	7.00 ³⁶		7.30 ⁵⁷

Table 1-1. Continued

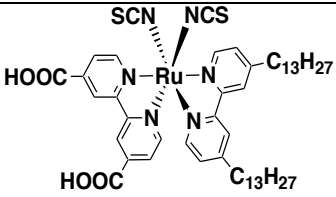
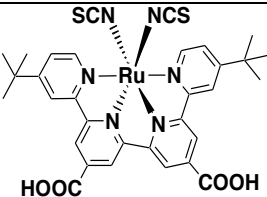
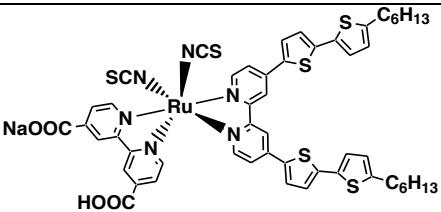
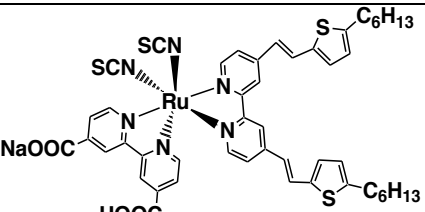
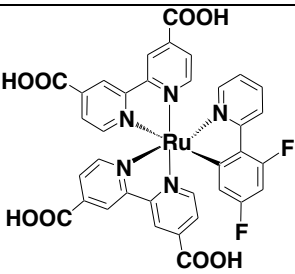
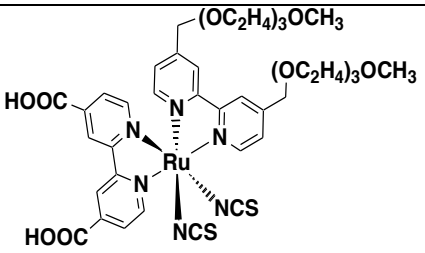
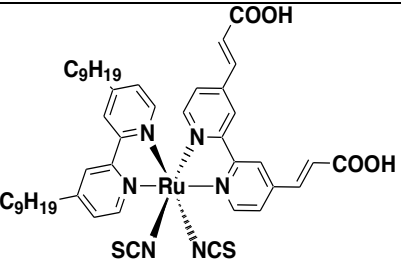
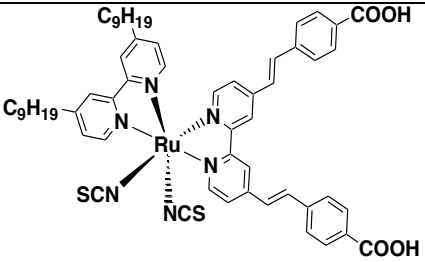
	9.60 ⁵⁷		5.58 ³⁹
	11.50 ⁵⁸		9.50 ³⁸
	10.10 ⁵⁹		8.40 ⁶⁰
	4.14 ⁶¹		4.41 ⁶¹

Table 1-1. Continued

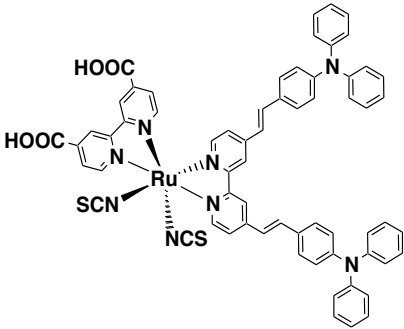
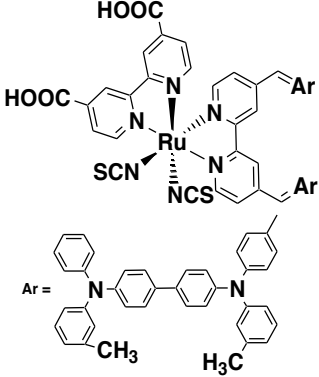
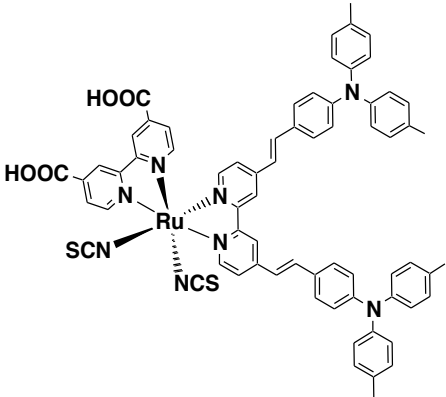
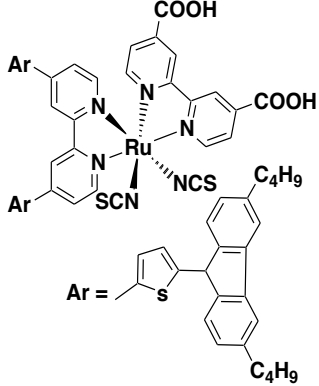
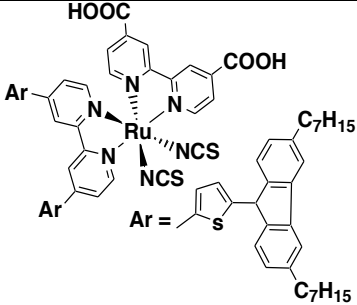
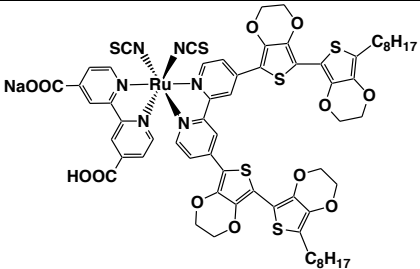
	1.50 ⁶²		3.40 ⁶²
	10.30 ⁶³		9.72 ⁶⁴
	8.89 ⁶⁴		9.02 ⁶⁵

Table 1-1. Continued

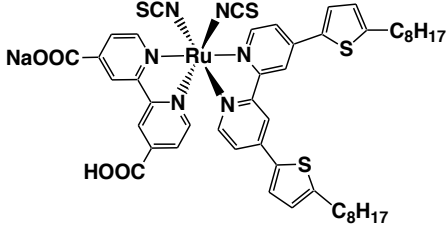
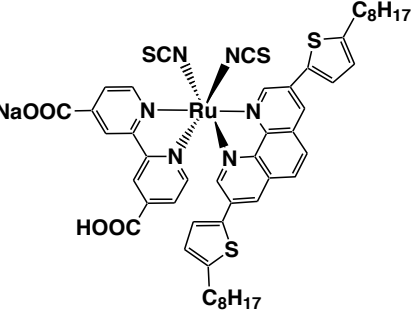
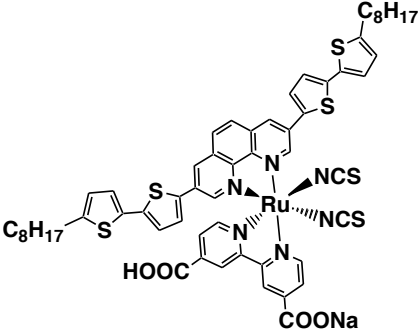
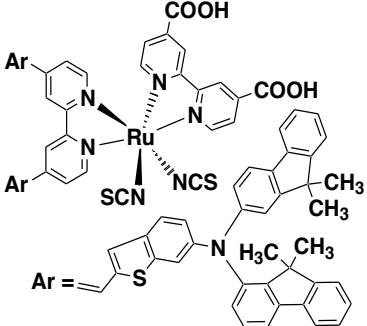
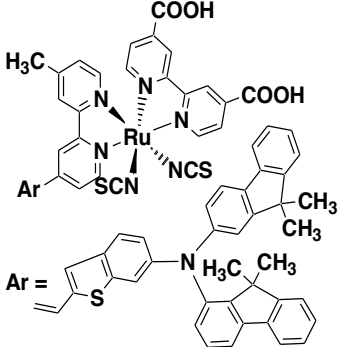
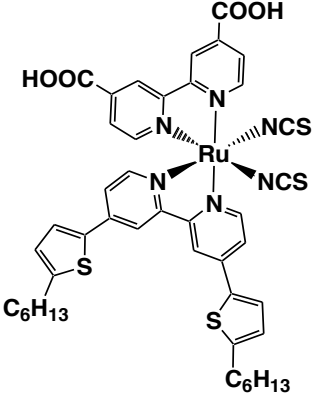
	7.38 ⁶⁵		6.02 ⁶⁶
	3.42 ⁶⁶		8.20 ⁶⁷
	9.16 ⁶⁷		11.00 ⁶⁸

Table 1-1. Continued

	9.50 ⁶⁸		10.00 ⁶⁹
	7.83 ⁷⁰		7.73 ⁷⁰
	10.70 ³⁹		10.57 ⁷¹
	10.53 ⁷²		5.65 ⁷³

Table 1-1. Continued

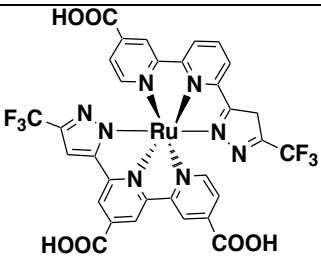
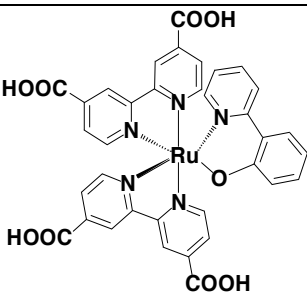
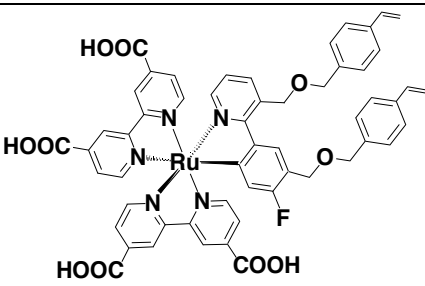
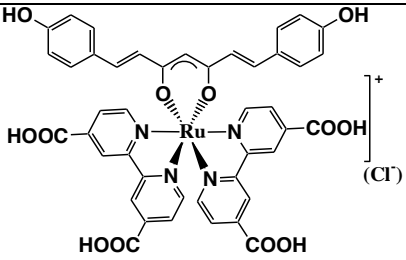
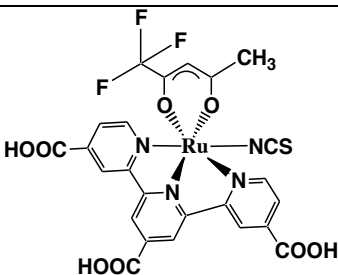
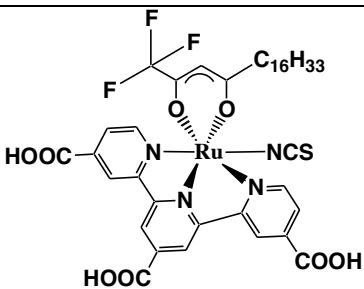
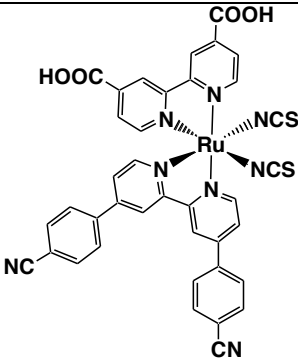
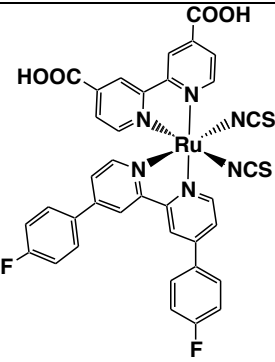
	1.14 ⁷³		1.84 ⁷⁴
	7.57 ⁷⁵		5.76 ⁷⁶
	5.31 ⁷⁷		7.60 ⁷⁷
	4.90 ⁷⁸		7.56 ⁷⁸

Table 1-1. Continued

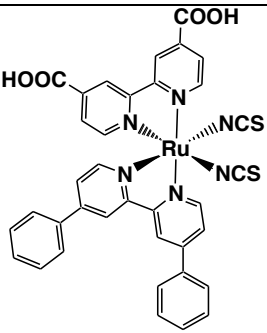
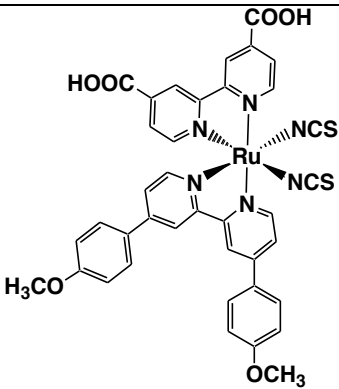
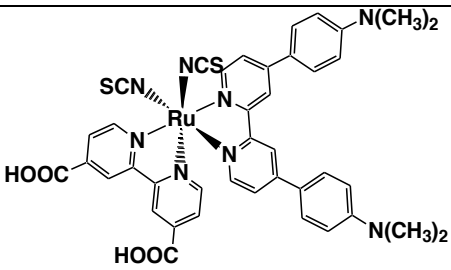
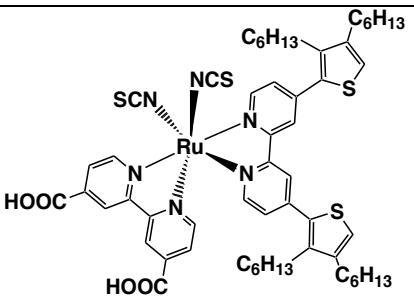
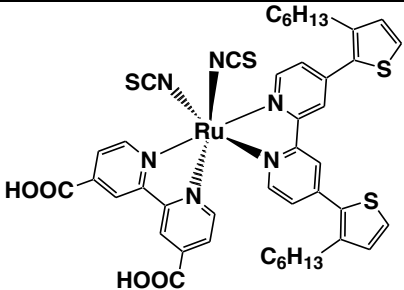
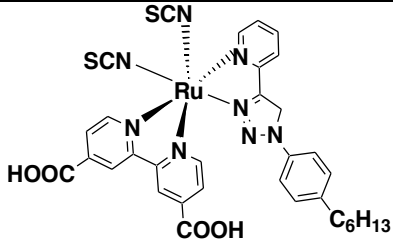
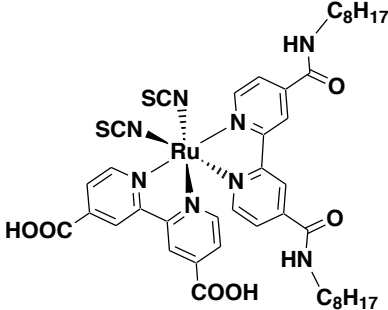
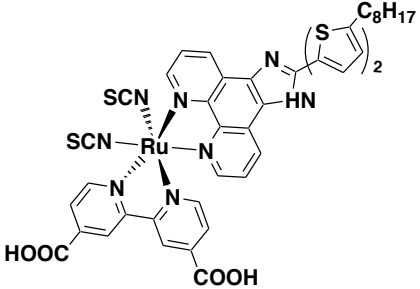
	7.72 ⁷⁸		8.30 ⁷⁸
	4.24 ⁷⁸		7.70 ⁷⁹
	7.08 ⁷⁹		4.70 ⁸⁰
	7.25 ⁸¹		9.50 ⁸²

Table 1-1. Continued

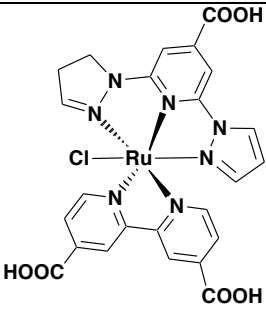
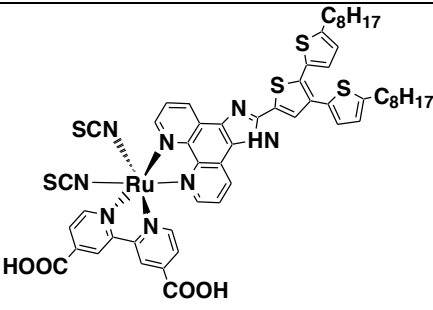
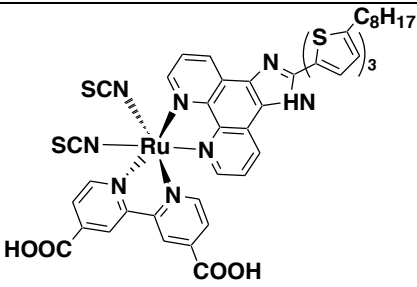
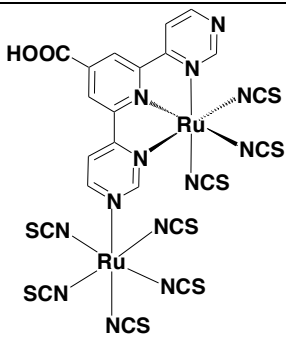
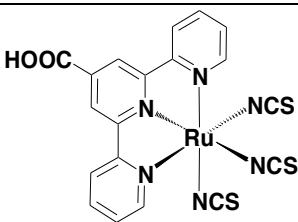
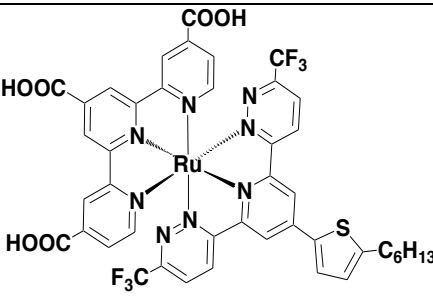
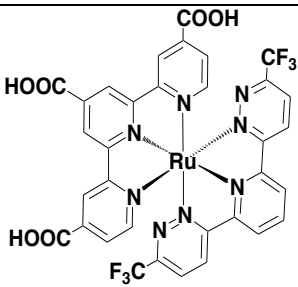
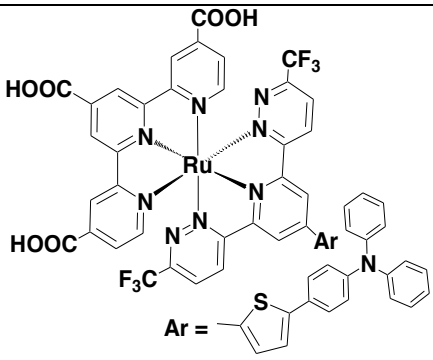
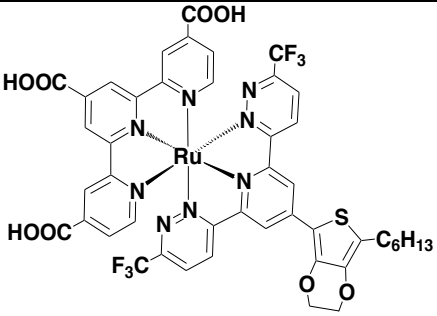
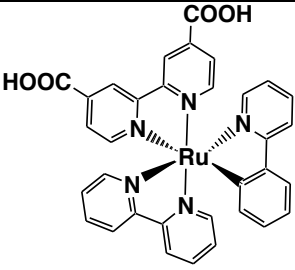
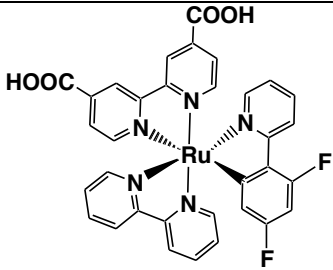
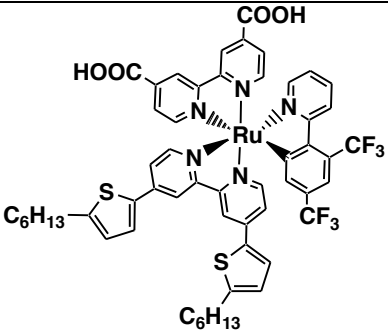
	1.90 ⁸³		6.40 ⁸²
	8.70 ⁸²		0.02 ⁸⁴
	2.48 ⁸⁴		10.5 ⁴⁰
	9.11 ⁴⁰		10.5 ⁴⁰

Table 1-1. Continued

	10.7 ⁴⁰		2.39 ⁸⁵
	4.02 ⁸⁵		8.80 ⁸⁶

1.6. The Usage of a Co-adsorbent

Another approach to improve the efficiency of DSSCs is to use a co-adsorbent to reduce the recombination reaction, aggregation among the dye-sensitizer, and to form a compact protective layer on TiO_2 .¹⁵ Due to its small size the co-adsorbent works as filler and fills the interspaces between the dye-sensitizers, forming a compact layer on the TiO_2 surface. Secondly, it can reduce the quenching and aggregation between dye-sensitizers. The dye segregation can reduce the electron injection efficiency, and bare TiO_2 can increase the electron recombination reactions at the interface of the TiO_2 /electrolyte. Co-adsorbents are

used along with dye-sensitizer to reduce the dye aggregation, and it improves the short circuit voltage (V_{oc}) of the device significantly.⁸⁷

The structure-property relationship revealed that the ideal characteristics for co-adsorbents are a) it should have a reactive group to anchor with TiO_2 surface and a hydrophobic bulky alkyl chain. b) The molecular structure should be designed carefully to avoid competitive adsorption among dye-sensitizers while effectively suppressing the quenching of photo-excited states and aggregation of dye-sensitizer on the TiO_2 surface. c) It should show molar absorptivity near the infrared region, and/or the region where the electrolyte shows strong absorptivity. d) It should reduce the electron recombination reactions at the interface of the TiO_2 /electrolyte by forming a compact protective layer on the bare TiO_2 surface.

Lim and co-worker reported that using stearic acid (SA) as a co-adsorbent along with dye-N719 improves photovoltaic performance significantly. The J_{sc} and solar-to-power conversion efficiencies of solar-devices increased by 25% as compared to controlled devices. It was suggested that the low dipole moment and high solubility of stearic acid retards the rate of dye-sensitizer anchoring during the competitive adsorption process, thereby establishing a compact and strongly bonded dye-sensitizer on the TiO_2 surface, and as a result lower dye-sensitizer aggregation and higher performance.⁸⁸

In 2012, Song and co-workers reported a promising co-adsorbent, 4-(bis(9,9-dimethyl-9H-flouren-2-yl)amino)benzoic acid (HC-Acid), for organic dye-sensitized solar cells. The co-adsorbent HC-acid shows an impressive photovoltaic performance when used with organic dye-sensitizer. The J_{sc} values increase from 14.96 mA cm^{-2} to 18.01 mA cm^{-2} ; V_{oc} values from 595 mV to 663 mV, and η (%) from 6.59 to 9.09.⁸⁹ These increases have been attributed

to the HC-Acid showing dual functionality when used with organic dye-sensitizers, firstly it harvests light at a lower wavelength region of the solar spectrum and secondly it reduces the π - π stacking interaction between aromatic moieties of the organic dye-sensitizer. As a result the overall performance of device increases.⁸⁹ The molecular structures of some co-adsorbents used in DSSCs to improve the performance of device are listed in Table 1-2.

Table 1-2. The molecular structures of some representative co-adsorbents used in DSSCs.

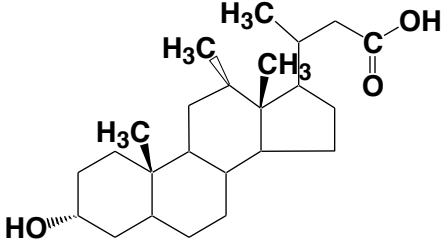
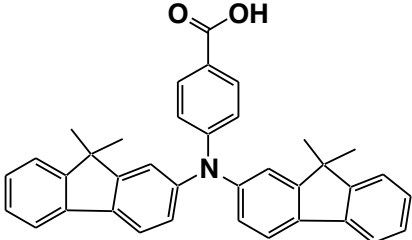
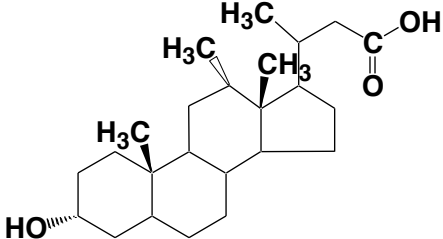
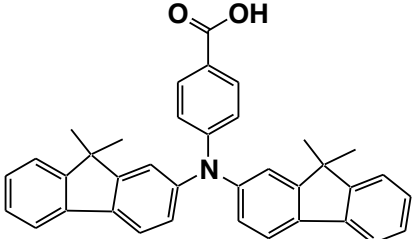
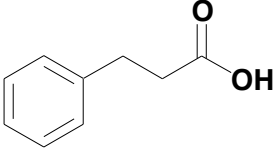
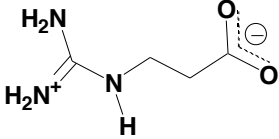
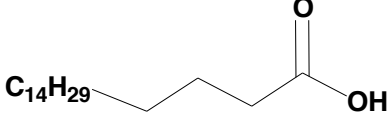
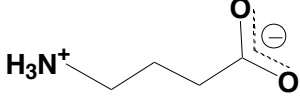
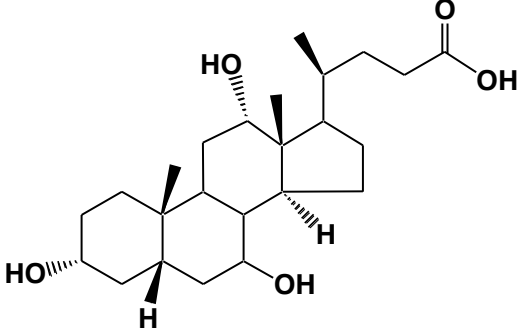
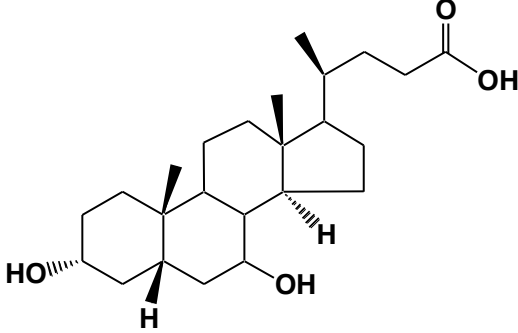
 <p>3-(3-Hydroxy-10,12,13-trimethyl-hexadecahydro-Cyclopenta[a]phenanthren-17-yl)-butyric acid (DCA)</p>	 <p>4-(bis(9,9-dimethyl-9H-flouren-2-yl)amino)benzoic acid (HC-Acid)</p>
 <p>3-(3-Hydroxy-10,12,13-trimethyl-hexadecahydro-Cyclopenta[a]phenanthren-17-yl)-butyric acid (DCA)</p>	 <p>4-(bis(9,9-dimethyl-9H-flouren-2-yl)amino)benzoic acid (HC-Acid)</p>

Table 1-2. Continued

 <p>3-phenylpropionic acid (PPA)</p>	 <p>4-guanidinobutyric acid (GBA)</p>
 <p>Stearic Acid (SA)</p>	 <p>4-aminobutyric acid (ABA)</p>
 <p>Cholic Acid (CHA)</p>	 <p>Chenodeoxy Cholic Acid (CDCA)</p>

L. Han and co-workers reported new donor-acceptor type co-adsorbents shown in Figure 1-13. These co-adsorbents consist of three units including electron donating, spacer and electron accepting groups.⁹⁰

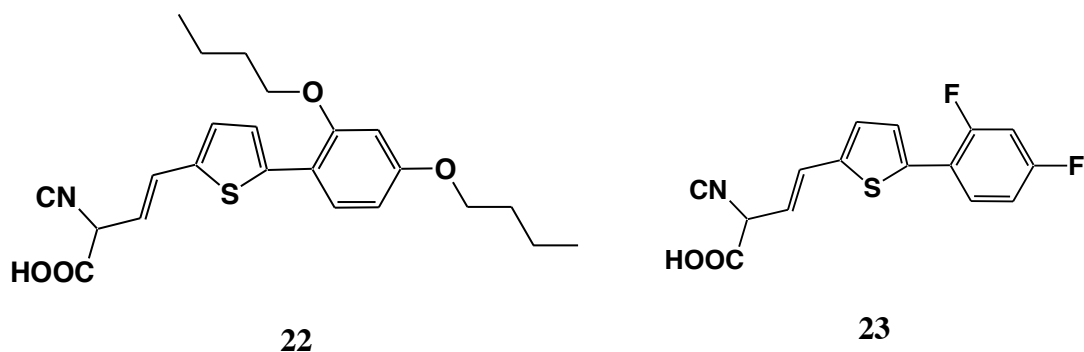


Figure 1-13. Molecular structure of donor-acceptor type co-adsorbents.

In the co-adsorbents **22-23**, the key role of butyloxy-substituted phenyl and fluorine-substituted phenylene is electron donation, where as the cyanoacetic acid group is an acceptor and anchor, and thiophene works as a p-spacer. The UV-visible spectra of co-adsorbents show strong absorption at 390nm and 360 nm respectively, attributed to intermolecular charge transfer between donor and acceptors in the co-adsorbent. These finds are verified by the IPCE spectra of black-dye, normally the black-dye shows a strong dip in IPCE spectra around 400 nm due to the competitive absorption of light by I_3^- . However, on employing co-adsorbents **22-23** along with black dye the dip in IPCE spectra is compensated for by injection of electrons from the co-adsorbent into the TiO_2 film that translates into increased light-to-power conversion efficiency (η) of DSSCs, from 10.70 to 11.4% and V_{oc} (mV) 727 to 743, a new certified efficiency record.⁹⁰

Gratzel and co-workers found that using 1-Decylphosphonic acid (Figure 1-14) as a co-adsorbent along with ruthenium bipyridyl complex (Z907) remarkably improved stability, short-circuit photocurrent density (J_{SC}) and efficiency of the device.⁵⁷

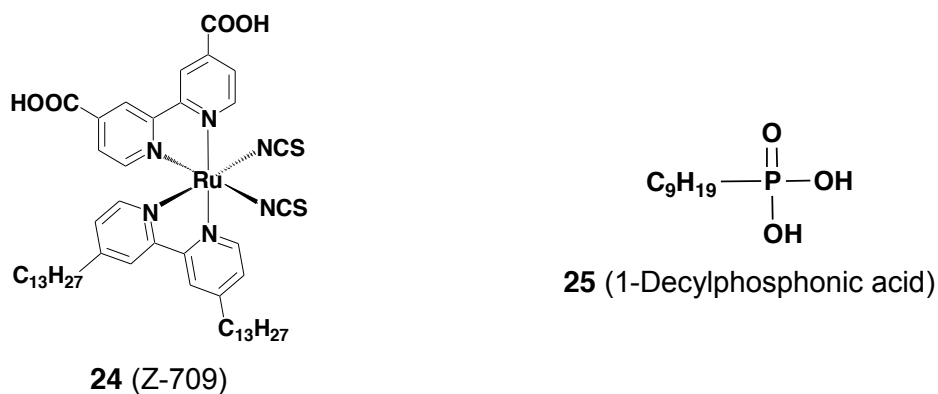


Figure 1-14. Molecular structure of Z-709 and 1-Decylphosphonic acid co-adsorbent.

The device prepared with Z-907 and a co-absorbent showed voltage output drops of only 20 mV, which is less than 3%, during 1000h of ageing at 80 °C, whereas the device prepared with Z-907 alone showed a decline of 90 Mv.⁵⁷

The addition of co-adsorbent with the dye-sensitizer does not always show a distinct improvement in performance of the device; it may even decrease the efficiency when there is no aggregation between dye-sensitizers. It was suggested that the dye-sensitizer itself forms a compact layer on the TiO₂ surface; preventing quenching and aggregation, while co-adsorbent might damage the protective layer of dye-sensitizers and consequently increase recombination reactions.⁹¹

1.7. The Interaction between Sensitizer and Electrolyte

Iodide/triiodide (I^-/I_3^-) is the most commonly used electrolyte in DSSCs, however, it limits (0.70 to 0.8 V) the attainable open-circuit voltage (V_{oc}) due to excessive loss of energy during the dye-sensitizer regeneration process, a substantial drawback of current DSSCs.⁹² To replace the I^-/I_3^- electrolyte, researchers have discovered and used several redox couples

that are relatively less corrosive and show potential to achieve high open-circuit voltage (V_{oc}) with promising solar-to-power conversion efficiencies.⁹³ These potential electrolytes include organic solvents, ionic liquids, conducting polymers and hole transport material (HTM).⁹⁴ Recently, Yella et al achieved the highest recorded efficiency of 12.3% in lab scale studies of DSSCs under 1 sun illumination (kW/m^2) by using cobalt ($\text{Co}^{2+}/\text{Co}^{3+}$) redox mediator. The cobalt ($\text{Co}^{2+}/\text{Co}^{3+}$) mediator has an advantage over the I^-/I_3^- because the cobalt mediator is surrounded by ligands that can further modify (Figure 1-15) the redox potential, and bulky groups can be introduced as insulating spacers to the ligands, which can reduce the recombination reaction between electrolyte and titania resulting in improved V_{oc} .⁹⁵ The molecular structure of some polypyridyl cobalt (II/III) redox mediators used in DSSCs is shown in Figure 1-15.

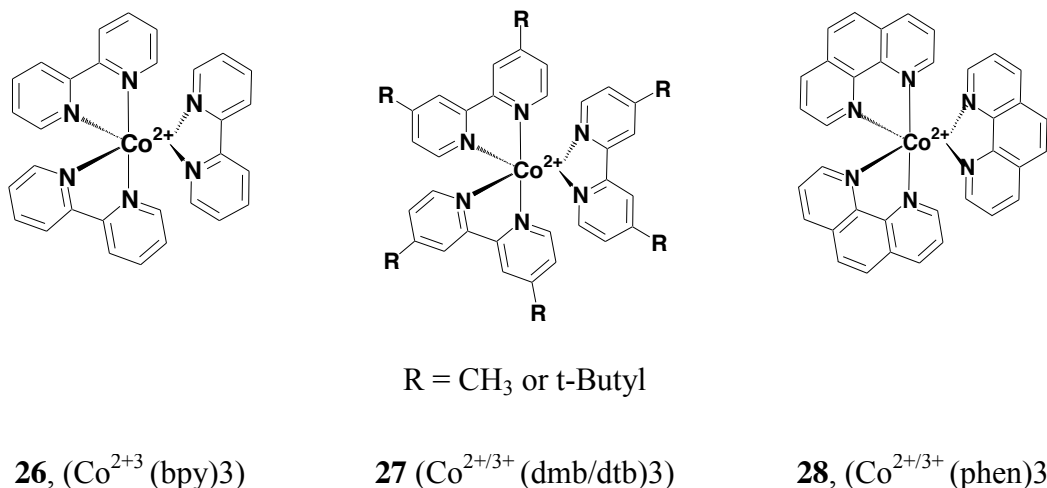


Figure 1-15. Molecular structure of the different cobalt polypyridyl redox mediators used in DSSCs.

However, cobalt ($\text{Co}^{2+}/\text{Co}^{+3}$) based electrolytes containing bulky groups limit the mobility of ions during diffusion through the electrolyte significantly less than that of iodine ions.⁹⁶

Interaction between dyes and electrolytes can increase charge recombination reactions, consequently reducing performance of the device. Recently, Reynal and co-workers reported a series of heteroleptic ruthenium (II) polypyridyl complexes (Figure 1-16) that contains electron-donating ($-\text{NH}_2$) or electron-withdrawing ($-\text{NO}_2$) groups. The presence of these groups can reduce the short circuit current (V_{oc}) significantly by the complex with the redox-active I-/I³⁻ - electrolyte.

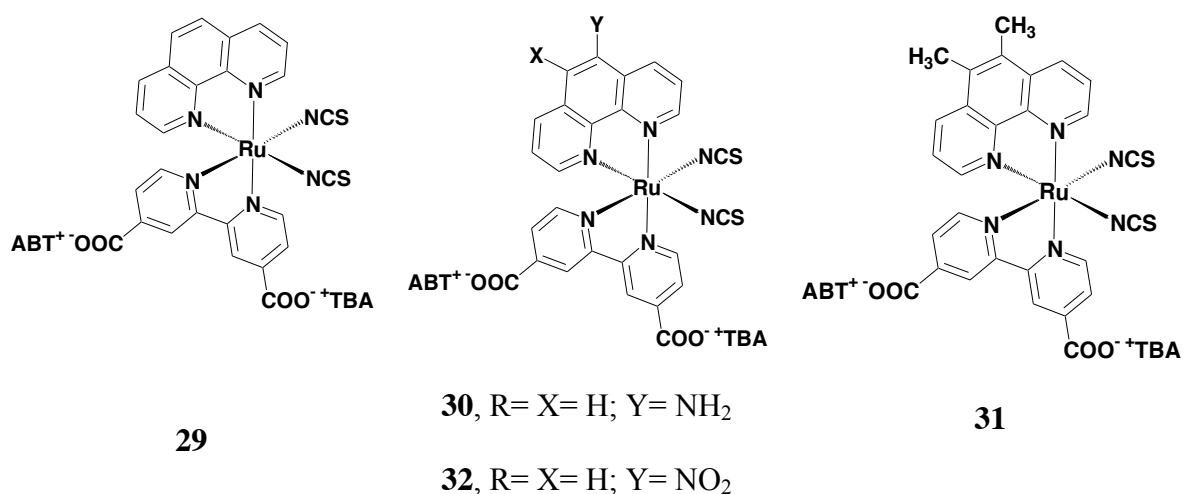


Figure 1-16. Molecular structure of heteroleptic ruthenium (II) polypyridyl dye-sensitizers (29-32) containing electron-donating ($-\text{NH}_2$) or electron-withdrawing ($-\text{NO}_2$) groups.

The UV-visible absorption of MLCT observed for complexes 29-32 are 522nm, 546nm, 531nm and 538 nm respectively, the $-\text{NH}_2$ and $-\text{NO}_2$ groups on the phenanthroline ligand caused a red shift in absorption spectra. The photovoltage (V_{oc}) was reduced remarkably, for

complexes **29** and **31** it was 0.67 and for complexes **30** and **32** was 0.48 and 0.44 respectively. It was suggested that reduction of V_{oc} is because of low electron regeneration from the electrolyte due to the electron recombination between $\text{TiO}_2/\text{electrolyte}$, and/or low yield of electron injection due to the quenching of complex-excited state by the electrolyte.⁹⁷ Halgfeldt et al investigated the relationship between open-circuit voltage and molecular structure of a series of organic dye-sensitizers by studying the degree of recombination between $\text{TiO}_2/\text{electrolyte}$ interfaces. They found that strong polarity of the dye-sensitizer facilitated formation of a complex between dye-sensitizer and electrolyte ($\text{I}_3^- / 3\text{I}^-$)⁹⁸, and as result the recombination reaction increases. Therefore, in order to keep the redox couple separate from the TiO_2 surface, it is necessary to reduce the formation of complexes between dye and electrolyte.

1.8. Electrolyte Additives

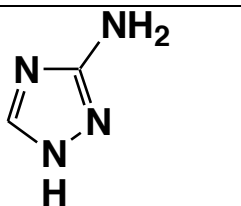
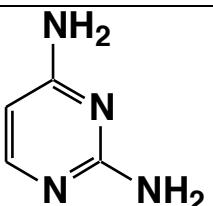
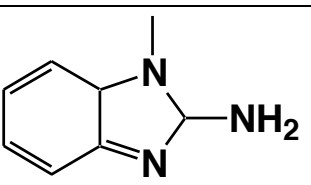
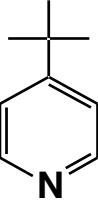
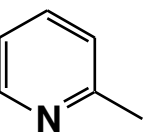
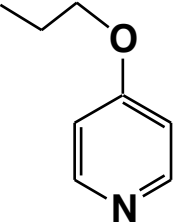
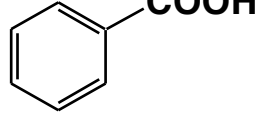
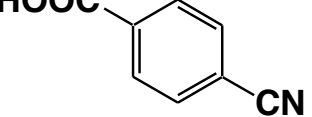
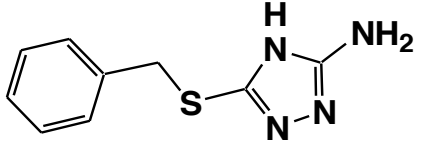
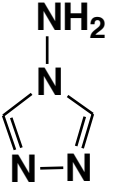
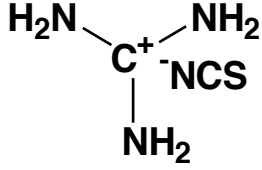
In addition to the main active redox couple, several other nitrogen containing heterocyclic derivatives including imidazole, triazole, benzimidazole and pyrimidine are commonly used as additives in the electrolyte to improve the photovoltaic performance of DSSCs.⁹⁹ The effects of additives are well understood playing a role in modification of redox couple potential, shifting of TiO_2/CB level, forming a compact layer on TiO_2 surface, reducing dye aggregation, and TiO_2 surface blocking from the electrolyte. Among the heterocyclic additives, imidazole has shown the best performance, with a V_{oc} of 0.85 V.⁹⁹ These additives adsorb onto the surface of the TiO_2 , elevating the level of the conduction band and increasing the V_{oc} . The amount of increase depends largely on the electron donating

power of the additives, large charge density, and donating capability. However, the addition of such additives reduces the electron injection efficiency from the dye-sensitizers to TiO_2 due to the increased TiO_2 -CB level, and as a result the J_{sc} decreases. Most alkaline organic additives uplift the level of the conduction band and hence increase the V_{oc} , but at the same time they increase electron recombination reactions. Attempts have been made to find additives that not only raise the TiO_2 -CB level, but also minimize the electron recombination reactions. Kopidakis and co-workers reported that guanidinium thiocyanate can slow the recombination reactions by a factor of about 20, and at the same time induced downshift in the TiO_2 -CB level, yet show an overall improvement in the open-circuit photovoltage.¹⁰⁰ Recently, Zhang and co-workers reported that the 4-guanidinobutyric acid (GBA) can shift the TiO_2 -CB level toward a more negative potential and reduce the interfacial back charge-transfer reaction; simultaneously. As a result, V_{oc} and solar-to-power conversion efficiency of the device increased significantly.¹⁰¹

Gratzel and co-worker reported that adding 4-tert-butylpyridine to the electrolyte dramatically increased the V_{oc} from 0.38 V to 0.72 V and the overall light-to-power conversion efficiency (η) from 7.12% to 10% without affecting the short-circuit photocurrent (J_{sc}).¹⁰² It was suggested that the increase in the open-circuit voltage and efficiency (η) by 4-tert-butylpyridine is due to the suppression of the dark current at the TiO_2 /electrolyte junction. The dark current arises from the reduction of triiodide by recombination of injected electrons from the TiO_2 conduction band. Another possible reason is the 4-tert-butylpyridine may form a complex with the lithium ion in the electrolyte to prevent migration of the lithium ion to the TiO_2 surface, suppressing recombination reactions. H. Kusama et al using

20 different aminotriazole as additives obtained a similar result. Most of the additives enhanced the V_{oc} and the solar-to-power conversion efficiency (η), but reduced the short circuit photocurrent density (J_{sc}) of the DSSC.¹⁰³ The molecular structures of some additives used in electrolytes to improve the V_{oc} of DSSCs are listed in Table 1-3.

Table 1-3. The molecular structures of some representative additives used in electrolytes.

 <p>1H-[1,2,4]Triazol-3-ylamine</p>	 <p>Pyrimidine-2,4-diamine</p>	 <p>1-Methyl-2,7a-dihydro-1H-benzoimidazol-2-ylamine</p>
 <p>4-tert-Butyl-pyridine</p>	 <p>2-Methyl-pyridine</p>	 <p>4-Propoxy-pyridine</p>
 <p>Benzoic acid</p>	 <p>4-Cyano-benzoic acid</p>	 <p>4-Methoxy-benzoic acid</p>
 <p>5-Benzylsulfanyl-4H-[1,2,4]triazol-3-ylamine</p>	 <p>[1,2,4]Triazol-4-ylamine</p>	 <p>Guanidinium thiocyanate</p>

H. Kusama and co-workers studied the influence of 20 different benzimidazole derivatives on the photovoltaic performance of the DSSCs. Adding benzimidazole additives remarkably enhanced the V_{oc} and the fill factor (ff), but reduced the J_{sc} values. They found that the greater the partial charge of the nitrogen atoms in position 3 of the benzimidazole groups, the larger the V_{oc} values, and the smaller the molecular size of the benzimidazole derivatives, the greater the V_{oc} values.¹⁰³

REFERENCES

1. O'Regan, B.; Grätzel, M. *Nature* **1991**, *153*, 737.
2. Tsubomura, H.; Matsumura, M.; Nomura, Y.; Amamiya, T. *Nature* **1976**, *261*, 402.
3. O'Regan, B.; Grätzel, M. *Nature* **1991**, *153*, 737.
4. Hardin, B. E.; Snaith, H. J.; Michael D. McGehee, M. D. *Nature photonics* **2012**, *6*, 162.
5. Bär, M.; Repins, I.; Contreras, M. A.; Weinhardt, L.; Noufi, R.; Heske, C. *Appl. Phys. Lett.* **2009**, *95*, 052106.
6. Green, M. A.; Emery, K.; Hishikawa, Y.; Warta, W. *Prog. Photovoltaics* **2010**, *18*, 144.
7. Bomben, P. G.; Theriault, K. D.; Berlinguette, C. P. *Eur. J. Inorg. Chem* **2011**, 1806.
8. Gordon, R. G. *MRS Bulletin* **2000**, *52*, 28.
9. Granqvist, C. G. *Sol. Energy Mater. Sol. Cells* **2007**, *91*, 1529.
10. Rhee, S. W.; W., K. *Korean J. Chem. Eng.* **2011**, *28*, 1481.
11. Grätzel, M. *Photochemistry Review* **2003**, *4*, 145.
12. Qin, Y.; Q., P. *International Journal of Photoenergy* **2012**, *2012*, 1.
13. Kuang, D.; Klein, C.; Ito, S.; Moser, J. E.; Baker, R. H.; Evans, N.; Durrant, F.; Grätzel, C.; Zakeeruddin, S. K.; Grätzel, M. *Adv. Mater* **2007**, *19*, 1133.
14. Kohle, O.; Gratzel, M. *Advanced Materials* **1997**, *9*, 904.
15. A., H.; Boschloo, G.; Sun, L.; Kloo, L.; Pettersson, H. *Chemical Review* **2010**, *110*, 6516.
16. Miao, W.; Choi, J. P.; Bard, A. J. *J. Am. Chem. Soc.* **2002**, *124*, 14478.
17. Drummond, T. G.; Hill, M. G.; Barton, J. K. *Nature Biotechnology* **2003**, *21*, 1192.

18. Welter, S.; Brunner, K.; Hofstraat, J. W.; DeCola, L. *Nature* **2003**, *421*, 54.
19. Grätzel, M. *Nature* **2001**, *414*, 338.
20. Juris, A.; Balzani, V.; Barigelletti, F.; Campagna, S.; Belser, P.; Von Zelewsky, A. *Coordination Chemistry Reviews* **1988**, *84*, 85.
21. Kalyanasundaram, K. *Photochemistry of Polypyridine and Porphyrin Complexes*; Academic Press: London, 1992; p 17.
22. Gratzel, M. *Journal of Photochemistry and Photobiology C: Photochemistry Reviews* **2003**, *4*, 145.
23. Hagfeldt, A.; Boschloo, G.; Sun, L.; Kloo, L.; Pettersson, H. *Chemical Reviews* **2010**, *110*, 6615.
24. Levinson, R.; Berdahl, P.; Akbari, H. *Solar Energy Materials & Solar Cells* **2005**, *89*, 351.
25. O'Regan, B.; Grätzel, M. *Nature* **1991**, *353*, 737.
26. Nazeeruddin, M. K.; Zakeeruddin, S. M.; Bake, R. H.; Jirousek, M.; Liska, P.; Vlachopoulos, N.; Shklover, V.; C., F.; Grätzel, M. *Inorg. Chem* **1999**, *38*, 6298.
27. Nazeeruddin, M. K.; Zakeeruddin, S. M.; R., B. H.; Jirousek, M.; Liska, P.; Gratzel, M. *Inorg. Chem.* **1999**, *38*, 6298.
28. K., M.; Zakeeruddin, S. M.; R., B. H.; Liska, P.; Gratzel, M. *J. Phys. Chem. B* **2003**, *107*, 8981.
29. Nazeeruddin, M. K.; Pe'chy, P.; Renouard, T.; Zakeeruddin, S. M.; Gratzel, M. *J. Am. Chem. Soc.* **2001**, *123*, 1613.
30. Kuang, D.; Ito, S.; Wenger, B.; Klein, C.; Moser, J. E.; Humphry, R. B.; Zakeeruddin, S. M.; Gratzel, M. *J. Am. Chem. Soc* **2006**, *128*, 4146.

31. Wang, P.; Zakeeruddin, S. M.; Moser, J.-E.; Humphry-Baker, R.; Comte, P.; Aranyos, V.; Hagfeldt, A.; Nazeeruddin, M. K.; Grätzel, M. *Advanced Materials* **2004**, *16*, 1806.
32. Jiang, K. J.; Masaki, N.; Xia, J. B.; Noda, S.; Yanagida, S. *Chem. Commun.* **2006**, 2460.
33. Yu, Q.; Liu, S.; Zhang, M.; Cai, N.; Wang, Y.; Wang, P. *J. Phys. Chem. C*, **2009**, *113*, 14559.
34. Nazeeruddin, M. K.; Pechy, P.; M., G. *J. Chem. Soc., Chem. Commun.* **1997**, *18*, 1705.
35. Islam, A.; Sugihara, H.; Yanagida, M.; Hara, K.; Fujihashi, G.; Tachibana, Y.; Katoh, R.; Murata, S.; Arakawa, H. *New J. Chem.* **2002**, *26*, 966.
36. Heimer, T. A.; Heilweil, E. J.; Bignozzi, C. A.; Meyer, G. J. *J. Phys. Chem. A* **2000**, *104*, 4256.
37. Yanagida, M.; Yamaguchi, T.; Kurashige, M.; Hara, K.; Katoh, R.; Sugihara, H.; Arakawa, H. *Inorg. Chem.* **2003**, *42*, 7921.
38. Kolemen, A.; A., B. O.; Cakmak, Y.; Barin, G.; Ela, S. E.; Marszalek, M.; Yum, J. H.; Zakeeruddin, M.; Nazeeruddin, M. K.; Grätzel, M.; Akkaya, E. U. *Chem. Sci.* **2011**, *2*, 949.
39. Islam, A.; Sugihara, H.; Yanagida, M.; Hara, K.; Fujihashi, G.; Tachibana, Y.; Katoh, R.; Murata, S.; Arakawa, H. *New J. Chem.* **2002**, *26*, 966.
40. Chou, C. C.; Wu, K. L.; Yun, C.; Hu, W. P.; Yu, S. J. *Angew. Chem. Int. Ed.* **2011**, *50*, 2054.
41. Barigelletti, F.; Ventura, B.; Collin, J. P.; Kayhanian, R.; Gavina, P.; Sauvage, J. P. *Eur. J. Inorg. Chem* **2000**, 113.

42. Juris, A.; Balzani, V.; Barigelletti, F.; Campagna, S.; Belser, P.; Von Zelewsky, A. *Coord. Chem. Rev.* **1988**, *84*, 85.
43. Polson, M.; Loiseau, F.; Campagna, S.; Hanan, G. *Chem. Comm.* **2006**, 1301.
44. Polson, M.; Medlycott, E.; Hanan, G.; Mikelsons, L.; Taylor, N.; Watanabe, M.; Tanaka, Y.; Loiseau, F.; Passalacqua, R.; Campagna, S. *Chem. Eur. J.* **2004**, 3640.
45. Son, S.; Park, K.; Lee, Y.; Kim, B.; Choi, C.; Lah, M.; Jang, Y.; Jang, D.; Chung, Y. *Inorg. Chem.* **2004**, *43*, 6896.
46. Son, S.; Park, K.; Lee, Y.; Kim, B.; Choi, C.; Lah, M.; Jang, Y.; Jang, D.; Chung, Y. *Inorg. Chem.* **2004**, *43*, 6896.
47. Duati, M.; Tasca, S.; Lynch, F.; Bohlen, H.; Vos, J.; Stagni, S.; Ward, M. *Inorg. Chem.* **2003**, *42*, 8377.
48. Constable, E.; Thompson, A.; Cherryman, J.; Liddiment, T. I. *Chim. Acta.* **1995**, *235*, 156.
49. Barigelletti, F.; Ventura, B.; Collin, J.; Kayhanian, R.; Gavina, P.; J.P., S. *Eur. J. Inorg. Chem.* **2000**, 113.
50. Huang, S. Y.; Schlichthor, G.; Nozik, A. J.; Gra1tzel, M.; Frank, A. J. *J. Phys. Chem. B* **1997**, *101*, 2576.
51. Listorti, A.; O'Regan, B.; Durrant, J. R. *Chem. Mater.* **2011**, *23*, 3381.
52. Clifford, J. N.; Ferrero, E. M.; Viterisi, A. L.; Palomares, E. *Chem. Soc. Rev.* **2011**, *40*, 1635.
53. Haque, S.; Handa, S.; Peter, K.; Palomares, E.; Thelakkat, M.; Durrant, J. R. *Angew. Chem. Int. Ed* **2005**, *44*, 5740.
54. Clifford, J. N.; Palomares, E.; Nazeeruddin, M. K.; Grätzel, M.; Nelson, J.; Li, X.;

- Long, N.; Durrant, J. R. *J. Am. Chem. Soc.* **2004**, *136*, 5225.
55. Huang, S. Y.; Schlichthörl, G.; Nozik, A. J.; Grätzel, M.; Frank, A. J. *J. Phys. Chem. B* **1997**, *101*, 2576.
56. O'Regan, B.; Grätzel, M. *Nature* **1991**, *353*, 737.
57. Wang, P.; Zakeeruddin, S. M.; Humphry-Baker, R.; Moser, J.-E.; Grätzel, M. *Advanced Materials* **2003**, *15*, 2101.
58. Chen, C. Y.; Wang, M.; Li†, J. Y.; Pootrakulchote, N.; Alibabaei, L. *ACS Nano* **2009**, *3*, 3103.
59. Bessho, T.; Yoneda, E.; Yum, J. H.; Guglielmi, M.; Tavernelli, I.; Imai, H.; Rothlisberger, U.; Nazeeruddin, M. K.; Grätzel, M. *J. Am. Chem. Soc.* **2009**, *131*, 5930.
60. Kuang, D.; Klein, C.; Ito, S.; Moser, J. E.; Baker, R.; Zakeeruddin, S. M.; Grätzel, M. *Adv. Funct. Mater.* **2007**, *17*, 154.
61. Jang, S. R.; Yum, J. H.; Klein, C.; Kim, K. J.; Wagner, P.; Officer, D.; Grätzel, M.; Nazeeruddin, M. K. *J. Phys. Chem. C* **2009**, *113*, 1998.
62. Karthikeyan, C. S.; Wietasch, H.; Thelakkat, M. *Advanced Materials* **2007**, *19*, 1091.
63. Yum, J. H.; Jung, I.; Baik, C.; Ko, J.; Nazeeruddin, M. K.; Grätzel, M. *Energy Environ. Sci.* **2009**, *2*, 100.
64. Chen, C. Y.; Chen, J. G.; Wu, S. J.; Li, J. Y.; Wu, C. G.; Ho, K. H. *Angew. Chem. Int. Ed.* **2008**, *47*, 7342.
65. Chen, C. Y.; Wu, S. J.; Li, J. Y.; Wu, C. G.; Ho, K. H. *Adv. Mater* **2007**, *19*, 3888.
66. Chen, C. Y.; Wu, S. J.; Wu, C. G.; Chen, J. G.; Ho, K. H. *Adv. Funct. Mater.* **2007**, *17*, 29.

67. Choia, H.; Baika, C.; Kima, S.; Kangb, M. S.; Xude, X.; Kangd, H. S.; Kanga, S. O.; Ko, J.; Nazeeruddin, M.; Grätzel, M. *New J. Chem.* **2008**, *32*, 2233.
68. Gao, F.; Wang, Y.; Shi, D.; Zhang, J.; Wang, M.; Jing, X.; Baker, R. H.; Wang, P.; Zakeeruddin, S. M.; Grätzel, M. *J. Am. Chem. Soc.* **2008**, *130*, 10720.
69. Shi, D.; Pootrakulchote, N.; Li, R.; Guo, J.; Wang, Y.; Zakeeruddin, S. M.; Grätzel, M.; Wang, P. *J. Phys. Chem. C* **2008**, *112*, 17046.
70. Jin, Z.; Masuda, H.; Yamanaka, N.; Minami, N.; Nakamura, T.; Nishikitani, Y. *J. Phys. Chem. C* **2009**, *113*, 2618.
71. Cao, Y.; Bai, Y.; Yu, Q.; Cheng, Y.; Liu, S.; Shi†, D.; Gao, F.; Wang, P. *J. Phys. Chem. C* **2009**, *113*, 6290.
72. Gao, F.; Wang, Y.; Zhang, J.; Shi, D.; Wang, M.; Baker, R. H.; Wang, P.; Zakeeruddin, S. M.; Grätzel, M. *Chem. Commun.* **2008**, 2635.
73. Chen, K. S.; Liu, W. H.; Wang, Y. H.; Lai, C. H.; Chou, P.; Lee, G.; Chen, K.; Chen, H. Y.; Chi, Y.; Tung, F. C. *Adv. Funct. Mater.* **2007**, *17*, 2964.
74. Zhao†, H. C.; Harney, J. P.; Huang, Y. T.; Yum, J. H.; Nazeeruddin, M. K.; Grätzel, M.; Tsai, M. K.; Rochford, J. *Inorg. Chem.* **2012**, *51*, 1.
75. Liu, K. Y.; Ko, C. Y.; Ho, K. C.; Lin, K. F. *Polymer* **2011**, *52*, 3318.
76. Ozawa, H.; Kawaguchi, H.; Okuyama, Y.; Arakawa, H. *Chem. Lett.* **2011**, *40*, 558.
77. Isalm, A.; Singh, S. P.; Yanagida, M.; Karim, M. R.; Han, L. *International Journal of Photochemistry* **2010**, *2011*, 7.
78. Han, W. S.; Han†, J. K.; Kim, H. Y.; Choi, M. J.; Kang, Y. S.; Pac, C.; Kang, S. O. *Inorg. Chem.* **2011**, *50*, 3271.
79. Anthonysamy.; Lee, Y.; Karunagaran, Y.; Ganapathy, V.; Rhee, S. W.; Karthikeyan,

- S.; Kim, K. S.; Ko, M. J.; Park, N. G.; Ju, M. J.; Kim, J. K. *J. Mater. Chem.* **2011**, *21*, 12389.
80. Stengel, I.; Mishra, A.; Pootrakulchote, N.; Moon, S.; Zakeeruddin, S. M.; Grätzel, M.; Bäuerle, P. *J. Mater. Chem.* **2011**, *21*, 3726.
81. Andrew, J.; Hallett.; Jones, J. E. *Dalton Trans.* **2011**, *40*, 3871.
82. Yin, J. F.; Chen, G. J.; Lu, Z.; Ho, K. C.; Lin, H. C.; Lu, K. L. *Chem. Mater.* **2010**, *22*, 4392.
83. Sivakumar, R.; Marcelis, A.; Anandan, S. *Journal of Photochemistry and Photobiology A: Chemistry* **2009**, *208*, 154.
84. Vougioukalakisa, G. C.; Stergiopoulou, T.; Kantonisa, G.; Kontosa, A. J. *Journal of Photochemistry and Photobiology A: Chemistry* **2010**, *214*, 22.
85. Bomben, P. G.; Koivisto, B. D.; Berlinguette, C. P. *Eur. J. Inorg. Chem.* **2011**, *11*, 1806.
86. Bchottomben, P. G.; J., g. T.; Schott, E.; P., B. C. *Angew. Chem. Int. Ed.* **2011**, *50*, 10682.
87. Ning, Z.; Tian, H. Photovoltage Improvement for Dye-sensitized Solar Cells. In *Dye-sensitized Solar Cells and solar Cell Performance*; Nova Science Publisher, Inc: New York, 2012; p 83.
88. Lim, J.; Kwon, Y. S.; Park, T. *Chem. Commun.* **2011**, *47*, 4147.
89. Song, H. M.; Seo, K. D.; Kang, M. S.; Choi, I. T.; Kim, S. K.; Eom, Y. K.; Ryu, J. H.; Ju, M. J.; K., K. H. *J. Mater. Chem.* **2012**, *22*, 3786.
90. Han, L.; Islam, A.; Chen, H.; Malapaka, C.; Chiranjeevi, B.; Zhang, S.; Yang, X.; Yanagida, M. *Energy Environ. Sci.* **2012**, *5*, 6057.

91. Ninga, Z.; Zhanga, Q.; Wua, W.; Tian, H. *Journal of Organometallic Chemistry* **2009**, *694*, 2705.
92. Yella, A.; Lee, H. W.; Tsao, H. N.; Yi, C.; Chandiran, A. K.; Nazeeruddin, M. K.; Diau, E. W. G.; Yeh, C. Y.; Zakeeruddin, S. M.; Grätzel, M. *Science* **2011**, *334*, 629.
93. Hardin, B. E.; Snaith, H. J.; McGehee, M. D. *nature photonics* **2012**, *6*, 162.
94. Hagfeldt, A.; Boschloo, G.; Sun, L.; Kloo, L.; Pettersson, H. *Chem. Rev.* **2010**, *110*, 6633.
95. Sapp, S. A.; Elliott, C. M.; Contado, C.; Caramori, S.; Bignozzi, C. A. *J. Am. Chem. Soc.* **2002**, *124*, 11215.
96. Nelson, J. J.; Amick, T. J.; Elliott, C. M. *J. Phys. Chem.* **2008**, *112*, 18255.
97. Reynal, A.; Forneli, A.; Ferrero, E. M.; S., D. A.; Ferran, A. V.; O'Regan, B. C.; Palomares, E. *J. Am. Chem. Soc.* **2008**, *130*, 13558.
98. Marinado, T.; Nonomura, K.; Nissfolk, J.; Karlsson, M. K.; Hagberg, D. P.; Sun, L.; Mori, S.; Hagfeldt, A. *Langmuir* **2010**, *26*, 2592.
99. Kusama, H.; H., A. *Journal of Photochemistry and Photobiology A: Chemistry* **2004**, *164*, 103.
100. Kopidakis, N.; Nathan, R.; Neale.; Frank, A. J. *J. Phys. Chem.* **2006**, *110*, 12485.
101. Zhang, Z.; Zakeeruddin, S. K.; O'Regan, B.; Baker, R. H.; Grätzel, M. *J. Phys. Chem. B* **2005**, *109*, 21818.
102. Nazeeruddin, M. K.; Kay, A.; Rodicio, I.; Baker, R. H.; Mueller, E.; Liska, P.; Vlachopoulos, N.; Graetzel, M. *J. Am. Chem. Soc.* **1993**, *115*, 6382.
103. Kusama, H.; Arakawa, H. *Journal of Photochemistry and Photobiology A: Chemistry* **2004**, *162*, 441.

CHAPTER 2

2. RESEARCH PERPOSAL

2.1. Research Objectives

The main objectives of this research are:

A. To develop novel bidentate Ru (II) polypyridyl complexes that exhibit better light harvesting, higher extinction coefficient, and are red shifted compared to the benchmark N719-dye, while maintaining the ground state oxidation potential (GSOP) and excited state oxidation potentials (ESOP) of these novel sensitizers thermodynamically favorable for the regeneration of the neutral dye- and electron injection, respectively. The strategy for achieving the above characteristics will be through narrowing HOMO/LUMO gap of the sensitizers while maintaining the LUMO of the dye above the conduction band edge via: a)- using low-lying LUMO (π^*) ligands such as bidentate ligands, and/or b)- displacing the Ru t_{2g} (HOMO) level upward while maintaining at least 0.2eV energy difference between the HOMO of the sensitizer and the redox potential of the electrolyte. The modification approach is schematically illustrated in Figure 2-1.

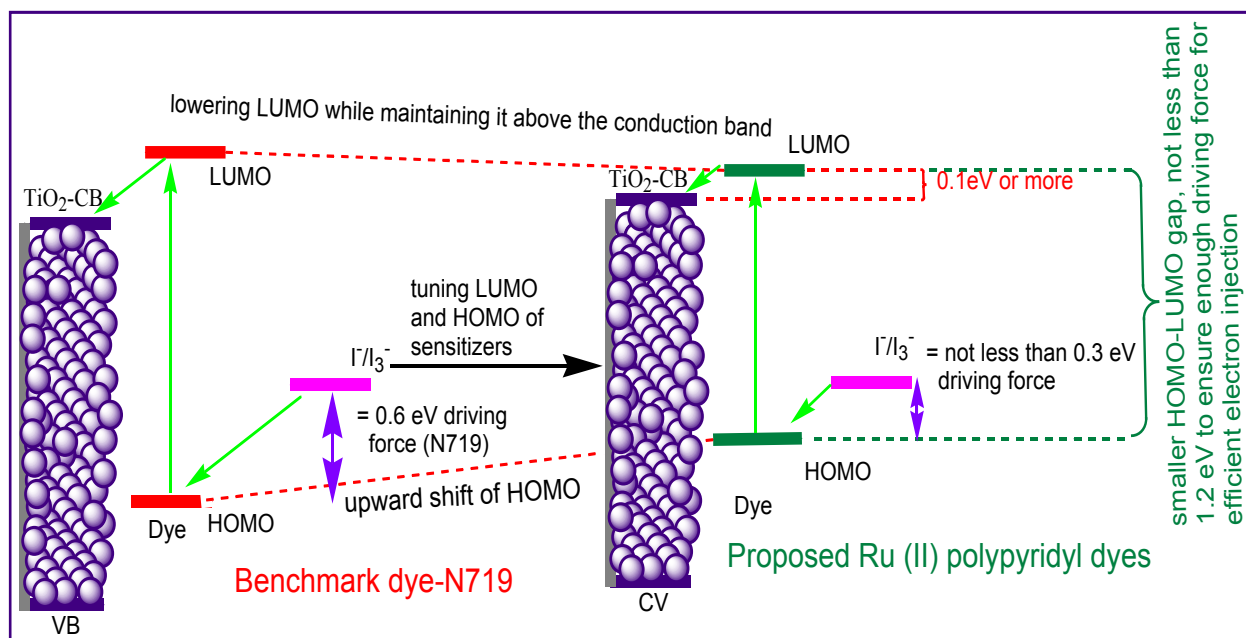


Figure 2-1. A Schematic showing the ground and excited state oxidation potentials (HOMO/LUMO gap) of N719 with respect to TiO_2 and electrolyte (I^-/I_3^-), and hypothetical representation of narrowing down the HOMO/LUMO gap of the proposed Ru (II) polypyridyl dyes.

The HOMO/LUMO gap can be tuned by functionalizing bipyridyl via Knoevenagel condensation, using strong electron donor antennas, in cyclic and/or acyclic forms. These antennas will be molecularly designed with different heteroatoms to study their effects on the GSOP and ESOP.

B. To understand the structure-property relationship of these sensitizers at the molecular level by studying their photophysical and photoelectrochemical properties (GSOP and ESOP), incident-photo-to-current conversion efficiency (IPCE), open-circuit voltage (V), and short-circuit photocurrent (J_{sc} , mAcm^{-2}), and total solar-to-electric conversion efficiency (η).

This study will help gain better understanding of the interrelationship between GSOP, ESOP, molar absorptivity, molecular structure of antenna with cyclic and/or acyclic electron donor,

excited state life time, electron injection and charge recombination's of the proposed sensitizers, which will aid in the molecular engineering of more efficient sensitizers for DSSCs in future studies.

2.2. Proposed Ru(II) Bipyridyl Sensitizers

The proposed building block of bidentate thiocyanated Ru (II) sensitizers and their general molecular structure are shown in Figure 2-2. The molecular components that will be incorporate to the bipyridyl moiety to manipulate their photophysical, electrochemical and photovoltaic properties. The main function and purpose of these components are briefly described in Figure 2-2.

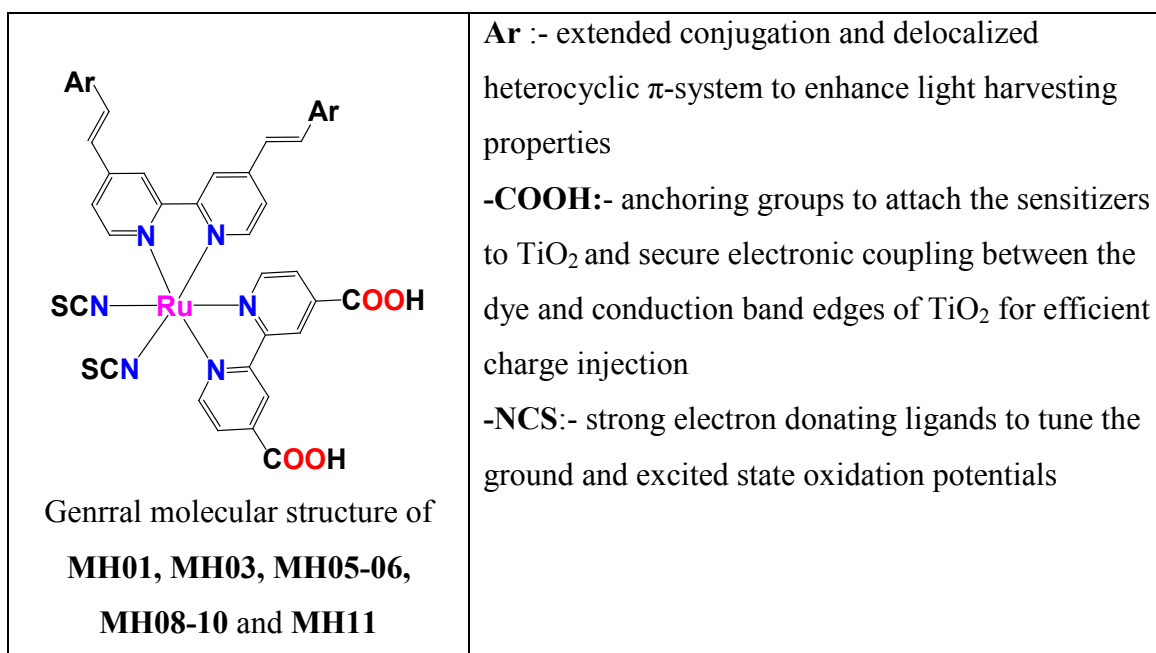
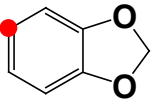
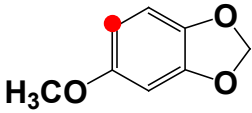
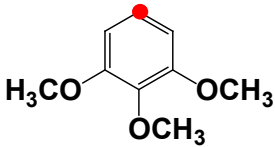
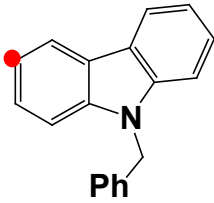
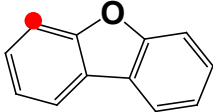
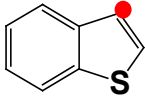
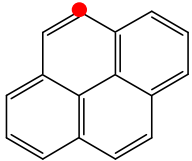


Figure 2-2. Proposed general structures of the bidentate Ru (II) polypyridyl complexes, and the function of each component is described.

Table 2-1. Ru (II) polypyridyl complexes and molecular structures of ligands (**Ar**)

Complexes	Ligands (Ar)	Complexes	Ligands (Ar)
MH01		MH03	
MH05		MH06	
MH08		MH09	
MH10		MH11	

CHAPTER 3

Cite this: *Phys. Chem. Chem. Phys.*, 2013, 15, 8401

Structure–property relationship of extended π -conjugation of ancillary ligands with and without an electron donor of heteroleptic Ru(II) bipyridyl complexes for high efficiency dye-sensitized solar cells†

Maqbool Hussain,^a Ahmed El-Shafei,^{*a} Ashraful Islam^b and Liyuan Han^b

Two new heteroleptic Ru(II) bipyridyl complexes **MH06** and **MH11** were designed, synthesized and characterized for DSSCs. While the ancillary ligand of **MH06** was molecularly engineered with a strong electron donating group coupled with an extended π -conjugated system, the ancillary ligand of **MH11** contained a longer π -conjugated system only. Molecular modeling, photophysical, and photovoltaic properties were compared under the same experimental conditions against the benchmark **N719**. In an effort to understand the structure–property relationship, their photovoltaic and photoelectrochemical properties including J_{sc} , V_{oc} , ground and excited state oxidation potentials, UV-Vis absorption, and molar extinction coefficients were studied. The UV-Vis results showed intense MLCT absorption peaks of **MH06** and **MH11** in the visible region with a red shift of 12 and 18 nm, respectively, with significantly higher molar extinction coefficients compared to **N719**. Tetrabutylammonium (TBA) substituted **MH11-TBA** demonstrated the most efficient IPCE of over 90% in the plateau region covering the entire visible spectrum and extending into the near IR region (ca. 890 nm), which showed a solar-to-power conversion efficiency (η) of 10.06%, significantly higher than that of the benchmark **N719** dye (9.32%). The superior performance in terms of the IPCE and J_{sc} of **MH11** can be attributed to the bulky and highly hydrophobic nature of the pyrene-based ancillary ligand, which behaves as a shielding barrier for hole-transport recombination between TiO₂ and the electrolyte. In addition, the IMPS results showed that the contribution of dyes to the conduction band shift of the TiO₂ level is almost similar, regardless of different substitutions on the bipy-moiety. This implies that the open-circuit photovoltage (V_{oc}) increases with reduced charge recombination in the presence of a thick layer of tetrabutyl ammonium ions (TBA) of the dye anchored on the surface of TiO₂.

Received 25th March 2013,

Accepted 25th March 2013

DOI: 10.1039/c3cp51260f

www.rsc.org/pccp

1. Introduction

Fossil fuel resources are limited and will significantly be diminished within the next fifty years. Therefore, sustainable and renewable energy sources are vital to fulfill the increasing global energy demand. Solar energy is abundant and ideal for remote and mobile applications. During the past two decades, dye-sensitized solar cells (DSSCs) have received considerable attention as a promising alternative source of renewable energy.^{1–4}

In 1976, a new approach to photovoltaic energy conversion by dye-sensitization was reported by Tsubomura. He demonstrated a solar-to-power conversion efficiency (η) of 1.5% using Rose Bengal as a dye-sensitizer and zinc oxide (ZnO) as a semiconductor.⁵ Nearly two decades later, in 1991, O'Regan and Grätzel achieved a remarkable efficiency of 7.9% using a Ru(II) bipyridyl complex (N3) as a sensitizer and TiO₂ as a semiconductor.⁶ To date the maximum efficiency achieved for DSSCs is 12.3% by co-sensitization of an organic (Y123) and a Zn-porphyrin complex (YD2-o-C8), using a Co(II/III)tris(bipyridyl) based redox electrolyte,⁷ which is about half of silicon-cell efficiency with module efficiencies ranging from 15% to 20%⁸ and comparable to thin-film technologies, which have achieved module efficiencies of 10–12.5%.⁷ The best performance of DSSCs

^a Polymer and Color Chemistry Program, North Carolina State University, Raleigh, NC 27695, USA. E-mail: Ahmed_El-Shafei@ncsu.edu

^b Photovoltaic Materials Unit, National Institute for Materials Science, 1-2-1 Sengen, Tsukuba, Ibaraki 305-0047, Japan

† Electronic supplementary information (ESI) available. See DOI: 10.1039/c3cp51260f

on a modular scale both in terms of overall conversion efficiency and stability was achieved using Ru(II) polypyridyl complexes^{9–11} owing to their strong metal-to-ligand charge transfer (MLCT) properties^{12–14} in the visible region between 400 nm to 600 nm,^{15–17} thermodynamically favorable ground and excited state oxidation potentials, long excited state lifetime,^{18–21} and photostability. Among the Ru(II) polypyridyl complexes, Ru(II) [*cis*-dithiocyanato-bis-2,2'-bipyridyl-4,4-dicarboxylate (N719, 11.20% η) has become the paradigm of a heterogeneous charge transfer (MLCT) sensitizer and has been extensively used in DSSCs technology. However, N719 is hydrophilic, owing to the presence of four COOHs and the absence of bulky ancillary ligands, which renders inferior hydrolytic stability, has a very low molar extinction coefficient and an inferior absorption in the NIR region of the solar spectrum. Preferably, a promising sensitizer for a single junction photovoltaic cell should be panchromatic and absorb energetic photons across a wide range of the solar spectrum, especially from 400 nm to 920 nm to effectively convert solar energy to electricity.

With the aforementioned in mind, we molecularly designed and synthesized two Ru(II) bipyridyl complexes **MH06** and **MH11** containing two different ancillary ligands with extended π -conjugation. **MH06** contains a strong electron donor coupled with an extended π -conjugated system (methoxynaphthalene) while **MH11** comprises an ancillary ligand of a longer π -conjugation (pyrene) with no electron donors. The structure–property relationship of these complexes was studied in terms of photoelectrochemical and photovoltaic properties and compared to that of the benchmark N719, under the same experimental conditions. The aim of introducing strong electron donating groups and extending the length of π -conjugation was to produce amphiphilic properties and accomplish better light harvesting across the visible region extending into the near-IR region, using a monolayer of dye-sensitizer molecules. The enhanced light harvesting was achieved while maintaining the excited state oxidation potential (ESOP) of the dye thermodynamically favorable for electron injection into the CB edge of the TiO₂ and the ground state oxidation potential (GSOP) of the dye more negative (–) than that of the electrolyte to regenerate the neutral dye.^{22–27} Fig. 1 shows a schematic

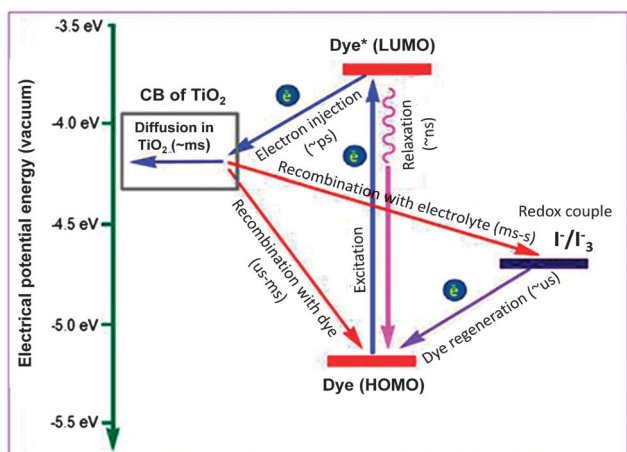


Fig. 1 Illustration of the thermodynamically favorable interfacial electron transfer processes in dye-sensitized solar cells.

illustration of the thermodynamically favorable interfacial electron transfer processes in dye-sensitized solar cells.

The molecular structures of the complexes **MH06**, **MH11** and **N719**, are shown in Fig. 2.

2. Experimental section

2.1. Synthesis of Ru(II) bipyridyl complexes

The synthesis of all ligands is provided in the ESI.† The solvents and chemicals were purchased from Sigma-Aldrich, Fisher Scientific or TCI-America, and used as received. Sephadex LH-20 was purchased from Fisher Scientific.

cis-(4,4'-Dicarboxy-2,ipyridine)(-bis-[2-(4-methoxy-naphthalen-1-yl)-vinyl]-2,2']bipyridine)(dithiocyanate)ruthenium(II) (**MH06**). The synthesis of **MH06** was carried out in a one-pot three-step reaction. The reactions were carried out in a 250 ml reaction flask equipped with a condenser and magnetic stirrer bar under argon. The flask was charged with anhydrous DMF (100 mL), dichloro-*p*-cymene-ruthenium(II) dimer (0.30 g, 4.899×10^{-4} mol) and 4,4'-bis-[2-(4-methoxy-naphthalen-1-yl)-vinyl]-[2,2']bipyridyl (0.5100 g, 9.797×10^{-4} mol). The reaction mixture was stirred at 90 °C for 4 h. Then, 2,2'-bipyridyl-4,4'-dicarboxylic acid was added (0.239 g, 9.797×10^{-4} mol) and the temperature was increased to 130 °C and allowed to run for 6 hours. After 6 hours, excess of NH₄NCS (0.5 g) was added to the reaction mixture and allowed to run for another 4 h at 130 °C. The last two steps of the reaction were monitored for completion by taking aliquots from the reaction mixture every 60 minutes and measuring its absorption spectrum until there was no increase in the absorbance of the MLCT peaks with respect to the π - π^* peak. The reaction mixture was cooled down to room temperature and DMF was removed using a rotary evaporator. Water was added to the flask, and the insoluble solid was vacuum filtered and washed with de-ionized water and ether. The product was dried overnight to give the crude product in 97% yield with respect to the starting material. The purification was carried out on a column using Sephadex LH-20 as the stationary phase and methanol as the mobile phase. ¹H-NMR, **MH06** (500 MHz, DMSO-d₆, 40 °C): δ /ppm 4.02 (s, 6H, -OCH₃), 7.07 (d, 2H, $J = 8.05$ Hz and 7.89 Hz (d, 2H, $J = 18.00$ Hz, CH=CH) 7.1–7.85 (m, 10H, ArH) 7.92 (s, 2H, ArH), 8.00–9.2 (m, 8H, ArH), 9.21 (d, 2H, $J = 5.85$ Hz, ArH), 9.47 (s, 2H, ArH), 14.00 (s, 2H, vs. weak, -COOH). ESI-MS: mass 982.1181; [M - 2H + TBA]⁻¹; theo. $m/z = 1222.3873$, found. $m/z 1222.3926$, error = 4.335 ppm. FT-IR (ATR): 2102 cm⁻¹ (-NCS stretch, N-bonded isomer, very strong); 1720 cm⁻¹ (C=O stretch of -COOH).

cis-(4,4'-Dicarboxy-2,ipyridine)(4,4'-bis-(2-pyren-1-yl-vinyl)-[2,2']bipyridine)(dithiocyanate)ruthenium(II) (**MH11**). **MH11** was prepared using the same procedure in 94% crude yield. The purification was performed in a column using Sephadex LH-20 as the stationary phase and methanol as the mobile phase. ¹H-NMR, **MH11** (500 MHz, DMSO-d₆, 40 °C): δ /ppm 7.51 (d, 2H, $J = 6.3$ Hz, and 7.83 Hz (d, 2H, $J = 15.95$ Hz, CH=CH), 7.85–8.50 (m, 16H, ArH), 8.54 (d, 2H, $J = 8.30$ Hz, ArH), 8.50 (s, 2H, ArH), 8.70–9.2 (m, 6H, ArH), 9.30 (s, 2H, ArH), 9.52 (d, 2H, $J = 6.1$ Hz, ArH), 13.12 (s, 2H, vs. weak, -COOH). ESI-MS: mass 910.0453,

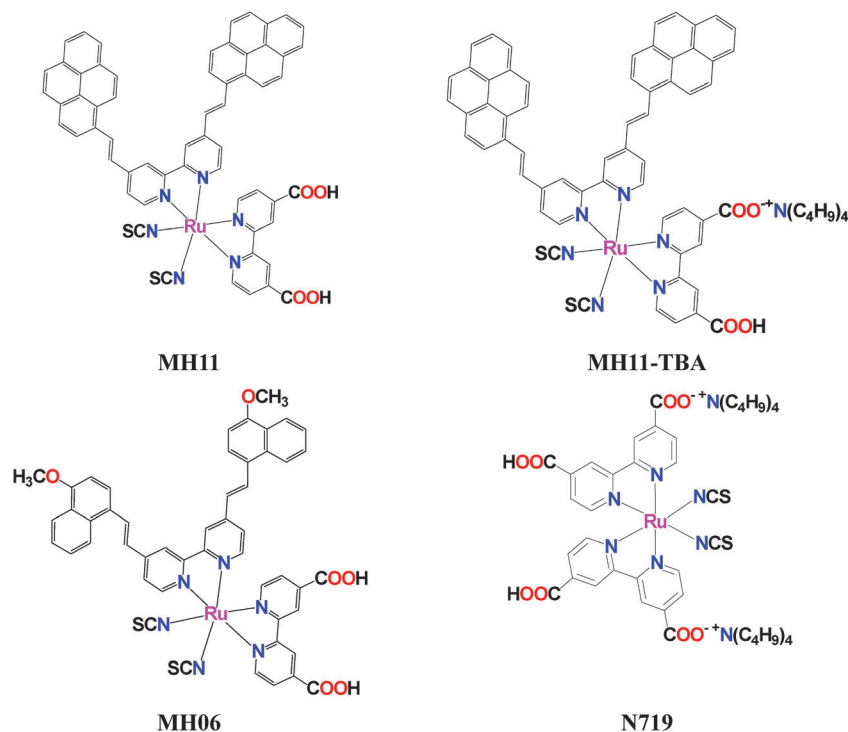


Fig. 2 Molecular structures of complexes MH06, MH11, MH11-TBA and N719.

$[M - 2H + TBA]^{-1}$, theo. $m/z = 1310.3974$, found $m/z = 1310.4038$, error = -4.884 ppm. FT-IR (ATR): 2101 cm^{-1} ($-\text{NCS}$ stretch, N-bonded isomer, very strong); 1718 cm^{-1} ($\text{C}=\text{O}$ stretch of $-\text{COOH}$).

2.2. UV-visible and emission properties

Fig. 3 illustrates a comparison between the UV-Vis absorption and emission spectra of MH06 and MH11 compared to N719, measured in DMF at a concentration of $2 \times 10^{-5}\text{ M}$, and the results are summarized in Table 1. Both MH06 and MH11 showed intense MLCT absorption peaks in the visible region at 541 nm ($21\,450\text{ M}^{-1}\text{ cm}^{-1}$) and 547 nm ($27\,000\text{ M}^{-1}\text{ cm}^{-1}$), with a red shift of 12 and 18 nm as compared to N719 of 530 nm ($14\,200\text{ M}^{-1}\text{ cm}^{-1}$), respectively. Because MH06 and MH11 comprise more extended π -conjugation and strong electron

Table 1 Absorption and luminescence properties of MH06, MH11 and N719

Complexes	Expt. ^a absorption spectrum (2×10^{-5} mol)		Emission ^b at 298 K λ_{em} (nm)
	λ_{max} (nm)	ϵ ($\text{M}^{-1}\text{ cm}^{-1}$)	
MH06	390; 541 ($d \rightarrow \pi^*$)	40 700; 21 450	806
MH11	414; 547 ($d \rightarrow \pi^*$)	51 550; 27 000	790
N-719	381; 529 ($d \rightarrow \pi^*$)	14 400; 14 200	746

^a UV-Vis spectra measured in DMF ($2 \times 10^{-5}\text{ M}$). ^b The emission spectra were obtained by exciting at the lowest MLCT band in DMF; all measurements were carried out at room temperature.

donating ancillary ligands, the metal based HOMO (t_{2g}) was destabilized, which furnished a better light harvesting as the result of a smaller HOMO–LUMO gap. In addition, the emission

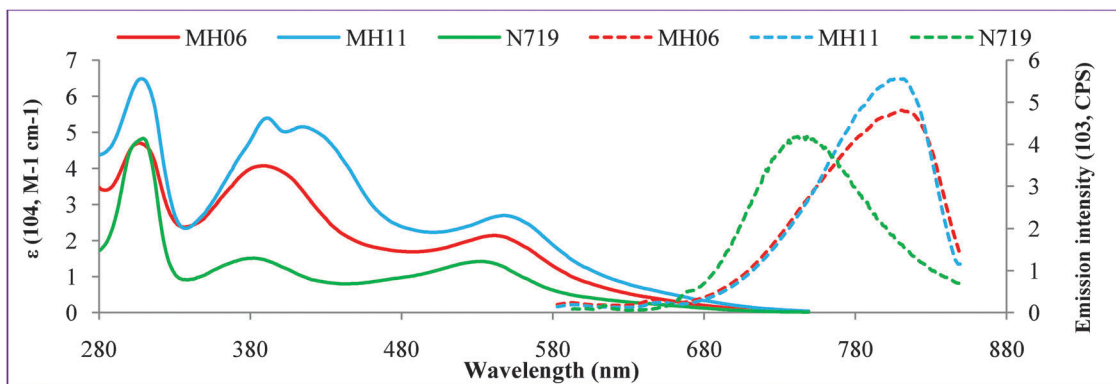


Fig. 3 UV-Vis absorption (solid line) and emission spectra (dashed line) of complexes MH06 and MH11 compared to N719, measured in DMF ($2 \times 10^{-5}\text{ M}$).

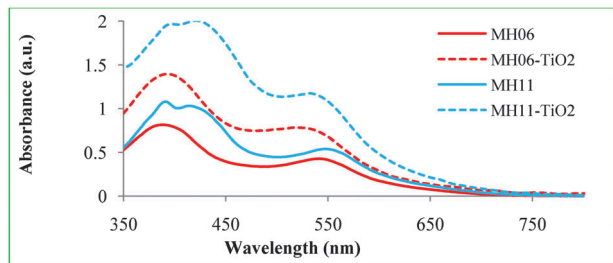


Fig. 4 UV-Vis absorption spectra of complexes **MH06** and **MH11** measured in DMF at 2×10^{-5} M (dashed line) and anchored to TiO_2 (solid line).

spectra demonstrated that the incorporation of strong electron-donor ligands furnished significantly stronger emission and more red shifted spectra than that of **N719**. Table 1 shows a summary of the absorption and emission properties of complexes **MH06** and **MH11** compared to **N719**.

Absorption spectra of **MH06** and **MH11** measured in DMF and after adsorption on transparent TiO_2 film are shown in Fig. 4. The absorption spectra profiles of both complexes in carboxylic acid form (in DMF) and carboxylate form (anchored- TiO_2) are almost similar and showed two broad absorption bands in the visible region, which originated from the MLCTs. The higher energy MLCT band is due to the charge-transfer transition from $\text{Ru} \rightarrow$ substituted bipyridyl-ligand and the lower energy MLCT band is due to a charge transition from $\text{Ru} \rightarrow$ 2,2'-bipyridyl-4,4'-dicarboxylic acid.²⁹ However, the deprotonation of carboxylic acid while anchoring to TiO_2 leads to a blue shift of the lower-energy MLCT band due to an increase in the energy of the LUMO of the 2,2'-bipyridyl-4,4'-dicarboxylic ligand as a consequence of destabilization of the LUMO. These findings are in agreement with the previously reported results for similar heteroleptic complexes.³⁰ Also, it can be clearly seen that **MH11** anchored to TiO_2 showed significantly better light harvesting properties than **MH06**, which can be attributed to the longer π -conjugation of **MH11**.

2.3. Ground and excited state oxidation potential properties

The ionization potential (IP) of **MH06**, **MH11** and **N719** anchored to TiO_2 film was measured using a photoemission yield spectrometer (Riken Keiki AC-3E), and the results are summarized in Table 2. The excited state oxidation potential (ESOP) energy values relative to the position of the TiO_2 conduction band are very important and determine the electronic coupling efficiency between the dye and the semiconductor. For a given species, the lowest singlet-to-singlet vertical electronic excitation (E_{0-0}) is defined as the difference between the excited and ground state oxidation potentials. Experimentally, the excited state oxidation potentials (ESOP) of **MH06**, **MH11** and **N719** can be estimated from eqn (1).

$$E_{0-0} = \text{ESOP} - \text{GSOP} \quad (1)$$

The experimental ionization potential (IP) values for **MH06**, **MH11** and **N719** were -5.51 , -5.49 and -5.76 eV. The IP values confirmed that the HOMO of these dyes is thermodynamically favorable for electron replenishment and efficient regeneration

Table 2 The excited state oxidation potential ($\text{Ru}^{3+/*}$) and the lowest singlet-singlet electronic transitions (E_{0-0}) for **MH06** and **MH11** compared to **N719**

Compound	Calculated energy (eV), TD-DFT (B3LYP/DGDZVP)			Experimental (eV)		
	E_{HOMO}	$\text{ESOP}_{\text{singlet}}$	$E_{0-0} = (S_0 - S_1)$	E_{0-0}^a	IP (HOMO) ^b	E^* ($\text{Ru}^{3+/*}$)
MH06	-5.467	-3.567	1.8992	1.848^a	-5.510	-3.662
MH011	-5.471	-3.554	1.9167	1.884^a	-5.490	-3.606
N719	-5.490	-3.490	2.00	1.990^a	-5.760	-3.770

Excited state oxidation potential = $\text{ESOP} = E^* (\text{Ru}^{3+/*})$; $\text{ESOP}_{\text{singlet}} = \text{GSOP} - E_{0-0}$; $E_{0-0} = (S_0 - S_1)$ = the lowest vertical excitation energy = the lowest singlet-singlet transition; GSOP = ground state oxidation potential = E_{HOMO} ; ^a E_{0-0} = based on the experimental absorption and emission spectra (DMF), calculated from the point of intersection. ^b IP = the experimental ionization potential measured using a photoemission yield spectrometer (Riken Keiki AC-3E); Excited-state oxidation potential, $E^* (\text{Ru}^{3+/*})$, was calculated from: $E^* (\text{Ru}^{3+/*}) = \text{IP} - E_{0-0}$. Calculated HOMO, ESOP, and E_{0-0} of **N719** were shown elsewhere.²⁸

of the dye through reaction with the redox couple I_3^-/I^- (-5.20 eV).³¹ The experimental excited-state oxidation potentials $E^* (\text{Ru}^{3+/*})$ of **MH06**, **MH11** and **N719** were -3.66 , -3.61 and -3.77 eV, respectively, which lay above the conduction band edge of nanocrystalline TiO_2 (-4.2 eV).³² Hence, efficient electron injection from the excited state of these dyes into the CB edge of TiO_2 is favorable, owing to the energetically favorable excited states of the dyes.

Table 2 also shows the calculated lowest singlet-to-singlet vertical electronic transition (E_{0-0}), using B3LYP/DGDZVP, of **MH06**, **MH11**, and **N719**, which are in excellent agreement with experimental results. Both the experimental and calculated transitions (E_{0-0}) demonstrated that **MH11** exhibited more energetically favorable ESOP and are better light harvesting sensitizers than **N719**, owing to its smaller E_{0-0} .

Calculated HOMO and LUMO isosurfaces of **MH06** and **MH11** (Fig. 5) showed that the HOMO electron density of **MH11**

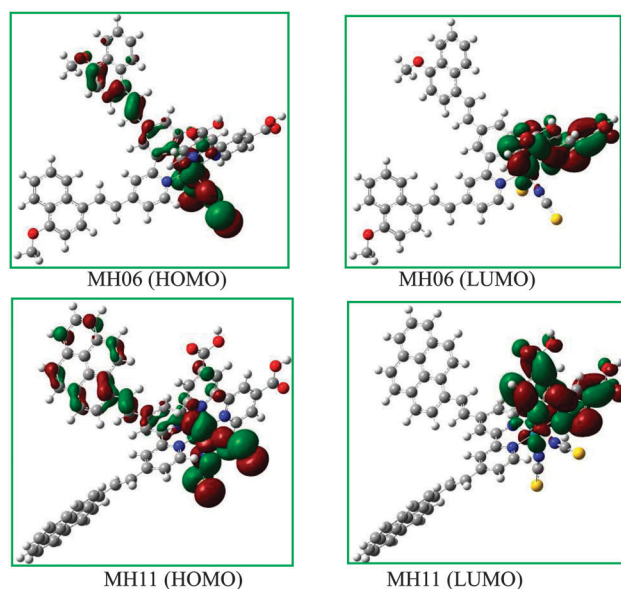


Fig. 5 Calculated HOMO and LUMO isosurfaces of **MH06** and **MH11**.

was considerably longer than that of **MH06** as it extended all the way through the conjugated system of the ancillary ligand, which explains the superior light harvesting of **MH11**. The LUMO hole distribution is mainly located on the bipyridyl carrying the carboxylic groups in both compounds.

2.4. Photovoltaic device characterization

The photovoltaic performance of complexes **MH06**, **MH11** and **N719** on a nanocrystalline TiO₂ electrode was studied under standard AM 1.5 irradiation (100 mW cm⁻²) using an electrolyte with a composition of 0.6 M dimethylpropyl-imidazolium iodide (DMPII), 0.05 M I₂, 0.1 M LiI and 0.3/0.5 M 4-ter-butylpyridine (TBP) in acetonitrile. Fig. 6 shows the incident-photon-to-current efficiency conversion (IPCE) spectra for the cells fabricated with complexes **MH06**, **MH11** and **N719**, where the incident photon-to-current conversion efficiency (IPCE) values are plotted as a function of wavelength.

The photocurrent action spectra of a solar device containing complex **MH11** demonstrated the most efficient sensitization over a broad wavelength range including the entire visible spectrum and extended into the near IR region (*ca.* 890 nm), with an impressive quantum efficiency of over 90% in the plateau region. It was also demonstrated that **MH11** exhibited more superior quantum efficiency in the visible as well as NIR regions than **N719**. Moreover, **MH11-TBA** showed better J_{sc} and hence IPCE due to the increase in ESOP, which led to more negative free energy between the ESOP and CB edge of TiO₂ and hence more efficient electron injection. While **MH11-TBA** achieved the maximum IPCE of 90% in the plateau region, **MH06** furnished a low IPCE of 70% in the same region.

The photovoltaic characteristics of **MH06**, **MH11**, **MH11-TBA** and **N719** were studied under simulated one sun illumination under standard conditions (AM 1.5, 1.00 W m⁻²).

The photovoltaic parameters including the short-circuit photocurrent density (J_{sc}), open-circuit voltage (V_{oc}), fill factors (ff) and overall cell efficiencies (η) are summarized in Table 3.

The solar cell sensitized with **MH11** showed a short-circuit photocurrent density (J_{sc}) of 19.7 mA cm⁻², an open-circuit photovoltage (V_{oc}) of 0.671 V, and a fill factor of 0.664, resulting in an overall conversion efficiency (η) of 8.78% with the

Table 3 Photovoltaic characteristics of **MH06** and **MH11** against **N719**

Complexes	TBP (M)	J_{sc} (mA cm ⁻²)	V_{oc} (V)	FF	η (%)
MH06	0.3	15.07	0.642	0.692	6.70
	0.5	14.44	0.649	0.691	6.49
MH11	0.3	19.477	0.654	0.679	8.66
	0.5	19.700	0.671	0.664	8.78
MH11-TBA	0.3	20.55	0.697	0.685	9.80
	0.5	20.54	0.713	0.687	10.06
N719	0.3	17.16	0.733	0.725	9.12
	0.5	16.85	0.749	0.739	9.32

Conditions: sealed cells; coadsorbate, DCA 20 mM; photoelectrode, TiO₂ (15 μ m thickness and 0.25 cm²); electrolyte, 0.6 M DMPII, 0.1 M LiI, 0.05 I₂ in AN; irradiated light, AM 1.5 solar light (100 mW cm⁻²). J_{sc} , short-circuit photocurrent density; V_{oc} , open-circuit photovoltage; FF, fill factor; η , total power conversion efficiency.

electrolyte containing 0.5 M TBP. It is likely that TBP is adsorbed on the TiO₂ surface to form a more protective layer between the electrolyte and the dye that also suppresses the recombination between the injected electron and the electrolyte at the TiO₂-dye-electrolyte junction. As a result, V_{oc} , J_{sc} and solar-to-power conversion efficiency of the device increased significantly. Tetrabutylammonium (TBA) substituted complex **MH11-TBA** furnished a short-circuit photocurrent density (J_{sc}) of 20.54 mA cm⁻², an open-circuit photovoltage (V_{oc}) of 0.71 V, and a fill factor of 0.68, resulting in an overall conversion efficiency (η) of 10.06%. This impressive increase in performance is because of the deprotonation of one carboxylic acid. The fully protonated **MH11** transfers most of its protons to the TiO₂ surface upon binding to Ti, thus decreasing J_{sc} due to the positive shift of the TiO₂-CB level. When compared to **MH11-TBA** under the same experimental device conditions, **N719** exhibited a J_{sc} of 16.85 mA cm⁻², a V_{oc} of 0.749 V, and a fill factor of 0.739, resulting in an overall conversion efficiency (η) of 9.32%. Fig. 7 shows the photocurrent-voltage curves obtained for solar cells fabricated using **MH06**, **MH11**, **MH11-TBA** and **N719** at standard AM 1.5 irradiation.

2.5. CEM and IMVS characterization

Intensity-modulated photovoltage spectroscopy (IMVS) is a powerful tool to investigate the band edge level of TiO₂ and charge recombination kinetics in DSSCs. In a previous study, charge recombinations between the N3 dye and the electrolyte were investigated and an analytical expression relating the V_{oc} to the interfacial recombination kinetics was derived.³³ In the present study, a theoretical IMVS model that considers a charge trapping-detrapping mechanism during the charge diffusion in the semiconductor and charge transfer from the CB-semiconductor to redox species at the semiconductor/electrolyte interface was used. This model is invaluable in elucidating the change in the open-circuit photovoltage (V_{oc}) because of the surface modification of the semiconductor oxide. IMVS measurements of **MH06**, **MH11**, **MH11-TBA** and **N719** showed a linear increase in V_{oc} as a function of electron density for all dyes, illustrated in Fig. 8. In addition, the result indicated that dyes contribution to the band edge shift is almost similar as the plots for all dyes overlapped with each other,

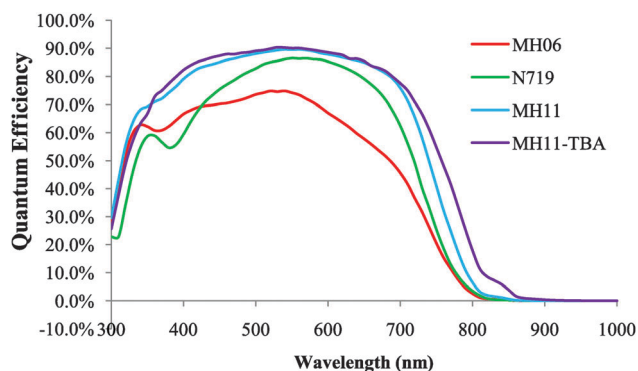


Fig. 6 Photocurrent action spectra (IPCE) obtained with dyes **MH06**, **MH11** and **N719** anchored on nanocrystalline TiO₂ film. The IPCE values are plotted as a function of wavelength of the exciting light.

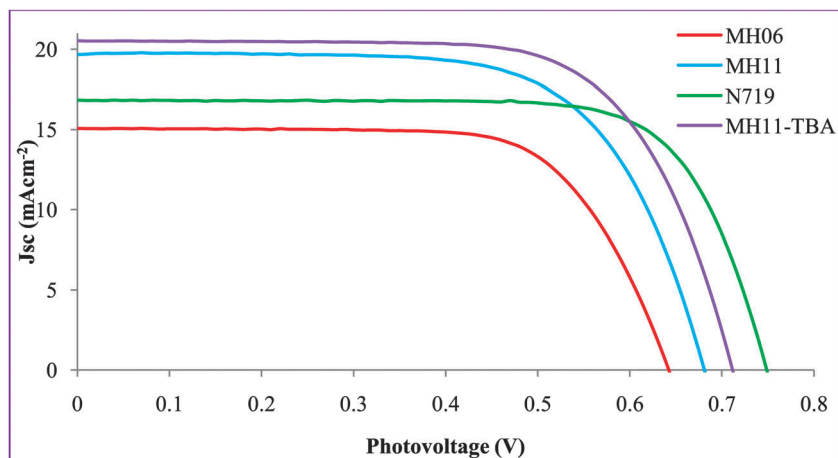


Fig. 7 Photocurrent voltage characteristics of DSSCs sensitized with the complexes **MH06**, **MH11**, **MH11-TBA** and **N719**. Electrolyte, 0.6 M DMPII, 0.1 M LiI, 0.05 I₂ in acetonitrile (AN).

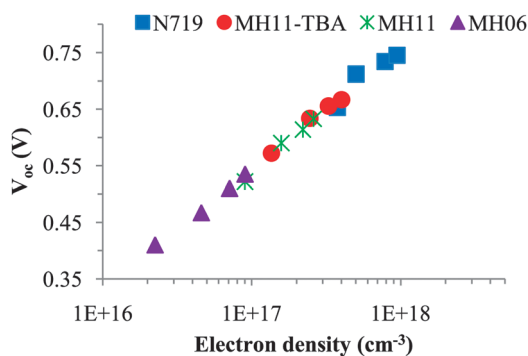


Fig. 8 V_{oc} as a function of electron density for DSSCs sensitized with **MH11**, **MH11-TBA**, **MH06** and **N719**. Electron density was measured by means of a charge extraction method.

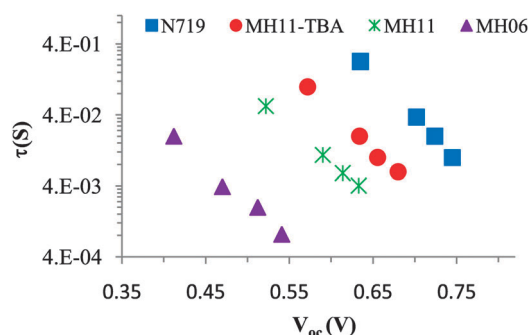


Fig. 9 Electron lifetime (τ) as a function of V_{oc} for DSSCs sensitized with **MH11**, **MH11-TBA**, **MH06** and **N719**. Electron lifetime was measured by means of intensity-modulated photovoltage spectroscopy.

regardless of different substitutions on the bpy-moiety. This implies that the open-circuit photovoltage (V_{oc}) is more likely dependent on charge recombination reactions rather than molecular structures of the dyes. Hence, the V_{oc} for all DSSCs containing **MH06**, **MH11**, **MH11-TBA** should be attributed to the extent of charge recombination which is ultimately related to the electron lifetime (τ) in TiO₂. Fig. 9 shows the electron lifetime (τ) as a function of V_{oc} . It can be clearly seen that TBA substituted complexes of **N719** and **MH11-TBA** showed impressive longer electron lifetime than **MH11** and **MH06**. This can be attributed to the formation of a compact thicker layer of TBA on the TiO₂ surface, which reduces the concentration of I₃⁻ ions in the vicinity of the TiO₂ surface, which explains the electrons longer lifetime and significant suppression of the charge recombination reactions at the electrolyte (I₃⁻ ions)/TiO₂ interface. Furthermore, from Fig. 9, it can be inferred that the electron lifetime of **MH11** in CB-TiO₂ is longer than that of **MH06**. This confirms that the use of bulky pyrene as an antenna in **MH11** acted as a shielding barrier between the redox and TiO₂. Fig. 10 shows a schematic diagram of **MH11** anchored onto a slab of the TiO₂ (101) surface demonstrating

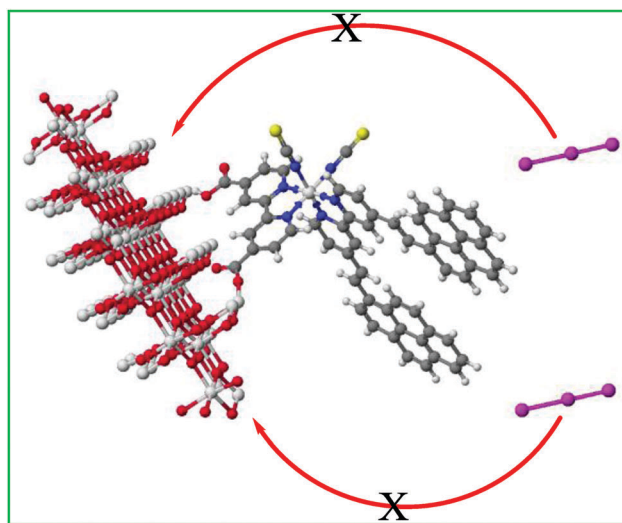


Fig. 10 Schematic representation of **MH11** anchored on an anatase slab of the TiO₂ (101) surface demonstrating the plausible mechanism that rationalizes the improvement in the J_{sc} of **MH11** as a result of reduced charge recombination between TiO₂ and the electrolyte owing to the presence of the bulky pyrene antenna.

the plausible mechanism of the reduction in charge recombinations between TiO_2 and the electrolyte for dye **MH11** owing to the bulky pyrene antenna, which resulted in a significant increase in the J_{sc} of **MH11**.

2.6. Electrochemical impedance spectroscopy characterization

Electrochemical impedance spectroscopy (EIS) is a powerful tool for characterizing the interfacial charge transfer process at TiO_2 /electrolyte and Pt/electrolyte interfaces in DSSCs. The EIS Nyquist and Bode plots for the DSSCs based on **MH06**, **MH11**, **MH11-TBA** and **N719** are shown in Fig. 11 and 12. The EIS Nyquist plots exhibited three characteristic peaks, the response in the intermediate frequency indicating that the electron recombination resistance increased in the order of **N719** > **MH11-TBA** > **MH11** > **MH06**. This is due to the formation of a thick layer of TBA on the TiO_2 , which reduces charge recombinations.

In Fig. 12, the frequency response plot is in the range of 1–100 Hz, which is indicative of the electron recombination between the electrolyte and TiO_2 and is related to the electron lifetime in the CB of TiO_2 . The electron lifetime depends on the density of charge traps, which is ultimately related to V_{oc} . The middle-frequency peaks of the DSSCs based on **N719** and **MH11-TBA** shifted to lower frequency, owing to the presence of a thick layer of TBA, relative to that of **MH11** and **MH06**, indicating a shorter recombination lifetime for the latter case.

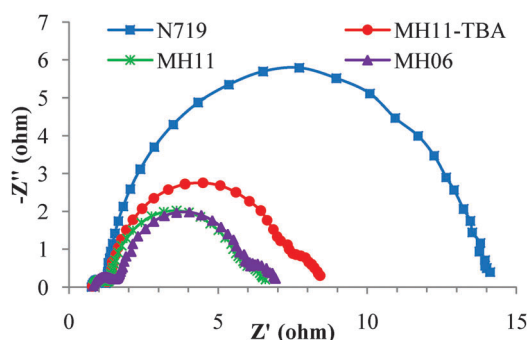


Fig. 11 EIS Nyquist plots for DSSCs sensitized with **MH11**, **MH11-TBA**, **MH06** and **N719**.

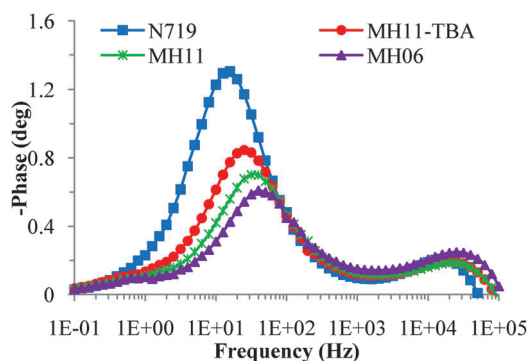


Fig. 12 EIS Bode plots for DSSCs sensitized with **MH11**, **MH11-TBA**, **MH06** and **N719**.

This trend is in agreement with the τ vs. V_{oc} results, implying that the formation of a thicker compact layer using TBA increases the lifetime of electrons in CB- TiO_2 , hence reducing the rate of charge recombination with the triiodide ions I_3^- .

3. Conclusions

In conclusion, the incorporation of strong electron donating groups and extension of the length of π -conjugation in the bipyridyl moiety furnished highly efficient light harvesting properties and bathochromic shift in the UV-Vis spectrum compared to the benchmark **N719** dye. The photovoltaic performance of **MH06**, **MH11** and **MH11-TBA** showed that **MH11-TBA** exhibited a significantly higher efficiency η (%) of 10.06 than **N719** (9.32) and **MH06** (6.70). Comparison of the photovoltaic performance of **MH06** and **MH11** showed that the structure of the ancillary ligand can have a significant effect on the photovoltaic performance of the sensitizer, as longer extended π -conjugation based on pyrene was shown to be significantly more effective than an electron donor with less π -conjugated ancillary ligand of methoxynaphthalene. In addition, the intensity-modulated photovoltage spectroscopy results showed that the open-circuit photovoltage (V_{oc}) is more dependent on the charge recombination process, where the charge recombinations were reduced owing to the thick layer of TBA, which resulted in an increase in the lifetime of electrons in CB- TiO_2 . Electrochemical impedance spectroscopy results showed that incorporation of a TBA unit into the molecular structure of dyes significantly suppressed the recombination process at the TiO_2 /dye/electrolyte interface.

References

- 1 M. K. Nazeeruddin, S. M. Zakeeruddin, R. H. Baker, M. Jirousek, P. Liska, N. Vlachopoulos, C. Shklover and M. Grätzel, *Inorg. Chem.*, 1999, **38**, 6298.
- 2 D. Kuang, S. Ito, B. Wenger, C. Klein, J. E. Moser, R. B. Humphry, S. M. Zakeeruddin and M. Grätzel, *J. Am. Chem. Soc.*, 2006, **128**, 4146.
- 3 P. Wang, S. M. Zakeeruddin, J. E. Moser, R. Humphry-Baker, P. Comte, V. Aranyos, A. Hagfeldt, M. K. Nazeeruddin and M. Grätzel, *Adv. Mater.*, 2004, **16**, 1806.
- 4 M. K. Nazeeruddin, P. T. Renouard, S. M. Zakeeruddin and M. Grätzel, *J. Am. Chem. Soc.*, 2001, **123**, 1613.
- 5 H. Tsubomura, M. Matsumura, Y. Nomura and T. Amamiya, *Nature*, 1976, **261**, 402.
- 6 B. O'Regan and M. Grätzel, *Nature*, 1991, **153**, 737.
- 7 B. E. Hardin, H. J. Snaith and M. D. M. Gehee, *Nat. Photonics*, 2012, **6**, 162.
- 8 M. Bär, I. Repins, M. A. Contreras, L. Weinhardt, R. Noufi and C. Heske, *Appl. Phys. Lett.*, 2009, **95**, 052106.
- 9 Y. Qin, *Int. J. Photoenergy*, 2012, **2012**, 1.
- 10 D. Kuang, C. Klein, S. Ito, J. E. Moser, R. H. Baker, N. Evans, F. Durrig, S. K. Zakeeruddin and M. Grätzel, *Adv. Mater.*, 2007, **19**, 1133.
- 11 O. Kohle and M. Grätzel, *Adv. Mater.*, 1997, **9**, 904.

- 12 P. G. Bchottomben and E. Schott, *Angew. Chem., Int. Ed.*, 2011, **50**, 10682.
- 13 A. Isalm, S. P. Singh, M. Yanagida, M. R. Karim and L. Han, *Int. J. Photochem.*, 2010, **2011**, 7.
- 14 G. Boschloo, L. Sun, L. Kloo and H. Pettersson, *Chem. Rev.*, 2010, **110**, 6516.
- 15 F. Gao, Y. Wang, D. Shi, J. Zhang, M. Wang, X. Jing, R. H. Baker, P. Wang, S. M. Zakeeruddin and M. Grätzel, *J. Am. Chem. Soc.*, 2008, **130**, 10720.
- 16 D. Shi, N. Pootrakulchote, R. Li, J. Guo, Y. Wang, S. M. Zakeeruddin, M. Grätzel and P. Wang, *J. Phys. Chem. C*, 2008, **112**, 17046.
- 17 J. H. Yum, I. Jung, C. Baik, J. Ko, M. K. Nazeeruddin and M. Grätzel, *Energy Environ. Sci.*, 2009, **2**, 100.
- 18 K. J. Jiang, N. Masaki, J. B. Xia, S. Noda and S. Yanagida, *Chem. Commun.*, 2006, 2460.
- 19 Q. Yu, S. Liu, M. Zhang, N. Cai, Y. Wang and P. Wang, *J. Phys. Chem. C*, 2009, **113**, 14559.
- 20 C. Chou, K. L. Wu, C. Yun, W. P. Hu and S. J. Yu, *Angew. Chem., Int. Ed.*, 2011, **50**, 2054.
- 21 P. G. Bomben, B. D. Koivisto and C. P. Berlinguette, *Eur. J. Inorg. Chem.*, 2011, 1806.
- 22 M. K. Nazeeruddin, P. Pechy and M. Grätzel, *J. Chem. Soc., Chem. Commun.*, 1997, **18**, 1705.
- 23 A. Islam, H. Sugihara, M. Yanagida, K. Hara, G. Fujihashi, Y. Tachibana, R. Katoh, S. Murata and H. Arakawa, *New J. Chem.*, 2002, **26**, 966.
- 24 T. A. Heimer, E. J. Heilweil, C. A. Bignozzi and G. J. Meyer, *J. Phys. Chem. A*, 2000, **104**, 4256.
- 25 M. Yanagida, T. Yamaguchi, M. Kurashige, K. Hara, R. Katoh, H. Sugihara and H. Arakawa, *Inorg. Chem.*, 2003, **42**, 7921.
- 26 A. Kolemen, Y. Cakmak, G. Barin, S. E. Ela, M. Marszalek, J. H. Yum, S. M. Zakeeruddin, M. K. Nazeeruddin, M. Grätzel and E. U. Akkaya, *Chem. Sci.*, 2011, **2**, 949.
- 27 A. Burke, S. L. Mende, S. Ito and M. Grätzel, *Chem. Commun.*, 2007, 234.
- 28 F. Angelis, S. Fantacci and A. Sellon, *Nanotechnology*, 2008, **19**, 424002.
- 29 M. K. Nazeeruddin, S. M. Zakeeruddin, M. J. Humphry-Baker, P. Liska, V. S. Vlachopoulos, C. H. Fischer and M. Grätzel, *Inorg. Chem.*, 1999, **38**, 6298.
- 30 C. H. Fischer and M. Grätzel, *Inorg. Chem.*, 1999, **38**, 6298.
- 31 P. Qu and G. J. Meyer, *Langmuir*, 2001, **17**, 6720.
- 32 G. Oskam, B. V. Bergeron, G. J. Meyer and P. C. Searson, *J. Phys. Chem. B*, 2001, **105**, 6867.
- 33 S. Y. Huang, G. Schlichthörl, A. J. Nozik, M. Grätzel and A. J. Frank, *J. Phys. Chem. B*, 1997, **101**(14), 2576.

Structure-property relationship of extended π -conjugation of ancillary ligands with and without electron donor of heteroleptic Ru (II) bipyridyl complexes for high efficiency dye-sensitized solar cells

Maqbool Hussain^a, Ahmed El-Shafei^{a*}, Ashraful Islam^b, Liyuan Han^b

^aPolymer and Color Chemistry Program, North Carolina State University, Raleigh, NC, 27695, USA

^bPhotovoltaic Materials Unit, National Institute for Materials Science, 1-2-1 Sengen, Tsukuba, Ibaraki 305-0047, Japan.

*Corresponding authors: Ahmed_El-Shafei@ncsu.edu

Supporting Information and Experimental Section

Materials.

The solvents and chemicals were either purchased from Sigma-Aldrich, Fisher Scientific or TCI-America or used as received. The aldehydes were purchased from Sigma-Aldrich with 99% purity. Sephadex LH-20 was purchased from Fisher Scientific.

1.1. Analytical Measurements.

1.1.1 UV-Vis Spectra

UV-Vis spectra were recorded in a 1cm path length quartz cell on a Cary 3 Spectrophotometer. A dimethylformamide solution of each complex of 2×10^{-5} M was prepared, and the absorbance was measured and extinction coefficient was calculated for each dye.

1.1.2. Fluorescence Spectra

Fluorescence spectra were recorded in a 1cm path length quartz cell using 2×10^{-5} M solutions on a Fluorolog-311. The emitted light was detected in the steady state mode using Hamamatsu R2658 detector. The emission was measured in the steady state mode by exciting at the λ_{max} (lower energy MLCT band) for each dye with exit and entrance slits set at 10nm.

1.1.3. Attenuated Total Reflectance Fourier-transform Infra Red Spectroscopy

Attenuated Total Reflectance-Fourier Transform Infra Red (ATR/FT-IR) spectra were recorded on a Thermo Nicolet, Nexus 470 FTIR Spectrophotometer with Omnic 7.2 software. The compound under investigation was placed in its powder form on a germanium crystal and a pressure probe was placed in position to apply consistent pressure on the sample. An average of 32 scans was used at a resolution of 4 cm^{-1} . The complexes and intermediates were characterized using the same parameters. Figures 1S, 2S, show the FT-IR of **MH06** and **MH11** in the pure form, respectively.

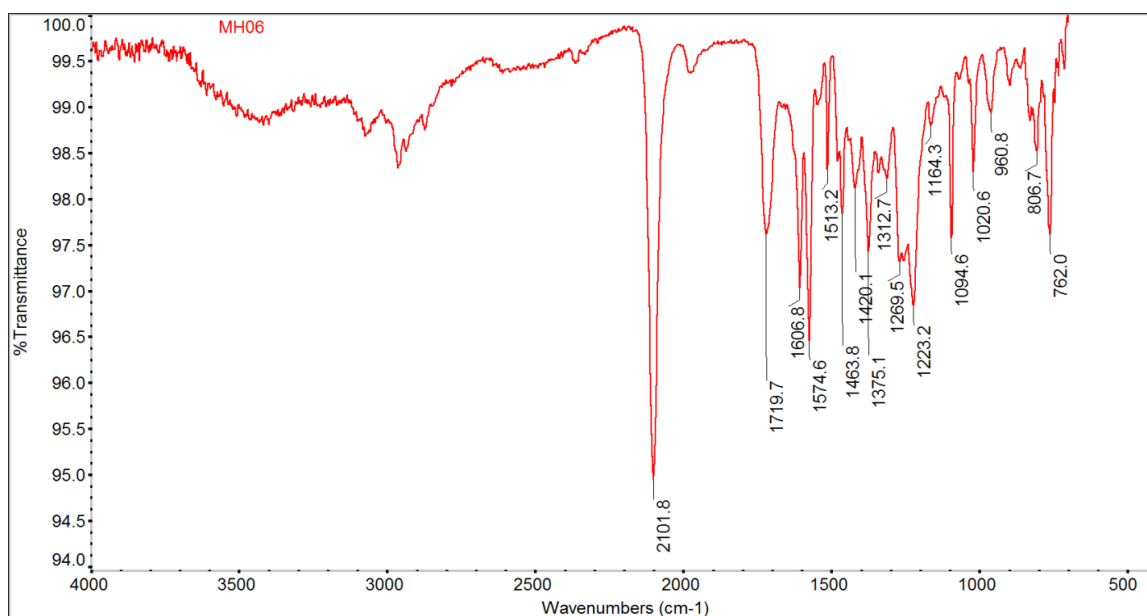


Figure 1S ATR/FT-IR of MH06.

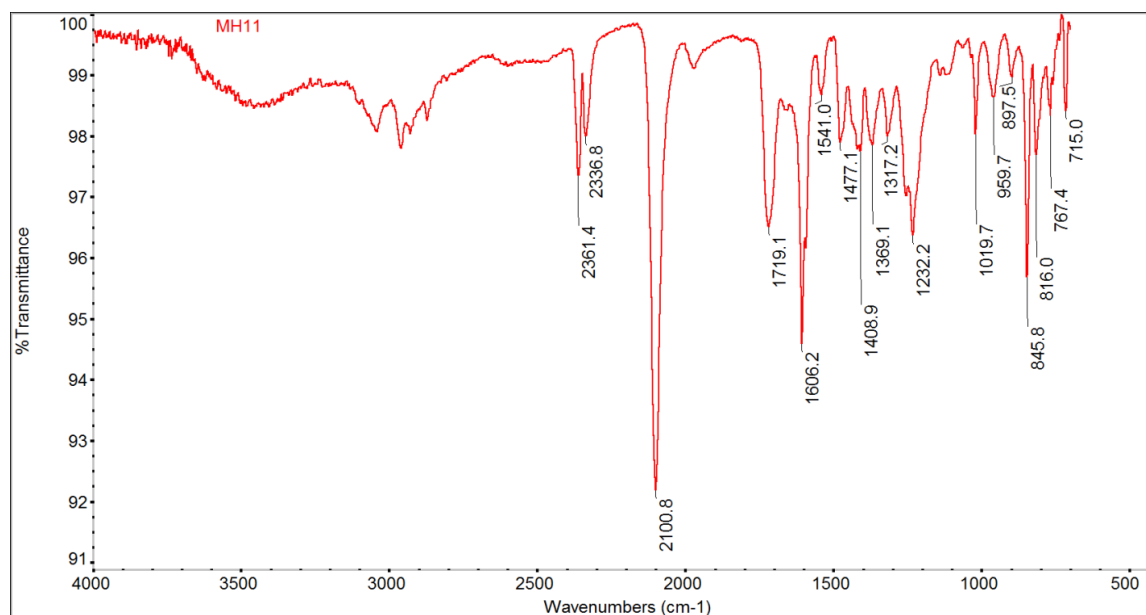


Figure 2S ATR/FT-IR of MH11.

1.1.4. Mass Spectroscopy

ESI-MS was recorded on an Agilent Technologies 6210 LC-TOF mass spectrometer in the negative ion mode. The sample was prepared in methanol in the presence of a small amount of tetrabutylammonium hydroxide (TBAOH). The fragmenter voltage was set at 220.0 V and results from 20 scans in the case of **MH06**, 40 scans in the case of **MH11** were averaged. Figures 3S-4S show the ESI-MS of **MH06** and **MH11** with one TBA per molecule, singly charged, with identical pattern of ruthenium isotopes.

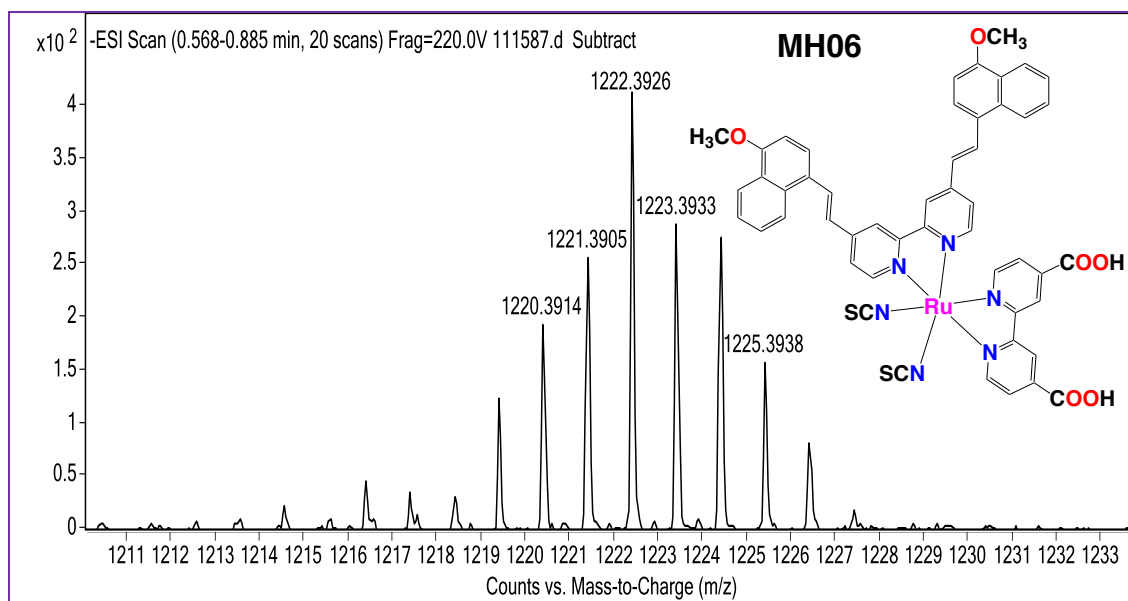


Figure 3S ESI mass spectrum of **MH06**, Mass 982.1181; $[M - 2H + TBA]^{-1}$; Theo. M/Z = 1222.3873, Found. M/Z 1222.3926, Error = 4.335 ppm.

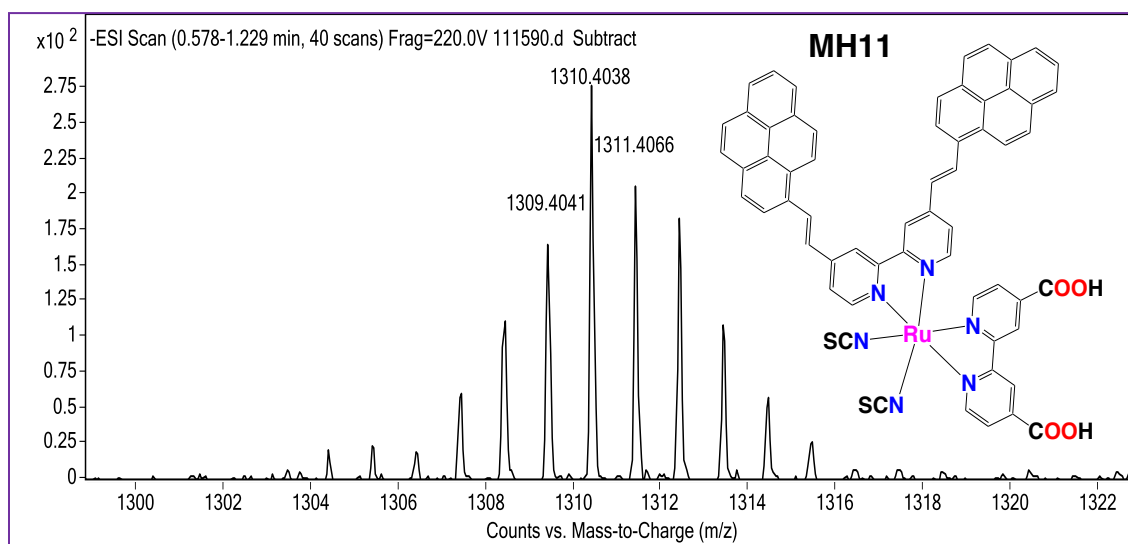


Figure 4S ESI mass spectrum of **MH11**, Mass 910.0453, $[M - 2H + TBA]^{-1}$, Theo. M/Z = 1310.3974, Found M/Z = 1310.4038, Error = -4.884 ppm.

1.2.5. ^1H -NMR Experiments

^1H -NMR experiments were recorded on a Bruker 500 MHz spectrometer at 40 °C using deuterated DMSO- d_6 as a solvent. Splitting patterns reported here are: s (singlet), d (doublet), dd, (double-of-doublet), t (triplet), p (pentet), and m (multiplet). Chemical shifts (δ) and coupling constants (J) are reported in ppm and Hertz (Hz), respectively. The aliphatic range 0-5ppm is not shown for brevity. Figures 5S-6S show the H-NMR for **MH06** and **MH11**, respectively.

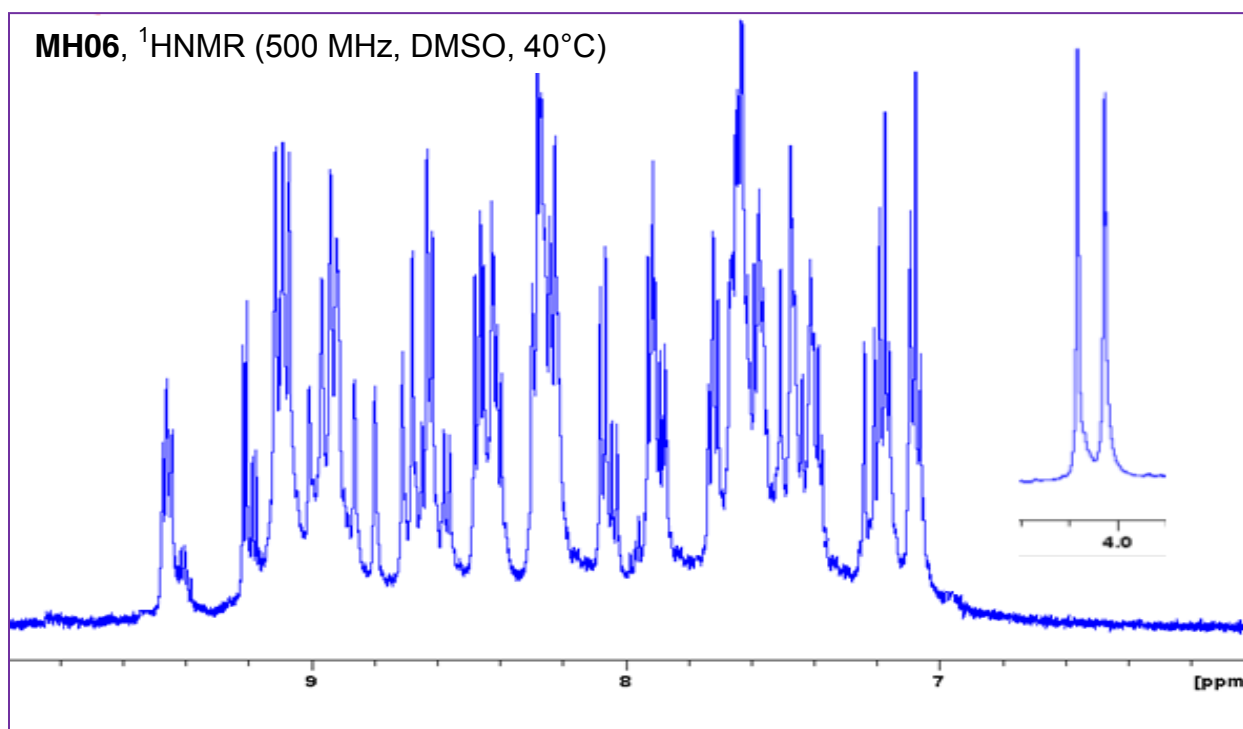


Figure 5S ^1H -NMR of **MH06**.

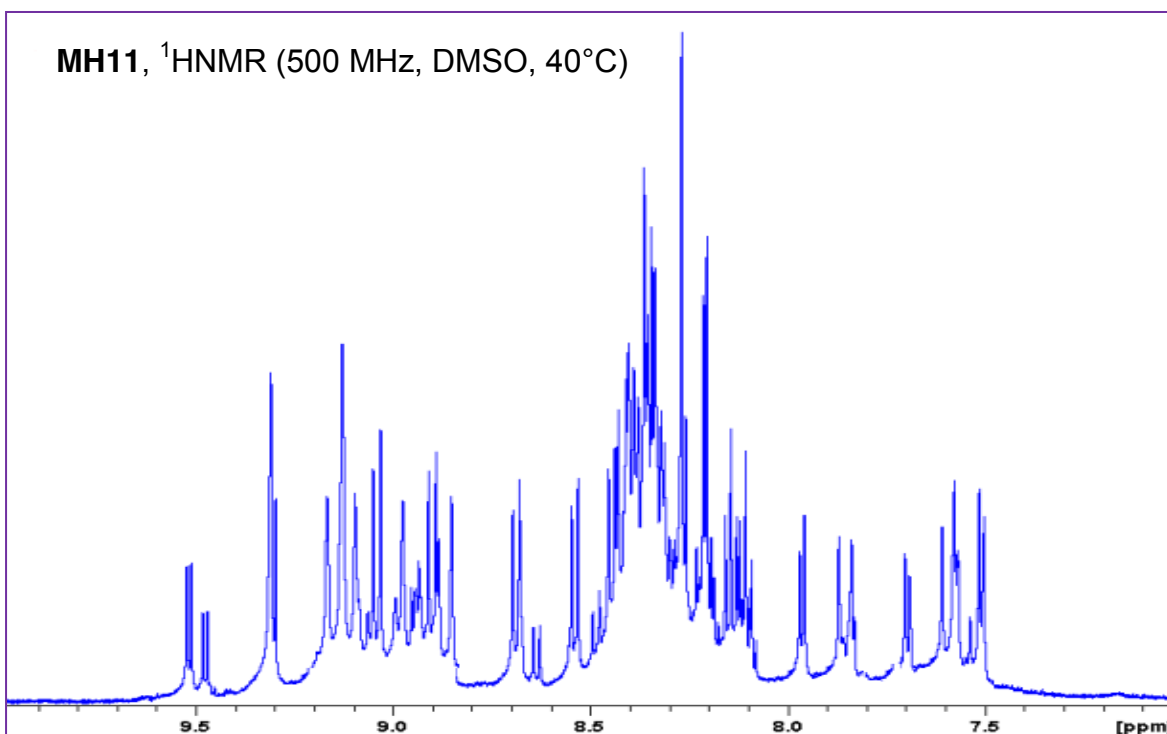


Figure 6S ¹H-NMR of MH11.

1.2.6. TiO₂ Electrode Preparation

A double-layer TiO₂ photoelectrode (10+5) μm in thickness with a 10 μm thick nanoporous layer and a 5 μm thick scattering layer (area: 0.25 cm²) were prepared using a reported method [1]. Fluorine doped tin oxide-coated glass electrodes (Nippon Sheet Glass Co., Japan) with a sheet resistance of 8-10 ohm⁻² and an optical transmission of greater than 80% in the visible range were screen printed using anatase TiO₂ colloids (particle size ~13nm) obtained from commercial sources (Ti-Nanoxide D/SP, Solaronix). Nanocrystalline TiO₂ thin films were deposited onto the conducting glass by screen-printing which was then sintered at 500 °C for 1 hour. The film thickness was measured with a Surfcom 1400A surface profiler (Tokyo Seimitsu Co. Ltd.). The electrodes were impregnated with a 0.05 M titanium tetrachloride solution and sintered at 500 °C. The films were further treated with 0.1M HCl aqueous solutions before examination [2]. The dye solutions (2 × 10⁻⁴ M) were prepared in 1:1:1 acetonitrile, *tert*-butyl alcohol and DMSO. Deoxycholic acid was added to the dye solution as a coadsorbent at a concentration of 20 mM.

The electrodes were immersed in the dye solutions and then kept at 25 °C for 20 hours to adsorb the dye onto the TiO₂ surface.

1.2.7. Fabrication of Dye-Sensitized Solar Cell.

Photovoltaic and IPCE measurements were made on sandwich cells, which were prepared using TiO₂ coated working electrodes and platinum coated counter electrodes, and were sealed using a 40 μm Syrlin spacer through heating of the polymer frame. The redox electrolyte consisted of a solution of 0.6 M DMPII, 0.05 M I₂, 0.1 M LiI and 0.3-0.5 M TBP in acetonitrile.

1.2.8. Photoelectrochemical Measurements

2.2.8.1. Photovoltaic measurements

Photovoltaic measurements of sealed cells were made by illuminating the cell through the conducting glass from the anode side with a solar simulator (WXS-155S-10) at AM 1.5 illuminations (light intensities: 100 mW cm⁻²).

1.2.8.2. Incident Photon to Current Efficiency (IPCE) Conversion

IPCE measurements were made on a CEP-2000 system (Bunkoh-Keiki Co. Ltd.). IPCE at each wavelength was calculated using Equation 2, where I_{SC} is the short-circuit photocurrent density (mAcm⁻²) under monochromatic irradiation, q is the elementary charge, λ is the wavelength of incident radiation in nm and P_0 is the incident radiative flux in Wm⁻² [3].

$$IPCE(\lambda) = 1240 \left(\frac{I_{SC}}{q\lambda P_0} \right) \quad \text{Equation 2}$$

The incident photon-to-current conversion efficiency was plotted as a function of wavelength.

1.2.8.3. Photoemission Yield Spectrometer (AC3) and $E_{0.0}$ Measurements

The experimental HOMO and $E_{0.0}$ energy values for **MH06** and **MH11** and **N719** were measured using a photoemission yield spectrometer and the experimental absorption/emission spectra point of overlap, respectively, and the procedure was described in detail elsewhere [4]. Figures 7S-9S show the HOMO energies of **MH06**, **MH11** and **N719**, respectively.

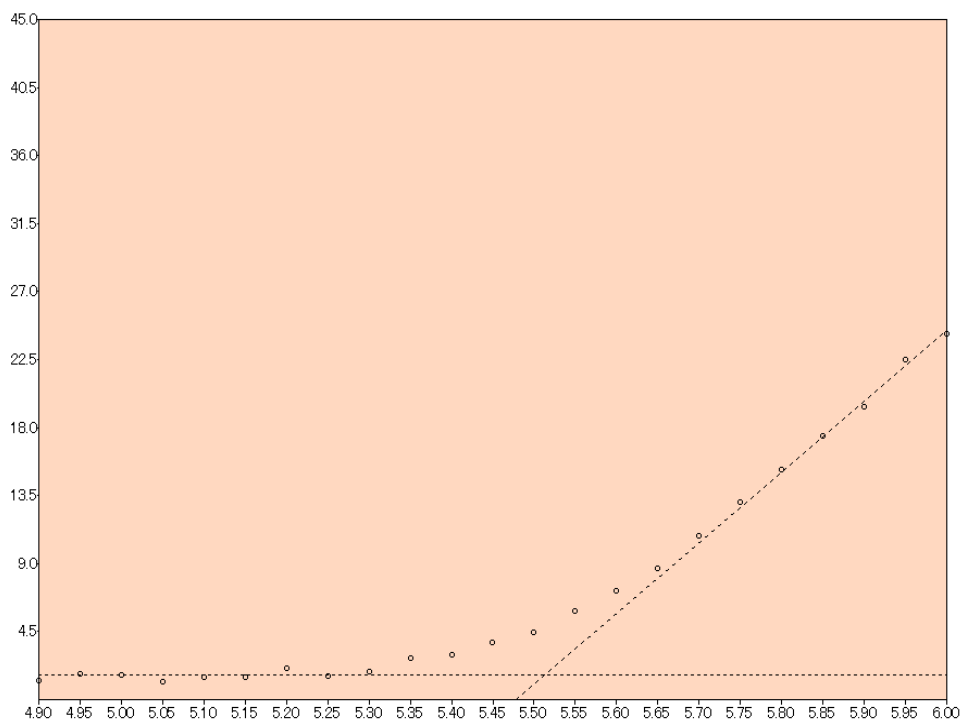


Figure 7S HOMO energy (-5.51 eV) of **MH06**.

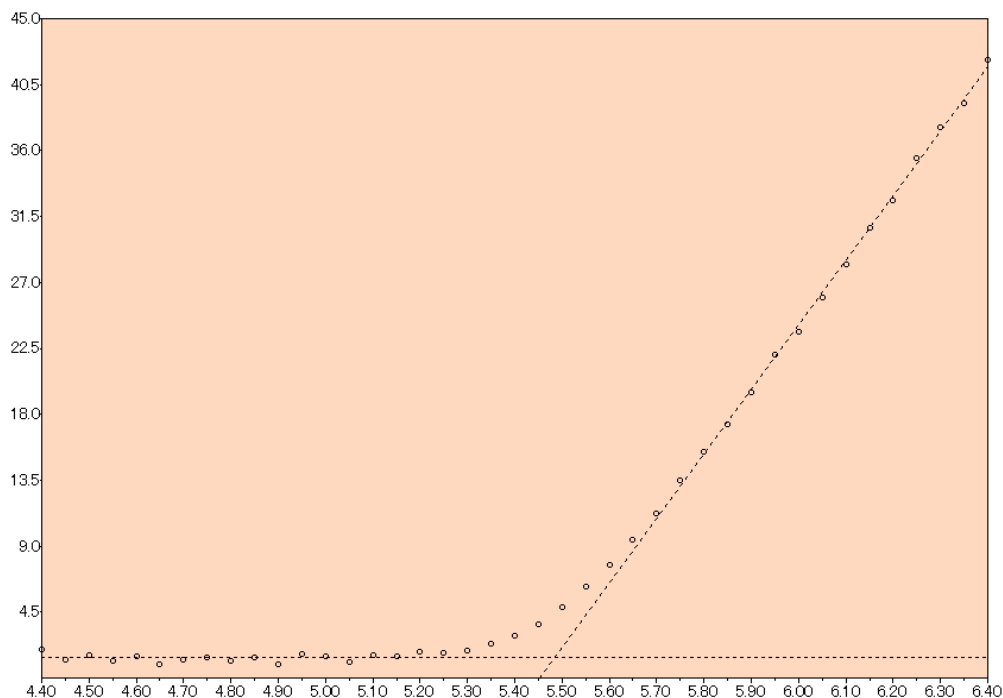


Figure 8S HOMO energy (-5.49eV) of **MH11**.

1.2.8.4. Photoluminescence emission decay

Emission decay spectra were recorded in DMF solutions while maintaining the optical absorbivity at 0.1 Abs, using a Fluorolog-311 at room temperature. The emission decays were recorded upon exciting at 454 nm using time-correlated single photon counting (TCSPC) procedure, after measurement the decay the data was further fitted using fitting model 2 (two-exponential) at a channel range of channel range 1000nm-3000nm.

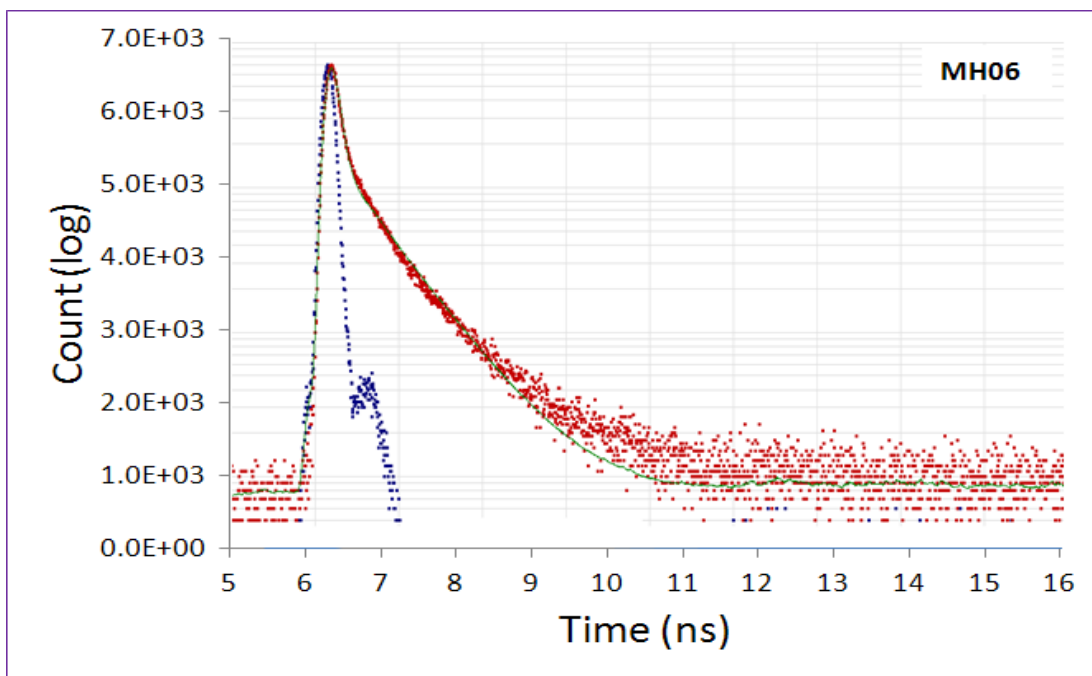


Figure 9S Time-Correlated Single Photon Counting (TCSPC), Emission Decay (6.25 ns)

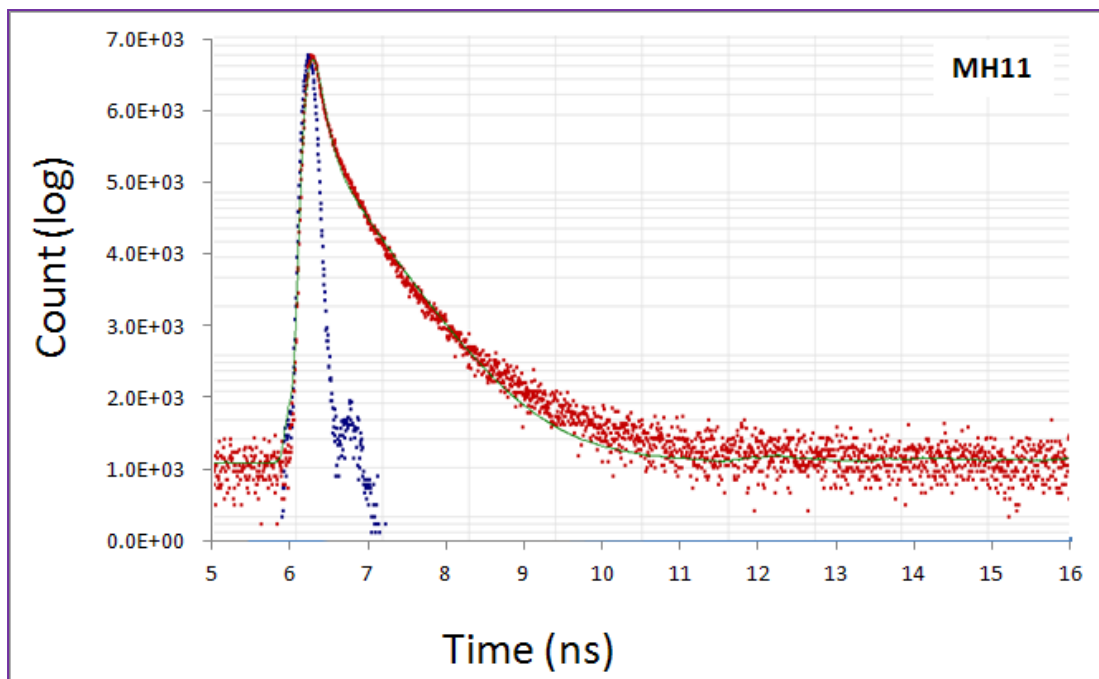


Figure 10S Time-Correlated Single Photon Counting (TCSPC), Emission Decay (6.47 ns)

1.2.9. Synthesis of Ligands

1.2.9.1. 4,4'-Bis-[2-(4-methoxy-naphthalen-1-yl)-vinyl]-[2,2']bipyridinyl

A 100 ml pressure tube was charged with a magnetic stirrer bar, 100 mL of anhydrous DMF, 4,4'-dimethyl-2,2'-bipyridine (1.000g, 5.428×10^{-3} mol) and 4-Methoxy-naphthalene-1-carbaldehyde (2.0203g, 1.085×10^{-2} mol, 5% excess was used to drive the reaction to completion), and three equivalent of $\text{Si}(\text{CH}_3)_3\text{Cl}$. The reaction temperature was raised to 100 °C and allowed to run for 48 hours with continuous stirring. At the end of the reaction, the solvent was removed using rotary evaporator, and the product was recovered by addition of water and filtration under vacuum to furnish the antenna ligand in 94% yield, which was used for the next step after washing with toluene. The other 4, 4'-Bis-(2-pyren-1-yl-vinyl)-[2, 2']bipyridinyl ligand was prepared using same procedure with a 96% yield.

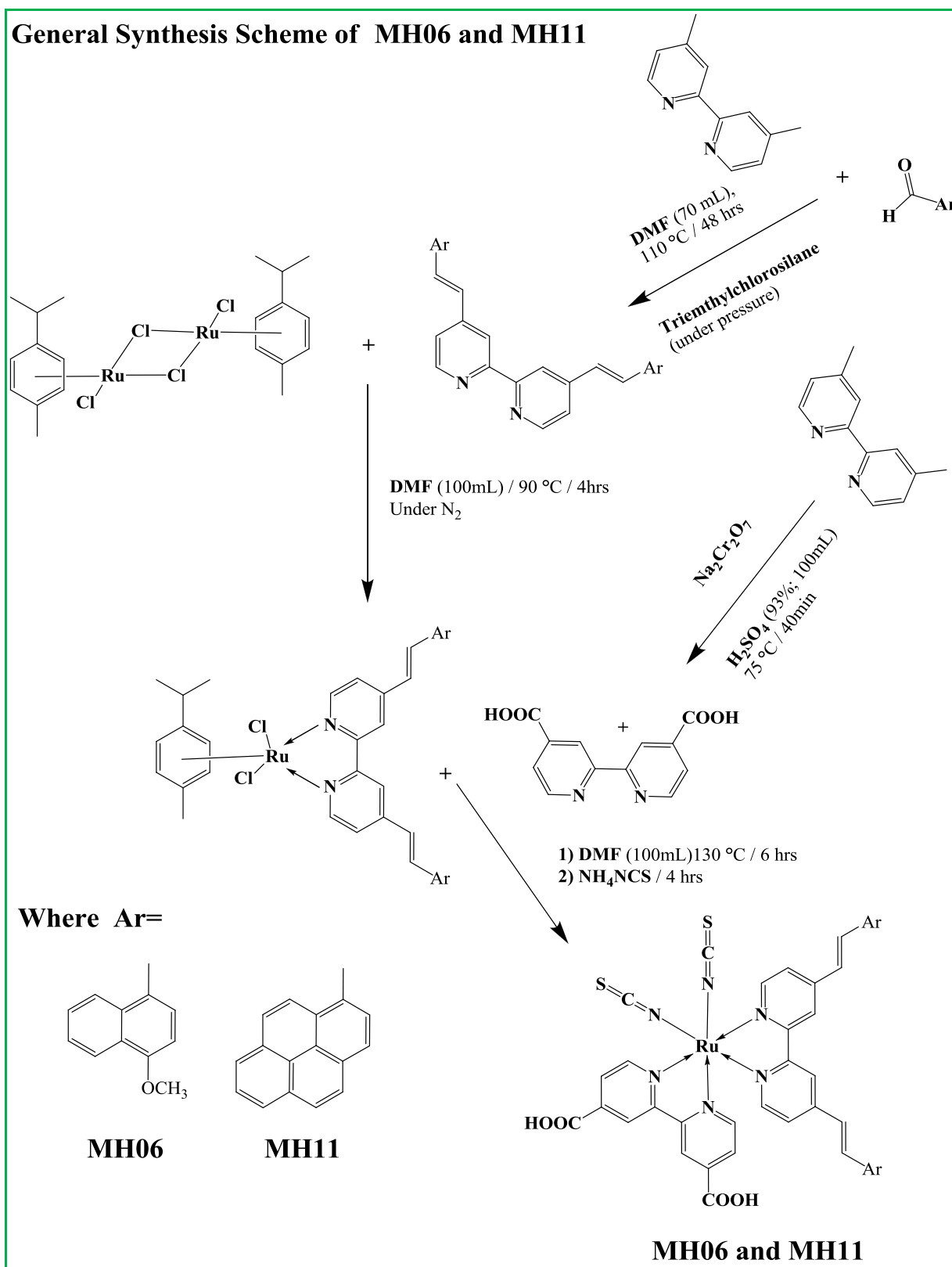
1.2.9.2 Synthesis of 2, 2'-Bipyridinyl-4, 4'-dicarboxylic acid

2, 2'-Bipyridinyl-4, 4'-dicarboxylic acid was synthesized in 93% yield according to a previously reported procedure [5]

1.2.9.3 Synthesis of complexes MH06 and MH11

The synthesis of MH06 was carried out in a one-pot three-step reaction. The reactions were carried out in a 250 ml reaction flask equipped with a condenser and magnetic stirrer bar under Argon. The flask was charged with anhydrous DMF (100mL), dichloro-(*p*-cymene)-ruthenium (II) dimer (0.30g, 4.899×10^{-4} mol) and 4,4'-Bis-[2-(4-methoxy-naphthalen-1-yl)-vinyl]-[2,2']bipyridinyl (0.5100g, 9.797×10^{-4} mol). The reaction mixture was stirred at 90 °C for 4h. Then, 2,2'-bipyridyl-4,4'-dicarboxylic acid was added (0.239 g, 9.797×10^{-4} mol) and the temperature was raised to 130°C and allowed to run for 6 hours. After the 6 hours, excess of NH_4NCS (0.5g) was added to the reaction mixture, and the reaction mixture was allowed to run for another 4h at 130°C. The last two steps of the reaction were monitored for completion by taking aliquots from the reaction mixture every 60 minutes and measuring its absorption spectrum until there was no increase in the absorbance of the MLCT peaks with respect to the π - π^* peak. The reaction mixture was cooled down to room temperature and DMF was removed using a rotary evaporator. Water was added to the flask, and the insoluble solid were vacuum

filtered and washed with de-ionized water and ether. The product was dried overnight to give the crude product in 97% yield, with respect to the starting material. Complexes **MH11** were prepared using same procedure in 94% crude yield. Scheme 1 summarizes the general synthetic route for complexes **MH06** and **MH 11**.



Scheme 1 General route for the synthesis of complexes **MH06** and **MH11**.

1.2.10 Purification

MH06 was purified on a column using Sephadex LH-20 as the stationary phase and pure methanol as the mobile phase. The crude dye of **MH06** was dissolved in a mixture of methanol and TBAOH and loaded on Sephadex LH-20, and the compound was eluted using methanol neat. The main band was collected and acidified using 0.1M HCl until the pH dropped to 3.0, and the acidified solution was kept in a refrigerator for 12 hours. Then, the precipitate was filtered, washed with plenty of deionized water to remove remaining HCl. The same purification procedure was repeated three times in order to obtain **MH11** in the pure form.

1.2.11. Molecular Modeling

Equilibrium molecular geometries of **MH08-10** and **N719** were calculated using the energy functional 3-Parameter (Exchange), Lee, Yang and Parr (B3LYP) [5,6] and the full-electron basis set Density Gauss double-zeta with polarization functions (DGDZVP) [7,8]. The geometry optimization calculations were followed by energy calculations using TD-DFT utilizing the energy functional B3LYP and the basis set DGDZVP. The solvent (DMF) effect was accounted for by using the polarizable continuum model (PCM), implemented in Gaussian 09, and the ground and excited states oxidation potentials were calculated. All DFT and TD-DFT jobs were submitted remotely at East Carolina University's Supercomputer Jasta.

References:

- 1- Wang, P., Zakeeruddin, S. M.; Comte, P.; Charvet, R.; Humphry- Baker, R.; Grätzel, M.
J. Phys. Chem. B **2003**, *107*, 14336.
- 2- Wang, Z., Yamaguchi, T., Sugihara, H., and Arkawa, H., *Langmuir* **21** (2005) 4272.
- 3- Islam, A., Chowdhury, FA; Chiba, Y; Komiya, R; Fuke, N; Ikeda, N; Nozaki, K; and Han, L., *Chem. Mater.* **18** (2006), pp. 5178-5185.
- 4- Islam, A., Sugihara, H., Hara, ., Singh, L. P., Katoh, R., Yanagida, M., Takahashi, Y., Murata, S., and Arakawa, H., *Inorg. Chem.*, 2001, **40** (21), pp 5371–5380.
- 5- Becke, A. D., *Phys. Rev. A* **1988**, *38*, 3098.
- 6- Lee, C. T., Yang, W. T., Parr, R. G., *Phys. Rev. B* **1988**, *37*, 785
- 7- Godbout, N., Salahub, D. R., Andzelm, J., and Wimmer, E., *Can. J. Chem.*, **70** (1992) 560.
- 8- Sosa, C., Andzelm, J., Elkin, B. C., Wimmer, E., Dobbs, K. D., and Dixon, D. A., *J. Phys. Chem.*, **96** (1992) 6630.

CHAPTER 4

Influence of Cyclic Versus Acyclic Oxygen-containing Electron Donor Ancillary Ligands on the Photocurrent, Photovoltage and Photostability for High Efficiency Dye-sensitized Solar Cells

Maqbool Hussain¹, Ahmed El-Shafei^{a*}, Ashraful Islam^b, and Liyuan Han^b

^aPolymer and Color Chemistry Program, North Carolina State University, Raleigh, NC, 27695, USA

^bPhotovoltaic Materials Unit, National Institute for Materials Science, 1-2-1 Sengen, Tsukuba, Ibaraki 305-0047, Japan

Corresponding authors: Ahmed_EL-Shafei@ncsu.edu

Abstract

Three novel heteroleptic amphiphilic polypyridyl Ru-complexes, MH01, MH03, and MH05, with oxygen-containing-electron-donor stilbazole-based ancillary ligands were synthesized to study the influence of cyclic-electron-donor (MH01), presence of freely rotating electron-donor auxochromes (MH03) *ortho* to the CH=CH bridge of stilbazole, and presence of only acyclic electron-donor methoxy (MH05) on molar extinction coefficient, light harvesting efficiency (LHE), ground and excited state oxidation potentials, and photovoltaic performance for DSSCs. Although MH05 has three electron donor methoxy groups, it achieved the lowest molar extinction coefficient of $18250\text{M}^{-1}\text{cm}^{-1}$ and exhibited the lowest photocurrent. The highest photocurrent density (J_{SC}) was observed for the longest interatomic distance between the CH=CH bridge of stilbazole moiety and cyclic-electron-donor auxochrome (MH01). It was also shown that while incorporation of a freely-rotating

(acyclic) electron-donor auxochrome *ortho* to the CH=CH (MH03) has little effect on the ground and excited state oxidation potentials, λ_{\max} of the low energy MLCT, and molar absorptivity, the lowest photovoltage and $\% \eta$ were observed. When compared under the same experimental device conditions using 0.3M t-butylpyridine (TBP), only MH01-TBA achieved 18% more in J_{SC} and 8.6% higher in η than the reference dye N719. To probe the interrelationship between the *cyclic-vs-acyclic oxygen-containing electron donor* of the ancillary ligands, and photocurrent and photovoltage of these dyes, the equilibrium molecular geometries of the ancillary ligands were calculated using DFT. The HOMO distribution on cyclic-vs-acyclic electron donor and the position of OMe in the ancillary ligands rationalized the fundamental science behind the photovoltaic performance and photostability of these dyes.

Keywords: dye solar cells, IPCE, auxochromes, electron donor, solar-to-electric conversion, molecular modeling, DFT and TD-DFT.

1. Introduction

Dye-sensitized solar cells (DSSCs) based on polypyridyl Ru (II) complexes have attracted strong attention from the academia and industry due to their unique photophysical and energy transfer properties including their broad spectral response, attractive excited state properties, multiple stable oxidation states [1-18] and high efficiency electron injection [19,20] for dye-sensitized solar cells (DSSCs). Although N719 is the most common dye for DSSCs, owing to the hydrophilic nature of N719, the long-term device stability is not satisfactory [21,22]. In this respect, efforts toward improving the long-term device stability had led to the

development of the amphiphilic sensitizer Z-907. However, the molar extinction coefficient of Z-907 was lower than N719 [23], owing to the presence of a long alkyl chain and absence of strong electron donor auxochrome. To improve the molar extinction coefficient while maintaining the amphiphilic properties, another generation of sensitizers was developed containing electron donor auxochrome coded Z-910[24], K-19 [25], and K73 [26]. The molecular structures of Z-907, Z-910, K19, and K73 (Figure 1) are based on extending the π -conjugation of bipyridyl to produce red shift in the metal-to-ligand charge transfer (MLCT) absorption peaks and incorporating electron-donor auxochrome (alkoxy groups) to enhance the molar extinction coefficient.

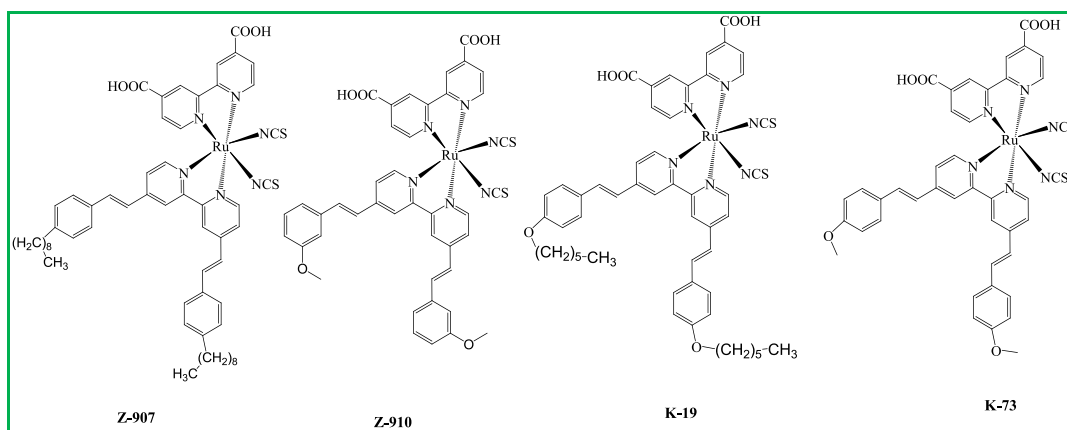


Figure 1. Molecular structures of Z-907, Z-910, K19, and K73.

However, no work was reported in the literature that addresses the interrelationship between the location and form of electron donor, cyclic-*vs*-acyclic, of oxygen-containing electron-donor ancillary ligands, and the photocurrent and photovoltage of polypyridyl Ru (II) complexes for DSSCs.

Here, we report a series of novel polypyridyl Ru (II) complexes (MH01, MH03, and MH05) that rationalizes the fundamental science of the structure-performance relationship for DSSCs.

Figure 2 shows the molecular structures of MH01-TBA, MH01, MH03 and MH05. MH01-TBA was synthesized by reacting MH01 with tetrabutylammonium hydroxide (TBA).

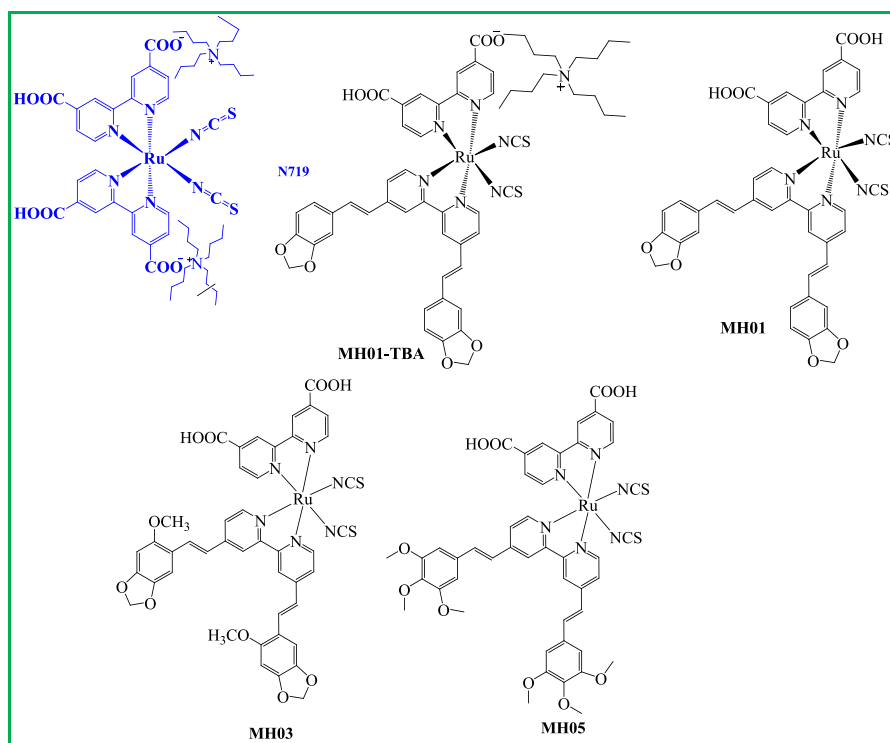


Figure 2. Molecular structures of dyes N719, MH01-TBA, MH01, MH03 and MH05.

2. Results and Discussion

2.1. Proposed reaction mechanism

Figure 3 shows the proposed reaction mechanism of the reaction between aromatic aldehydes and 2,2'-dimethylbipyridyl in presence of trimethylsilylchloride. The reaction was carried out at 100°C in a pressure tube. Due to the electron negativity of the nitrogens in the bipyridyl moiety, a proton loss from the methyl group at the 4-position initiates an electron rearrangement in one of the pyridyl ring followed by a nucleophilic attack of the pyridyl-N at the electron deficient silicon and displacing a chloride ion. Restoring the aromaticity in the pyridyl ring leads to a nucleophilic attack on the electron deficient carbon of the carbonyl of the aldehyde followed by a loss of trimethylsilanol and hydrolysis, which furnishes a stilbazole analog. The same reaction mechanism takes place at the other pyridyl ring to give the bisubstituted stilbazole analog.

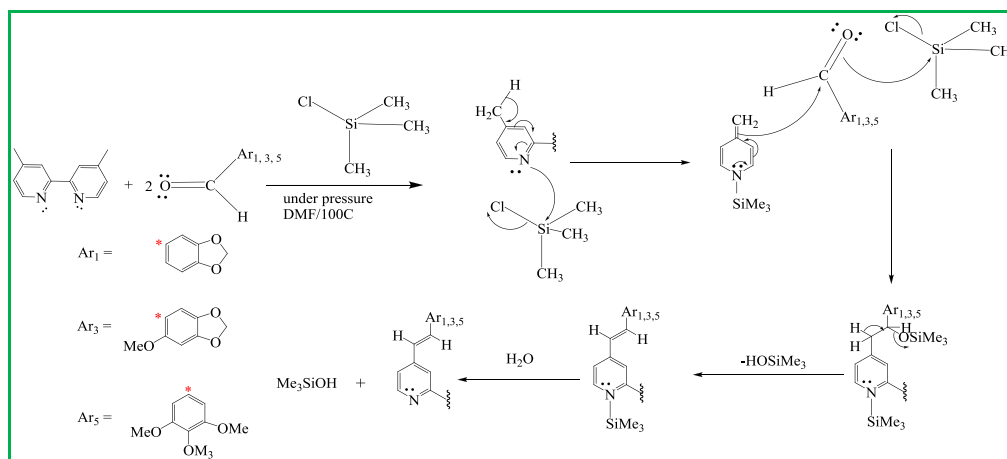


Figure 3. Proposed reaction mechanism for the synthesis of bistilbazoles ancillary ligands (Ar₁, Ar₃, Ar₅) of M01, MH03 and MH05.

2.2. UV-Visible Spectra

Figure 4 shows a comparison between the absorption and emission spectra of N719 versus MH01-05, measured in DMF (2×10^{-5} mol). The spectrophotometric properties are summarized in Table 1. MH01, MH03 and MH05 showed intense and broad bands at 367nm ($47,250 \text{ M}^{-1}\text{cm}^{-1}$), 404 ($41,250\text{M}^{-1}\text{cm}^{-1}$) and 358nm ($66,800 \text{ M}^{-1}\text{cm}^{-1}$) and broad metal-to-ligand-charge-transfer (MLCT) peaks at 545nm ($21,500 \text{ M}^{-1}\text{cm}^{-1}$), 544 ($21,350 \text{ M}^{-1}\text{cm}^{-1}$) 542nm ($31400 \text{ M}^{-1}\text{cm}^{-1}$), respectively, which are bathochromically shifted by 12-15 nm compared to that of N719. From the data presented in Table 1, it is evident that the lower energy MLCT peaks of these new dyes exhibited higher molar extinction coefficient and are more bathochromically shifted than that of N719. However, **MH05** exhibited the lowest molar extinction coefficient among the new dyes. The enhanced bathochromic shift of the low energy MLCT of MH01, MH03 and MH05 rendered these sensitizers better light harvesting dyes for DSSCs in the NIR region.

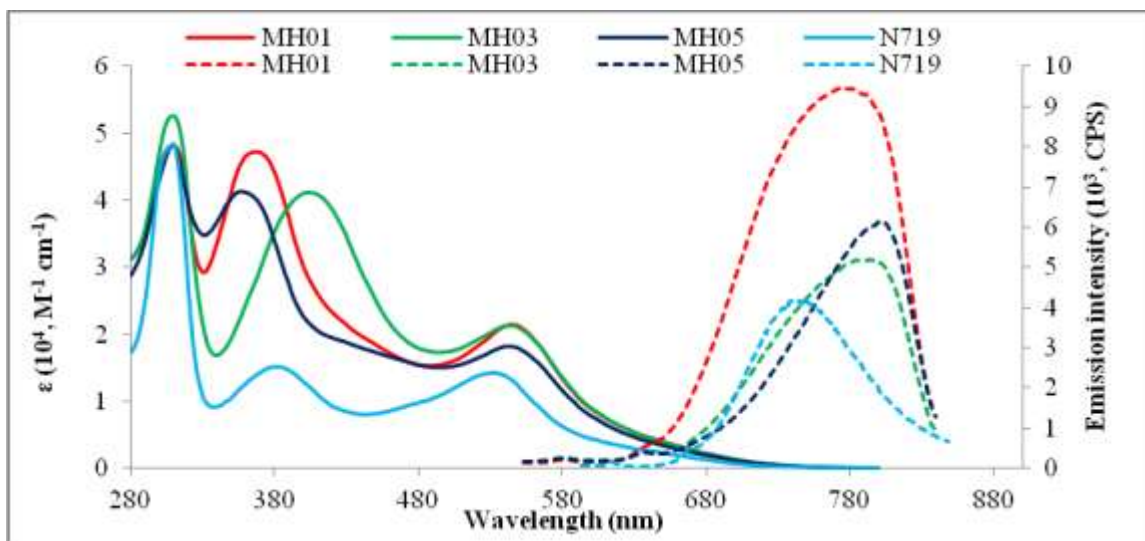


Figure 4. UV-Vis absorption (solid line) and emission (dotted line) spectra of complexes MH01, MH03 and MH05 compared to reference dye N719, measured in DMF (2×10^{-5} M).

Table 1. Absorption, luminescence and electrochemical properties MH01, MH03 and MH05 against N719.

Sensitizer	Expt. ^a Absorption Spectrum(2×10^{-5} M)		Emission ^b at 298K (2×10^{-5} M)
	λ_{\max} (nm)	ϵ ($M^{-1} \text{ cm}^{-1}$)	λ_{em} (nm)
MH01	367; 545 (d$\rightarrow$$\pi^*$)	47,250; 21,500	770
MH03	404; 544 (d$\rightarrow$$\pi^*$)	41,250; 21,350	784
MH05	358; 542 (d \rightarrow π^*)	42,500; 18250	799
N-719	381; 529 (d$\rightarrow$$\pi^*$)	14,400; 14,200	746

^a Measured in DMF (2×10^{-5} M) at room temperature; ^b The emission spectra were obtained by exciting at the lowest MLCT band in DMF.

2.3. Electrochemical Data

The ionization potential (IP) of MH01, MH03, MH05 and N719 bound to nanocrystalline TiO₂ film was measured using a photoemission yield spectrometer (Riken Keiki AC-3E), and the results are shown in Table 2. The measured photoemission yield spectra on TiO₂ are shown in ESI. The experimental ionization potentials values for MH01, MH03, MH05 and N719 were -5.53, -5.50, 5.52, and 5.76 eV, respectively. These results confirmed that the energy difference between the Ru^{3+/2+} potential (IP) of these dyes and the I₃⁻/I⁻ redox couple (-5.20 eV) [27] is large enough for efficient regeneration of the dye through reaction with iodide. Table 2 summarizes the experimental and calculated E_{0-0} , the ground and excited state oxidation potentials of the aforementioned dyes. The excited state oxidation potential E^* (Ru^{3+/*}) were estimated using Equation 1, where E (Ru^{3+/2+}) is the oxidation potential of the ground state and E_{0-0} is the energy difference between the lowest excited singlet and ground states. The resulting E^* (Ru^{3+/*}) values are shown in Table 2. The experimental excited-state oxidation potentials E^* (Ru^{3+/*}) of dyes MH01, MH03 and MH05 were -3.61, -3.62 and -3.63eV, respectively, which lay above the conduction band edge of nanocrystalline TiO₂ (-4.2 eV) [28]. Hence, excited-state electron injection from the excited state into the conduction band edge of TiO₂ is thermodynamically favorable.

$$E^*(\text{Ru}^{3+/*}) = E(\text{Ru}^{3+/2+}) - E_{0-0} \quad \text{Eq. 1}$$

2.4. DFT/TD-DFT Calculations

Following geometry optimization and vertical electronic excitation calculations, the ground and excited state oxidation potentials were calculated. Table 2 shows the calculated Highest Occupied Molecular Orbital (HOMO), the excited state oxidation potential ($\text{Ru}^{3+/*}$), and the lowest singlet-singlet electronic transitions (E_{0-0}) for MH01, MH03 and MH05 compared to N719, which were in excellent agreement with the experimental results.

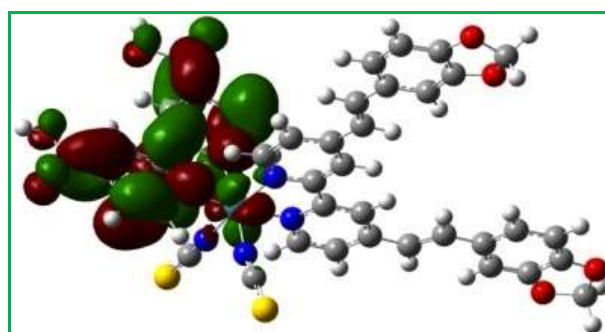
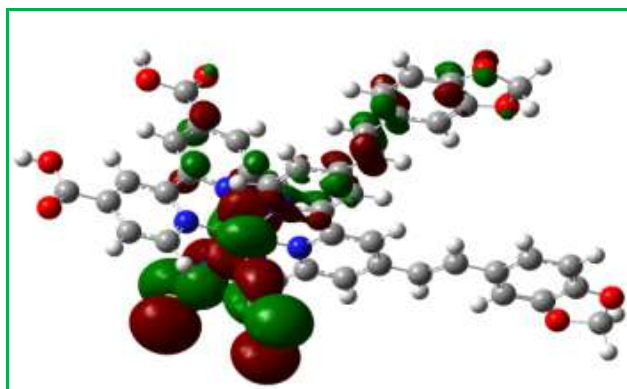
Table 2. Experimental versus calculated ground and excited state oxidation potentials for MH01, MH03 and MH05.

Compound	Calculated Energy (eV), TD-DFT			Experimental (eV)		
	E_{HOMO}	$\text{ESOP}_{\text{singlet}}$	$E_{0-0} = (S_0-S_1)$	$*E_{0-0}$	GSOP (HOMO)	E^* ($\text{Ru}^{3+/*}$)
MH01	-5.54	-3.65	1.89	*1.92	-5.53	-3.61
MH03	-5.42	-3.56	1.86	*1.88	-5.50	-3.62
MH05	-5.48	-3.57	1.91	*1.89	-5.52	-3.63
N719	-5.49	-3.49	2.00	*1.99	-5.76	-3.77

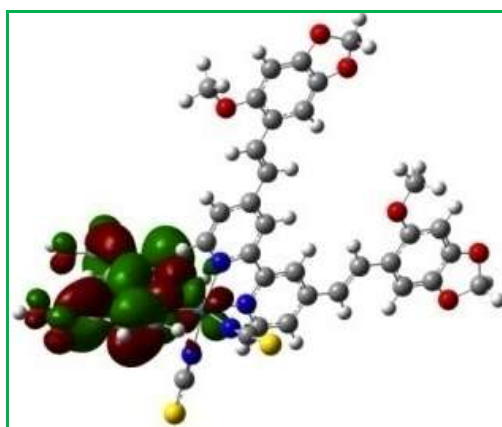
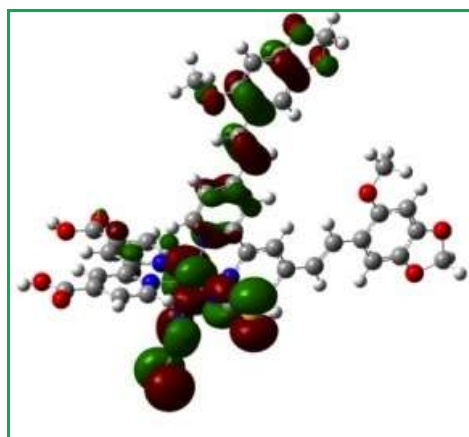
ESOP = excited state oxidation potential; $\text{ESOP}_{\text{singlet}} = \text{GSOP} - E_{0-0}$; $E_{0-0} = (S_0-S_1)$ = the lowest vertical excitation energy = the lowest singlet-singlet transition; $*E_{0-0}$ = based on the experimental absorption and emission spectra (DMF), calculated from the point of overlap; GSOP = ground state oxidation potential was measured using a photoemission yield spectrometer (Riken Keiki AC-3E). GSOP and ESOP of N719 were calculated elsewhere [29]. Calculations were performed using TD-DFT implemented in Gaussian 09, using the energy functional B3LYP and basis set DGDZVP.

The MO calculations analyses of MH01, MH03 and MH05 showed that the HOMO is delocalized not only on Ru and NCS but also on the ancillary ligands carrying *meta-para-*

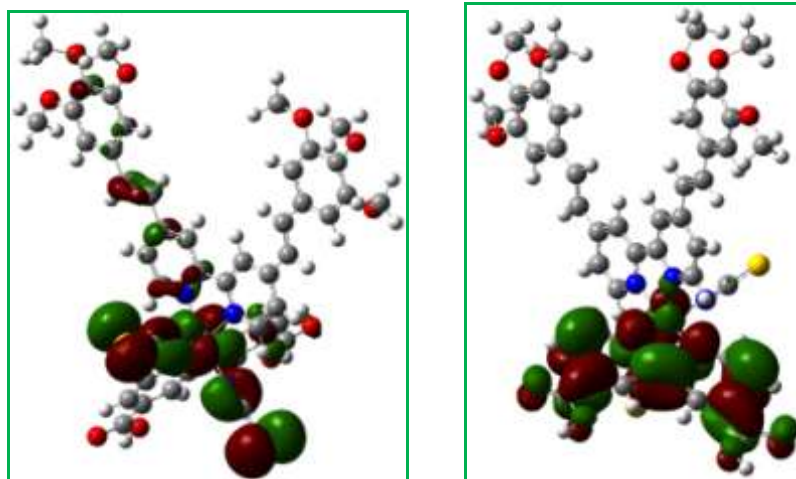
cyclic auxochromes (MH01 and MH03). However, in the case of MH05 (acyclic), the HOMO distribution on the electron ancillary ligands was negligible. This elucidated that the presence of *meta-para*-cyclic electron donor auxochromes linked to bipyridyl through CH=CH spacer forms a stilbazole linkage with enhanced electron rich regime on the ancillary ligand, which contributed significantly to the ligand-to-ligand charge transfer (LLCT). This is likely due to stronger *p*-orbitals overlap between the electron donor oxygen in the cyclic form and aromatic stilbazole because the lone pairs of electrons on the oxygen are in better alignment with the *p*-orbitals of the aromatic system. In the case of MH05, it is clear from the DFT calculation that the distribution of the HOMO on the ancillary ligand is negligible, which suggests that the charge transfer from the ancillary ligand to the LUMO is not strong. In the case of MH03, the HOMO distribution on the ancillary ligand is strong due to the presence of OMe in the *ortho* position. However, in order for a strong electronic overlap between the electron donor synthon, the CH=CH bridge and stilbazole moiety, a free rotation of the electron donor around the CH=CH bridge is required. It is likely that the presence of OMe *ortho* to the CH=CH bridging group precludes free rotation of the electron donor and locks the conformation, which would prevent the electronic overlap of similar HOMO lobes and that would weaken the electronic overlap with the stilbazole moiety. As shown in Figure 5, the HOMO lobes on the electron moiety and the bridging group CH=CH are opposite to each other (red-green not red-red) and a free rotation is required for a strong electronic overlap between similar HOMO lobes to occur. The calculated LUMOs of MH01, MH03 and MH05 were delocalized on the acceptor bipyridyl ligand and extended to the carboxylic group, (Figure 5).



MH01



MH03



MH05

Figure 5. Calculated HOMO (left) and LUMO (right) isosurfaces of MH01, MH03 and MH05.

ATR-FTIR Spectral Data

ATR-FIR spectra for MH01, MH03 and MH05 exhibited strong and intense absorption peaks at 2102-2104 cm^{-1} , corresponding to the isothiocyanate (N-bonded isomer) group. The spectra also showed strong absorption peak at 1720 cm^{-1} corresponding to the carbonyl of COOH in MH01, MH03 and MH05 and broad peaks at 3437 cm^{-1} , corresponding to the OH of COOH.

2.6. Photovoltaic Properties

The photovoltaic performance of dyes MH01, MH03 and MH05 on nanocrystalline TiO_2 electrode was studied under standard AM 1.5 irradiation (100 mW cm^{-2}) using an electrolyte with a composition of 0.6 M dimethylpropyl-imidazolium iodide (DMPH), 0.05 M I_2 , 0.1 M

LiI and 0.3-0.5 M 4-ter-butylpyridine (TBP) in acetonitrile. Figure 6 shows the incident-photon-to-current efficiency conversion (IPCE) spectra for the cells fabricated with dyes MH01-TBA, MH01, MH03 and MH05 and N719, where the incident photon-to-current conversion efficiency (IPCE) values are plotted as a function of wavelength. Dye MH01-TBA demonstrated the most efficient sensitization of nanocrystalline TiO₂ over the whole visible range extending into the near IR region (ca. 860 nm) with quantum efficiency of about 90% in the plateau region.

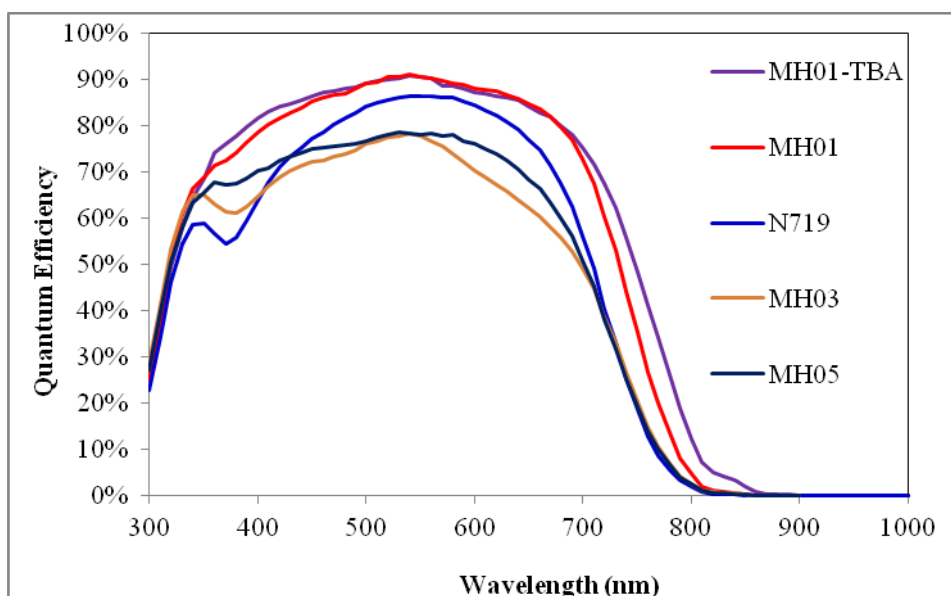


Figure 6. Photocurrent action spectra (IPCE) obtained with dyes MH01-TBA, MH03, MH01-05 and N719 anchored on nanocrystalline TiO₂ film.

The short-circuit photocurrent density (J_{SC}), open-circuit voltage (V_{OC}), fill factors (FF) and overall cell efficiencies (η) for each dye-TiO₂ electrode are summarized in Table 3. The photovoltaic performance parameters of MH01-TBA, MH01, MH03 and MH05, and N719-

sensitized cells were studied using electrolyte containing 0.3TBP. N719 and MH01-TBA were also studied using 0.5 TBP concentrations. Under the same experimental device conditions, MH01-TBA showed higher photocurrent and greater total conversion efficiency than N719, and this improvement was attributed to the superior light harvesting efficiency (LHE) of MH01-TBA in the high and low energy photons regions compared to N719. The short-circuit photocurrent of N719 decreased as the TBP concentrations increased due to upward shift in the conduction band and decrease in the negative free energy [30]. On the other hand, the open-circuit voltage increased significantly and the fill factor increased slightly as the TBP concentration increased. It is likely that TBP was adsorbed on the bare TiO_2 surface and formed a thick layer that suppressed the recombination between the injected electron and I_3^- ions. Using 0.5TBP in the case of MH01, the J_{sc} decreased as expected but the increase in the V_{oc} was an infinitesimal.

Table 3. Photovoltaic performance^a of complexes MH01-TBA, MH01, MH03 and MH05 against N719.

Dye	TBP (M)	J_{sc} (mA cm ⁻²)	V_{oc} (V)	FF	η (%)
MH01	0.3	19.59	0.659	0.702	9.08
	0.5	18.81	0.671	0.654	8.24
MH01-TBA	0.3	20.09	0.688	0.717	9.91
MH03	0.3	15.96	0.520	0.638	5.29
MH05	0.3	15.86	0.668	0.685	7.25
N719	0.3	17.16	0.733	0.725	9.12
	0.5	16.85	0.749	0.739	9.32

^a Conditions: sealed cells; coadsorbate, DCA 20 mM; photoelectrode, TiO₂ (15 μ m thickness and 0.25 cm²); electrolyte, 0.6 M DMPII, 0.1 M LiI, 0.05 I₂ in AN; irradiated light, AM 1.5 solar light (100 mW cm⁻²). J_{sc} , short-circuit photocurrent density; V_{oc} , open-circuit photovoltage; FF , fill factor; η , total power conversion efficiency.

Figure 7 shows photocurrent-voltage curves of sandwich-type sealed solar cells based on MH01-TBA, MH01, MH03 and MH05 and N719 at standard AM 1.5 irradiation using an electrolyte of 0.6M dimethylpropyl-imidazolium iodide (DMPII), 0.05 M I₂, 0.1 M LiI, and 0.3M or 0.5M 4-tert-butylpyridine (TBP) in acetonitrile. As shown in Table 3, under the same experimental device conditions with the electrolyte containing 0.3 M TBP under standard AM 1.5 irradiation (100 mW cm⁻²), the solar cell sensitized with MH01-TBA showed the best performance in terms of short-circuit photocurrent density 20.09mA cm⁻², an open-circuit photovoltage of 0.688 V, and a fill factor of 0.702, corresponding to an overall conversion efficiency (η) of 9.91% compared to 9.12% of N719. Hence, this class of electron donor cyclic auxochrome is considered as an attractive class of sensitizers for high efficiency

DSSCs. Furthermore, through molecular modeling and tuning LHE and electron injection, more efficient sensitizers can be developed.

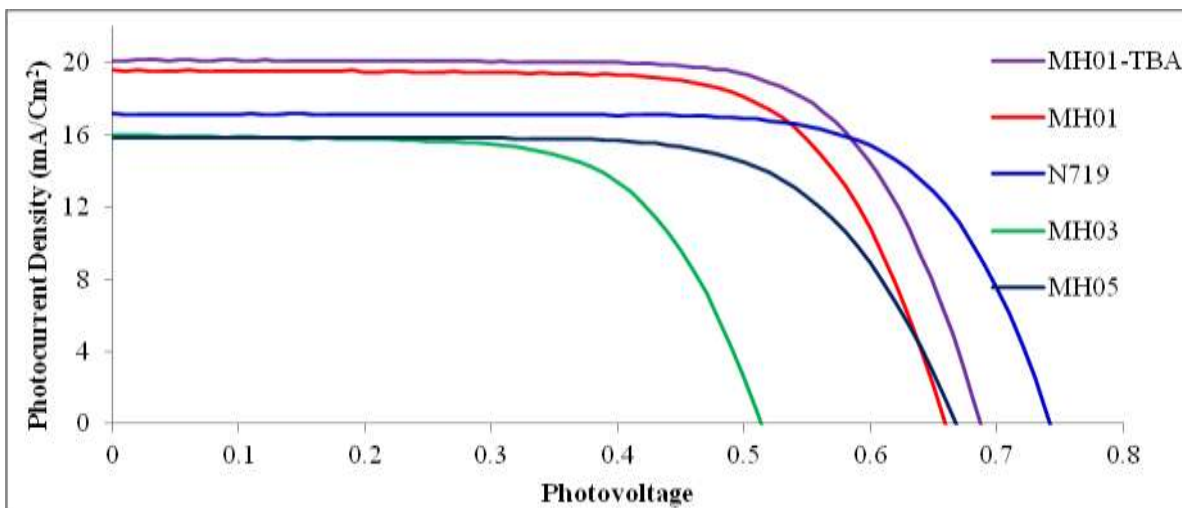


Figure 7. Photocurrent voltage characteristics of DSSCs sensitized with the complexes MH01-TBA, MH01, MH03, MH05 and N719. Electrolyte, 0.6 M DMPH, 0.1 M LiI, 0.05 I₂ in acetonitrile (AN).

2.7. CEM and IMVS characterization

To further understand the molecular structure dependent V_{oc} for N719, MH01, MH01-TBA, MH03 and MH05, we first measured the relative conduction band position of TiO₂ by means of a charge extraction method. Fig. 8 shows V_{oc} as a function of electron density for all dyes. A linear increase in V_{oc} as a function of electron density was observed for all DSCs. Notably, the plots for all dyes overlapped with each other, indicating that all of the dyes have almost the same effect on the conduction band of TiO₂ regardless of the substituents on the bpy. Therefore, the molecular structure dependent V_{oc} for all DSCs should be attributed to the extent of charge recombination that is related to the electron lifetime (τ) in TiO₂. Intensity-

modulated photovoltage spectroscopy was used to measure τ , and Fig. 9 shows the relationship between τ and electron density for all DSCs. At a certain electron density, τ increase in the order of N719 > MH01-TBA > MH01 > MH05 > MH03. MH01-TBA exhibited a much longer τ than MH03 and MH05 at the same electron density, implying that the recombination between electrons on the TiO₂ surface and I₃⁻ ions in the electrolyte was considerably suppressed by the presence of TBA, and isomerization of the electron donors as the life time decreased from MH01 to MH03 to MH05.

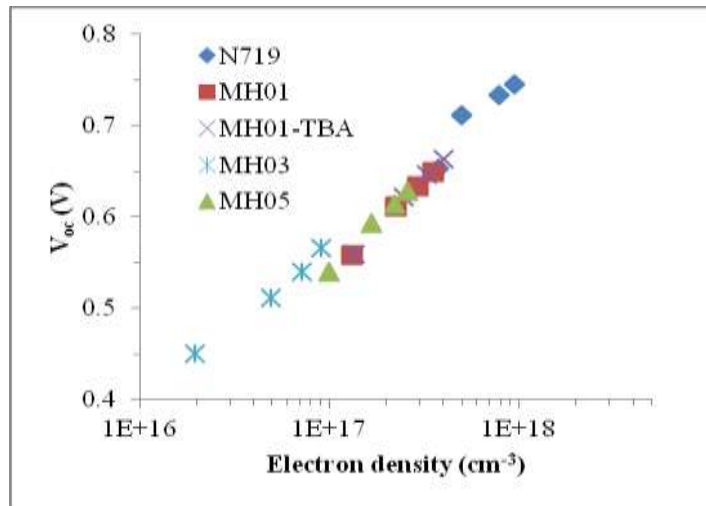


Figure 8. V_{oc} as a function of electron density for DSCs sensitized with N719, MH01, MH01-TBA, MH03 and MH05. Electron density was measured by means of a charge extraction method.

2.8. EIS characterization

Electrochemical impedance spectra was performed to study electron lifetimes and photoinduced electron injection properties under open circuit and illuminated conditions. Fig. 10 and Fig.11 show the EIS Nyquist and Bode plots, respectively, for the DSSCs based on

N719, MH01-TBA, MH01, MH03 and MH05 dyes. As shown in Fig. 10, the Nyquist plots exhibited the radius of the second semicircle, indicating that the electron recombination resistance increased in the order of N719 > MH01-TBA > MH01 > MH05 > MH03.

In the Bode phase plot (as shown in Fig. 11), the middle frequency peak in the 1-100 Hz range is indicative of the electron recombination between electrolyte and TiO₂. The middle-frequency peaks of the DSCs based on N719 and MH01-TBA shift to lower frequency relative to that of MH03 and MH05, indicating a shorter recombination lifetime for the latter case. This trend is in accordance with the τ vs. V_{oc} results, which is in agreement with the fact that MH01-TBA exhibited higher V_{oc} values (0.688V) than MH03 (0.520 V) or MH05 (0.668V).

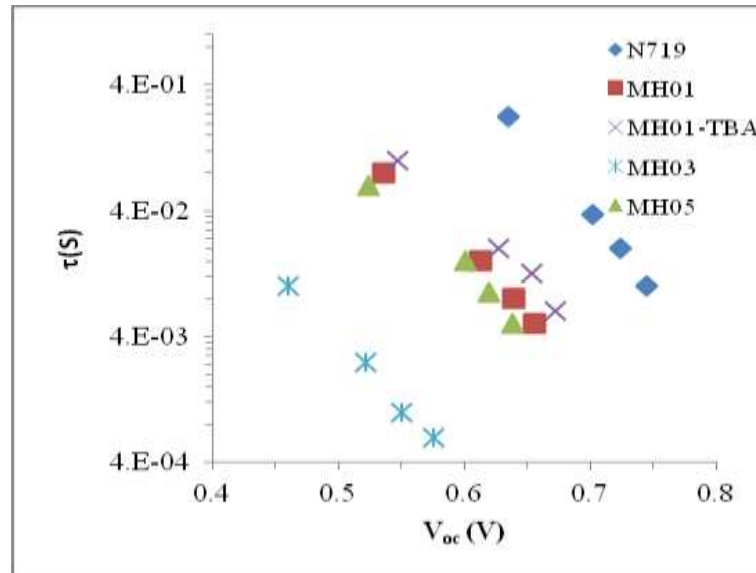


Figure 9. Electron lifetime (τ) as a function of V_{oc} for DSCs sensitized with N719, MH01, MH01-TBA, MH03 and MH05. Electron lifetime was measured by means of intensity-modulated photovoltage spectroscopy.

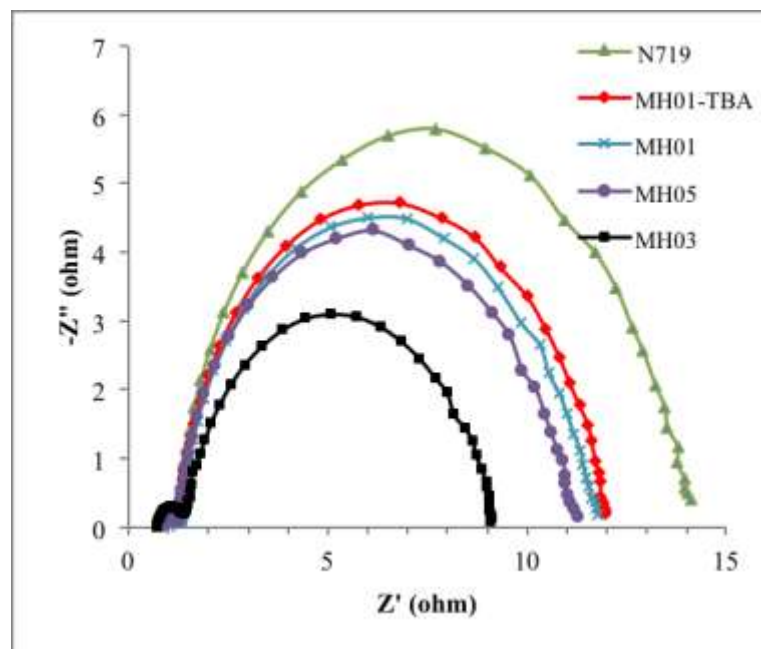


Figure 10. EIS Nyquist plots for DSCs sensitized with N719, MH01, MH01-TBA, MH03 and MH05.

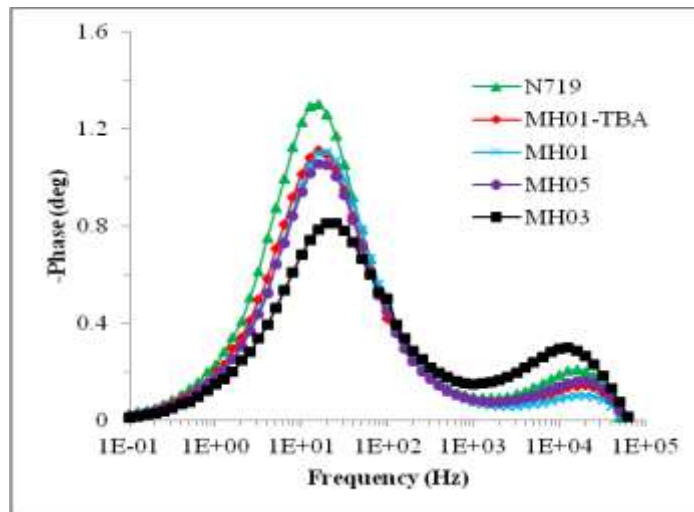


Figure 11. EIS Bode plots for DSCs sensitized with N719, MH01, MH01-TBA, MH03 and MH05.

2.9. Long-term stability measurements of dyes and devices

Stability is a key factor for evaluating the practical application of DSSCs. Each component as well as sealing technique of a device can impact its stability at different extents during long-term application under severe environment. In DSSCs, the dye should be stable enough under light irradiation as a precondition for long-term stable device. Katoh and coworkers have developed a simple and efficient method to evaluate the stability of sensitizer dyes in a short period of time [31]. Since the most unstable state of the sensitizer is in its regeneration process, the corresponding sensitizers must remain stable in the cation state for at least 10s to be capable of realizing a 10-year operation cycle. To shorten the experiment period, we can accelerate the dye aging process by light irradiation on dye-loaded TiO_2 electrode. Without electrolyte, dye regeneration could occur only by receiving injected electrons from TiO_2 , which takes 10^4 – 10^3 times longer than that in complete solar cell device. After

45 min of light irradiation on sensitized TiO₂ electrodes fabricated from MH01 and MH03, the absorbance of MH01 remained almost the same while that of MH03 decreased to some extent (Figure 12A & 12B). Meanwhile, the color purple of MH01 loaded TiO₂ film did not change throughout the whole experiment while MH03 based film faded quickly from purple to light red. Such difference in responses to light irradiation between MH01 and MH03 reveal that the photo-stability of the former is significantly higher, confirming the detrimental effect of the OMe group *ortho* to the CH=CH bridge in MH03. It is likely that the presence of the OMe in the *ortho* position with respect to the bridging group CH=CH increases the electron density on the bridge, which increases its susceptibility to photodegradation. For further evaluation of long-term stability of MH01-based DSSC, a less volatile electrolyte (containing 0.6 M 1-propyl-3-methylimidazolium iodide, 0.15 M iodine, 0.1 M guanidiniumthiocyanate and 0.5 M NMBI in 3-methoxypropionitrile) was employed. Hence the photovoltaic performance of device in this experiment is a little lower than the above-mentioned volatile electrolyte device. Figure 13 shows the variations of photovoltaic parameters during a long-term accelerated aging on MH01 based solar cell. Values for V_{oc} , J_{sc} , FF , and η were recorded over a period of 1000 h. After continuously soaking in full sunlight at 60°C, the overall efficiency of the MH01-based DSSC maintain at 95% of the initial value. This demonstrates that the amount of dye on the TiO₂ surface remained intact after long time light soaking confirming its superior photostability. These results suggest the great potential that MH01 holds for DSSCs practical applications.

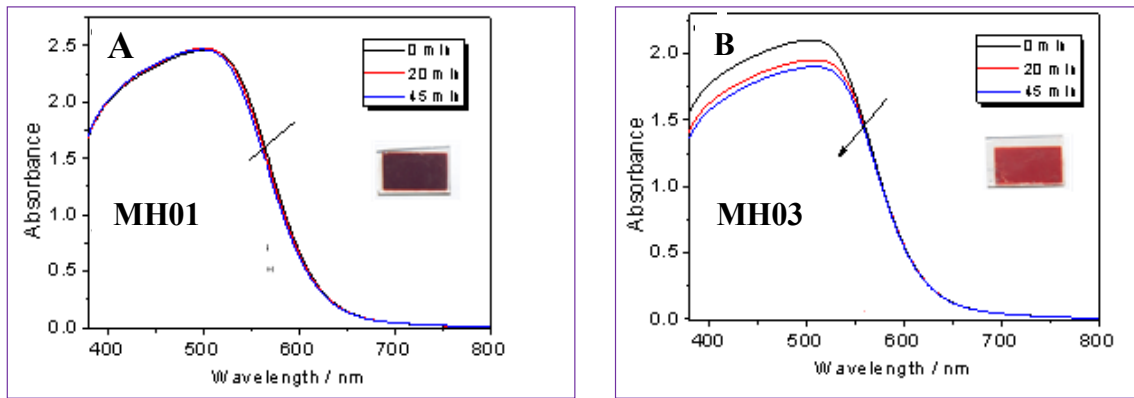


Figure 12. Absorption spectra of (c) MH01 and (d) MH03 adsorbed on nanocrystalline TiO₂ films before (black line) and after light irradiation for 20 min (red line) and 45 min (blue line).

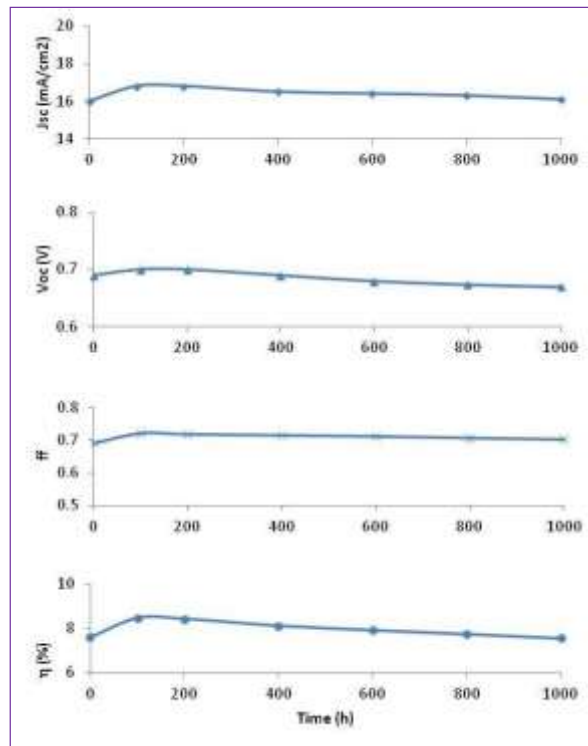


Figure 13. Evolutions of photovoltaic performance parameters for MH01-based DSSC under one sun soaking at 60°C over a period of 1000 h.

Acknowledgement

The authors are grateful for Prof. H. S. Freeman for his valuable discussion and suggestions with the Knoevenagel reaction mechanism

Conclusions

Compared to N719 under the same experimental device conditions, it was demonstrated that the novel Ru (II) based complex MH01-TBA achieved 34% more in molar absorptivity, 18% more in photocurrent, and 8.6% more in total solar-to-electric conversion efficiency. The superior performance of MH01-TBA was attributed to the presence of cyclic oxygen containing ancillary antenna, which enhanced the LHE and the photocurrent of MH01. It was shown that the form of electron donor, cyclic versus acyclic, and the presence of OMe at the *ortho* position with the respect to the bridge of the stilbazole plays a key role in the molar extinction coefficient, life time of electron in TiO₂, photocurrent density (J_{sc}), photostability and total solar-to-electric conversion efficiency. MH01, which contains *meta-para*-cyclic electron donor exhibited the highest molar extinction coefficient, longest electron lifetime in TiO₂, highest photocurrent and total conversion efficiency. It is likely that the conjugation between the lone pairs of electrons of the *p*-orbital of the two oxygen atoms in the cyclic form (MH01) form stronger overlap and conjugation with the *p*-orbital of the aromatic stilbazole system than the acyclic form (MH05), which translated into enhanced light harvesting in MH01. Owing to the presence of OMe in the *ortho* position in MH03, it exhibited the shortest lifetime in TiO₂ nanoparticles, lowest photostability and lowest solar-to-electron conversion efficiency. Although MH05 possesses three freely rotating OMe (acyclic), its $\% \eta$ was lower than that of MH01, which possess two-electron donors in the cyclic form. This is expected because electron donor substituents at the *meta* position are weaker electron donors compared to electron donors at the *ortho* and/or *para* positions.

Owing to the high efficiency and superior long-term stability of MH01 over 1000h at 60°C as it retained 95% of its original photovoltaic performance, there is a great potential for its use in DSSCs practical applications. These new findings confirm that the location and form of electron donors whether cyclic-or-acyclic have significant impact on the photovoltaic performance of dyes for DSSCs.

REFERENCES

1. N. E. Tokel, and A. J. Bard, *J. Am. Chem. Soc.*, 1972, 94, 2862
2. M. M. Richter, A. J. Bard, W. Kim and R. H. Schmehl, *Anal. Chem.*, 1998, **70**, 310.
3. W. Miao, J. P. Choi and A. J. Bard, *J. Am. Chem. Soc.*, 2002, **124**, 14478.
4. S. Welter, K. Brunner, J. W. Hofstraat and L. De Cola, *Nature.*, 2003, **421**, 54.
5. J. Slinker, D. Bernards, P. L. Houston, H. D. Abrufia, S. Bernhard and G. G. Malliaras, *Chem. Comm.*, 2003, 2392.
6. G. Kalyuzhny, M. Buda, J. McNeill., P. Barbara and A. J. Bard, *J. Am. Chem. Soc.*, 2003, **125**, 6272.
7. H. Rudmann, S. S. Himada and M. F. Rubner, *J. Am. Chem. Soc.*, 2003, **124**, 4918.
8. X. Gong, P. K. Ng and W. K. Chan, *Adv. Mater.*, 1980, **10**, 1337.
9. K. M. Maness, R. H. Terrill, T. J. Meyer, R. W. Murray and R. M. Wightman, *J. Am. Chem. Soc.*, 1996, **118**, 10609.
10. T. G. Drummond, M. G. Hill and J. K. Barton, *Nat. Biotechnol.*, 2003, **21**, 1192.
11. P. D. Beer, *Acc. Chem. Res.*, 1998, **31**, 71.
12. Y. Z. Hu, Q. Xiang and R. P. Thummel, *Inorg. Chem.*, 2002, **41**, 3423.
13. F. Barigelletti and L. Flamigni, *Chem. Soc. Rev.*, 2000, **29**, 1.
14. R. Ballardini, V. Balzani, A. Credi, M. T. Gandolfi and M. Venturi, *Acc. Chem. Res.*, 2001, **34**, 445.
15. V. Balzani, S. Campagna, G. Denti, A. Juris, S. Serroni and M. Venturi, *Acc. Chem. Res.*, 1998, **31**, 26.

16. M. Grätzel, *Nature.*, 2001, **414**, 338.
17. J. P. Sauvage, J. P. Collin, J. C. Chambron, S. Guillerez, C. Coudret, V. Balzani, F. Barigelletti, L. DeCola and L. Flamigni, *Chem. Rev.*, 1994, **94**, 993.
18. M. Grätzel. *J. Photochem. Photobiol., C.* 2003, **4**, 145.
19. M. K. Nazeeruddin, F. De Angelis, S. Fantacci, A. Selloni, G. Viscardi, P. Liska, S. Ito, B. Takeru and M. Grätzel, *J. Am. Chem. Soc.*, 2005, **127**, 16835.
20. L. Han, A. Islam, H. Chen, C. Malapaka, B. Chiranjeevi, S. Zhang, X. Yang and M. Yanagida, *Energy Environ. Sci.*, 2012, **5**, 605.
21. P. Wang, S. M. Zakeeruddin, J. E. Moser, M. K. Nazeeruddin, T. Se-Kiguchi and M. Grätzel, *Nat. Mater.*, 2003, **2**, 402.
22. P. Wang, S. M. Zakeeruddin, R. Humphry-Baker, J. E. Moser and M. Grätzel, *Adv. Mater.*, 2003, **15**, 2101.
23. S. M. Zakeeruddin, M. K. Nazeeruddin, R. Humphry-Baker, P. Quagliotto, C. Barolo, G. Viscardi and M. Grätzel, *Langmuir.*, 2002, **18**, 952.
24. P. Wang, S. M. Zakeeruddin, J. E. Moser, R. H. Eaker, P. Comte, V. Aranyos, A. Hagfeldt, M. K. Nazeeruddin and M. Grätzel, *Adv. Mater.*, 2004, **16**, 1806.
25. P. Wang, C. Klein, R. H. Baker, S. M. Zakeeruddin, M. Grätzel, *J. Am. Chem. Soc.* 2005, **127**, 808.
26. D. Kuang, S. Ito, B. Wenger, C. Klein, J. E. Moser, R.H. Baker, S. M. Zakeeruddin and M. Grätzel. *J. Am. Chem. Soc.*, 2006, **128**, 4146.
27. G. Oskam, B. V. Bergeron, G. J. Meyer and P. C. Searson, *J. Phys. Chem., B.* 2001, **105**, 6867.

28. A. Hagfeld and M. Grätzel, *Chem. Rev.*, **1995**, 95, 49.
29. F. D. Angelis, S. Fantacci and A. Selloni, *Nanotechnology.*, 2008, **19**, 424002.
30. S.A. Haque, E. Palomares, B.M. Cho, A.N.M. Green, N. Hirata, D.R. Klug and J.R. Durrant, *Journal of the American Chemical Society*, 2005, 127(10), 3456.
31. R. Katoh, A. Furube, S. Mori, M. Miyashita, K. Sunahara, N. Koumura and K. Hara *Energy Environ. Sci.*, 2009, **2**, 542.

Supporting Information

**Influence of Cyclic Versus Acyclic Oxygen-containing Electron Donor Ancillary Ligands on
the Photocurrent, Photovoltage and Photostability for High Efficiency
Dye-sensitized Solar Cells**

Maqbool Hussain^a, [Ahmed El-Shafei](mailto:Ahmed.El-Shafei@ncsu.edu)^{a*}, Ashraful Islam^b, and Liyuan Han^b

^aPolymer and Color Chemistry Program, North Carolina State University, Raleigh, NC,
27695, USA

^bPhotovoltaic Materials Unit, National Institute for Materials Science, 1-2-1 Sengen,
Tsukuba, Ibaraki 305-0047, Japan

Corresponding authors: [Ahmed EL-Shafei@ncsu.edu](mailto:Ahmed.El-Shafei@ncsu.edu)

Materials.

The solvents and chemicals were either purchased from Sigma-Aldrich and Fisher Scientific or TCI-America, used as received. Sephadex LH-20 was purchased from Fisher Scientific.

1.1. Analytical Measurements.

1.1.1 UV-Vis Spectra

UV-Vis spectra were recorded in a 1cm path length quartz cell on a Cary 3 Spectrophotometer. A dimethylformamide solution of each complex of 2×10^{-5} M was prepared, and the absorbance was measured and extinction coefficient was calculated for each dye.

1.1.2. Fluorescence Spectra

Fluorescence spectra were recorded in a 1cm path length quartz cell using 2×10^{-5} M solutions on a Fluorolog-311. The emitted light was detected in the steady state mode using Hamamatsu R2658 detector. The emission was measured in the steady state mode by exciting at the λ_{max} (lower energy MLCT band) for each dye with exit and entrance slits set at 10nm.

1.1.3. Attenuated Total Reflectance Fourier-transform Infra Red Spectroscopy

Attenuated Total Reflectance-Fourier Transform Infra Red (ATR/FT-IR) spectra were recorded on a Thermo Nicolet, Nexus 470 FTIR Spectrophotometer with Omnic 7.2 software. The compound under investigation was placed in its powder form on a germanium crystal and a pressure probe was placed in position to apply consistent pressure on the sample. An average of 32 scans was used at a resolution of 4 cm^{-1} . The complexes and intermediates were characterized using the same parameters. Figures 1S, 2S, and 3S show the FT-IR of MH01, MH03 and MH05 in the pure form, respectively.

MH01: 2102 cm^{-1} (-NCS stretch, N-bonded isomer, very strong); 1719 cm^{-1} (C=O stretch of -COOH)

MH03: 2103 cm^{-1} (-NCS stretch, N-bonded isomer, very strong); 1719 cm^{-1} (C=O stretch of -COOH)

MH05: 2101 cm^{-1} (-NCS stretch, N-bonded isomer, very strong); 1720 cm^{-1} (C=O stretch of -COOH)

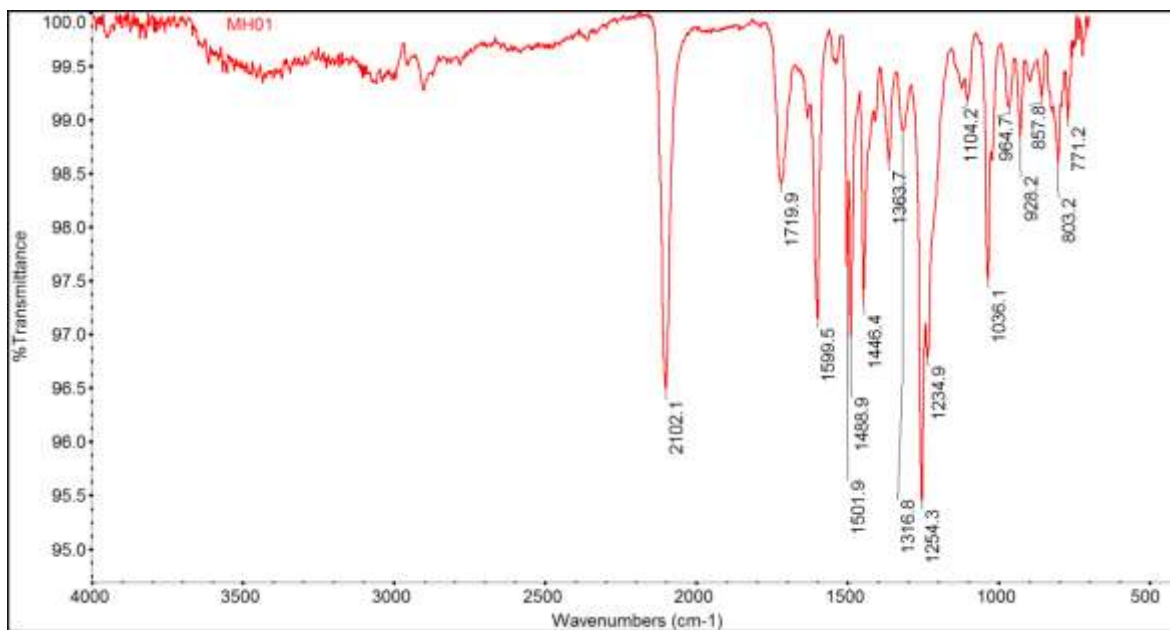


Figure 1S ATR/FT-IR of MH01.

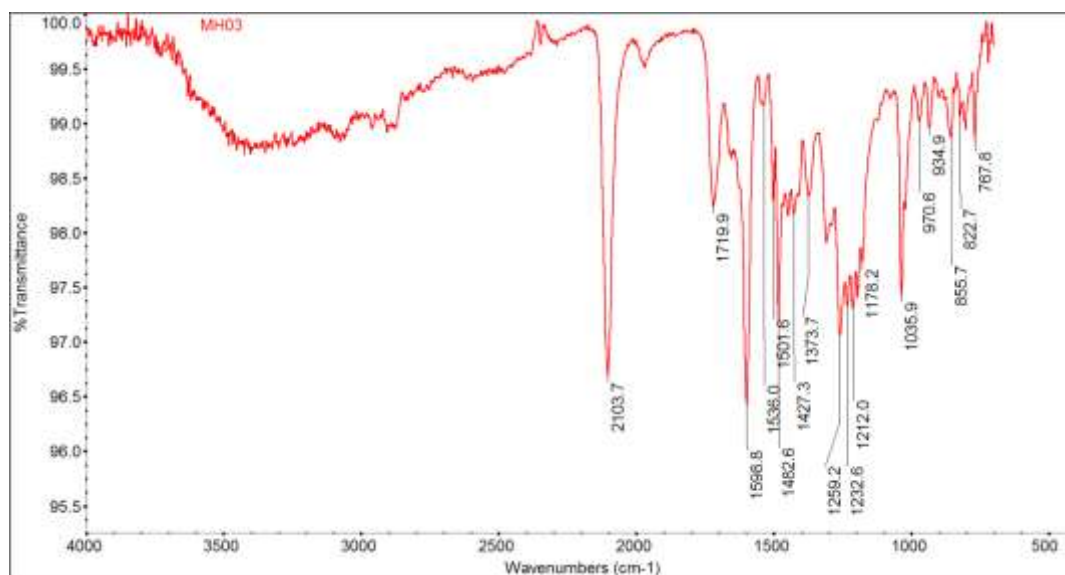


Figure 2S ATR/FT-IR of MH03.

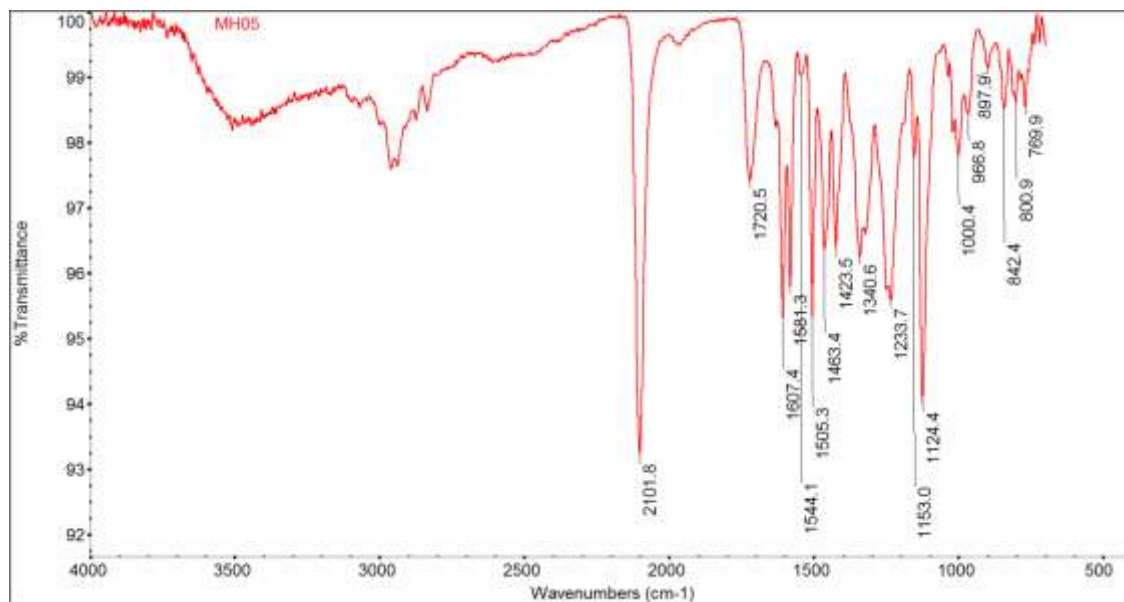


Figure 3S ATR/FT-IR of MH05.

1.1.4. Mass Spectroscopy

ESI-MS was recorded on an Agilent Technologies 6210 LC-TOF mass spectrometer in the negative ion mode. The sample was prepared in methanol in the presence of a small amount of tetrabutylammonium hydroxide (TBAOH). The fragmenter voltage was set at 220.0 V and results from 19 scans in the case of MH01, 14 scans in the case of MH02-03, 32 scans for MH04 and 22 scans in the case of MH05 were averaged. Figures 6S-10S show the -ESI-MS of MH01-04 and MH05 with one TBA per molecule, singly charged, respectively. The ESI-MS patterns shown in Figures 4S-6S are the pattern of ruthenium isotopes.

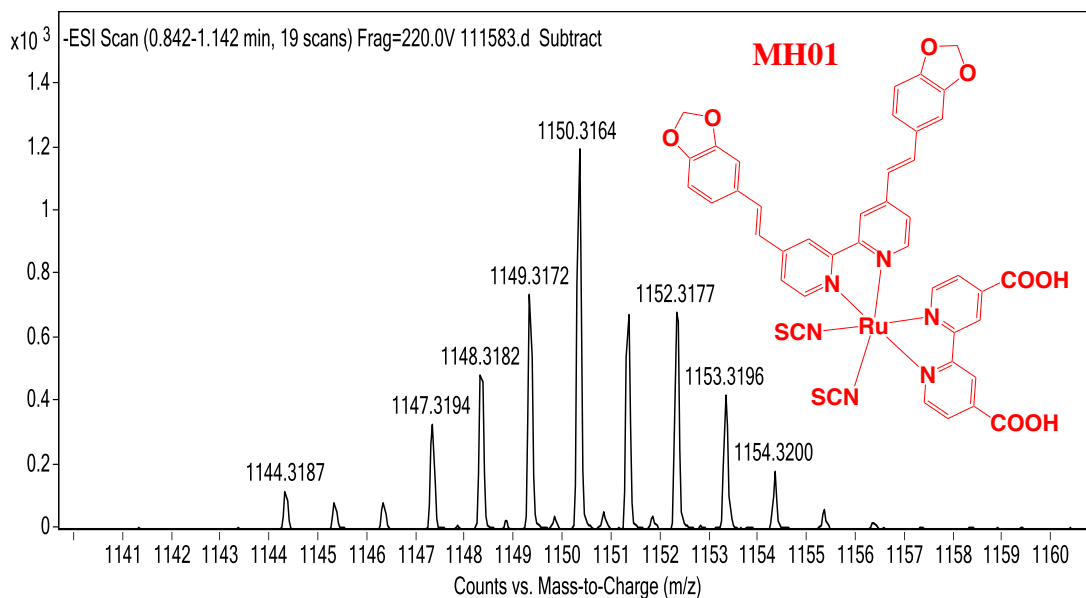


Figure 4S ESI mass spectrum of MH01, Mass 910.0454; $[M - 2H + TBA]^{-1}$; Theo. M/Z = 1150.3145, Found. M/Z 1150.3164, Error = 1.651 ppm.

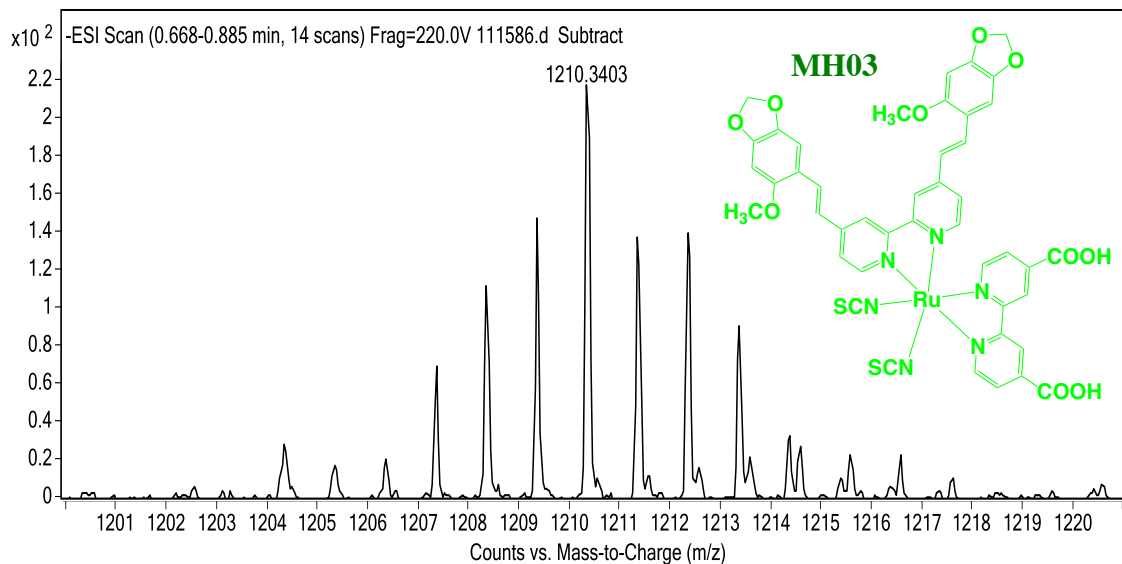


Figure 5S ESI mass spectrum of MH03, Mass 970.0665, $[M - 2H + TBA]^{-1}$, Theo. M/Z = 1210.3356, Found M/Z = 1210.3403, Error = 3.883 ppm.

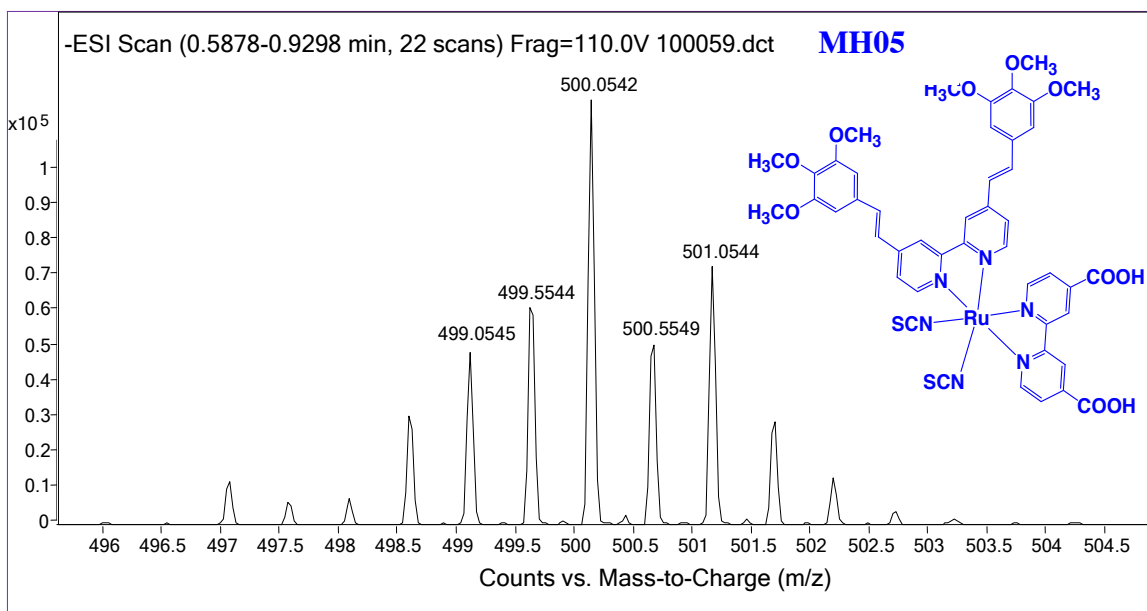


Figure 6S ESI mass spectrum of MH05; Mass 1002.1291 $[M - 2H]^{-2}$; Theo. $m/2 = 500.0567$, Found $m/2 = 500.0542$, Error = -5.02 ppm.

1.1.5. $^1\text{H-NMR}$ Experiments

$^1\text{H-NMR}$ experiments were recorded on a Bruker 500 MHz spectrometer at 40 °C using deuterated DMSO- d_6 as a solvent unless otherwise specified. Splitting patterns reported here are: s (singlet), d (doublet), dd, (double-of-doublet), t (triplet), p (pentet), and m (multiplet). Chemical shifts (δ) and coupling constants (J) are reported in ppm and Hertz (Hz), respectively. The aliphatic range 0-5ppm is not shown for brevity, unless needed. Figures 7S-9S show the $^1\text{H-NMR}$ for the ancillary ligands AL01, AL03, and AL05, respectively, Figures 10Sa-c show the $^1\text{H-NMR}$ (recorded on a Bruker 600MHz) of MH01-TBA, and Figures 11S-13S show the $^1\text{H-NMR}$ of MH01, MH03, and MH05, respectively.

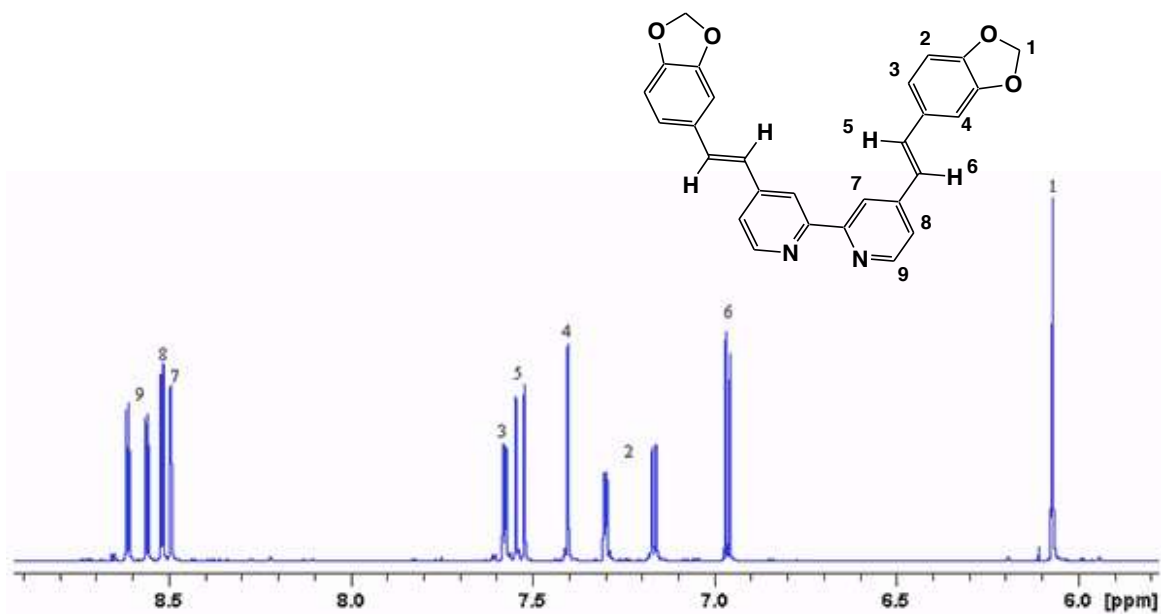


Figure 7S ^1H -NMR spectrum of the ancillary ligand of MH01 (AL01).

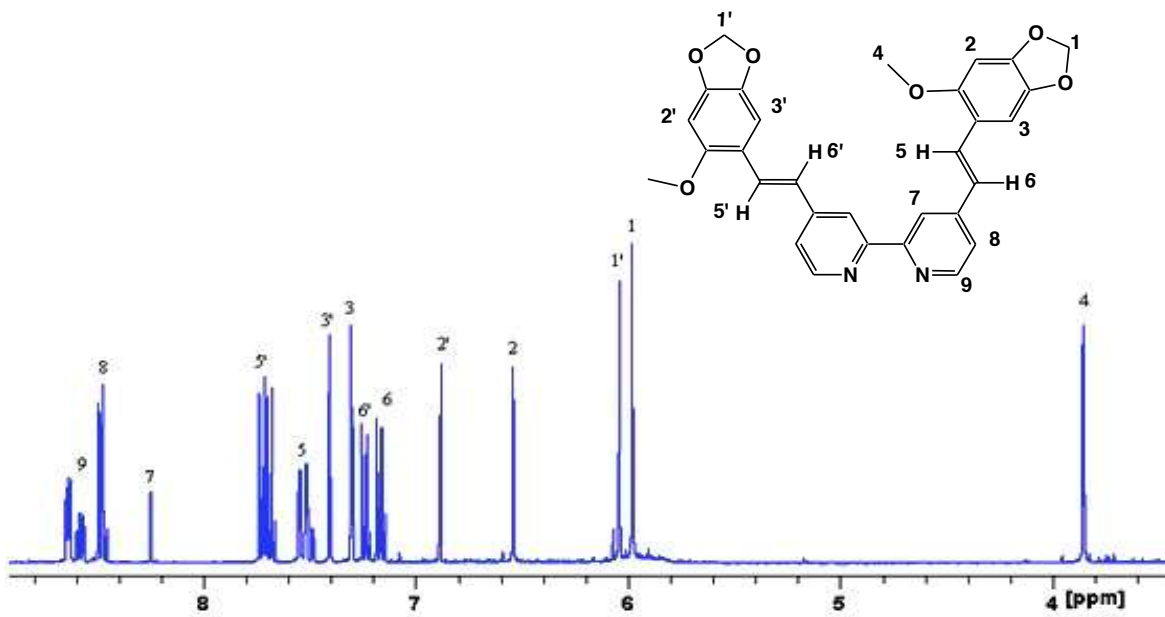


Figure 8 ^1H -NMR spectrum of ancillary ligand of MH03 (AL03).

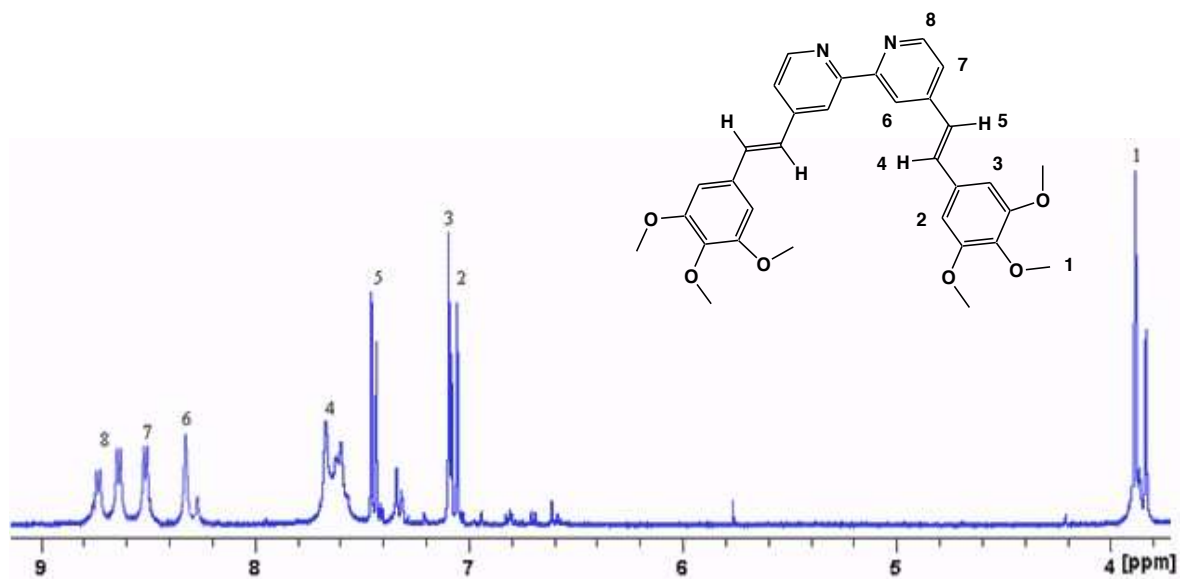


Figure 9S ¹H-NMR spectrum of ancillary ligand of MH05 (AL05).

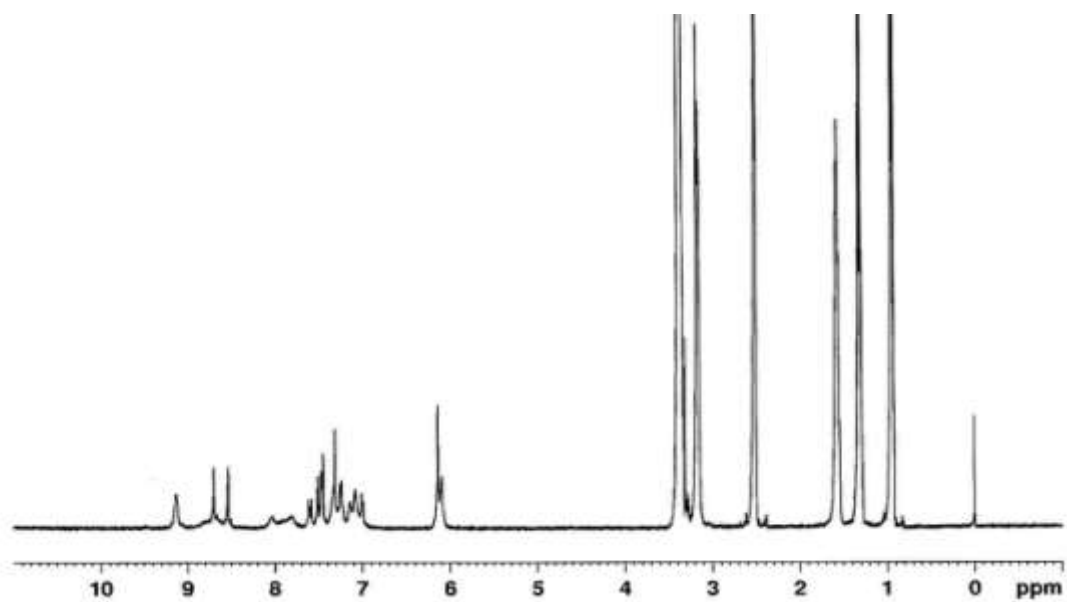


Figure 10Sa ¹H-NMR spectrum of MH01-TBA.

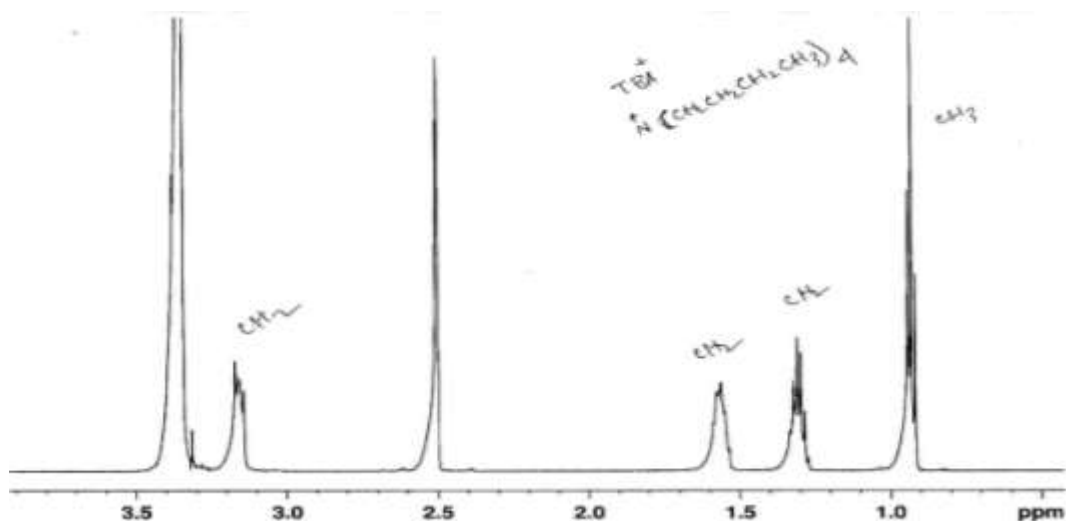


Figure 10Sb Zoom-in spectrum on the aliphatic region of MH01-TBA.

¹H-NMR, MH01 (500 MHz, DMSO, 40 °C): δ /ppm 6.3 (s, 4H, CH₂), 7.10 (d, 2H, $J = 11.0$ Hz and 7.02 (d, 2H, $J = 11.41$ Hz, CH=CH), 7.29 (d, 2H, $J = 7.3$ Hz, ArH), 7.57 (s, 2H, ArH), 7.59 (d, 2H, $J = 7.1$ Hz, ArH), 7.60 (s, 2H, ArH), 7.82 (d, 2H, $J = 8.20$ Hz, ArH), 8.88 (s, 2H, ArH), 9.04 (s, 2H, ArH), 9.08 (d, 2H, $J = 8.1$ Hz, ArH), 9.39 (d, 2H, $J = 7.9$ Hz, ArH).

¹H-NMR, MH03 (500 MHz, DMSO, 40 °C): δ /ppm 3.92 (s, 6H, CH₃), 6.01 (s, 4H, CH₂), 6.53 (d, 2H, $J = 9.8.0$ Hz and 6.61 (d, 2H, $J = 11.2$ Hz, CH=CH), 7.86 (d, 2H, $J = 7.9$ Hz, ArH), 7.95 (s, 2H, ArH), 8.29 (d, 2H, $J = 8.5$ Hz, ArH), 8.9 (s, 2H, ArH), 9.06 (s, 2H, ArH), 8.29 (d, 2H, $J = 8.5$ Hz, ArH), 9.06 (s, 2H, ArH), 9.1 (d, 2H, $J = 8.6$ Hz, ArH).

¹H-NMR, MH05 (500 MHz, DMSO, 40 °C): δ /ppm 3.88 & 3.92 (s, 18H, -OCH₃) 6.17 (s, 2H, ArH), 6.26 (s, 2H, ArH), 6.92 (d, 2H, $J = 5.5$ Hz, and 7.35 (d, 2H, $J = 16.59$ Hz, CH=CH),

7.50-7.80 (m, 4H, ArH), 8.89 (s, 2H, ArH), 9.12 (s, 2H, ArH), 9.16 (d, 2H, $J = 5.9$ Hz, ArH), 9.46 (d, 2H, $J = 5.7$ Hz, ArH) 14.14 (s, 2H, v. weak, -COOH).

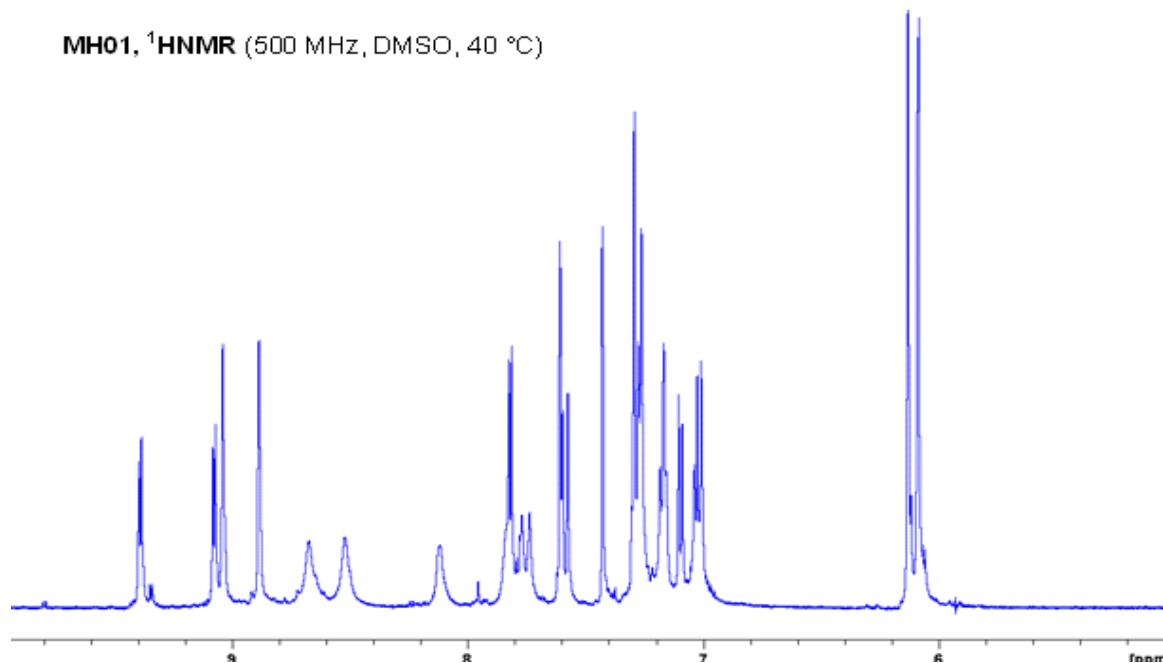


Figure 11S $^1\text{H-NMR}$ spectrum of MH01.

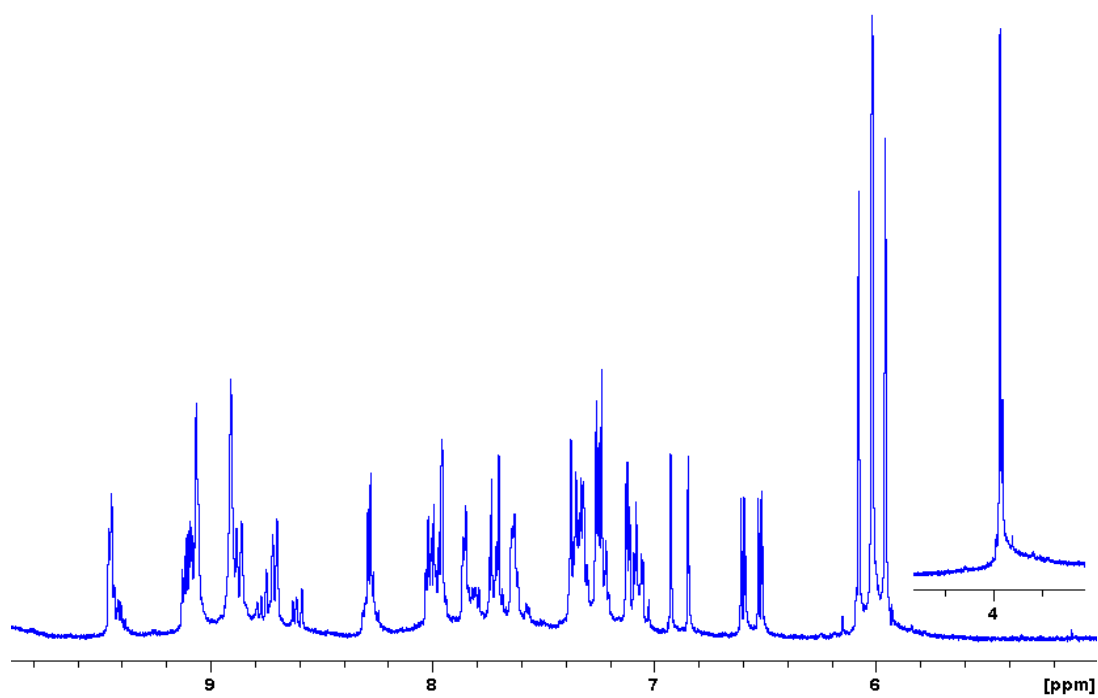


Figure 12S $^1\text{H-NMR}$ spectrum of MH03

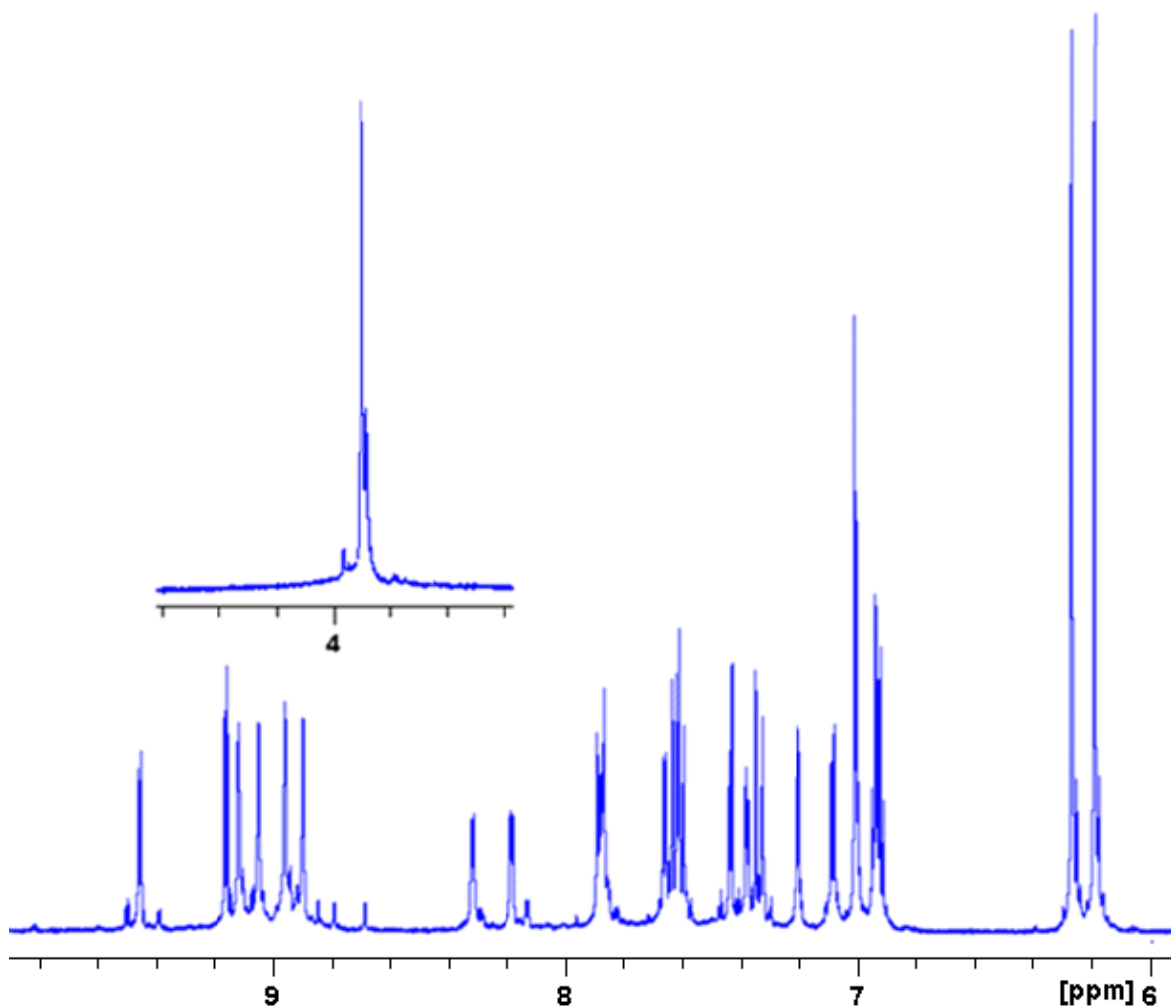


Figure 13S ^1H -NMR spectrum of MH05.

1.1.6. Elemental Analysis

MH01, Chemical Formula: $\text{C}_{42}\text{H}_{28}\text{N}_6\text{O}_8\text{RuS}_2$, Calcd. C, 55.44; H, 3.10; N, 9.24. Found: C, 55.21; H, 3.15; N, 9.13.

MH03, Chemical Formula: $\text{C}_{44}\text{H}_{32}\text{N}_6\text{O}_{10}\text{RuS}_2$, Calcd. C, 54.48; H, 3.33; N, 8.66. Found: C, 54.27; H, 3.41; N, 8.55.

MH05, Chemical Formula: $C_{46}H_{40}N_6O_{10}RuS_2$, Calcd. C, 55.14; H, 4.02; N, 8.39. Found: C, 55.01; H, 4.11; N, 8.26.

1.2.6. TiO₂ Electrode Preparation

A double-layer TiO₂ photoelectrode (10+5) μm in thickness with a 10 μm thick nanoporous layer and a 5 μm thick scattering layer (area: 0.25 cm^2) were prepared using a reported method [1]. Fluorine doped tin oxide-coated glass electrodes (Nippon Sheet Glass Co., Japan) with a sheet resistance of 8-10 ohm^{-2} and an optical transmission of greater than 80% in the visible range were screen printed using anatase TiO₂ colloids (particle size $\sim 13\text{nm}$) obtained from commercial sources (Ti-Nanoxide D/SP, Solaronix). Nanocrystalline TiO₂ thin films were deposited onto the conducting glass by screen-printing which was then sintered at 500 °C for 1 hour. The film thickness was measured with a Surfcom 1400A surface profiler (Tokyo Seimitsu Co. Ltd.). The electrodes were impregnated with a 0.05 M titanium tetrachloride solution and sintered at 500 °C. The films were further treated with 0.1M HCl aqueous solutions before examination [2]. The dye solutions (2×10^{-4} M) were prepared in 1:1:1 acetonitrile, *tert*-butyl alcohol and DMSO. Deoxycholic acid was added to the dye solution as a coadsorbent at a concentration of 20 mM. The electrodes were immersed in the dye solutions and then kept at 25 °C for 20 hours to adsorb the dye onto the TiO₂ surface.

1.2.7. Fabrication of Dye-Sensitized Solar Cell

Dye-Sensitized Solar Cell were prepared using TiO₂ coated working electrodes and platinum coated counter electrodes, and were sealed using a 40 μm Syrlin spacer through heating of

the polymer frame. The redox electrolyte consisted of a solution of 0.6 M DMPII, 0.05 M I₂, 0.1 M LiI and 0.3-0.5 M TBP in acetonitrile.

1.2.8. Photoelectrochemical Measurements

2.2.8.1. Photovoltaic measurements

Photovoltaic measurements of sealed cells were made by illuminating the cell through the conducting glass from the anode side with a solar simulator (WXS-155S-10) at AM 1.5 illuminations (light intensities: 100 mW cm⁻²).

1.2.8.2. Incident Photon to Current Efficiency (IPCE) Conversion

IPCE measurements were made on a CEP-2000 system (Bunkoh-Keiki Co. Ltd.). IPCE at each wavelength was calculated using Equation 2, where I_{SC} is the short-circuit photocurrent density (mAcm⁻²) under monochromatic irradiation, q is the elementary charge, λ is the wavelength of incident radiation in nm and P_0 is the incident radiative flux in Wm⁻² [3].

$$\text{IPCE}(\lambda) = 1240 \left(\frac{I_{\text{SC}}}{q\lambda P_0} \right) \quad \text{Equation 2}$$

The incident photon-to-current conversion efficiency was plotted as a function of wavelength.

1.2.8.3. Photoemission Yield Spectrometer (AC3) and $E_{0,0}$ Measurements

The experimental HOMO and $E_{0,0}$ energy values for MH01, MH02, MH05 and **N719** were measured using a photoemission yield spectrometer and the experimental

absorption/emission spectra point of overlap, respectively, and the procedure was described in detail elsewhere [4]. Figures 10S-13S show the HOMO energies of MH01, MH03, MH-05 and N719, respectively.

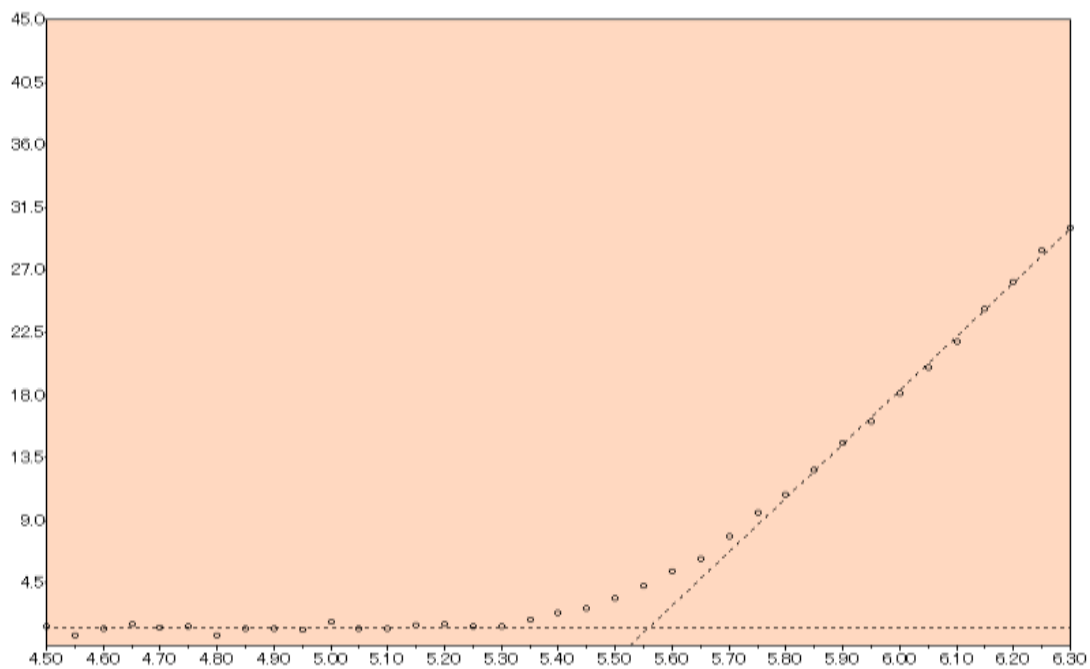


Figure 10S HOMO energy (-5.52eV) of MH01.

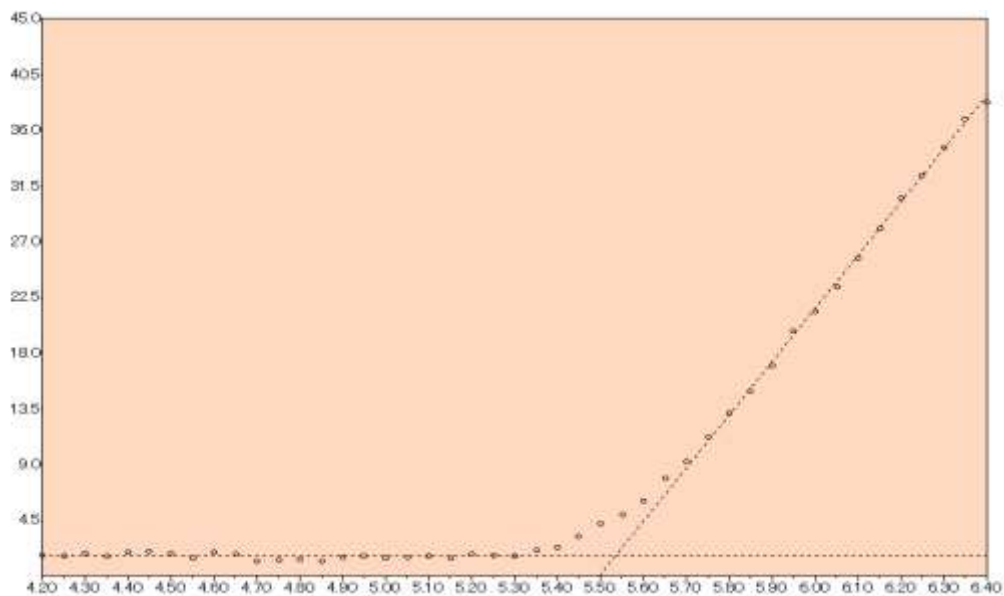


Figure 11S HOMO energy (-5.50eV) of MH03.

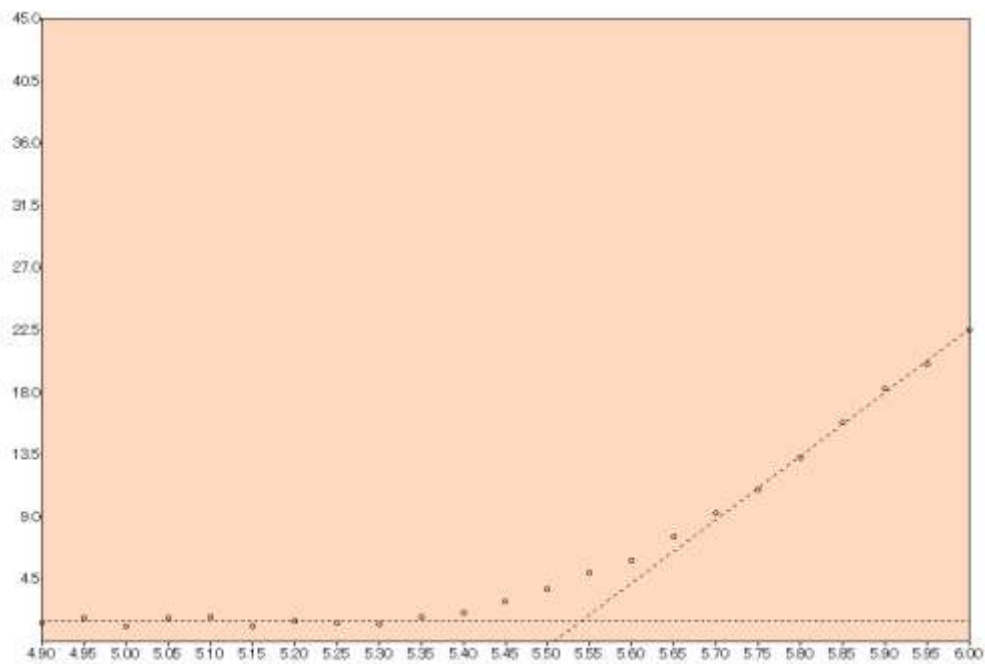


Figure 12S HOMO energy (-5.51eV) of MH05.

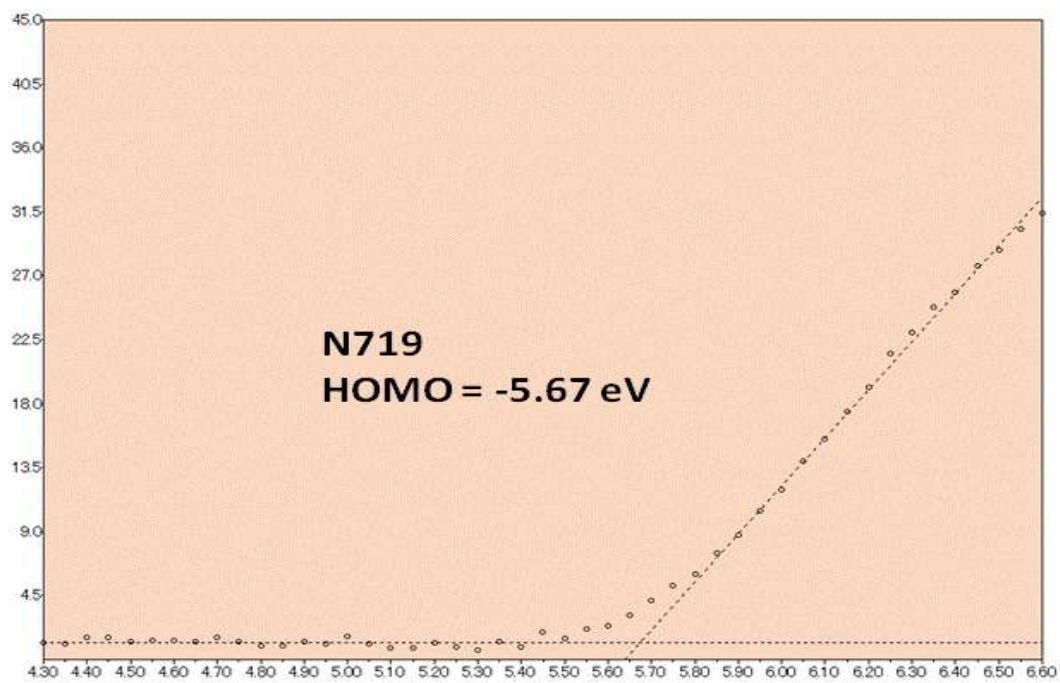


Figure 13S HOMO energy (**-5.67eV**) of N719.

1.2.8.4. Electrochemical impedance spectroscopy (EIS) and intensitymodulated photovoltage spectroscopy (IMVS) measurements

The IMVS spectra were measured with a potentiostat (Solartron1287) equipped with a frequency response analyzer (Solartron1255B) at an open-circuit condition, based on a monochromatic illumination (420 nm) controlled by Labview system, to obtain the photovoltaic response induced by the modulated light. The modulated light was driven with a 10% AC perturbation current superimposed on a DC current in a frequency range from 0.1 to 10^6 Hz. The charge extraction method (CEM) was performed with the same monochromatic light source. The solar cell was illuminated at an open-circuit condition for 5 s to attain a

steady state and then the light source was switched off when the device simultaneously switched to a short-circuit condition to extract the charges generated at that light intensity. The electrochemical impedance spectra were measured with an impedance analyzer (Solartron Analytical, 1255B) connected with a potentiostat (Solartron Analytical, 1287) under illumination using a solar simulator (WXS-155S-10: Wacom Denso Co. Japan). EIS spectra were recorded over a frequency range of 10^2 to 10^6 Hz at 298 K. The applied bias voltage and AC amplitude were set at the V_{oc} of the DSCs. The applied bias voltage and AC amplitude were set at the V_{oc} of the DSCs. The electrical impedance spectra were characterized using Z-View software (Solartron Analytical).

1.2.9. Synthesis

1.2.9.1 Ligands

1.2.9.1.1 4,4'-Bis-(2-benzo[1,3]dioxol-5-yl-vinyl)-[2,2']bipyridinyl

A 100 ml pressure tube was charged with a magnetic stirrer bar, 100 mL of anhydrous DMF, 4,4'-dimethyl-2,2'- bipyridine (1.000g, 5.428×10^{-3} mol) and Benzo[1,3]dioxole-5-carbaldehyde (1.712g, 1.085×10^{-2} mol, 5% excess was used to drive the reaction to completion), and three equivalent of $\text{Si}(\text{CH}_3)_3\text{Cl}$. The reaction temperature was raised to 100 °C and allowed to run for 48 hours with continuous stirring. At the end of the reaction, the solvent was removed using rotary evaporator, and the product was recovered by addition of

water and filtration under vacuum to furnish the antenna ligand in 91% yield, which was used for the next step after washing with toluene.

1.2.9.1.2 4,4'-Bis-[2-(6-methoxy-benzo[1,3]dioxol-5-yl)-vinyl]-[2,2']bipyridinyl

The title ligand was synthesized in 92% yield the procedure described above in 1.2.9.1.1.

1.2.9.1.3 4,4'-Bis-[2-(3,4,5-trimethoxy-phenyl)-vinyl]-[2,2']bipyridinyl

The title ligand was synthesized in 90% yield according the procedure described above in 1.2.9.1.1.

1.2.9.2 Synthesis of 2, 2'-Bipyridinyl-4, 4'-dicarboxylic acid

2, 2'-Bipyridinyl-4, 4'-dicarboxylic acid was synthesized in 93% yield according to a previously reported procedure [5]

1.2.9.3 Synthesis of complexes MH01, MH01-TBA, MH03 and MH05

1.2.9.3.1 Synthesis of MH01, modified from Graetzel Method

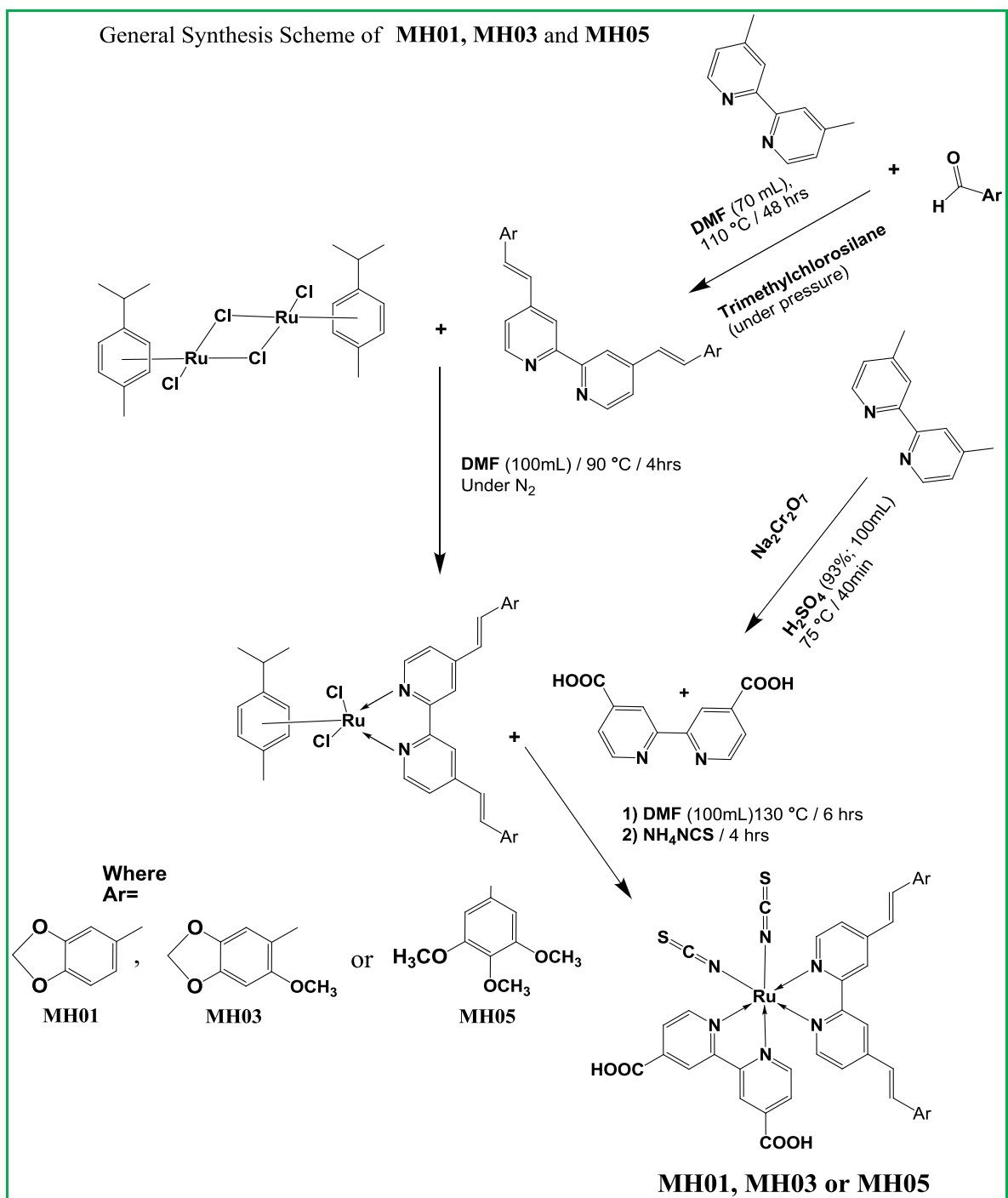
The synthesis of **MH01** was carried out in a one-pot three-step reaction. The reactions were carried out in a 250 ml reaction flask equipped with a condenser and magnetic stirrer bar under Argon. The flask was charged with anhydrous DMF (100mL), dichloro-(*p*-cymene)-ruthenium (II) dimer (0.30g, 4.899×10^{-4} mol) and 4,4'-Bis-(2-benzo[1,3]dioxol-5-yl-vinyl)-[2,2']bipyridinyl (0.435 g, 9.797×10^{-4} mol). The reaction mixture was stirred at 90 °C for

4h. Then, 2,2'-bipyridyl-4,4'-dicarboxylic acid was added (0.239 g, 9.797×10^{-4} mol) and the temperature was raised to 130°C and allowed to run for 6 hours. After the 6 hours, excess of NH₄NCS (0.5g) was added to the reaction mixture, and the reaction mixture was allowed to run for another 4h at 130°C. The last two steps of the reaction were monitored for completion by taking aliquots from the reaction mixture every 60 minutes and measuring its absorption spectrum until there was no increase in the absorbance of the MLCT peaks with respect to the π - π^* peak. The reaction mixture was cooled down to room temperature and DMF was removed using a rotary evaporator. Water was added to the flask, and the insoluble solid were vacuum filtered and washed with de-ionized water and ether. The product was dried overnight to give the crude product in 94% yield, with respect to the starting material.

Synthesis of MH01-TBA

MH01-TBA was synthesized by adding MH01 (0.1g) to 20 mL of H₂O/MeOH (11:9) and tetrabutylammonium hydroxide (0.0285g), and the pH of the solution was kept at 9. To this solution, 0.1g of tetrabutylammonium thiocyanate was added. The resulting solution was filtered to remove any insoluble material, and the pH was adjusted to 4.0 using dilute HCl. A dense precipitate formed immediately and the suspension was concentrated to 10 mL. The solution was filtered using a sintered glass crucible, and the precipitate was dried under vacuum to yield tetrabutylammonium salt, MH01-TBA, which was confirmed using ¹H-NMR.

Complexes MH01, MH03, and MH05 were synthesized according the above procedure in 93%, 95%, 95% and 91% yield, respectively. Scheme 1 summarizes the general synthetic route for complexes MH01, MH03 and MH05.



Scheme 1 General route for the synthesis of complexes MH01, MH03 and MH05.

1.2.10 Purification

MH01 was purified on a column using Sephadex LH-20 as the stationary phase and pure methanol as the mobile phase. The crude dye of MH01 was dissolved in a mixture of methanol and TBAOH and loaded on Sephadex LH-20, and the compound was eluted using methanol neat. The main band was collected and acidified using 0.1M HCl until the pH dropped to 2.0, and the acidified solution was kept in a refrigerator for 48 hours. Then, the precipitate was filtered, washed with plenty of de-ionized water to remove remaining HCl. The same purification procedure was repeated three times in order to obtain MH01 in the pure form. Complexes MH03 and MH05 was purified using the above procedure.

1.2.11 Molecular Modeling

Equilibrium molecular geometries of MH01, MH03, and MH05 were calculated using the energy functional 3-Parameter (Exchange), Lee, Yang and Parr (B3LYP) [6,7] and the full-electron basis set Density Gauss double-zeta with polarization functions (DGDZVP) [8,9]. The geometry optimization calculations were followed by energy calculations using TD-DFT utilizing the energy functional B3LYP and the basis set DGDZVP. The solvent (DMF) effect was accounted for by using the polarizable continuum model (PCM), implemented in Gaussian 09, and the ground and excited states oxidation potentials were calculated. All DFT and TD-DFT jobs were submitted remotely at East Carolina University's Supercomputer Jasta.

REFERENCES

1. P. Wang, S. M. Zakeeruddin, P. Comte, R. Charvet, R. Humphry-Baker, M. Grätzel, M. J. *Phys. Chem. B* **2003**, 107, 14336-14341.
2. Z. Wang, T. Yamaguchi, H. Sugihara, H. Arkawa, *Langmuir*, 2033, 21, 4272-4276.
3. A. Islam, F. A. Chowdhury, Y. Chiba, R. Komiya, N. Fuke, N. Ikeda, K. Nozaki, L. Han, *Chem. Mater.* **2006**, 18, 5178-5185.
4. A. Islam, H. Sugihara, H. Hara, L. P. Singh, R. Katoh, M. Yanagida, Y. Takahashi, S. Murata, S., H. Arakawa, *Inorg. Chem.* **2001**, 40 5371–5380.
5. N. Garelli, P. Vierling, *J. Org. Chem.* **1992**, 57, 3046-3051.
6. Becke, A. D., *Phys. Rev. A* **1988**, 38, 3098.
7. Lee, C. T., Yang, W. T., Parr, R. G., *Phys. Rev. B* **1988**, 37, 785
8. Godbout, N., Salahub, D. R., Andzelm, J., and Wimmer, E., *Can. J. Chem.*, **70** (1992) 560.
9. Sosa, C., Andzelm, J., Elkin, B. C., Wimmer, E., Dobbs, K. D., and Dixon, D. A., *J. Phys. Chem.*, **96** (1992) 6630.

CHAPTER 5

RESEARCH ARTICLE

Structure–property relationship of hetero-aromatic-electron-donor antennas of polypyridyl Ru (II) complexes for high efficiency dye-sensitized solar cells

Ahmed El-Shafei^{1*}, Maqbool Hussain¹, Ashraful Islam² and Liyuan Han²¹ Polymer and Color Chemistry Program, North Carolina State University, Raleigh, NC 27695, USA² Photovoltaic Materials Unit, National Institute for Materials Science, 1-2-1 Sengen, Tsukuba, Ibaraki 305-0047, Japan

ABSTRACT

Three novel heteroleptic amphiphilic polypyridyl Ru-complexes, coded **MH08–10**, with hetero-aromatic electron-donor ancillary ligands containing N-benzylcarbazole (**MH08**), dibenzofurane (**MH09**) and benzothiophene moieties (**MH10**) were synthesized to study the influence of different heterocyclic electron donors on the interrelationship of photophysical and electrochemical properties, and device performances for dye-sensitized solar cells (DSSCs). **MH08** showed a remarkably high molar extinction coefficient of $27,650 \text{ M}^{-1}\text{cm}^{-1}$. **MH08–TBA** was synthesized from **MH08** by converted one COOH group into $-\text{COO}^{-}\text{N}(\text{C}_4\text{H}_9)_4$ to investigate the effect of deprotonating one carboxylic group on the Fermi level and electron injection. When compared under the same experimental device conditions using 0.3M t-butylpyridine (TBP), the short-circuit photocurrent density (J_{SC}) and total conversion efficiency ($\% \eta$) of **MH08–10** were **MH08**>**MH09**>**MH10**. The differences in $\% \eta$ and J_{SC} of **MH08–10** were ascribed to the conjugation length coupled with the electron donation and hole-transport strength of the ancillary ligands, which were in the following order N-benzylcarbazole>dibenzofurane>benzothiophene. Moreover, **MH08–TBA** showed J_{SC} of 19.56 mAcm^{-2} and $\% \eta$ of 9.76% compared to 17.16 mAcm^{-2} and 9.12% of the benchmark dye **N719**. The superior performance of **MH08–TBA** was attributed to its better light harvesting and enhanced incident-photon-to-current efficiency (IPCE) conversion. DFT/TD-DFT calculations utilizing the energy functional B3LYP and the full-electron basis set DGDZVP were performed to calculate HOMO and LUMO energies, vertical electronic excitations, lowest singlet-singlet electronic transitions ($E_{0,0}$), and excited state oxidation potentials. Excellent agreement was found between the experimental results and calculated data. Copyright © 2013 John Wiley & Sons, Ltd.

Supporting information may be found in the online version of this article.

KEYWORDS

dye solar cells; efficiency; photocurrent; photovoltage; ground state oxidation potential

*Correspondence

Ahmed El-Shafei, Polymer and Color Chemistry Program, North Carolina State University, Raleigh, NC, 27695, USA.

E-mail: Ahmed_El-Shafei@ncsu.edu

Received 13 August 2012; Revised 10 October 2012; Accepted 19 November 2012

1. INTRODUCTION

Dye-sensitized solar cells (DSSCs) based on polypyridyl Ru (II) complexes have received considerable interest in industry and academia due to their exceptional photophysical and unique and strong charge transfer (MLCT) properties, low cost production and high efficiency [1–21]. DSSCs were first demonstrated by O'Regan and Grätzel in 1991 [22]. It was not until the year 2005 that Grätzel *et al.* showed a breakthrough record in total efficiency using **N719** [23]. **N719**, however, lacks absorption in the red and near-infra red (NIR) regions,

and exhibits weak incident-photon-to-current conversion efficiency (IPCE) in the range 350–450 nm with a sharp drop at 380 nm [24], induced by competitive light absorption by triiodide anions [20,24–27], owing to the higher molar extinction coefficient of triiodide. The energy gap between the ground state oxidation potential of **N719** (–5.79 eV) [24] and redox potential of the electrolyte (–5.20 eV) [28] is about 0.6 eV, as shown in Figure 1, which is a greater driving force than needed to drive the reaction to completion between the electrolyte and oxidized dye to regenerate the neutral dye [29]. This large energy gap leads to a significant energy loss of

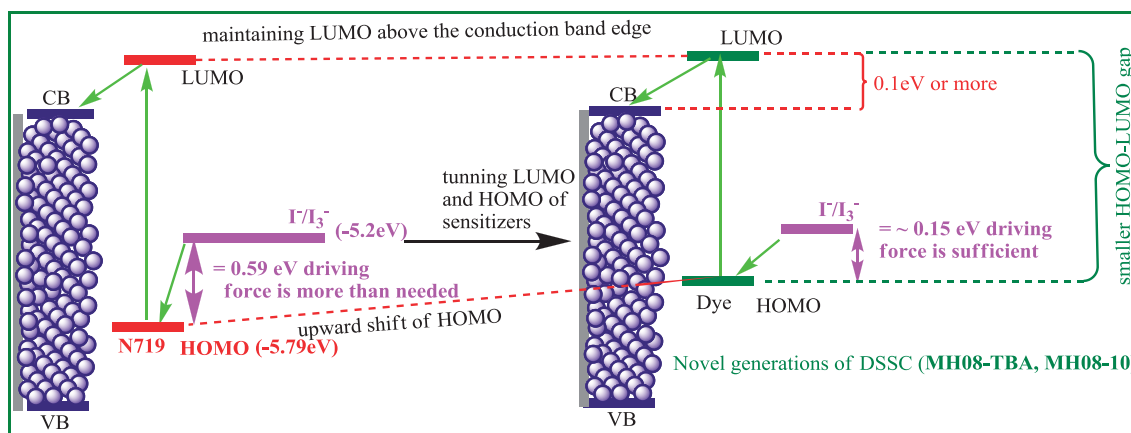


Figure 1. Tuning highest occupied molecular orbital/lowest unoccupied molecular orbital gap of MH08–MH10 for high efficiency dye-sensitized solar cells.

~0.45 eV as only ~0.15 eV energy gap is needed as a driving force for the regeneration of the neutral dye.

Although work was performed on functionalizing bipyridyl with different ancillary ligands [30–48], to increase the light harvesting efficiency (LHE) of N719 congeners, no work was reported that shows the unique molecular engineering that furnishes the delocalization of highest occupied molecular orbital (HOMO) on the electron donor segment of the ancillary ligand.

In the present study, we report the synthesis, photophysics, molecular modeling and photovoltaic performance of

three novel amphiphilic polypyridyl Ru (II) complexes coded **MH08–MH10** (Figure 2), compared with the champion dye **N719** under the same experimental conditions. The amphiphilic ancillary ligands of **MH08–MH10** were designed with different conjugation lengths and electron donation strengths, to systematically study the interrelationship between the molecular structures of the ancillary ligands, molar extinction coefficient, HOMO–LUMO energy gap, delocalization of the HOMOs on the ancillary ligand, photophysical properties and photovoltaic performance. The ancillary ligands of **MH08–MH10** were based

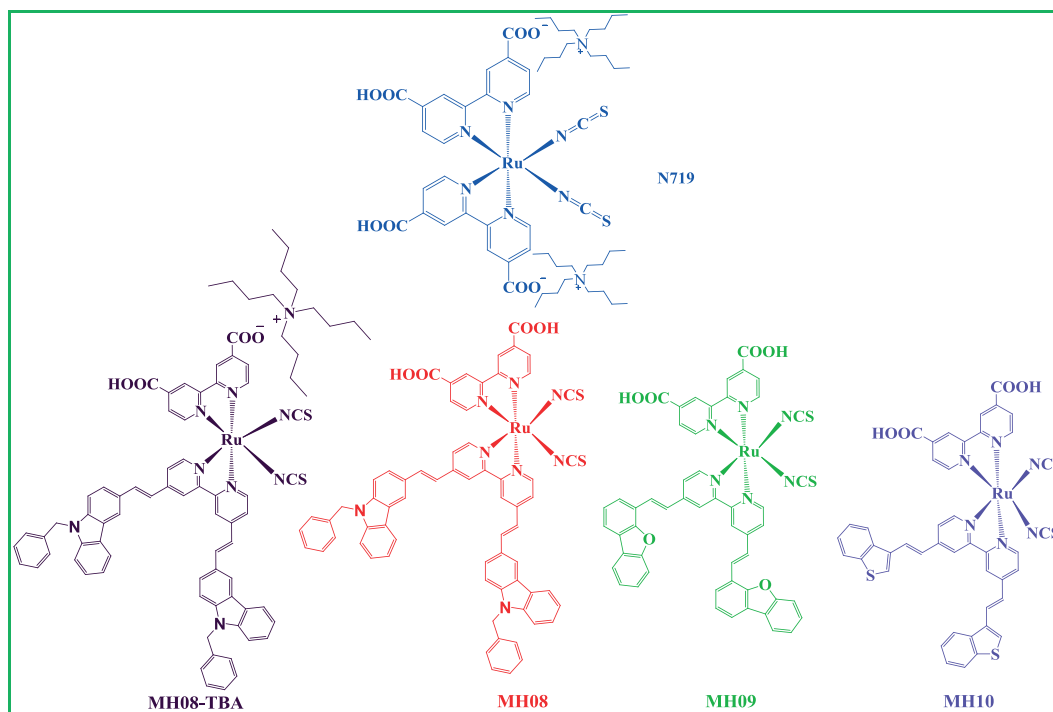


Figure 2. Molecular structures of dyes MH08-TBA, MH08–MH10 and N719.

on N-benzylcarbazole, dibenzofurane, and benzothiophene, respectively. Although the conjugation length of the ancillary ligands of carbazole and dibenzofurane is the same, they are longer than that of benzothiophene. Moreover, N-benzylcarbazole is a stronger electron donor moiety than dibenzofurane. **MH08-TBA** was synthesized to study the influence of one carboxylic proton on the J_{SC} and total conversion efficiency.

The **MH08-MH10** exhibited significantly higher molar extinction coefficient for both high and low energy MLCT peaks than that of **N719**, with **MH08** exhibiting remarkably high molar extinction coefficients of 64,200 and 27,650 $M^{-1} cm^{-1}$ for the high and low energy MLCT, respectively. The enhanced red shift and molar absorptivity of **MH08-MH10** increased their LHE across a wider range of the solar spectrum, which translated into higher J_{SC} ($mAcm^{-2}$). Moreover, we are showing for the first time that linking N-benzylcarbazole to bipyridyl through $CH=CH$ significantly impacts the delocalization of the HOMO and extends the HOMO delocalization to the carbazole with large coefficient, resulting in more intense and broad peak of the high energy MLCT.

2. EXPERIMENTAL SECTION

2.1. Materials

The solvents and chemicals were either purchased from Sigma-Aldrich, Fisher Scientific or TCI-America and used as received. Sephadex LH-20 was purchased from Fisher Scientific.

2.2. Ultraviolet-visible Spectra absorption and fluorescence spectra

Ultraviolet-visible spectra were recorded in a 1 cm path length quartz cell on a Cary 3 Spectrophotometer (Agilent Technologies, Santa Clara, CA, USA). A dimethylformamide (anhydrous) solution of each complex of $2 \times 10^{-5} M$ was prepared, the absorbance was measured, and extinction coefficient was calculated for each dye.

Fluorescence and emission decay were measured in a 1 cm path length quartz cell using $2 \times 10^{-5} M$ solutions (DMF) on a FluoroLog-3 spectrofluorometer (Jobin Yvon). The emitted light was detected in the steady state mode using Hamamatsu R2658 detector (Horiba Jobin Yvon Inc, Edison, NJ, USA). The emission was measured in the steady state mode by exciting at the λ_{max} (lower energy MLCT band) for each dye with exit and entrance slits set at 10 nm. The time-correlated single photon counting (TCSPC) lifetime was measured using a pulse laser (460 nm, NanoLED) at 1 MHz repetition rate for a duration of 1.3 ns, and time of arrival of the photon counting range was adjusted to 200 ns and the channel range to 1000–3500 nm to accrue the emission decay, and the data were analyzed using DAS6 software from Jobin Yvon.

2.3. Fourier transform-infrared spectroscopy

Attenuated total reflectance-Fourier transform infrared (ATR/FT-IR) spectra were recorded on a Thermo Nicolet, Nexus 470 FTIR Spectrophotometer with OMNIC 7.2 software (Thermo Fisher Scientific, Madison, WI, USA). The compound under investigation was placed in its powder form on a germanium crystal, and a pressure probe was placed in position to apply consistent pressure on the sample. An average of 32 scans was used at a resolution of $4 cm^{-1}$. The complexes were characterized using the same parameters. Figures S2, S3, and S4 of the electronic supplementary information (ESI) show the FT-IR of **MH08-MH10** in the pure form, respectively.

MH08: 2101 cm^{-1} (-NCS stretch, N-bonded isomer, very strong); 1723 cm^{-1} (C=O stretch of -COOH)

MH09: 2101 cm^{-1} (-NCS stretch, N-bonded isomer, very strong); 1720 cm^{-1} (C=O stretch of -COOH)

MH10: 2101 cm^{-1} (-NCS stretch, N-bonded isomer, very strong); 1718 cm^{-1} (C=O stretch of -COOH)

2.4. Mass spectrometry

Electrospray ionization mass spectrometry was recorded on an Agilent Technologies (Sta. Clara, CA, USA) 6210 LC-TOF mass spectrometer in the negative ion mode. The sample was prepared in methanol in the presence of a small amount of tetrabutylammonium hydroxide. The fragmenter voltage was set at 220.0 V, and results from 63 scans in the case of **MH08**, 29 scans in the case of **MH09**, and 14 scans for **MH10** were averaged. Figures S5–S7 of the ESI show the ESI-MS of **MH08**, **MH09**, and **MH10** with one TBA per molecule, singly charged, respectively. The ESI-MS patterns shown in Figures S5–S7 (ESI) are the pattern of ruthenium isotopes.

2.5. Proton nuclear magnetic resonance experiments

Proton nuclear magnetic resonance (1H -NMR) experiments were recorded on a Bruker 500 MHz spectrometer (Bruker Corp., Billerica, MA, USA) at 40 °C using deuterated DMSO- d_6 as a solvent. Splitting patterns reported here are: s (singlet), d (doublet), dd, (doublet-of-doublet), t (triplet), p (pentet), and m (multiplet). Chemical shifts (δ) and coupling constants (J) are reported in ppm and Hertz (Hz), respectively. The aliphatic range 0–5 ppm is not shown for brevity. Figures S8–S10 (ESI) show the 1H -NMR for **MH08**, **MH09**, and **MH10**, respectively.

1H -NMR, **MH08** (500 MHz, DMSO, 40 °C): δ/ppm 5.68 (2s, 4H, 2CH₂), 7.19 (d, 2H, $J=7.1$ Hz) and 7.27 (d, 2H, $J_{trans}=16.6$ Hz, CH=CH), 7.21–7.56 (m, 10H, ArH), 7.60–8.00 (m, 14H, ArH), 8.00–8.3 (m, 6H, ArH), 8.29 (d, 2H, $J=7.6$ Hz, ArH), 8.63 (s, 2H, ArH), 9.16 (d, 2H, $J=5.95$ Hz, ArH).

¹H-NMR, MH09 (500 MHz, DMSO, 40 °C): δ /ppm 7.44 (d, 2H, $J=7.40$ Hz and 7.70 (d, 2H, $J_{\text{trans}}=16.4$ Hz, CH=CH), 7.47 (t, 2H, $J=3.6, 4.7$ Hz, ArH), 7.57 (t, 2H, $J=7.5, 7.6$ Hz, ArH), 7.80 (t, 2H, $J=8.4, 8.0$ Hz, ArH), 7.86–8.02 (m, 10H, ArH), 8.12–8.28 (m, 6H, ArH), 8.90 (s, 2H, ArH), 9.24 (d, 2H, $J=5.95$ Hz, ArH).

¹H-NMR, MH10 (500 MHz, DMSO, 40 °C): δ /ppm 7.40 (s, 2H, ArH), 7.47 (t, 4H, $J=7.8, 7.1$ Hz, ArH), 7.50–7.68 (m, 6H ArH, CH=CH), 7.90 (d, 2H, $J=5.6$ Hz, ArH), 8.05 (d, 2H, $J=8.2$ Hz, ArH) 8.12 (d, 2H, $J=8.0$ Hz, ArH), 8.35 (s, 2H, ArH), 8.2 (d, 2H, $J=8.0$ Hz, ArH), 8.95 (s, 2H, ArH), 9.19 (d, 2H, $J=5.90$ Hz, ArH).

2.6. TiO₂ electrode preparation

A double-layer TiO₂ photoelectrode (10 + 5 μm in thickness) with a 10- μm thick nanoporous layer and a 5- μm thick scattering layer (area: 0.25 cm²) were prepared using a reported method [49]. Fluorine doped tin oxide-coated glass electrodes (Nippon Sheet Glass Co., Japan), with a sheet resistance of 8–10 Ω^{-2} and an optical transmission of greater than 80% in the visible range, were screen printed using anatase TiO₂ colloids (particle size ~13 nm) obtained from commercial sources (Ti-Nanoxide D/SP, Solaronix). Nanocrystalline TiO₂ thin films were deposited onto the conducting glass by screen-printing, which was then sintered at 500 °C for 1 h. The film thickness was measured with a Surfcom 1400A surface profiler (Tokyo Seimitsu Co. Ltd., Japan). The electrodes were impregnated with a 0.05 M titanium tetrachloride solution and sintered at 500 °C. The films were further treated with 0.1 M HCl aqueous solutions before examination [50]. The dye solutions (2 $\times 10^{-4}$ M) were prepared in 1 : 1 : 1 acetonitrile, *tert*-butyl alcohol and DMSO. Deoxycholic acid was added to the dye solution as a coadsorbent at a concentration of 20 mM. The electrodes were immersed in the dye solutions and then kept at 25 °C for 20 h to adsorb the dye onto the TiO₂ surface.

2.7. Fabrication of dye-sensitized solar cell

Photovoltaic and IPCE measurements were made on sandwich cells, which were prepared using TiO₂ coated working electrodes and platinum coated counter electrodes, and were sealed using a 40 μm Surlyn spacer through heating of the polymer frame. The redox electrolyte consisted of a solution of 0.6 M DMPII, 0.05 M I₂, 0.1 M LiI and 0.3–0.5 M TBP in acetonitrile.

2.8. Photoelectrochemical measurements

Photovoltaic measurements of sealed cells were made by illuminating the cell through the conducting glass from the anode side with a solar simulator (WXS-155S-10) at AM 1.5 illuminations (light intensities: 100 mW cm⁻²).

2.9. Incident photon to current efficiency conversion

Incident photon to current efficiency measurements were made on a CEP-2000 system (Bunkoh-Keiki Co. Ltd.,

Tokyo, Japan). IPCE at each wavelength was calculated using Equation (1), where I_{SC} is the short-circuit photocurrent density (mA cm⁻²) under monochromatic irradiation, q is the elementary charge, λ is the wavelength of incident radiation in nm and P_0 is the incident radiative flux in W m⁻² [51].

$$IPCE(\lambda) = 1240 \left(\frac{I_{\text{SC}}}{qP_0} \right) \quad (1)$$

The IPCE conversion was plotted as a function of wavelength.

2.10. Photoemission yield spectrometer (AC3) and E₀₋₀ measurements

The experimental HOMO and E₀₋₀ energy values for MH08–MH10 and N719 were measured using a photoemission yield spectrometer and the experimental absorption/emission spectra point of overlap, respectively, and the procedure was described in detail elsewhere [52]. Figures S11–S14 (ESI) show the HOMO energies of MH08, MH09, MH10 and N719, respectively.

2.11. Synthesis

2.11.1. Ligands: 4,4'-bis-(4-benzyl-9H-carbazole) [2,2']bi-pyridinyl

A 100 ml pressure tube was charged with a magnetic stirrer bar, 100 mL of anhydrous DMF, 4,4'-dimethyl-2,2'-bipyridine (1.000 g, 5.428 $\times 10^{-3}$ mol) and 9-benzyl-9H-carbazole-3-carbaldehyde (3.255 g, 1.085 $\times 10^{-2}$ mol, 5% excess was used to drive the reaction to completion), and three equivalent of (CH₃)₃SiCl. The reaction temperature was raised to 100 °C and allowed to run for 48 h with continuous stirring. At the end of the reaction, the solvent was removed using rotary evaporator, and the product was recovered by addition of water and filtration under vacuum to furnish the antenna ligand in 93% yield, which was used for the next step after washing with toluene.

4,4'-bis-(2-dibenzofuran-4-yl-vinyl)-[2,2']bipyridinyl and 4,4'-bis-(2-benzo[b]thiophen-3-yl-vinyl)-2,2'-bipyridinyl were synthesized according to the same procedure reported above.

2.11.2. Synthesis of 2, 2'-bipyridinyl-4, 4'-dicarboxylic acid

2,2'-Bipyridinyl-4,4'-dicarboxylic acid was synthesized in 93% yield according to a previously reported procedure [53].

2.11.3. Synthesis of complexes MH08–MH10

2.11.3.1. Synthesis of MH08. The synthesis of MH08 was carried out in a one-pot three-step reaction. The reactions were carried out in a 250 ml reaction flask equipped with a condenser and magnetic stirrer bar under Argon. The flask was charged with anhydrous DMF (100 mL), dichloro-(*p*-cymene)-ruthenium (II) dimer (0.30 g, 4.899 $\times 10^{-4}$ mol) and 4,4'-bis-(4-benzyl-9H-carbazole)-2,2'-bipyridinyl (0.704 g, 9.797 $\times 10^{-4}$ mol). The reaction mixture

was stirred at 90 °C for 4 h. Then, 2,2'-bipyridyl-4,4'-dicarboxylic acid was added (0.239 g, 9.797×10^{-4} mol), and the temperature was raised to 130 °C and allowed to run for 6 h. After 6 h, excess of NH_4NCS (0.5 g) was added to the reaction mixture, and the reaction mixture was allowed to run for another 4 h at 130 °C. The last two steps of the reaction were monitored for completion by taking aliquots from the reaction mixture every 60 min and measuring its absorption spectrum until there was no increase in the absorbance of the MLCT peaks with respect to the $\pi\text{-}\pi^*$ peak. The reaction mixture was cooled down to room temperature and DMF was removed using a rotary evaporator. Water was added to the flask, and the insoluble solid was vacuum filtered and washed with deionized water and ether. The product was dried overnight to give the crude product in 92% yield, with respect to the starting material.

Complexes **MH09** and **MH10** were synthesized according to the previously described procedure in 94% and 91% yield, respectively. Scheme 1 (ESI) summarizes the general synthetic route for complexes **MH08–MH10**.

2.12. Molecular modeling. Equilibrium molecular geometries of **MH08–MH10** and **N719** were calculated using the energy functional 3-parameter (Exchange), Lee, Yang and Parr (B3LYP) [54,55] and the full-electron basis set density Gauss double-zeta with polarization functions (DGDZVP) [56,57]. The geometry optimization calculations were followed by energy calculations using time-dependent density functional theory (TD-DFT) utilizing the energy functional B3LYP and the basis set DGDZVP. The solvent (DMF) effect was accounted for by using the polarizable conductor calculation model (PCM), implemented in Gaussian 09, and the ground and excited states oxidation potentials were calculated. All DFT and TD-DFT jobs were submitted remotely at East Carolina University's Supercomputer Jasta.

3. RESULTS AND DISCUSSION

3.1. Ultraviolet-visible absorption

The photophysical properties were studied using ultraviolet-visible (UV-vis), emission and emission decay

spectrophotometry. Figure 3 shows a comparison between the absorption and emission spectra of **N719** and **MH08–MH10**, measured under the same experimental conditions in dimethylformamide (DMF) (2×10^{-5} M). The spectrophotometric properties are summarized in Table I. **MH08** showed two intense absorption peaks in the visible region at 396 ($64,200 \text{ M}^{-1} \text{ cm}^{-1}$) and 545 nm ($27,650 \text{ M}^{-1} \text{ cm}^{-1}$), but **MH09** showed two low molar extinction MLCT peaks at 432 nm ($17,400 \text{ M}^{-1} \text{ cm}^{-1}$) and 548 nm ($19,650 \text{ M}^{-1} \text{ cm}^{-1}$).

In the case of **MH10**, the two MLCT peaks were observed at 364 and 545 nm with the extinction coefficient 39,300 and $19,600 \text{ M}^{-1} \text{ cm}^{-1}$, respectively. Among these dyes, the two MLCT peaks of **MH09** exhibited the lowest extinction coefficient, possibly because of the higher electron negativity of oxygen of dibenzofurane. Moreover, the low energy MLCT peaks of **MH08–MH10** are red shifted by 15–18 nm compared with that of **N719**, indicating better light harvesting. However, the high energy MLCT peak of **MH10** was hypsochromically shifted (364 nm), and the extinction coefficients of the high and low energy peaks of **MH08–MH10** are considerably greater than those of **N719**, with **MH08** being the highest. In addition, emission spectra demonstrated that incorporation of strong electron-donor hetero-aromatic antennas of carbazole-analog (**MH08**) or dibenzofurane-analog (**MH09**) furnished emission spectra that are significantly stronger and more red shifted than that of **N719**. The emission decay lifetime, measured using time-correlated single photon counting (TCSPC) in DMF, showed that the lowest-excited state lifetime of **MH08**, **MH09**, **MH10**, and **N719** are 9, 105, 86, and 78 ns, respectively, Figure S1 (ESI).

Figure 4 shows a comparison of the absorption spectra of **MH08–MH10** adsorbed on nanoporous TiO_2 . Comparison of the absorption spectra in the solid state and in solution revealed that the two spectra have similar patterns. However, the absorption spectrum on the TiO_2 electrode is broader for both high and low energy MLCTs, but slightly blue-shifted for the low energy MLCT compared with those in solution. The shift to higher energy can be attributed to a perturbation in the energy levels of the ground and excited states of the dyes in the solid state compared with that in solution, resulting from the interaction between the dye and the TiO_2 electrode. The broadening of the high and low energy MLCT

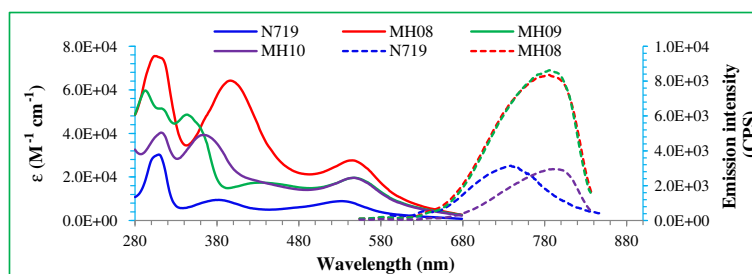


Figure 3. Ultraviolet-visible absorption (solid-line) and emission spectra (dashed-line) of complexes **MH08–MH10** compared with **N719**, measured in DMF (2×10^{-5} M).

Table I. Absorption, luminescence properties for MH08–MH10 and N719.

Sensitizer	Expt. ¹ absorption spectrum (2×10^{-5} mole)		Emission ² at 298 K	Emission ³ decays
	λ_{\max} (nm)	ϵ ($M^{-1} \text{ cm}^{-1}$)	λ_{em} (nm)	(ns)
MH08	396; 545 (d \rightarrow π^*)	64,200; 27,650	786	9
MH09	432; 548 (d \rightarrow π^*)	17,400; 19,650	784	105
MH10	364; 547 (d \rightarrow π^*)	39,300; 19,600	792	85
N-719	381; 530 (d \rightarrow π^*)	14,400; 14,200	746	78

¹Measured in DMF (2×10^{-5} M) at room temperature.

²The emission spectra were obtained by exciting at the lowest MLCT band in DMF.

³Measured at room temperature in DMF using time-correlated single photon counting experiment.

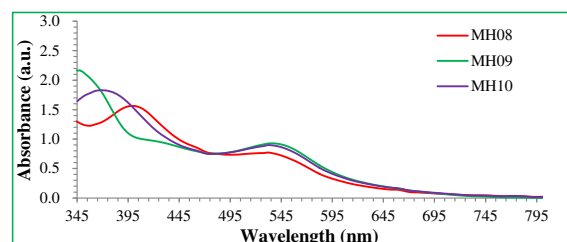


Figure 4. Absorption spectra of MH08–MH10 adsorbed on nanoporous TiO₂.

peaks is desirable for harvesting more photons across a wider range of the solar spectrum, which leads to greater photocurrent.

3.2. Electrochemical data

The ionization potential (IP) of MH08–MH10 and N719 bound to nanocrystalline TiO₂ film was measured using a photoemission yield spectrometer (Riken Keiki AC-3E), and the results are given in Table II. Typical photoemission yield spectra for complexes MH08–MH10 on TiO₂ are shown in the ESI. The experimental IP values for MH08–MH10 were -5.34 , -5.40 , and 5.50 eV, respectively. The energy difference between the Ru^{3+/2+} potential (IP) of dyes MH08–MH10 and the I₃⁻/I⁻ redox couple (-5.20 eV) [28] was large enough for efficient regeneration of the neutral dye

through reduction of the oxidized dye with iodide. The excited state oxidation potential $\{E^*(\text{Ru}^{3+/2+})\}$ values were estimated using Equation (2), where $E(\text{Ru}^{3+/2+})$ is the oxidation potential of the ground state and E_{0-0} is the energy difference between the lowest excited and ground states. The resulting $E^*(\text{Ru}^{3+/2+})$ values are shown in Table II. The experimental excited-state oxidation potentials $E^*(\text{Ru}^{3+/2+})$ of sensitizers MH08–MH10 were -3.42 , -3.47 and -3.63 eV, respectively, which lay above the conduction band edge (-4.2 eV) [58] of nanocrystalline TiO₂. These $E^*(\text{Ru}^{3+/2+})$ values of MH08–MH10 suggested that the efficiency of electron injection and charge separation from the excited state into the CB edge of TiO₂ is in the following order: MH08 > MH09 > MH10 because of the more negative free energy of MH08 > MH09 > MH10.

$$E^*(\text{Ru}^{3+/2+}) = E(\text{Ru}^{3+/2+}) - E_{0-0} \quad (2)$$

3.3. Density functional theory/Time-dependent density functional theory calculations

Following geometry optimization and vertical electronic excitation calculations, the ground and excited state oxidation potentials were calculated. Table II shows the calculated HOMO, the excited state oxidation potential $E^*(\text{Ru}^{3+/2+})$ and the lowest singlet–singlet electronic transitions (E_{0-0}) for MH08–MH10 compared with N719, which are in excellent agreement with the corresponding experimental values.

Table II. Calculated and experimental ground and excited states energy levels for TiO₂, MH08–MH10 and N719.

Compound	Calculated energy (eV), TD-DFT (B3LYP/DGDZVP)			Experimental (eV)		
	E_{HOMO}	$\text{ESOP}_{\text{singlet}}$	$E_{0-0} = (S_0-S_1)$	* E_{0-0}	**IP (HOMO)	$E^*(\text{Ru}^{3+/2+})$
MH08	-5.440	-3.562	1.8774	* 1.918	-5.34	-3.42
MH09	-5.490	-3.564	1.926	* 1.930	-5.40	-3.47
MH10	-5.480	-3.565	1.915	* 1.866	-5.50	-3.63
N719	-5.490	-3.490	2.000	* 1.990	-5.76	-3.77

HOMO, highest occupied molecular orbital; ESOP = $E^*(\text{Ru}^{3+/2+})$, excited state oxidation potential; $\text{ESOP}_{\text{singlet}} = -E_{\text{HOMO}} - E_{0-0}$; $E_{0-0} = (S_0-S_1)$, the lowest vertical excitation energy, the lowest singlet–singlet transition; GSOP, E_{HOMO} , ground state oxidation potential.

* E_{0-0} , based on the experimental absorption and emission spectra (DMF), calculated from the point of overlap.

**IP, Ru^{3+/2+}, GSOP, the ionization potential measured using a photoemission yield spectrometer (Riken Keiki AC-3E); $E^*(\text{Ru}^{3+/2+})$, excited-state oxidation potential was calculated from: $E^*(\text{Ru}^{3+/2+}) = \text{Ru}^{3+/2+} - *E_{0-0}$. Calculated HOMO, ESOP, and E_{0-0} of N719 were performed elsewhere [59].

The MO analyses of **MH08** (Figure 5) showed that the HOMO is delocalized on Ru, NCS and extended to carbazole antenna with large coefficient, which is unprecedented. However, in the case of **MH09** and **MH10**, the HOMO was mainly delocalized on Ru and NCS. Considering both the conjugation length, nature of the hetero atoms and delocalization of the HOMO in the different antennas, the strength of the hetero-aromatic antennas as electron donor and hole-transport system can be described in the following order: N-benzylcarbazole > dibenzofurane > benzothiophene.

Hence, one should expect that the strength of electron donor and hole-transport, efficiency of charge separation, short-circuit photocurrent density (J_{SC}), and ESOP $\{E^*(Ru^{3+/2+})\}$ are interrelated and should be in the following order: **MH08** > **MH09** > **MH10**, which is consistent with the experimental J_{SC} ($mAcm^{-2}$) results (Tables II and III). Figure 5 shows that the LUMOs of **MH08–MH10** are delocalized on the electron acceptor bipyridyl to which the anchoring group is attached. Compared with the experimental CB edge of TiO_2 4.2 eV, the experimental and calculated (TD-DFT)

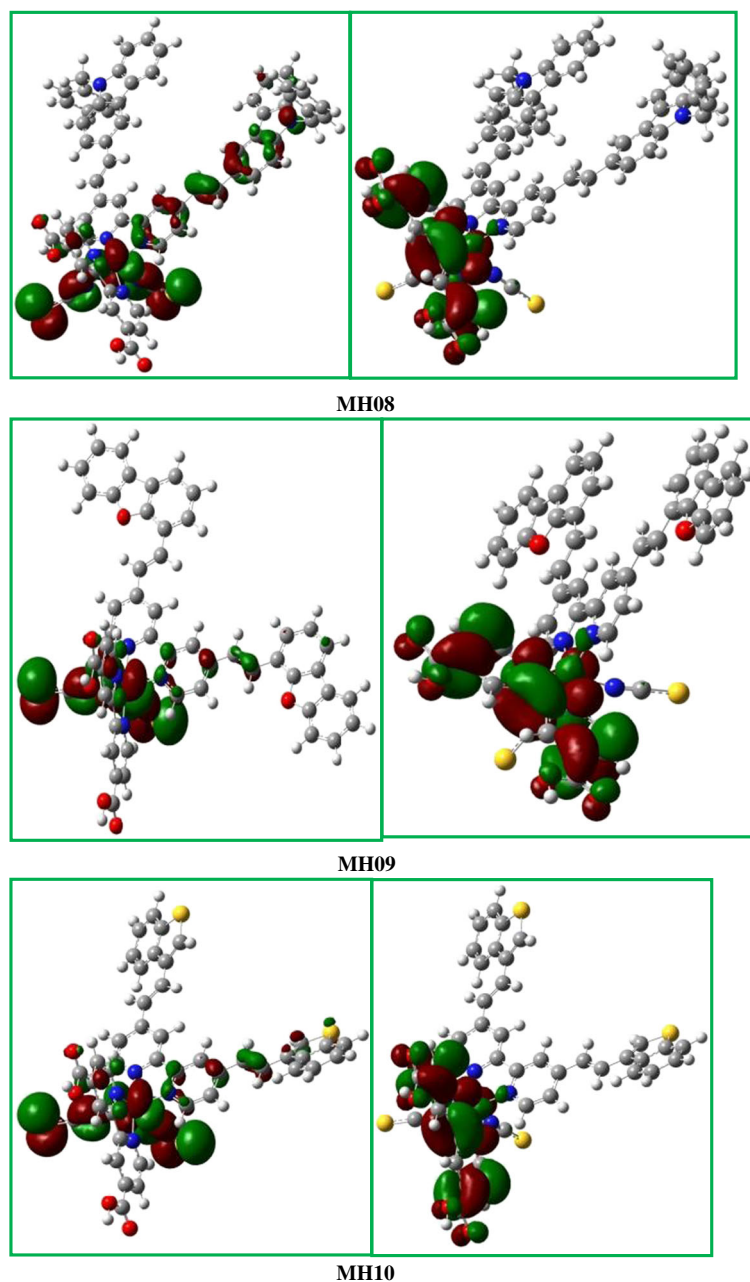


Figure 5. Calculated isosurfaces of the highest occupied molecular orbital (left) and lowest unoccupied molecular orbital (right) for **MH08–MH10**.

Table III. Photovoltaic performance¹ of ruthenium complexes MH08-TBA, MH08-MH10 and N719.

Dye	TBP (M)	J_{SC} (mA cm ⁻²)	V_{OC} (V)	FF	η (%)
MH08	0.3	19.80	0.658	0.711	9.27
MH08-TBA	0.3	19.56	0.683	0.731	9.76
MH09	0.3	19.26	0.653	0.711	8.94
MH10	0.3	18.21	0.630	0.691	7.92
N719	0.3	17.16	0.733	0.725	9.12
	0.5	16.85	0.749	0.739	9.32

¹Conditions: sealed cells; coadsorbate, DCA 20 mM; photoelectrode, TiO₂ (15 μ m thickness and 0.25 cm²); electrolyte, 0.6 M DMPiI, 0.1 M LiI, 0.05 I₂ in acetonitrile; irradiated light, AM 1.5 solar light (100 mW cm⁻²). J_{SC} , short-circuit photocurrent density; V_{OC} , open-circuit photovoltage; FF, fill factor; η , total power conversion efficiency.

ground and excited states oxidation potentials confirmed that MH08-MH10 are thermodynamically favorable for efficient electron injection and dye regeneration, respectively.

3.4. Attenuated total reflectance-Fourier transform infrared spectral data

Attenuated total reflectance-Fourier transform infrared spectra for MH08-MH10 exhibited strong and intense absorption peak at 2101 cm⁻¹, corresponding to the isothiocyanate (N-bonded isomer) group. The spectra also showed strong absorption peaks at 1723, 1720, and 1718 cm⁻¹ corresponding to the carbonyl stretch of COOH in MH08-MH10, respectively.

3.5. Photovoltaic properties

Figure 6 shows the IPCE spectra for the cells fabricated with dyes MH08-TBA, MH08-MH10 and N719, where the IPCE values are plotted as a function of wavelength.

Dye MH08 demonstrated the most efficient sensitization of nanocrystalline TiO₂ over the whole visible range

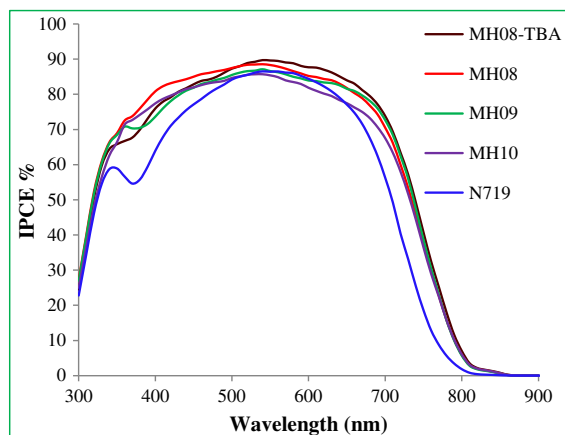


Figure 6. Photocurrent action spectra (incident photon to current conversion efficiency) obtained with dyes MH08-TBA, MH08, MH09, MH10 and N719 anchored on nanocrystalline TiO₂ film.

extending into the NIR region (ca. 860 nm) and showed an IPCE value of about 90% in the plateau region. Moreover, the IPCEs of dyes MH08-TBA and MH08-MH10 did not exhibit the sharp drop that N719 exhibited at 380 nm (Figure 6) because of the greater molar extinction coefficient of dyes MH08-MH10 in the region 350–450 nm. Although MH08-TBA showed better performance beyond 540 nm up to 860 nm, MH08 showed superior IPCE performance in the high energetic photons region 300–540 nm, which explains why the J_{SC} of MH08 was slightly higher than MH08-TBA. Taking into account the reflection and absorption losses by the conducting glass, the efficiency of electric current generation reaches about 100% over a broad wavelength range extending from 450 to 650 nm.

Compared with N719, MH08-TBA, MH08 and MH09 exhibited superior IPCE performance in the entire range 300–860 nm with the IPCE of N719 attenuated at 820 nm. Although the IPCE of N719 outperformed that of MH10 in the range 530–660 nm, the quantum efficiency of MH10 exceeded N719 throughout the rest of the spectrum. These results strongly suggest that MH08-MH10 are better light harvesters and sensitizers for TiO₂ in the NIR region.

The short-circuit photocurrent density (J_{SC}), open-circuit photovoltage (V_{OC}), fill factors (FF) and overall cell efficiencies (η) for each dye-TiO₂ electrode are summarized in Table III. Under the same experimental device conditions, MH08-TBA showed higher photocurrent and greater total conversion efficiency than N719, and this improvement was attributed to the superior LHE and more efficient charge separation in MH08-TBA, which translated into higher quantum efficiency throughout the visible region and NIR region up to 860 nm.

The photovoltaic performance parameters of MH08-TBA, MH08-MH10 and N719-sensitized cells were studied using electrolytes with 0.3 M TBP. Conversion of MH08 to MH08-TBA led to slight decrease in the J_{SC} from 19.80 to 19.56 mA cm⁻², but the V_{OC} increased from 0.658 to 0.683 because of the upward shift in the Fermi level, due to decrease in H⁺ concentration in the device, being more negative, and the FF increased from 0.711 to 0.731. In the case of N719, the J_{SC} decreased from 17.16 to 16.85 mA cm⁻², but the V_{OC} increased from 0.733 to 0.749 V and FF increased from 0.725 to 0.739 as the TBP concentration increased from 0.3 to 0.5 M. It is suggested that TBP was adsorbed on the bare TiO₂ surface and suppressed the recombination between the injected electron and I₃⁻ ions. It is also likely that TBP shifts the CB of the TiO₂ upwards, reducing the gap between the excited state of the dye and CB edge of TiO₂. This leads to less negative free energy of electron injection, and consequently slightly lower J_{SC} . It should also be noted that the V_{OC} of N719 > MH08 > MH09 > MH10.

Figure 7 shows photocurrent-voltage curves of sandwich-type sealed solar cells based on MH08-TBA, MH08-MH10 and N719 at standard AM 1.5 irradiation using an electrolyte of 0.6 M dimethylpropyl-imidazolium iodide (DMPiI), 0.05 M I₂, 0.1 M LiI, and 0.3 M 4-tert-butylpyridine (TBP) in acetonitrile. As shown in Table III, the solar cell sensitized

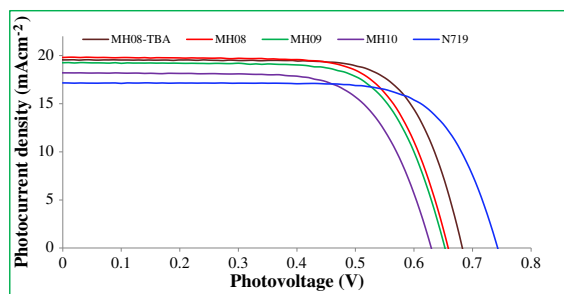


Figure 7. Photocurrent voltage characteristics of dye-sensitized solar cells sensitized with the complexes MH08-TBA, MH08, MH09, MH10 and N719. Electrolyte, 0.6 M DMPII, 0.1 M LiI, 0.05 I₂ in acetonitrile.

with **MH08-TBA** demonstrated the best DSSCs performance showing a J_{sc} of 19.56 mA cm^{-2} , a V_{oc} of 0.683 V, and an FF of 0.731, corresponding to an overall conversion efficiency (η) of 9.76% with the electrolyte containing 0.3 M TBP under standard AM 1.5 irradiation (100 mW cm^{-2}), which is 7% higher than **N719** of $\eta = 9.12\%$ under the same experimental conditions. Under these conditions, solar cells sensitized with **MH08** showed overall conversion efficiency (η) of 9.27%.

On the other hand, solar cells sensitized with **MH09** and **MH10** showed J_{sc} of 19.3 and 18.2 mA cm^{-2} , V_{oc} of 0.653 and 0.630 V, and FF of 0.711 and 0.691, corresponding to an overall conversion efficiency (η) of 8.94% and 7.92%, respectively. These results showed, undoubtedly, that the incorporation of N-benzylcarbazole (**MH08**) achieved more efficient electron donation, better hole-transport, and longer conjugation length ancillary ligand, which led to higher J_{sc} , V_{oc} , and η than dibenzofurane (**MH09**) or benzothiophene (**MH10**) analogs. It should be noted that although the conjugation lengths of the ancillary ligands in **MH08** and **MH09** are the same, they are longer than that of **MH10**.

Figure 8 depicts the interrelationship between the experimental ESOP and J_{sc} of **MH08–MH10**. These results clearly showed that as the ESOP became less negative, the J_{sc} increased. Hence, the more negative free energy of electron injection, the higher the J_{sc} .

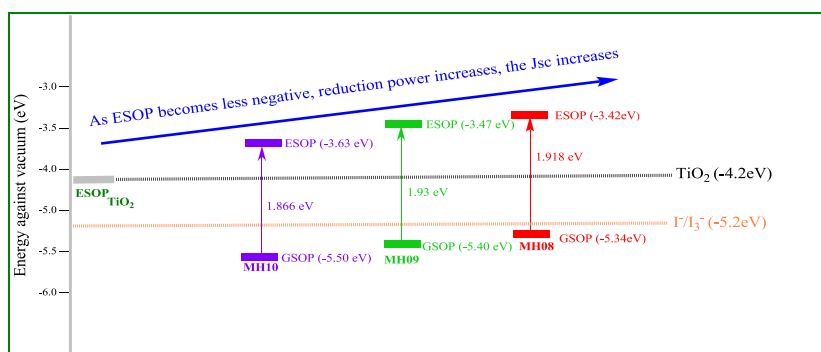


Figure 8. Interrelationship between experimental ESOP and J_{sc} of **MH08–MH10**.

Moreover, N-benzyl carbazole produced the most destabilization of the t_{2g} (HOMO). Therefore, these important results will be utilized, with the aid of molecular modeling, in our laboratory to design more efficient carbazole-based dyes for higher efficiency DSSCs.

4. CONCLUSIONS

Incorporation of hetero-aromatic electron-donor antennas into polypyridyl Ru(II) complexes conferred amphiphilic properties, owing to the hydrophobic nature of the antennas, and enhanced LHE and short-circuit photocurrent density significantly. When compared under the same experimental conditions, dyes containing N-benzylcarbazole antenna furnished the most destabilized t_{2g} , highest J_{sc} and total conversion efficiency compared with **MH09**, **MH10** and **N719**. Use of DFT/TD-DFT calculations was shown to be effective in the prediction of GSOP, ESOP, and E_{0-0} , which were in excellent agreement with the experimental results. Ancillary ligands comprised of carbazole antenna directly attached to bipyridyl via the CH=CH without electron donor spacer have significant impact on the delocalization of the HOMO and lead to large HOMO coefficient on the electron donor. Analysis of the short-circuit photocurrent density and excited state oxidation potential values of **MH08–MH10** showed that as the excited state oxidation potential increased and became less negative, the short-circuit photocurrent density increased considerably.

ACKNOWLEDGEMENTS

The authors are grateful to the Department of Textile Engineering, Chemistry, and Science Department at NC State for the financial support. This work was partially supported by Core Research for Evolutional Science and Technology (CREST) of the Japan Science and Technology Agency.

REFERENCES

1. McConnell RM. Assessment of dye-sensitized solar cell. *Renewable Sustainable Energy Rev* 2002; **6**: 273–293.
2. Asbury JB, Ellingson RJ, Ghosh HN, Ferrere S, Nozik AJ, Lian T. Femtosecond IR study of excited state relaxation and electron injection dynamics of Ru (dcbpy)₂(NCS)₂ in solution and on nanocrystalline TiO₂ and Al₂O₃ thin films. *The Journal of Physical Chemistry. B* 1999; **103**: 3110–3119.
3. Ellingson RJ, Asbury JB, Ferrere S, Ghosh HN, Sprague JR, Lian T, Nozik AJ. Dynamics of Electron Injection in Nanocrystalline Titanium Dioxide Films Sensitized with [Ru(4,4'-Dicarboxy-2,2'-Bipyridine)₂(NCS)₂] by Infrared Transient Absorption. *The Journal of Physical Chemistry. B* 1998; **102**: 6455–6458.
4. van de Lagemaat J, Frank AJ. Nonthermalized electron transport in dye-sensitized nanocrystalline TiO₂ films: transient photocurrent and random-walk modeling studies. *The Journal of Physical Chemistry. B* 2001; **105**: 11194–11205.
5. Hara K, Horieuchi H, Katoh R, Singh LP, Sugihara H, Sayama KM, Murata S, Tachiya M, Arakawa H. Effect of ligand structure on the efficiency of electron injection from excited Ru-phenanthroline complexes to nanocrystalline TiO₂ films. *The Journal of Physical Chemistry. B* 2002; **106**: 374.
6. Islam A, Sugihara H, Singh LP, Katoh R, Nagawa Y, Yanagida M, Takahashi Y, Murata S, Arakawa H. Synthesis and photophysical properties of ruthenium (II) charge transfer sensitizers containing 4,4'-dicarboxy-2,2'-biquinoline and 5,8-dicarboxy-6,7-dihydro-dibenzo [1,10]-phenanthroline. *Inorganica Chimica Acta* 2001; **322**: 7–16.
7. Kubo W, Kitamura T, Hanabusa K, Wada Y, Yanagida S. Quasi-solid-state dye-sensitized solar cells using room temperature molten salts and a low molecular weight gelator. *Chemical Communications* 2002; **4**: 374–375.
8. Boschloo G, Lindstrom H, Magnusson E, Holmberg A, Hagfeldt A. Optimization of dye-sensitized solar cells prepared by compression method. *Photochem. Photobiol., A: Chem.* 2002; **148**: 11–15.
9. Hagfeldt A, Grätzel M. Molecular Photovoltaics. *Accounts of Chemical Research* 2000; **33**: 269–277.
10. Ferrere S, Gregg BA. Large Increases in Photocurrents and Solar Conversion Efficiencies by UV Illumination of Dye Sensitized Solar Cells. *The Journal of Physical Chemistry. B* 2001; **105**: 7602–7605.
11. Heimer TA, Heilweil J, Bignozzi CA, Meyer GJ. Electron injection, recombination, and halide oxidation dynamics at dye-sensitized metal oxide interfaces. *Journal of Physical Chemistry A* 2000; **104**: 4256–4262.
12. Nogueira AF, Durrant JR, De Paoli M-A. Dye-Sensitized Nanocrystalline Solar Cells Employing a Polymer Electrolyte. *Advanced Materials* 2001; **13**: 826–830.
13. Oskam G, Bergeron BV, Meyer GJ, Searson PC. Pseudohalogens for dye-sensitized TiO₂ photoelectrochemical cells. *The Journal of Physical Chemistry. B* 2001; **105**: 6867–6873.
14. Sauve' G, Cass ME, Doig SJ, Lauermaun I, Pomykal K, Lewis NS. High Quantum Yield Sensitization of Nanocrystalline Titanium Dioxide Photoelectrodes with cis-Dicyanobis(4,4'-dicarboxy-2,2'-bipyridine) osmium (II) or Tris(4,4'-dicarboxy-2,2'-bipyridine)osmium(II) Complexes. *Journal of Physical Chemistry* 2000; **104**: 3488–3491.
15. De Paoli M-A, Machado DA, Nogueira AF, Longo C. All-polymeric electrochromic and photoelectrochemical devices: new advances. *Electrochimica Acta* 2001; **46**: 4243–4249.
16. Hou Y-J, Xie P-H, Zhang B-W, Cao Y, Xiao X-R, Wang W-B. Influence of the Attaching Group and Substituted Position in the Photosensitization Behavior of Ruthenium Polypyridyl Complexes. *Inorganic Chemistry* 1999; **38**: 6320–6322.
17. Kumara GRA, Konno A, Shiratsuchi K, Tsukahara J, Tennakone K. Dye-Sensitized Solid-State Solar Cells: Use of Crystal Growth Inhibitors for Deposition of the Hole Collector. *Chemistry of Materials* 2002; **14**: 954–955.
18. Lemon B, Hupp JT. Effect of Secondary Substituent on the Physical Properties, Crystal. Zirconium Dioxide/Solution Interfaces. *The Journal of Physical Chemistry. B.* 1999; **103**: 3797–3799.
19. Lees AC, Kleverlaan CJ, Bignozzi CA, Vos JG. Photophysical Properties of TiO₂ Surfaces Modified with Dinuclear RuRu and RuOs Polypyridyl Complexes. *Inorganic Chemistry* 2001, **40**, 5343–5349.
20. Han L, Islam A, Chen H, Malapaka C, Chiranjeevi B, Zhang S, Yang X, Yanagida M. Porphyrin-sensitized solar cells with cobalt (II/III)-based redox electrolyte exceed 12% efficiency. *Energy Environ. Sci.* 2012; **5**: 6057–6060.
21. Yella A, Lee H-W, Tsao HN, Yi C, Chandiran AK, Nazeeruddin MK, Diao EW-G, Yeh C-Y, Zakeeruddin SM, Grätzel M. Porphyrin-sensitized solar cells with cobalt (II/III)-based redox electrolyte exceed 12 percent efficiency. *Science* 2011; **334**: 629–634.
22. Oregan B, Grätzel M. A low-cost, high-efficiency solar cell based on dye-sensitized colloidal TiO₂ films. *Nature* 1991; **353**: 737–740.
23. Nazeeruddin MK, De Angelis F, Fantacci S, Selloni A, Viscardi G, Liska P, Ito S, Takeru B, Grätzel M. Combined experimental and DFT-TDDFT computational study of photoelectrochemical cell ruthenium sensitizers. *Journal of the American Chemical Society* 2005; **127**: 16835–16847.

24. Nazeeruddin MK, Kay A, Rodicio I, Humphry-Baker R, Müller E, Liska P, Vlachopoulos N, Grätzel M. Conversion of Light to Electricity by cis-X2Bis(2,2'-bipyridyl-4,4'-dicarboxylate)ruthenium(II) Charge-Transfer Sensitizers (X = Cl-, Br-, I-, CN-, and SCN-) on Nanocrystalline TiO₂ Electrodes. *Journal of the American Chemical Society* **115**, 6382–6390.
25. Wang M, Chamberland N, Breau L, Moser J, Humphry-Baker R, Marsa B, Zakeeruddin SM, Grätzel M. *Nature Chemistry* 2010; **2**: 385–389.
26. Nusbaumer H, Moser J, Zakeeruddin SM, Nazeeruddin MK, Grätzel M. Zakeeruddin SM, Nazeeruddin MK, Grätzel M. Co^{II}(dbbip)₂²⁺ complex rivals tri-iodide/iodide redox mediator in dye-sensitized photovoltaic cells *The Journal of Physical Chemistry. B* 2001; **105**: 10461–10465.
27. Tiana H, Sun L, Mater J. Iodine-free redox couples for dye-sensitized solar cells. *Chem.* 2011; **21**: 10592–10601.
28. Oskam G, Bergeron BV, Meyer GJ, Searson PC. Pseudohalogens for Dye-Sensitized TiO₂ Photoelectrochemical Cells. *The Journal of Physical Chemistry. B* 2001; **105**: 6867–6873.
29. Islam A, Sugihara H, Arakawa H. Molecular design of ruthenium(II) polypyridyl photosensitizers for efficient nanocrystalline TiO₂ solar cells. *J. Photochem. Photobiol., A* 2003; **158**: 131–138.
30. Nazeeruddin MK, PJchy P, Renouard T, Zakeeruddin SM, Humphry-Baker R, Comte P, Liska P, Cevey L, Costa E, Shklover V, Spiccia L, Deacon GB, Bignozzi CA, Grätzel M. Engineering of efficient panchromatic sensitizers for nanocrystalline TiO₂-based solar cells. *Journal of the American Chemical Society* 2001; **123**: 1613–1624.
31. A Islam, H Sugihara, M Yanagida, K Hara, G Fujihashi, Y Tachibana, R Katoh, S Murata, H Arakawa, Efficient panchromatic sensitization of nanocrystalline TiO₂ films by b-diketonato ruthenium polypyridyl complexes. *New J. Chem.* 2002, **26**, 966–968.
32. Wang P, Zakeeruddin SM, Moser JE, Nazeeruddin MK, Sekiguchi T, Grätzel M. A stable quasi-solid-state dye-sensitized solar cell with an amphiphilic ruthenium sensitizer and polymer gel electrolyte. *Nature Materials* 2003; **2**: 402–407.
33. Campbell WM, Jolley KW, Wagner P, Wagner K, Walsh PJ, Gordon KC, Schmidt-Mende L, Nazeeruddin MK, Wang Q, Grätzel M, Officer DL. Highly Efficient Porphyrin Sensitizers for Dye-Sensitized Solar Cells. *Journal of Physical Chemistry C* 2007; **111**: 11760–11762.
34. Wang ZS, Cui Y, Hara K, Dan-oh Y, Kasada C, Shinpo A. A High-Light-Harvesting-Efficiency Coumarin Dye for Stable Dye-Sensitized Solar Cells. *Advanced Materials* 2007; **19**: 1138–1141.
35. Yum JH, Walter P, Huber S, Rentsch D, Geiger T, Nuesch F, De Angelis F, Grätzel M, Nazeeruddin MK. Efficient far red sensitization of nanocrystalline TiO₂ Films by an Unsymmetrical Squaraine Dye. *Journal of the American Chemical Society* 2007; **129**: 10320–10321.
36. Choi H, Baik C, Kang SO, Ko J, Kang MS, Nazeeruddin MK, Grätzel M. Highly Efficient and thermally stable organic sensitizers for Solvent-Free Dye-Sensitized Solar Cells. *Angewandte Chemie* 2008; **120**: 333–336; *Angew. Chem. Int. Ed.* 2008, **47**, 327.
37. Kuang D, Uchida S, Humphry-Baker R, Zakeeruddin SM, Grätzel M. Organic Dye-Sensitized Ionic Liquid Based Solar Cells: Remarkable Enhancement in Performance through Molecular Design of Indoline Sensitizers. *Angewandte Chemie* 2008; **120**: 1949–1953; *Angew. Chem. Int. Ed.* 2008, **47**, 1923.
38. Wang P, Zakeeruddin SM, Moser J-E, Humphry-Baker R, Comte P, Aranyos V, Hagfeldt A, Nazeeruddin MK, Grätzel M. Stable New Sensitizer with Improved Light Harvesting for Nanocrystalline Dye-Sensitized Solar Cells. *Advanced Materials* 2004; **16**: 1806–18011.
39. Klein C, Nazeeruddin MK, Liska P, Censo DD, Hirata N, Palomares E, Durrant JR, Grätzel M. Engineering of a Novel Ruthenium Sensitizer and its Application in Dye-Sensitized Solar Cells for Conversion of Sunlight into Electricity. *Inorganic Chemistry.* 2005; **44**: 178–180.
40. Wang P, Klein C, Humphry-Baker R, Zakeeruddin SM, Grätzel M. A high molar extinction coefficient sensitizer for stable dye-sensitized solar cells. *Journal of the American Chemical Society* 2005; **127**: 808–809.
41. Jiang KJ, Masaki N, Xia JB, Noda S, Yanagida S. A novel ruthenium sensitizer with a hydrophobic 2-thiophen-2-yl-vinyl-conjugated bipyridyl ligand for effective dye sensitized TiO₂ solar cells. *Chemical Communications* 2006; **23**: 2460–2462.
42. Kuang D, Klein C, Ito S, Moser JE, Humphry-Baker R, Evans N, Duriaux F, Grätzel C, Zakeeruddin SM, Grätzel M. High-Efficiency and Stable Mesoscopic Dye-Sensitized Solar Cells Based on a High Molar Extinction Coefficient Ruthenium Sensitizer and Nonvolatile Electrolyte. *Advanced Materials* 2007; **19**: 1133–1137.
43. a) Bisquert J. Theory of the Impedance of Electron Diffusion and Recombination in a Thin Layer. *The Journal of Physical Chemistry. B* 2002; **106**: 325–333; b) Bisquert J. Chemical capacitance of nanostructured semiconductors: its origin and significance for nanocomposite solar cells. *Physical Chemistry Chemical Physics* 2003; **5**: 5360–5364; c) van de Lagemaat J, Park NG, Frank AJ. Influence of Electrical Potential Distribution, Charge Transport, and Recombination on the Photopotential and Photocurrent Conversion Efficiency of Dye-Sensitized Nanocrystalline TiO₂ Solar Cells: A Study by Electrical

- Impedance and Optical Modulation Techniques. *The Journal of Physical Chemistry. B* **2000**; *104*: 2044–2052; d) Bisquert J, Zaban A, Greenshtein M, Mora-Sero I. *Journal of the American Chemical Society* 2004; **126**: 13550.
44. Clifford JN, Palomares E, Nazeeruddin MK, Grätzel M, Nelson J, Li X, Long NJ, Durrant JR. Molecular control of recombination dynamics in dye-sensitized nanocrystalline TiO₂ films: Free energy vs distance dependence. *Journal of the American Chemical Society* 2004; **126**: 5225.
45. Chen CY, Wu SJ, Wu CG, Chen JG, Ho KC. A ruthenium complex with super high light-harvesting capacity for dye-sensitized solar cells. *Angewandte Chemie* 2006; **118**, 5954; *Angew. Chem. Int. Ed.* 2006, *45*, 5822–5825.
46. Chen CY, Wu SJ, Wu CG, Chen JG, Ho KC. A New Route to Enhance the Light-Harvesting Capability of Ruthenium Complexes for Dye-Sensitized Solar Cells. *Advanced Materials* 2007, **19**, 3888–3891.
47. Wang P, Zakeeruddin SM, Moser JE, Nazeeruddin MK, Sekiguchi T, Grätzel M. A stable quasi-solid-state dye-sensitized solar cell with an amphiphilic ruthenium sensitizer and polymer gel electrolyte. *Nature Materials* 2003; **2**: 402–407.
48. Wang P, Zakeeruddin SM, Humphry-Baker R, Moser JE, Grätzel M. Molecular-Scale Interface Engineering of TiO₂ Nanocrystals: Improve the Efficiency and Stability of Dye-Sensitized Solar Cells. *Advanced Materials* 2003; **15**: 2101–2104.
49. Wang P, Zakeeruddin SM, Comte P, Charvet R, Humphry-Baker R, Grätzel M. Enhance the performance of dye-sensitized solar cells by co-grafting amphiphilic sensitizer and hexadecylmalonic acid on TiO₂ Nanocrystals. *The Journal of Physical Chemistry. B* 2003; **107**: 14336–14341.
50. Wang Z, Yamaguchi T, Sugihara H, Arkawa H. Significant efficiency improvement of the black dye-sensitized solar cell through protonation of TiO₂ Films. *Langmuir* 2005; **21**: 4272–4276.
51. Islam A, Chowdhury FA, Chiba Y, Komiya R, Fuke N, Ikeda N, Nozaki K, Han L. Synthesis and characterization of new efficient tricarboxyterpyridyl (β -diketonato) ruthenium(II) sensitizers and their applications in dye-sensitized solar cells. *Chemistry of Materials* 2006; **18**: 5178–5185.
52. Islam A, Sugihara H, Hara K, Singh, LP, Katoh, R, Yanagida, M, Takahashi, Y, Murata, S, Arakawa, H. Dye sensitization of nanocrystalline titanium dioxide with square planar platinum(II) diimine dithiolate complexes. *Inorganic Chemistry* 2001; **40**(21): 5371–5380.
53. Garelli N, Vierling P. Synthesis of new amphiphilic perfluoroalkylated bipyridines. *Journal of Organic Chemistry* 1992; **57**(11): 3046–3051.
54. Becke AD. Density-functional exchange-energy approximation with correct asymptotic behavior. *Physical Review A* 1988; **38**: 3098–3100.
55. Lee CT, Yang WT, Parr RG. Development of the Colle-Salvetti correlation-energy formula into a functional of the electron density. *Physical Review B* 1988; **37**: 785–789.
56. Godbout N, Salahub DR, Andzelm J, Wimmer E. Optimization of Gaussian-type basis sets for local spin density functional calculations. Part I. Boron through neon, optimization technique and validation. *Canadian Journal of Chemistry* 1992; **70**: 560–571.
57. Sosa C, Andzelm J, Elkin BC, Wimmer E, Dobbs KD, Dixon DA. A local density functional study of the structure and vibrational frequencies of molecular transition-metal compounds. *Journal of Physical Chemistry* 1992; **96**: 6630–6636.
58. Hagfeld A, Grätzel M. Light-Induced Redox Reactions in Nanocrystalline Systems. *Chemical Reviews* 1995; **95**: 49–68.
59. De Angelis F, Fantacci S, Selloni A. Alignment of the dye's molecular levels with the TiO₂ band edges in dye-sensitized solar cells: a DFT–TDDFT study. *Nanotechnology* 2008; **19**: 424002–424009.

Supporting Information and Experimental Section

Structure-activity Relationship of Hetero-aromatic-electron-donor Antennas for High Efficiency Dye-sensitized Solar Cells (DSSCs)

Ahmed El-Shafei^{a*}, Maqbool Hussain^a, Ashrafal Islam^b, Liyuan Han^b

^aPolymer and Color Chemistry Program, North Carolina State University, Raleigh, NC, 27695, USA.

^bPhotovoltaic Materials Unit, National Institute for Materials Science, 1-2-1 Sengen, Tsukuba, Ibaraki 305-0047, Japan.

*Corresponding Authors: Ahmed_El-Shafei@ncsu.edu

1.1. Analytical Measurements.

1.1.1. Fluorescence and Time-correlated Single Photon Counting (TCSPC) Lifetime

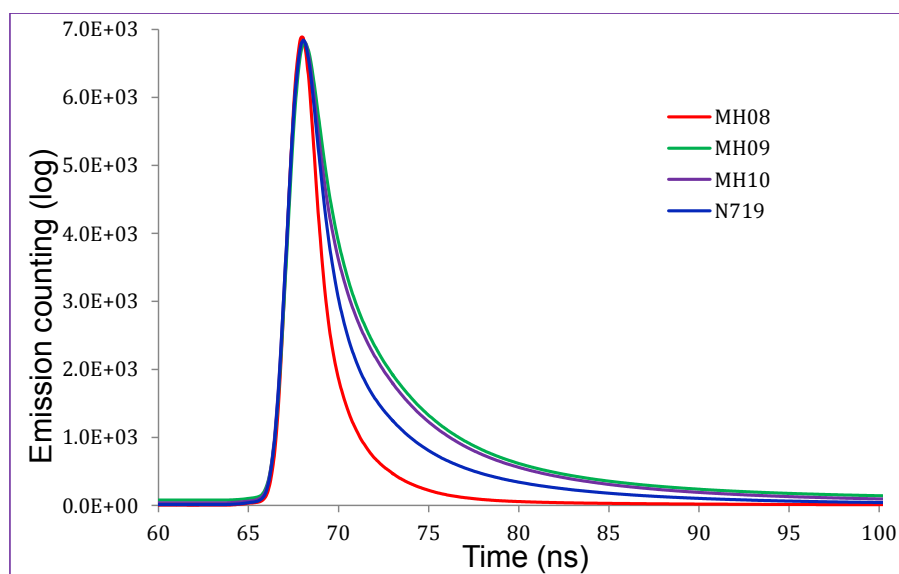


Figure S1 Time-resolved photoluminescence decays of complexes **MH08-10** in DMF (anhydrous). The emission decays were recorded by exciting at 454 nm at 0.1 optical absorbivity. The decay data was fitted using 3-exponential at a channel range of 1000 nm-3000 nm. The lowest excited state lifetime 9 ns, 105 ns, 85 ns, respectively. The excited state lifetime of MH08-10 is long enough to allow sufficient amount of electron injection into TiO₂ before the complexes relaxes back to its ground state.

1.1.2. Attenuated Total Reflectance Fourier-transform Infra Red Spectroscopy

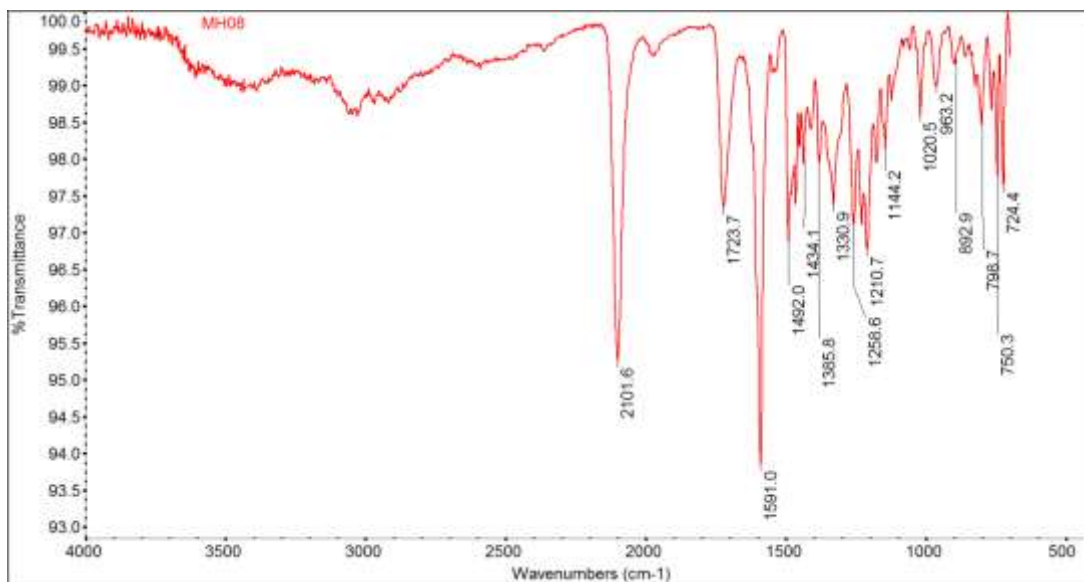


Figure S2 ATR/FT-IR spectrm of MH08.

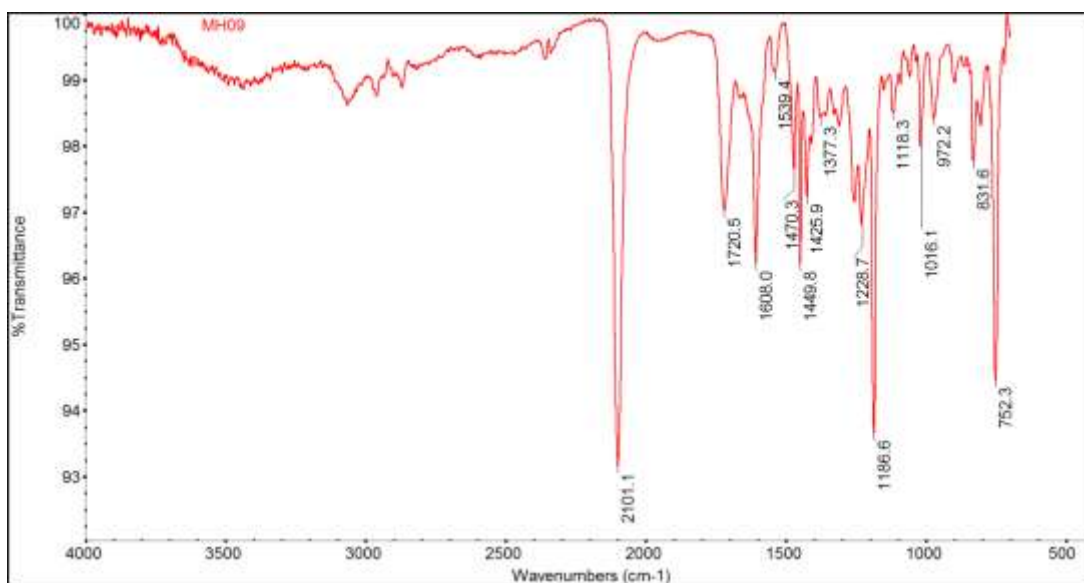


Figure S3 ATR/FT-IR spectrm of MH09.

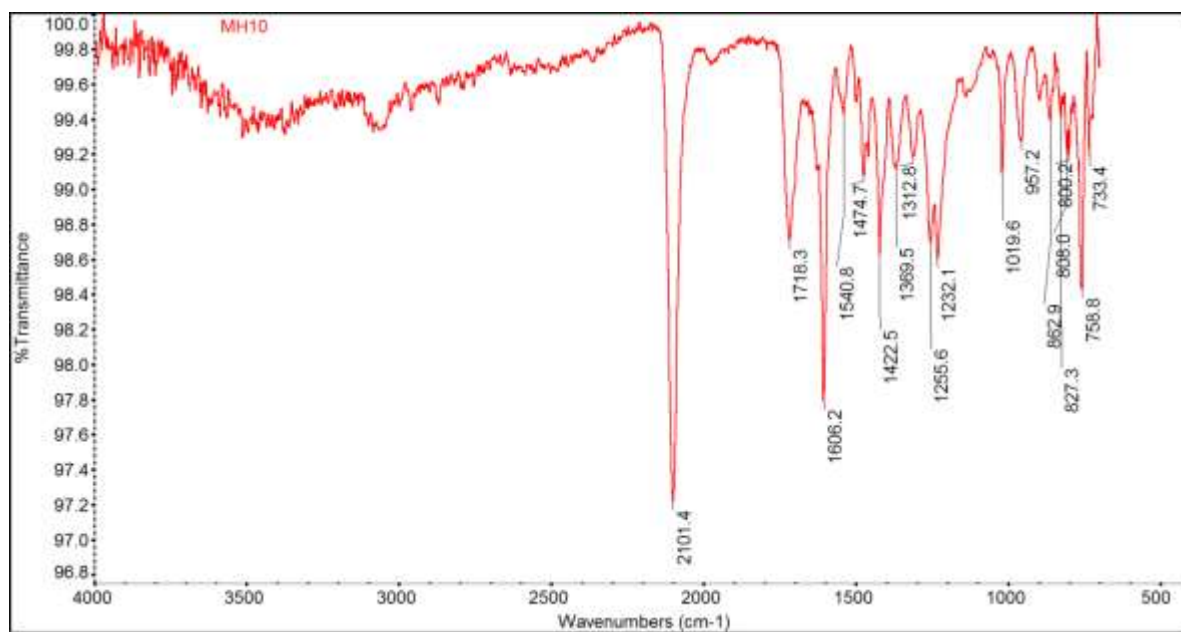


Figure S4 ATR/FT-IR spectrm of **MH10**.

1.1.3. Mass Spectroscopy

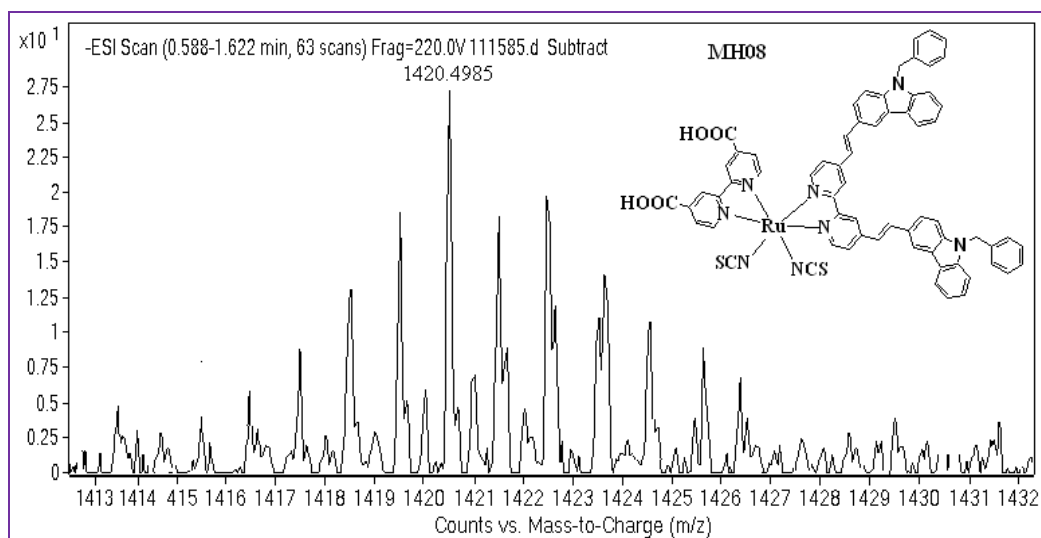


Figure S5 ESI mass spectrum of **MH08**, Mass 1180.2127; $[M - 2H + TBA]^{-1}$, Theo. M/Z = 1420.4975, Found M/Z = 1420.4985, Error = 0.725 ppm.

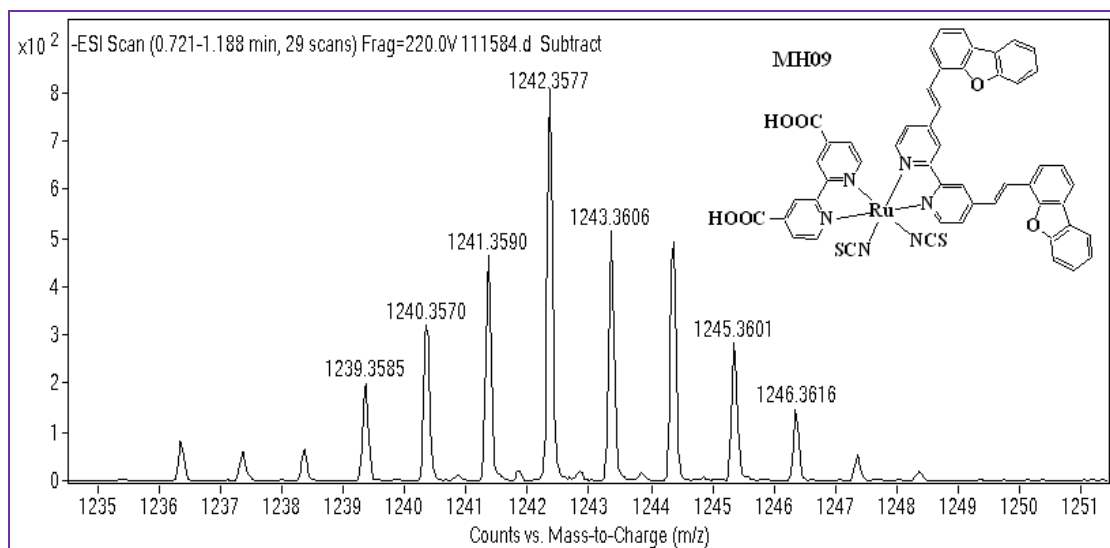


Figure S6 ESI mass spectrum of **MH09**, Mass 1002.0868; $[M - 2H + TBA]^{-1}$, Theo. M/Z 1242.3559, Found M/Z = 1242.3577, Error = 1.4488 ppm.

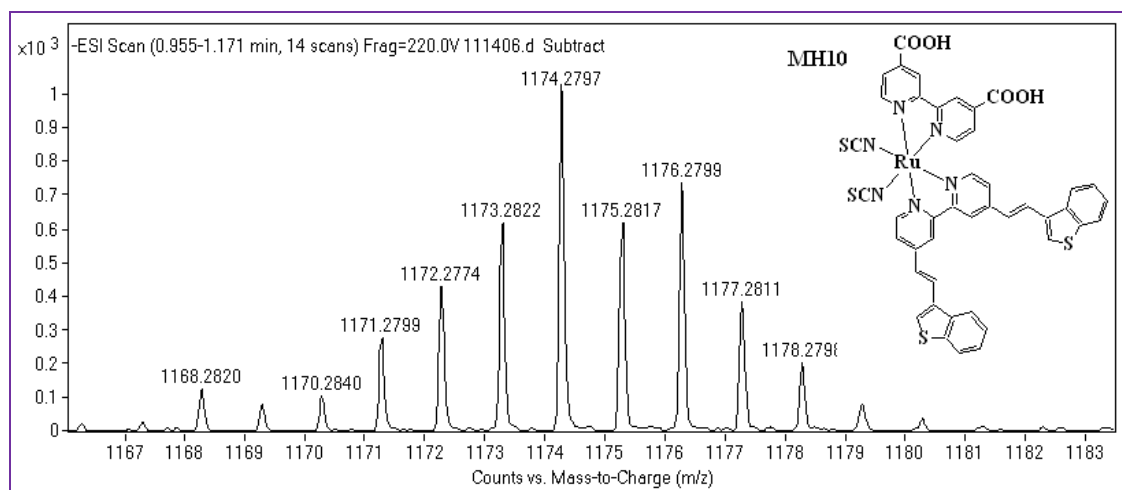


Figure S7 ESI mass spectrum of **MH10**, Mass 934.0098; $[M - 2H + TBA]^{-1}$, Theo. $M/Z = 1174.2789$, Found $M/Z = 1174.2797$, Error = 0.62165ppm.

1.1.4. ^1H -NMR Experiments

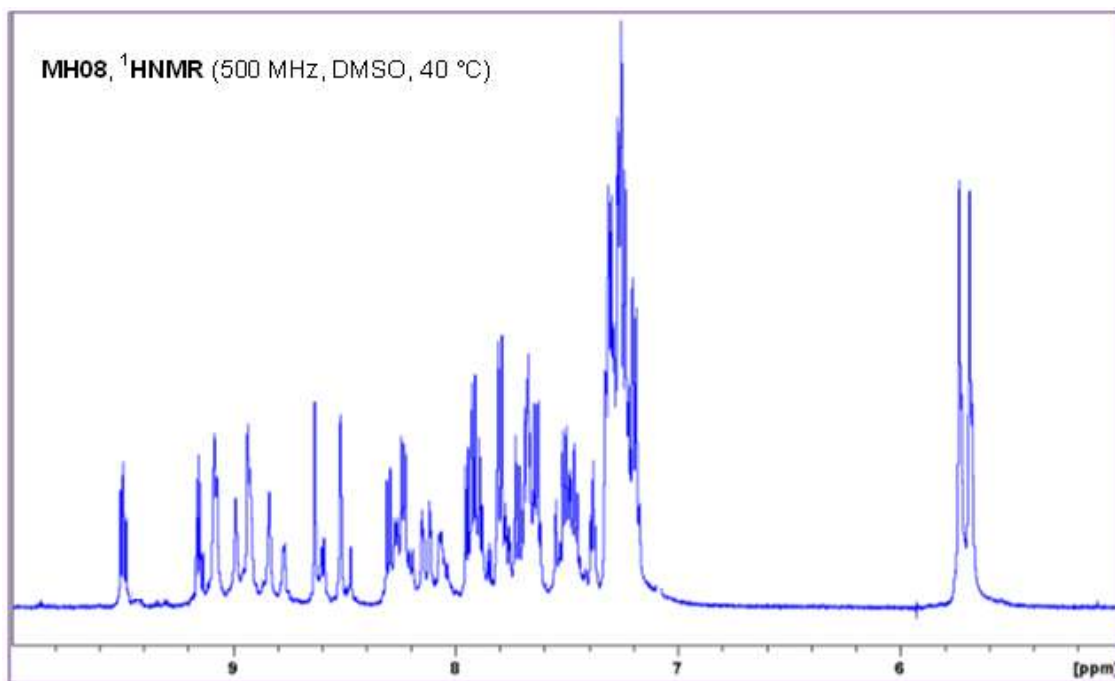


Figure S8 H-NMR spectrm of **MH08**.

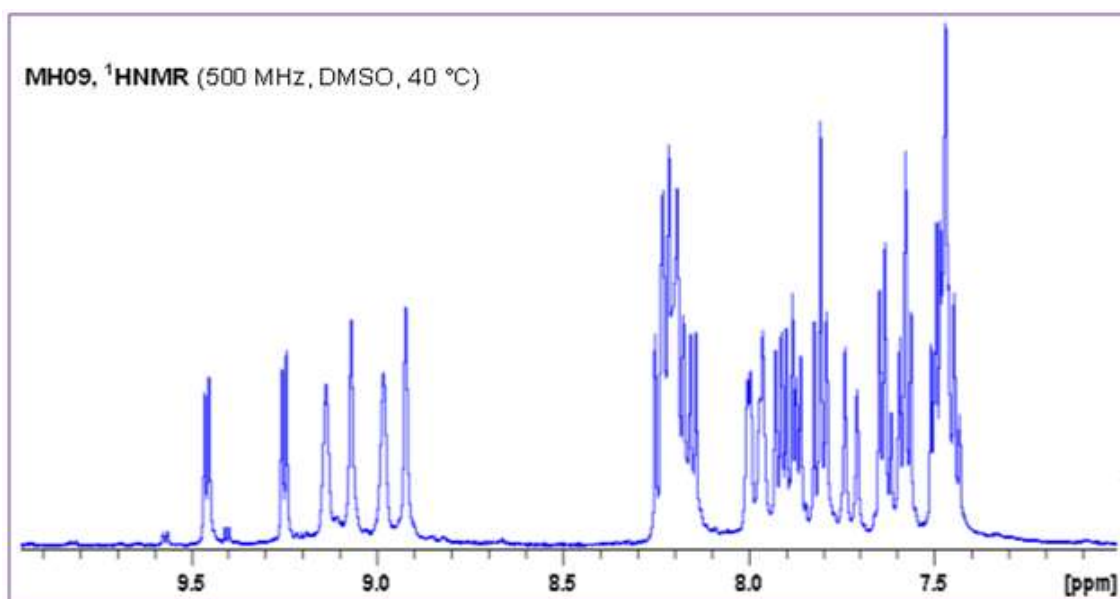


Figure S9 H-NMR spectrm of **MH09**.

1.2. Photoelectrochemical Measurements

1.2.1. Photoemission Yield Spectrometer (AC3) and $E_{0,0}$ Measurements

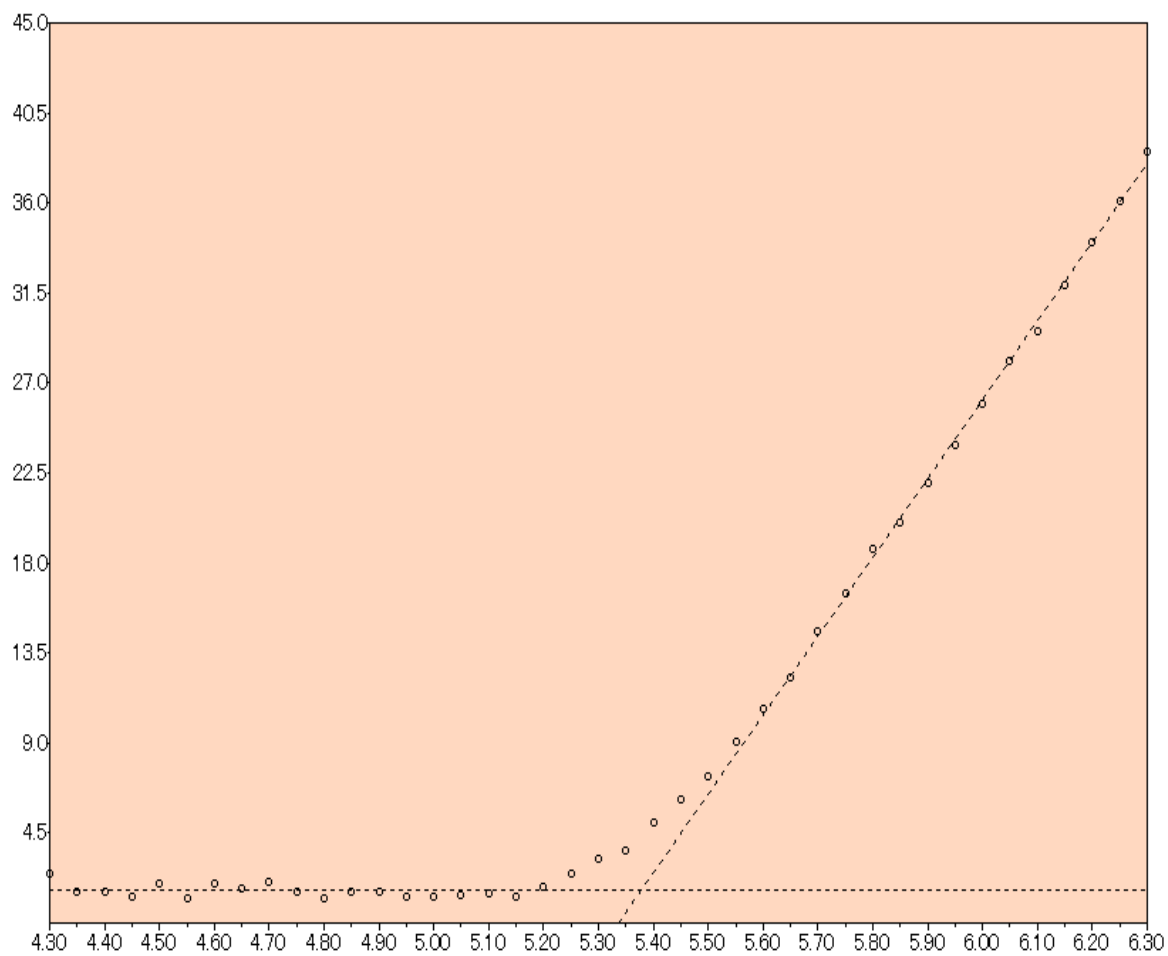


Figure S11 HOMO (-5.34eV) of **MH08**.

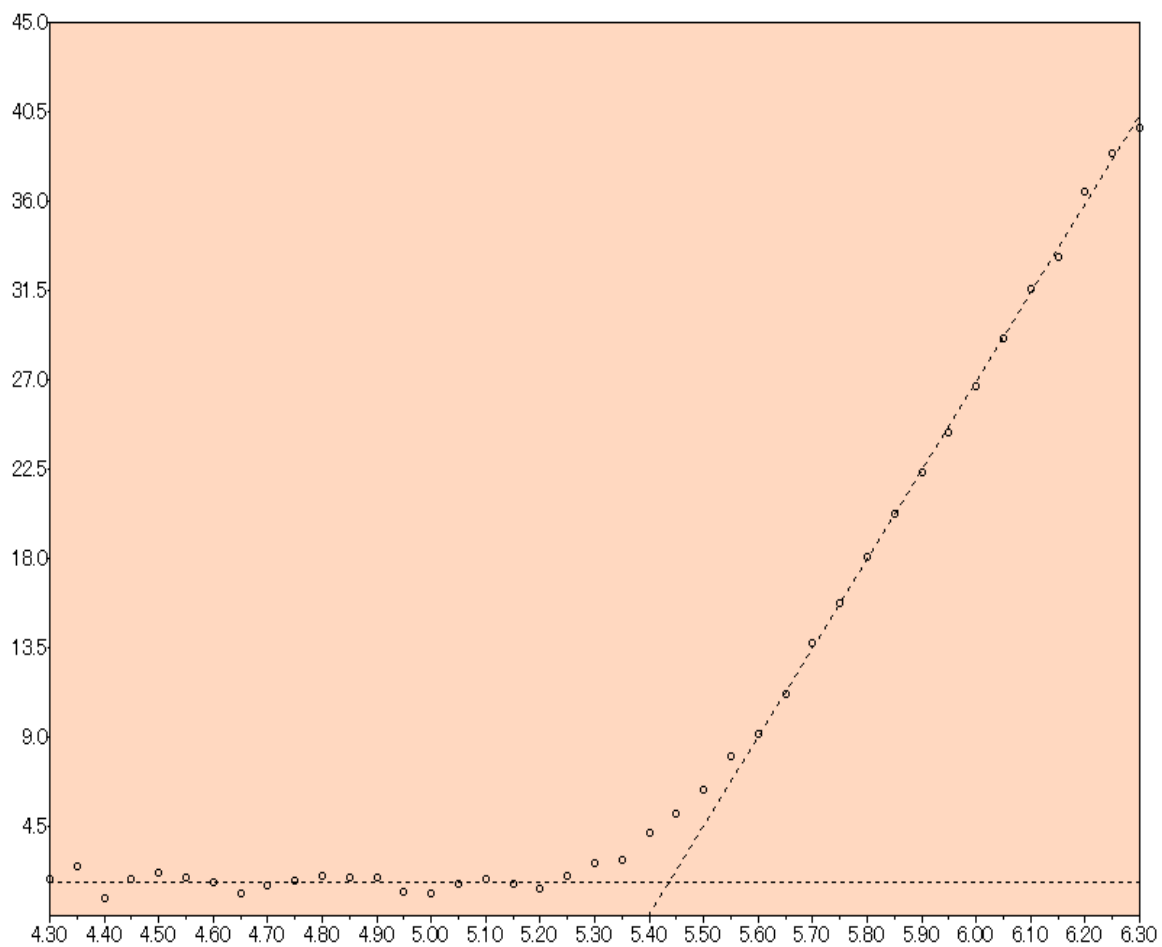


Figure S12 HOMO energy (-5.40eV) of MH09.

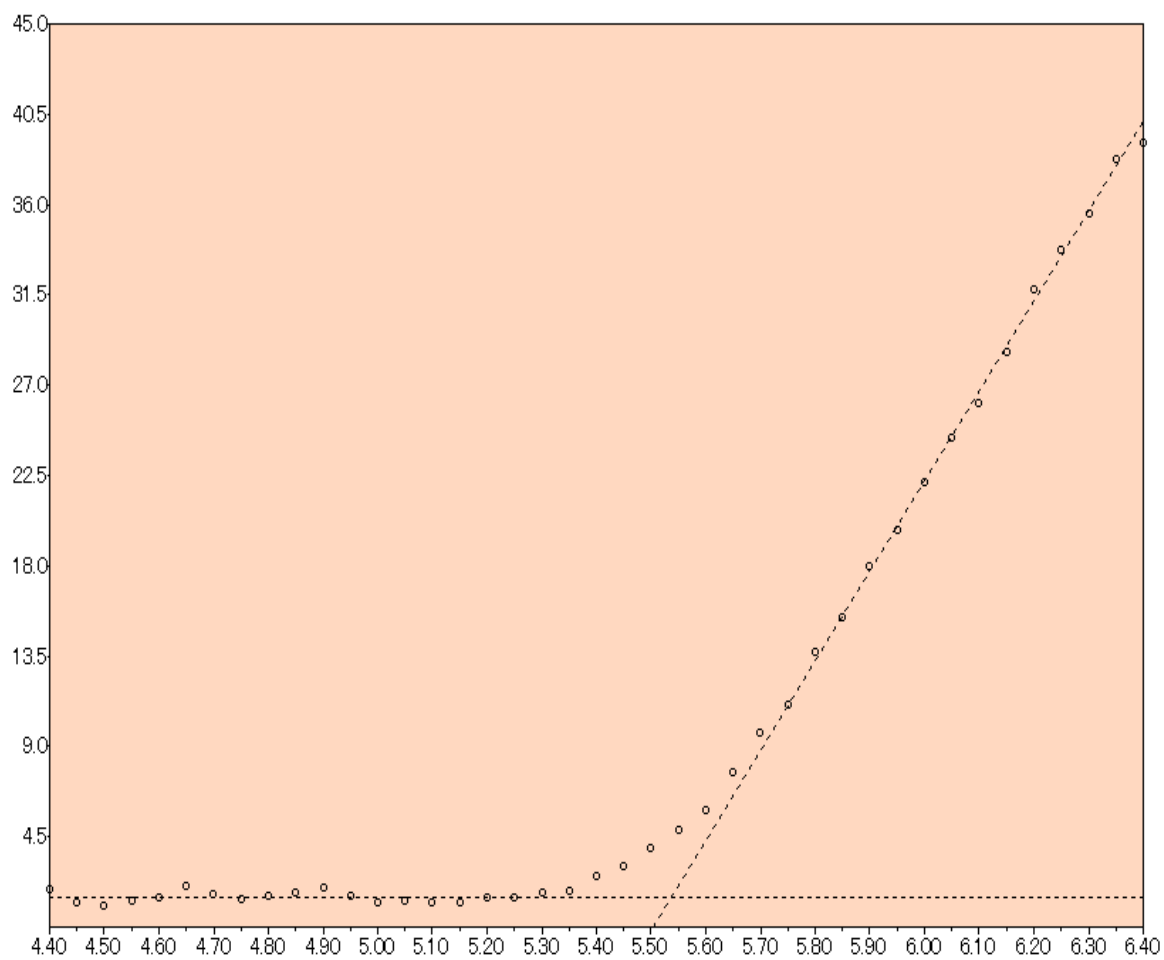


Figure S13 HOMO energy (-5.50eV) of MH10.

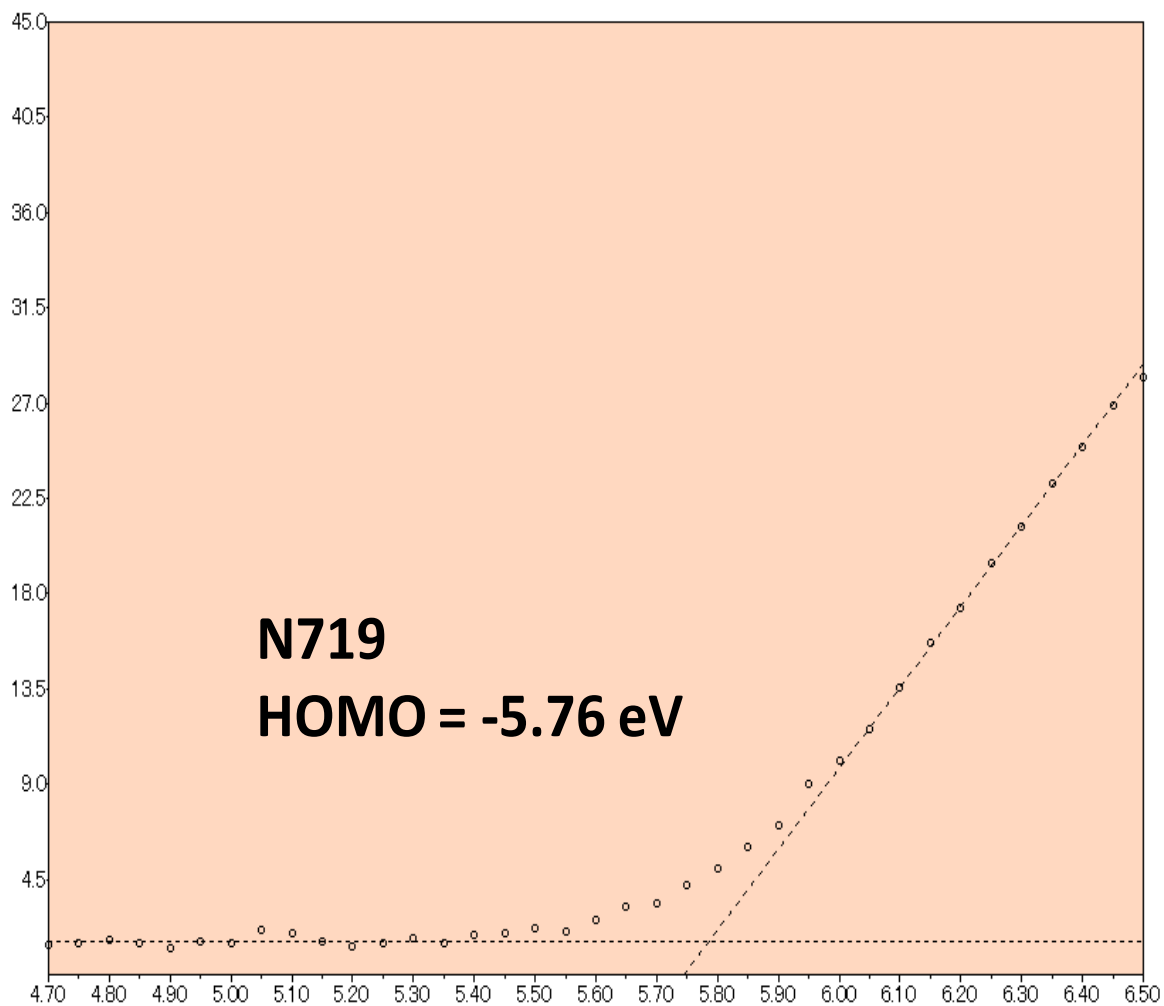
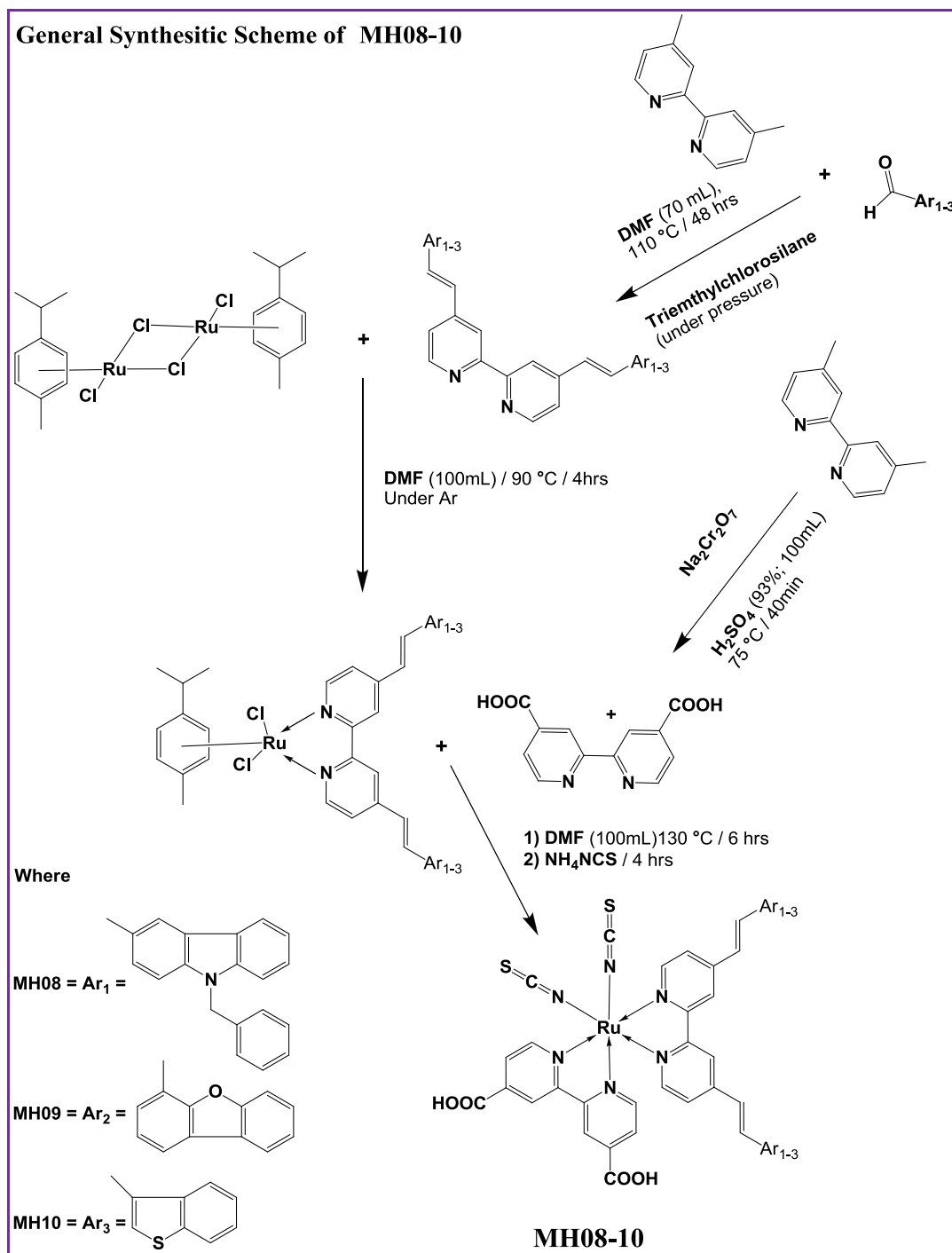


Figure S14 HOMO energy (-5.67eV) of N719.

1.3. Synthesis



Scheme S1. General route for the synthesis of complexes **MH08-10**.

1.4. Purification

MH08 was purified on a column using Sephadex LH-20 as the stationary phase and pure methanol as the mobile phase. The crude dye of **MH08** (0.5g) was dissolved in a mixture of methanol (5mL) and TBAOH (1mL) and loaded on Sephadex LH-20, and the compound was eluted using methanol neat. The main band was collected and acidified using 0.1M HCl until the pH dropped to 2.0, and the acidified solution was kept in a refrigerator for 48 hours. Then, the precipitate was collected by filtration, washed with de-ionized water to remove residual HCl. The same purification procedure was repeated three times in order to obtain **MH08** in the pure form. Complexes **MH09** and **MH10** were purified using the above procedure.

GENERAL CONCLUSIONS

In the current investigation, new heterocyclic ancillary ligands of **Ar1**, **Ar3** and **Ar5-10** were molecularly designed with strong electron donating groups coupled with an extended π -conjugated system to study the influence of different heterocyclic electron donors on the interrelationship of photophysical, electrochemical properties, and device photovoltaic performances for DSSCs. The experimental results showed that incorporation of strong electron donating groups and extending the conjugations on bipyridyl moiety furnished highly efficient light harvesting properties and bathochromic shift as compared to benchmark dye-**N719**. The UV-spectral profile of all complexes is almost similar and showed two broad absorption bands in the visible region. In addition, the experimental ground and excited state oxidation potentials values illustrated that the strong electron donating groups destabilized the metal-HOMO (t_{2g} of Ru (II)) more than that of ligand-LUMO resulting smaller HOMO/LUMO gap as compared to **N719**.

The impressive light harvesting performance of **MH01-TBA**, **MH08-TBA**, **MH11-TBA**, furnished better photocurrent and higher solar-to-power conversion efficiency of 9.91%, 9.76%, and 10.06% respectively, compare to 9.32% of the benchmark dye-**N719**, under the same experimental condition. In contrast, despite impressive light harvesting properties of **MH03**, **MH05** and **MH09-10**, due to the nature of the electron donor.

Tetrabutylammonium (TBA) substituted **MH01-TBA**, **MH05-TBA** and **MH11-TBA** demonstrated significantly higher solar-to-power conversion efficiency and open-circuit photovoltage (V_{oc}) than that of the corresponding free acid.